

# Sensitivity of Pusher Propeller Performance and Noise Emissions to the Upstream Wake Characteristics

An Experimental and Numerical Study

October 23, 2015

Master of Science Thesis

V.V. Channa

Technische Universiteit Delft





**SENSITIVITY OF PUSHER PROPELLER  
PERFORMANCE AND NOISE EMISSIONS TO THE  
UPSTREAM WAKE CHARACTERISTICS  
AN EXPERIMENTAL AND NUMERICAL STUDY  
OCTOBER 23, 2015**

MASTER OF SCIENCE THESIS

For obtaining the degree of Master of Science in Aerospace Engineering  
at Delft University of Technology

**V.V. Channa**

Thesis Registration Number: 056#15#MT#FPP

Faculty of Aerospace Engineering - Delft University of Technology



DELFT UNIVERSITY OF TECHNOLOGY  
DEPARTMENT OF AERODYNAMICS, WIND ENERGY, FLIGHT PERFORMANCE AND PROPULSION

The undersigned hereby certify that they have read and recommend to the Faculty of Aerospace Engineering for acceptance a thesis entitled "**Sensitivity of Pusher Propeller Performance and Noise Emissions to the Upstream Wake Characteristics**" by **V.V.Channa** in partial fulfillment of the requirements for the degree of **Master of Science**.

Dated: October 23, 2015

Exam committee:

---

Prof. dr. ir. L.L.M. Veldhuis

---

Ir. Tomas Sinnige

---

Dr. D. Ragni

---

Ir. W.A. Timmer



# PREFACE

Delft -October 23, 2015

During the past one year, I had the opportunity to work with a lot of people who have helped me during the course of my master thesis project. I would like to take this opportunity to thank all of them.

First of all, I owe my deepest gratitude to my daily supervisor Ir.Tomas Sinnige for giving me an opportunity to work on this thesis topic. I sincerely appreciate his enthusiasm and the time he devoted to discuss all my doubts throughout the study. His constant support, feedback and evaluation of my work have greatly helped me throughout this study. I would also like to thank my supervisor Prof.dr.ir.Leo L.M.Veldhuis for his guidance. I am grateful to have you as my supervisor. Your critical feedback and constant encouragement was a driving force in the successful completion of this work. Also, I am thankful to Prof.Dr.-Ing.Georg Eitelberg and Prof.Dr.D.Ragni for their participation and help in reviewing my work. I would also take this opportunity to thank the staff at the aerospace department for arranging everything that I required during the period of my thesis work.

I would also like to thank all my friends here in Delft for making my stay, a happy and a memorable experience. Finally, I would like to thank my parents and sisters for their selfless love and motivation during this final phase of my master's degree.

V.V.Channa



# SUMMARY

Open rotors are considered to have the potential to improve the fuel economy of aircraft significantly by improving the propulsive efficiency compared to the current generation turbofan engines. One of the possible configurations for the open rotors is the aft fuselage mounted contra-rotating pusher propeller. The aft-fuselage mounted contra-rotating pusher propeller is considered as an alternate option for future generation commercial aircraft as it offers significant benefits in terms of interior noise and ground clearance compared to the wing mounted propeller aircraft. However, the pusher configuration is subjected to non-uniform flow due to the upstream pylon wake resulting in unsteady blade loading. These non-uniformities affect the aerodynamic performance and noise emissions of the propeller and hence a study of the sensitivity of the pusher propeller performance and noise emissions to the upstream pylon wake is required.

The objective of this research is to analyse the sensitivity of the pusher propeller performance and noise emissions to the upstream wake by both experiments and numerical computations. With the limitations of the experimental setup, the experiments are conducted on a tractor propeller with a pylon in front of it. The experiments are conducted at Delft University of Technology in two campaigns. The first campaign at TU Delft's Vertical tunnel followed by the second campaign at TU Delft's Open jet Facility. The first campaign at the Vertical tunnel focussed on propeller noise emissions whereas the second campaign at the Open Jet facility focussed on pylon wake profiles, propeller performance and propeller noise emissions. To validate the experiments, a numerical model was developed using an existing propeller lifting line code coupled with an analytical model to estimate the effect of pylon wake on pusher propeller performance and noise emissions.

The pylon wake velocity measurements in the freestream direction are affected by the presence of the downstream propeller. With a decrease in advance ratio, the negative pressure gradient upstream of the propeller decreases the non-dimensional wake displacement thickness and the non-dimensional wake velocity deficit. The non-dimensional wake displacement thickness decreases by 66% and non-dimensional velocity deficit decreases by 60% with a decrease in advance ratio from 1.8 (zero thrust condition) to 0.6. Similar results are also obtained with the cylinder-splitterplate installed configuration. An increase in pylon-propeller spacing resulted in a decrease in non-dimensional wake displacement thickness and non-dimensional wake velocity deficit. The non-dimensional wake displacement thickness decreases by 20% and non-dimensional velocity deficit decreases by 45% with an increase in pylon-propeller spacing from 40% to 100% of the diameter of the propeller. Similar results are obtained at different freestream velocities. The non-dimensional root mean square of the velocity fluctuation in the freestream direction decreased with decrease in advance ratio due to the higher propeller induced velocity in the freestream direction. An increase in spacing resulted in a decrease in root mean square of the velocity fluctuation indicating the fluctuations dissipated with increase in spacing. Pylon wake profiles are also computed numerically based on Schlichting wake model. The wake profiles measured at zero thrust condition and computed numerically are in good agreement, with differences in velocity deficit of the order of 2%. A slight asymmetry is observed in the measured wake velocity profiles.

The propeller performance results indicated that the rotating shaft balance used could not measure the pylon installation effect accurately. The measured offset in propeller performance is attributed to the harmonic vibration of RSB. Within the limitation of the accuracy of RSB, the propeller performance measurements for different pylon-propeller spacings remained constant. The change in the momentum deficit in the pylon wake with increase in pylon-propeller spacing is small enough to effect the performance of the propeller. Propeller performance measurements are also recorded for different cylinder-splitter plate configuration to evaluate the effect of varied inflow conditions into the propeller. The cylinder splitter plate configuration has less impact than the pylon installed configuration as the vortices in the wake of cylinder-splitter plate lower the local angle of attack of the propeller blade sections and decrease the performance of the propeller. Numerical computations are also performed to evaluate the effect of the pylon wake on the propeller performance. The effect of installation increases with increase in advance ratio. The thrust

coefficient and torque coefficient showed an increase of 12% and 8%, respectively. An increase in pylon spacing decreased the effect of installation on the propeller performance. The effect of reduced dynamic pressure and increased angle of attack in the pylon wake region is evaluated separately. It is observed that the effect of reduced dynamic pressure is very small when compared to the effect of increased angle of attack. The experimental measurements recorded to evaluate the installation effects for the cylinder-splitter plate installed configuration is not comparable to the numerical evaluations as the flow quality behind the pylon and cylinder-splitter plate are different.

The experimental noise measurements indicated an increase in sound pressure levels with the installation of pylon. The effect of installation is seen as tones at blade passage frequency. A decrease in advance ratio showed an increase in the sound pressure level due to the increase in blade section loading and helical Mach number at a local blade section. The Flyover directivity pattern indicated an increase in sound pressure level at all flyover angles measured. The increase in sound pressure level due to the installation of pylon is prominent both upstream and downstream of the propeller due to the low sound pressure level observed for the isolated configuration. Azimuthal directivity pattern indicated a decrease in noise emissions at  $\phi = 180^\circ$  and  $\phi = 270^\circ$ . This is probably due to the destructive interference of steady and unsteady loading noise sources at these azimuthal angles. Increase in the pylon-propeller spacing decreased the sound pressure level by decreasing the unsteady loading noise. The installation of cylinder-splitter plate upstream of the propeller resulted in similar noise levels as the pylon-installed configuration. Numerical evaluations showed that the computed sound pressure levels are underpredicted for the isolated configuration at low freestream velocities. This is likely due to the decrease in radiation efficiency at low freestream velocity for a 8-bladed propeller. The sound pressure level for the pylon-installed configuration computed showed an increase across all the flyover angles. The increase is prominent along the propeller axis as the isolated propeller noise levels are very low along the propeller axis.

From the experimental and numerical investigations performed, the effect of pylon spacing on the propeller performance is negligible whereas the effect on the propeller noise emissions is significant. This result is of significance as it can be used as an advantage in the design of the pusher propeller. Improved understanding of the time accurate propeller performance by using advanced measurement systems can provide a better understanding of the propeller performance and noise generating mechanisms.

# CONTENTS

<b>Preface</b>	<b>v</b>
<b>Summary</b>	<b>vii</b>
<b>1 Introduction</b>	<b>1</b>
1.1 The Open Rotor Engine . . . . .	1
1.2 History of Open Rotor Research . . . . .	2
1.3 Current Research on Open Rotor Engines . . . . .	2
1.4 Possible Design Choices of Open Rotor . . . . .	3
1.4.1 Tractor vs Pusher Configuration . . . . .	4
1.4.2 Wing vs Fuselage Mounted Propulsion System . . . . .	5
1.4.3 Single Rotation vs Contra Rotation . . . . .	5
1.4.4 Gearless vs Geared Propulsion System . . . . .	6
1.5 Propeller Performance . . . . .	6
1.5.1 Installation Effect on a Pylon Wake . . . . .	7
1.5.2 Installation Effect on Propeller Thrust . . . . .	8
1.6 Propeller Noise Emissions . . . . .	9
1.6.1 Installation Effect on Propeller Noise . . . . .	10
1.6.2 Effect of Pylon Spacing . . . . .	11
1.7 Research Aim and Objectives . . . . .	11
1.8 Outline of the Thesis Project . . . . .	12
<b>2 Experimental Setup</b>	<b>15</b>
2.1 Experimental Campaign Overview . . . . .	15
2.2 Coordinate System . . . . .	16
2.3 Testing Equipment and Facility . . . . .	16
2.3.1 Wind tunnel Facility . . . . .	17
2.3.2 Propeller Models . . . . .	18
2.3.3 Upstream Objects . . . . .	20
2.3.4 Microphones . . . . .	21
2.4 Processing of Pylon Wake Profile Measurements . . . . .	22
2.5 Processing of Propeller Performance Measurements . . . . .	24
2.6 Processing of Propeller Noise Measurements . . . . .	25
<b>3 Experimental Results: Pylon Wake Profiles</b>	<b>27</b>
3.1 Measurement Overview . . . . .	27
3.2 Isolated Configuration . . . . .	28
3.2.1 Effect of Advance Ratio . . . . .	28
3.3 Pylon-Installed Configuration . . . . .	29
3.3.1 Effect of Advance Ratio . . . . .	29
3.3.2 Effect of Pylon-Propeller Spacing . . . . .	33
3.4 Effect of Upstream Objects . . . . .	36
<b>4 Experimental Results: Propeller Performance</b>	<b>39</b>
4.1 Measurement Overview . . . . .	39
4.2 Reproducibility of the Measurement Data . . . . .	39
4.3 Isolated Configuration . . . . .	41
4.3.1 Rotation-Averaged Propeller Performance . . . . .	41
4.3.2 Time-Averaged Propeller Performance . . . . .	41
4.3.3 Effect of Reynolds Number . . . . .	42
4.3.4 Spectral Analysis of Thrust and Torque Signals . . . . .	43

4.4	Pylon Installed Configuration . . . . .	45
4.4.1	Rotation-Averaged Propeller Performance . . . . .	46
4.4.2	Time-Averaged Propeller Performance . . . . .	47
4.4.3	Spectral Analysis of Thrust and Torque Signals . . . . .	49
4.5	Effect of Pylon-Propeller Spacing: Time-Averaged Propeller Performance . . . . .	49
4.6	Cylinder-Splitter Plate Installed Configuration . . . . .	51
4.6.1	Time-Averaged Propeller Performance . . . . .	51
4.6.2	Effect of Upstream Object-Propeller Spacing . . . . .	52
<b>5</b>	<b>Experimental Results: Propeller Noise Emissions</b>	<b>55</b>
5.1	Measurement Overview . . . . .	55
5.2	Reproducibility of the Measurement Data . . . . .	56
5.2.1	Consecutive Measurements . . . . .	56
5.2.2	Non-Consecutive Measurements . . . . .	57
5.3	Isolated Configuration . . . . .	60
5.3.1	Propeller Noise Spectra . . . . .	60
5.3.2	Effect of Advance Ratio . . . . .	62
5.3.3	Flyover Directivity . . . . .	64
5.4	Pylon-Installed Configuration . . . . .	65
5.4.1	Propeller Noise Spectrum . . . . .	65
5.4.2	Effect of Advance Ratio . . . . .	67
5.4.3	Flyover Directivity . . . . .	68
5.4.4	Effect of Advance Ratio on the Flyover Directivity of Pylon-Installed Configuration . . . . .	70
5.4.5	Azimuthal Directivity . . . . .	71
5.4.6	Effect of Pylon-Propeller Spacing . . . . .	72
5.5	Cylinder-Splitter Plate Installed Configuration . . . . .	74
<b>6</b>	<b>Numerical Setup</b>	<b>77</b>
6.1	Pylon Wake Profiles . . . . .	77
6.2	Propeller Performance . . . . .	77
6.2.1	Isolated Configuration . . . . .	77
6.2.2	Pylon-Installed Configuration . . . . .	80
6.3	Propeller Tonal Noise Emissions . . . . .	85
6.3.1	Isolated Configuration . . . . .	85
6.3.2	Pylon-Installed Configuration . . . . .	87
<b>7</b>	<b>Numerical Results: Pylon Wake Profiles</b>	<b>89</b>
7.1	Operating Conditions . . . . .	89
7.2	Pylon Wake Profiles . . . . .	89
7.2.1	Effect of Freestream Velocity . . . . .	89
7.2.2	Effect of Pylon-Propeller Spacing . . . . .	90
7.2.3	Effect of Pylon Drag Coefficient . . . . .	91
<b>8</b>	<b>Numerical Results: Propeller Performance</b>	<b>93</b>
8.1	Operating Conditions . . . . .	93
8.2	Isolated Configuration . . . . .	93
8.3	Pylon-Installed Configuration . . . . .	96
8.3.1	Angle of Attack Distribution . . . . .	96
8.3.2	Loading Distribution . . . . .	97
8.3.3	Time-Accurate Propeller Performance . . . . .	99
8.3.4	Time-Averaged Propeller Performance . . . . .	100
8.3.5	Effect of Angle of Attack and Dynamic Pressure . . . . .	101
8.4	Effect of Pylon-Propeller Spacing . . . . .	102
8.5	Wake Sensitivity Analysis . . . . .	103

<b>9 Numerical Results: Propeller Noise Emissions</b>	<b>107</b>
9.1 Operating Conditions . . . . .	107
9.2 Isolated Configuration . . . . .	107
9.2.1 Effect of Advance Ratio. . . . .	108
9.2.2 Axial Directivity . . . . .	109
9.3 Pylon-Installed Configuration. . . . .	111
9.3.1 Effect of Advance Ratio. . . . .	111
9.3.2 Effect of Installation . . . . .	112
9.3.3 Axial Directivity . . . . .	112
<b>10 Comparison of Experimental and Numerical Results</b>	<b>115</b>
10.1 Pylon Wake Profiles . . . . .	115
10.2 Propeller Performance . . . . .	115
10.2.1 Isolated Configuration . . . . .	116
10.2.2 Pylon-Installed Configuration . . . . .	117
10.3 Propeller Noise Emissions . . . . .	118
10.3.1 Isolated Configuration . . . . .	118
10.3.2 Pylon-Installed Configuration . . . . .	118
<b>11 Conclusions and Recommendations</b>	<b>121</b>
11.1 Conclusions. . . . .	121
11.2 Recommendations . . . . .	123
<b>Bibliography</b>	<b>125</b>
<b>A RSB Calibration Matrix</b>	<b>127</b>
<b>B Microphone Corrections</b>	<b>129</b>
B.1 Microphone Frequency Response Correction . . . . .	129
B.2 Shear Layer Refraction Correction . . . . .	130
<b>C Additional Results</b>	<b>133</b>
C.1 Propeller Noise Emissions . . . . .	133



# 1

## INTRODUCTION

Open rotors are considered to have the potential to improve the fuel economy of aircraft significantly by improving the propulsive efficiency compared to the current generation turbofan engines. One of the possible configurations for the open rotors is the aft fuselage mounted contra-rotating pusher propeller. The aft-fuselage mounted contra-rotating pusher propeller is considered as an alternate option for future generation commercial aircraft as it offers significant benefits in terms of interior noise and ground clearance compared to the wing mounted propeller aircraft. The pusher configuration is subjected to non-uniform flow due to the upstream pylon wake resulting in unsteady blade loading. These non-uniformities affect the aerodynamic performance and noise emissions of the propeller and hence a study of the sensitivity of pusher propeller performance and noise emissions to the upstream pylon wake is required.

The current chapter presents an overview of open rotor research. The concept of the open rotor engine in terms of technology is elaborated in Section 1.1, followed by research done in the past which is presented in Section 1.2. Next, the current research in the field of open rotors with an emphasis on future challenges is treated in Section 1.3. Then, some of the possible design choices for open rotor engines such as tractor/pusher, single/contra rotation, gear/gearless, wing/fuselage mounted are discussed in terms of cost, performance, noise, weight and technology readiness in Section 1.4. Subsequently, the performance and noise characteristics of pusher propeller are dealt in Section 1.5 and Section 1.6, respectively. Thereafter, the research aim and objectives are discussed in Section 1.7. Finally, the outline of the current thesis report is elaborated in Section 1.8.

### 1.1. THE OPEN ROTOR ENGINE

The invention of the turbofan engine made a significant impact in the field of aircraft propulsion. Turbofan engines are similar to turbojets except with an additional large ducted fan in front driving the engine. The role of the fan is to ensure a large amount of air to enter the engine and thereby producing greater thrust at constant SFC. The engine thrust generated and the propulsive efficiency are given by Equation 1.1 and Equation 1.2.

$$F = \dot{m}(U_{\text{jet}} - U_{\infty}) \quad (1.1)$$

$$\eta_{\text{prop}} = \frac{2}{1 + \frac{U_{\text{jet}}}{U_{\infty}}} \quad (1.2)$$

where By analysing Equation 1.1 and Equation 1.2, two ways of generating thrust are identified:

- To move a large amount of air from  $U_{\infty}$  to a low velocity ( $U_{\text{jet}}$ ) which leads to an increase in propulsive efficiency due to the low  $\frac{U_{\text{jet}}}{U_{\infty}}$  ratio.
- To move a small amount of air from  $U_{\infty}$  to a high velocity ( $U_{\text{jet}}$ ) which leads to a decrease in propulsive efficiency due to the high  $\frac{U_{\text{jet}}}{U_{\infty}}$  ratio.

The historical trend in the development of turbofan engines is related to the development of high bypass ratio turbofan engines. A higher bypass ratio at constant flight velocity leads to an increase in the propulsive efficiency by reducing the jet velocity. However, an increase in the bypass ratio results in an increase in nacelle drag and overall weight of the engine, thereby increasing fuel consumption. The removal of the shroud leads to a reduction in the weight and drag of the engine and ultra high bypass ratios such as 30 can be attained [1]. The noise levels of an unshrouded propeller are high when compared to a turbofan as the acoustic attenuation in the shroud due to the usage of liners is no longer available.

The conventional propeller was the first means of aircraft propulsion. The conventional propeller is an unshrouded rotor having 2-6 straight and narrow blades which are designed to create a region of high pressure on one side and low pressure on the other to generate thrust. The propeller imparts a small increment in velocity to a large volume of air and hence the fuel spent to generate a given thrust is small. However, the efficiency of a conventional propeller decreases at high speeds due to high drag associated with blade thickness. Due to the limitations of the conventional propeller at high speeds, an improved version of unshrouded propeller called the propfan came into existence. The propfan has a higher number of blades (>6), reduced rotor diameter, thin airfoil sections and highly swept blades which improved aerodynamic efficiency at high speeds. The propfan suffers from energy losses in the slipstream due to swirl generated. One method of recovering the lost swirl energy is to use another set of blades behind the first one. The second set of blades rotate in the opposite direction to the first so that the swirl in the wake of the propfan is reduced [2]. This improves the aerodynamic performance of the rotor, however the second rotor introduces new noise sources such as interaction tones and noise from the tip vortices of the first rotor impinging on the second rotor [2, 3].

## 1.2. HISTORY OF OPEN ROTOR RESEARCH

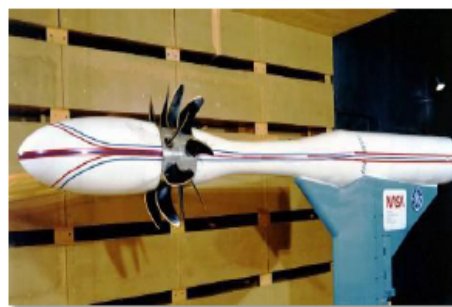
The advantage of the higher propulsive efficiency of open rotors was known and scientifically established in the 1970s. The first effort to demonstrate open rotor technology was started in 1976 by NASA under the project name Advanced Turboprop at NASA Lewis research center [4]. Hamilton Standard initially developed the SR-1 propeller with a single row of swept blades in 1978 [5]. With the success of the tests performed on the small scale model, Hamilton Standard soon developed the SR-7L which is very close to the size of a commercial model. Flight tests conducted at Mach 0.8 at 12000 ft confirmed the results obtained on the small scale propeller. NASA continued the development of the Advanced Turboprop with Allison and Pratt and Whitney which resulted in the 578-DX Engine in 1989 [6] (see Figures 1.1b and 1.2). General Electric (GE) developed an Unducted Fan (UDF) which was tested on an MD-80 airframe in 1989. The GE unducted fan was a gearless contra rotating pusher system (refer Figure 1.1a). NASA's Advanced Turboprop was a single rotating tractor system and included a complicated gear box. NASA's Advanced Turboprop and GE's UDF proved to be highly successful in flight tests with 20-30% fuel savings compared to the then existing propulsion technology. However, the economic situation with fuel prices at a low made the Advanced Turboprop project irrelevant [5]. In the UK, Rolls Royce also began a Propfan research program in the 1980s which was tested in a transonic wind tunnel in 1990. The propfans are noisy when compared to the turbofans which makes it difficult to achieve the existing noise certifications. Also, any shift to an alternate technology of contra-rotating open rotors would result in a change in airport infrastructure and maintenance equipment prompted to continue the use of turbofan engines [1].

## 1.3. CURRENT RESEARCH ON OPEN ROTOR ENGINES

Modern challenges to the aircraft industry are quite different from the ones faced in the 1980s. Due to the rising air traffic, environmental concerns related to aircraft emissions are now a major driving force in open rotor research. The International Air Traffic Authority (IATA) has set a challenging goal of 50% reduction in carbon emission levels by 2050 compared to the baseline emissions (2005). The targets set by NASA (US) and ACARE (Europe) are also similar. In addition, oil prices have risen to a high leading to increased operational costs for the airlines and thus, it is important to manufacture fuel efficient aircraft. Airlines have also suffered loss of revenues due to a reduction in number of working hours per day as the aircraft noise emissions affect the communities living near the airport particularly at night. Noise regulations



(a) GE Unducted fan on an MD-80 aircraft [7]



(b) Unducted fan testing at NASA [7]

**Figure 1.1:** Testing of Open rotors in the 1980s [7]**Figure 1.2:** PW/Allison 578 DX on MD-80 aircraft [7]

have become strict both in the US and Europe and hence reducing the noise emissions is a matter of great importance for aircraft manufacturers and airlines. The International Civil Aviation Organisation (ICAO) revised the certification norms over time as the flight traffic increased considerably. The current generation of aircraft is required to pass the chapter 4 noise regulations which are 10dB higher than the 1980 standards [1]. It is likely the norms will be revised to chapter 14 in the future when the open rotor is expected to enter the market. Effective perceived noise level (EPNL) and noise contours are the standards which are monitored during the certification process. NASA has set the target to reduce the noise "footprint" area (noise contours) for a single event of landing and takeoff by 55% compared to the baseline area (chapter 4). It is of the view that tonal noise is often more annoying than broadband noise. Rotor tones of both the forward and aft rotor and the interaction tones are the main noise sources in a contra-rotating open rotor system. The advances in aerodynamic design and acoustics made possible the development of fuel efficient open rotors with decreased noise emissions [7]. Several research studies have been performed by industry and academia to make the open rotor technology a reality. NASA's Environmentally Responsible Project (ERP) and Subsonic Fixed wing Project (SFP) have focussed their research on open rotor performance and noise [6]. The EU-funded New Aircraft Concepts REsearch project (NACRE) aims to integrate the open rotor to the aircraft. The Clean sky Joint Technology Initiative (JTI) by the EU includes the demonstration of open rotor technology with ground and flight validation. In the UK, Rolls Royce coordinated the validation of Radical Engine Architecture systems (DREAM) project with 40 partners to design and test the open rotor at low and high speed wind tunnels in DNW, ARA and Tsagi [1]. To summarise, a number of projects have been initiated to develop open rotor technology and utilise its potential to address the needs of the aircraft industry.

## 1.4. POSSIBLE DESIGN CHOICES OF OPEN ROTOR

There are many possible options for the design of an open rotor engine with each design having its own benefits and limitations. Mann and Stuart [8] and Godston and Reynolds [9] have carried out extensive studies on the possible design options for an open rotor engine. In their studies, they have listed out the following as the possible choices for a future open rotor engine.

- Tractor / Pusher configuration of the propeller

**Table 1.1:** The differences between a tractor and pusher propeller configuration [9]

Parameter	Tractor	Pusher	Overall
Performance	Pressure and Temperature rise ( $\Delta$ Thrust = +3.9% and $\Delta$ SFC = -1.3%) and Inlet pressure losses are higher for tractor ( $\Delta$ Thrust = -3%)	Loss of thrust and Higher SFC due to cooling bleed ( $\Delta$ Thrust = -0.6% and $\Delta$ SFC = +0.5%) and tailpipe losses ( $\Delta$ Thrust = -0.7% and $\Delta$ SFC = +0.7%)	Overall, tractor configuration performs better than the pusher configuration ( $\Delta$ Thrust = +0.6% and $\Delta$ SFC = -0.6% for the tractor)
Cost	Nacelle and pylon are slightly less costly for the tractor compared to the pusher	Maintenance cost is higher because of poor accessibility of the gear box	Overall, the pusher configuration acquisition and maintenance cost are higher than the tractor configuration costs
Weight	Pylon for the tractor is longer and heavier than for the pusher propeller	The pusher configuration needs additional cooling provisions for the propfan and heat shield for the gear box	Overall, the pusher configuration is heavier than the tractor configuration
Noise	Engine, gear box noise and propfan noise are identical for tractor and pusher	Pylon effects on the propfan results in a noise penalty of 1dB	Pusher configuration is 1 dB louder than the tractor configuration

- Wing- / Fuselage- mounted propulsion system
- Single- / Contra-rotation
- Gear / Gearless drive system

All the above possible options are discussed in the below subsections.

#### 1.4.1. TRACTOR VS PUSHER CONFIGURATION

Godston and Reynolds [9] compared the tractor and pusher configurations in terms of performance, cost, weight and noise at an engine and aircraft level using analytical techniques. The comparison at an engine level is represented in the Table 1.1 and is discussed here. The pressure and temperature rise across the propfan will result in an increase of 3.9% thrust and 1.3% fuel consumption decrease for the tractor compared to the pusher configuration. The inlet pressure recovery losses are higher for the tractor configuration with reduction of 3% in thrust. The cooling system required for the pusher configuration requires additional gas generator flow from the first stage compressor. This results in a loss of thrust (0.6% thrust) and additional consumption of fuel (0.5% SFC) for the pusher configuration. The larger diameter of the nacelle and the lobed nozzle of the pusher configuration would result in higher nacelle drag. Overall assessment for the complete configuration which includes the pylon, wing-fuselage interaction showed an advantage for the tractor configuration with 0.6% higher thrust and 0.6% lower fuel consumption. In terms of weight, the additional cooling provisions of the engine and heat rejection system add a weight disadvantage to the pusher configuration. The pylon has been assessed to be shorter and lighter for the pusher configuration. Overall, the pusher is heavier than the tractor configuration. The power turbine support system and propfan cooling air system also adds to the total cost of the pusher engine. In addition, the maintenance cost for the heat rejection system is high due to the poor accessibility for on the wing repairs. The presence of the pylon in front of the pusher configuration results in an unsteady loading on the propeller blades which result in a noise penalty of 1dB[9].

At an aircraft level, the pusher is superior in performance to the tractor due to a shorter pylon which reduces pylon drag and pylon weight. In addition, the tractor requires a larger and heavier vertical tail as the thrust line is situated further outboard [9]. Thus, each configuration has its own advantages with no clear winner between the pusher and tractor from the above analysis.

**Table 1.2:** Wing Mounted SR tractor [8]

Pros	Cons
<ul style="list-style-type: none"> <li>• FOD environment</li> <li>• Lower structural wing weight</li> <li>• Good aircraft balance</li> </ul>	<ul style="list-style-type: none"> <li>• Cabin noise</li> <li>• Disturbed wing flow</li> <li>• Poor cabin flexibility</li> <li>• Freight hold access</li> <li>• Structure borne noise and vibration</li> </ul>

**Table 1.3:** Rear Fuselage Mounted CR pusher [8]

Pros	Cons
<ul style="list-style-type: none"> <li>• Low cabin noise</li> <li>• Wing having a clean flow</li> <li>• Passenger acceptability</li> </ul>	<ul style="list-style-type: none"> <li>• Foreign Object Damage (FOD)</li> <li>• Wing wake interactions with the propeller</li> <li>• Trim drag</li> <li>• Aircraft balance</li> <li>• Structure borne noise and vibration</li> </ul>

### 1.4.2. WING VS FUSELAGE MOUNTED PROPULSION SYSTEM

Tables 1.2 and 1.3 show the pros and cons for the wing mounted single-rotation tractor configuration and the rear fuselage mounted contra-rotation pusher configuration, respectively. One of the disadvantages of the wing mounted single rotation tractor configuration is its noise characteristics. The wing mounted SR tractor configuration with its directivity pattern in both forward and rearward directions, would require heavier acoustic insulation across the entire fuselage. This would result in an increase in the weight of the aircraft. A rear fuselage mounted pusher installation with the engine positioned far away from the center of the cabin requires lighter acoustic insulation than the wing mounted configurations, resulting in weight savings to the total aircraft weight. In spite of its disadvantages, the wing mounted tractor installation has its own advantages with the wing acting as a flow straightener of the propeller slip stream. The rotational velocity in the slipstream can be reduced by the presence of the wing behind the propeller [8]. This swirl recovery would aid in improved take-off and landing performance and also improves the SFC.

### 1.4.3. SINGLE ROTATION VS CONTRA ROTATION

Contra Rotating Open Rotors (CROR) straighten the flow aft of the front rotor which results in an efficiency improvement. Generation of swirl by the front rotor utilises energy which does not contribute to thrust. An aft rotor rotating in the opposite direction to that of the front rotor cancels the swirl in the propeller slipstream, thereby increasing propeller efficiency. However, the addition of the aft rotor increases the weight and cost of the engine. In addition, the rotor-rotor interaction tones result in an extra noise source. CRORs increase the overall complexity and require additional maintenance due to the presence of an extra rotor.

#### 1.4.4. GEARLESS VS GEARED PROPULSION SYSTEM

The turboprop planes of the 1950s required high maintenance because of the gear mechanisms used [5]. The propulsion system of the Advanced Turboprop project initiated by the NASA was originally a geared system with a complicated gearbox developed along with Pratt and Whitney. GE's UDF was a gearless drive system which was successful in eliminating the problems of gearbox maintenance. However, both systems have their advantages and disadvantages. The lack of a gearbox results in only one of the turbine and the rotor running at optimal speeds. Geared drive systems with their flexibility in speed and loading are quieter than gearless drive systems. Also, the use of a gear box increases the efficiency of the overall system as both the propfan and power turbine can be run at optimum efficiencies which yield fuel burn and economic advantages [9].

### 1.5. PROPELLER PERFORMANCE

The propeller performance is often expressed in terms of three performance parameters: thrust coefficient ( $C_T$ ), torque coefficient ( $C_Q$ ) and efficiency ( $\eta$ ) which vary with the advance ratio ( $J$ ). The power coefficient is also used in place of the torque coefficient. Typical performance curves of a propeller for different freestream velocities and advance ratios are given in Figure 1.3. All the normalized performance parameters and the advance ratio are expressed as follows:

$$C_T = \frac{T}{\rho n^2 D^4} \quad (1.3)$$

$$C_Q = \frac{Q}{\rho n^2 D^5} \quad (1.4)$$

$$C_P = 2\pi \frac{P}{\rho n^3 D^5} \quad (1.5)$$

$$\eta = \frac{J C_T}{2\pi C_Q} \quad (1.6)$$

$$J = \frac{U_\infty}{nD} \quad (1.7)$$

where

$C_T$  = Thrust Coefficient

$C_Q$  = Torque Coefficient

$C_P$  = Power Coefficient

$\eta$  = efficiency

$J$  = Advance ratio

$\rho$  = density

$T$  = Thrust

$Q$  = Torque

$P$  = Power

$n$  = rotational speed

$D$  = diameter

$U_\infty$  = freestream velocity

The amount of lift generated by the propeller blade section depends its local angle of attack. As the local angle of attack increases, the lift on the blade section increases. An increase in the advance ratio results in a decrease in the local angle of attack of the blade section. This can be understood from Figure 1.4. As the rotational speed of the propeller increases, the local angle of attack increases and thereby the lift generated by the blade section increases leading to an increase in the overall thrust generated by the blade section assuming that the forward speed of the propeller is kept constant. At very high rotational speeds, the local angle of attack can be large, resulting in blade stall with a decrease in the propeller thrust and power coefficient. This can be observed from Figure 1.3 at low advance ratios. At high advance ratios, the angle of attack is low and the propeller generates low thrust. In the case of windmilling, the angle of attack on the blades would be negative and blade is pulled instead of being pushed.

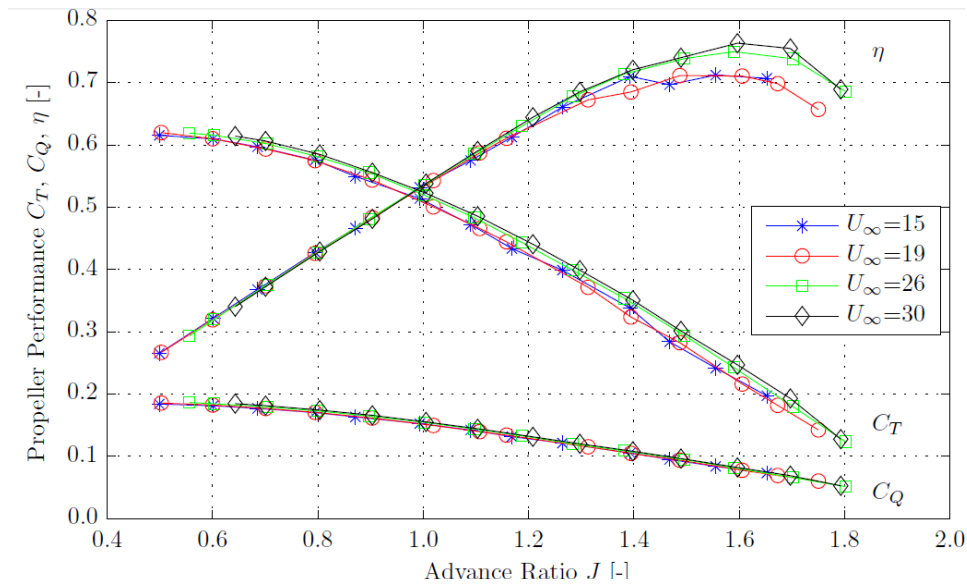


**Figure 1.3:** Typical performance curves for varying advance ratio and freestream velocities [10]

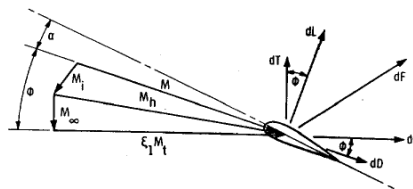


**Figure 1.4:** Vector relationships on a local section of blade [11]

The real flow on a propeller aircraft is far from ideal as it is subjected to various non-uniformities. Some of the sources of unsteadiness in a pusher propeller aircraft are

- angle of attack or side slip
- upstream wing and pylon wake interaction
- turbulence and gusts
- engine exhaust stack interaction with the root of propeller blades

These non-uniformities affect the performance of the propeller and the parameters which drive the non-uniform flow need a greater attention [12]. The angle of attack, propeller position and rotational direction of the propeller influence the aerodynamics of the overall flow. It is therefore necessary to understand the unsteady effects in a pusher propeller in real flight conditions.

### 1.5.1. INSTALLATION EFFECT ON A PYLON WAKE

Although the wake velocity distribution from a streamlined surface is understood, the interaction of a downstream propeller on the incoming wake is complex and any study on the influence of the propeller on the wake will be useful in analysing the propeller performance in the installed configuration. Studies were conducted at NASA by Soderman and Horne to determine the effects of propeller rotation on the upstream wake characteristics [13]. The experiments conducted on a scaled model of a pusher propeller under the influence of the empennage wake showed that the wake just behind the empennage was similar to the flat plate near wake and downstream the velocity deficit in the wake was reduced when compared with the velocity deficit of the wake in isolated configuration. Interference effects with the fuselage resulted in a broad wake and these

effects were found to be diminishing at positions away from the fuselage centreline. The wake characteristics in propeller ON/OFF modes were observed to be similar except at very near and just ahead of the propeller where the flow velocity was greater than the freestream velocity. The wake width was nearly the same in both conditions. The wake characteristics are shown in Figure 1.5.

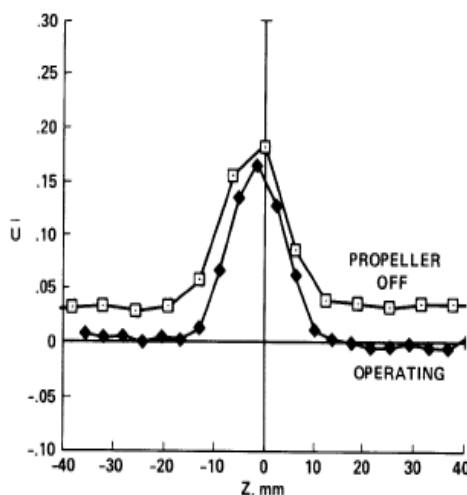


**Figure 1.5:** Wake characteristics in propeller on and off operating modes [13]

The velocity deficit on y-axis is slightly negative for the propeller operating mode ON suggesting the velocity is greater than the freestream velocity. The shape and width of the wake were retained in spite of the presence of the propeller. The acceleration effects of the propeller clearly suggest the stream tube entering the propeller plane is diverted inboard of the propeller tip and this movement gets reduced at the tip. It is also expected that the wake velocity deficit would decrease as one would move away from the empennage in streamwise direction. Figure 1.6 shows the exponential-like decay of maximum wake deficit with the streamwise position for different empennage configurations. The Y-tail generated smaller wake deficit due to the smaller chord and thickness used. The empennage wake widths were plotted against the streamwise coordinate in Figure 1.7 to show wake growth characteristics. There is a lot of scatter in the data shown and one could observe wider wakes far downstream from the empennage. In general, it can be concluded that no major effects such as wake widening, increase in velocity deficit were observed on the wake due the rotation of propeller [13].

### 1.5.2. INSTALLATION EFFECT ON PROPELLER THRUST

With the pusher propeller configuration being considered as an option for the next generation passenger aircraft configuration because of the promise of significant fuel savings, it is important to address the disadvantages this configuration has. The propeller inflow is distorted due to the presence of the upstream pylon. This results in an unsteady variation in thrust levels as each blade passes through the wake. The unsteady variation of the thrust increases the vibratory loads on the blades and thereby, decreases the blade fatigue life. These loads can be transmitted to the aircraft fuselage through the engine mounting. Booth, Gentry and Takallu performed experiments to analyse the effect of a wake on a pusher propeller using a model propeller in the wake of a pylon model. The installed thrust levels for the pusher propeller are observed to be higher than the isolated thrust levels, especially for high advance ratios [14]. The pylon wake reduces the inflow velocity and hence increases the angle of attack of the blades at a constant advance ratio resulting in higher thrust levels. Also, the increase in turbulence due to the wake results in a higher effective Reynolds number and thereby improves the performance of the propeller blades. The time average propeller thrust was found to have a favourable installation effect [14].

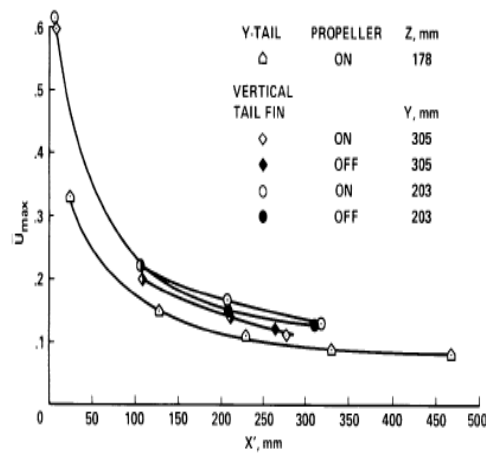


Figure 1.6: Maximum velocity deficit plotted against streamwise coordinate [13]

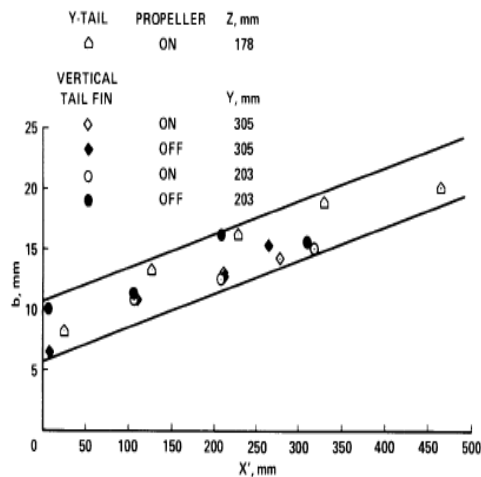


Figure 1.7: Wake width plotted against streamwise coordinate [13]

## 1.6. PROPELLER NOISE EMISSIONS

Propeller noise generating mechanisms can be classified in terms of their time dependency [2, 15].

- **Steady noise sources**

Steady sources are the noise sources which are constant and periodic for an observer on the rotating blade. Steady state noise sources are divided into three categories.

- **Linear thickness noise**

Each blade occupies a volume. When the blade is rotated, it displaces the same volume of air physically. Due to the periodic displacement of air which is governed by the rotational speed, blade volume and shape, thickness noise which is periodic in nature is produced. The amplitude and frequency of the noise generated is dependent on the blade volume and the rotational speed respectively. Thickness noise can be represented by a distribution of pulsating spheres (monopoles). A pulsating sphere is a point source where the sound is produced by the mass

outflow variation from the source [2, 15].

– **Linear loading noise**

Loading noise is generated when the pressure distributions on the rotating blade airfoil generate thrust and torque due to the motion of the blade relative to the surrounding medium. Loading noise can be represented by a set of stationary dipole sources. Dipole source generates sound by the injection of momentum rather than mass outflow. For a subsonic blade speed, the loading noise is linear and dominates the tonal noise emissions [2, 15].

– **Non-linear noise**

At transonic speeds, non-linear noise due to the viscous nature of the medium and propagation effects contributes significantly high to the overall noise emissions. These can be modelled as a quadrupole source. A quadrupole source is equivalent to two identical dipoles in opposite phase. The net flux of fluid flow is zero and hence the net force is zero as well. It is the fluctuating stress on the fluid that generates the sound waves [2, 15].

• **Unsteady noise sources**

Unsteady noise is produced due to random or periodic loading on the blades which are time dependent in the blade frame of reference.

– **Periodic noise**

Unsteady periodic loading can occur due to the angle of attack on an SR propeller, aerodynamic interference on a CR propeller etc. Periodic loading occurs sometimes due to the ingestion of a vortex produced upstream into the propeller.

– **Random noise**

Random noise is produced due to the turbulent nature of the flow just upstream of the propeller.

All the above components of propeller noise can have following characteristics- harmonic noise, broadband noise and narrow-band noise.

Harmonic noise as the name suggests is a periodic noise which can be identified by discrete frequencies as a multiple of blade passage frequency. Broadband noise is random in nature and contains different frequency components as a continuous spectrum. Narrow-band noise is close to periodic. The signal may appear periodic but does not repeat with time [2].

### 1.6.1. INSTALLATION EFFECT ON PROPELLER NOISE

The flow incoming into the propeller can be significantly influenced by the installation configuration. Experiments conducted by Shivashankara [16] on the noise emissions for an isolated contra-rotating propeller, propeller along with fuselage, propeller with pylon and propeller along with pylon and fuselage vary significantly. Noise emissions for the completely installed configuration are shown in Figure 1.8. The installation of the pylon increased the noise emissions (compared to the isolated configuration) which is primarily at the front rotor blade passage frequency and its harmonics [3, 16]. The azimuthal directivity pattern of pylon-rotor interaction (without the fuselage effects) at 1BPF is shown in Figure 1.9 [16]. The front rotor noise emissions would be related to the pylon wake, the fuselage-pylon interference flow and boundary layer on the fuselage. Adding the fuselage alone had a negligible impact on the noise emissions whereas the pylon alone configuration increased the front rotor noise emissions substantially. For the completely installed configuration, the noise emissions increased marginally which is probably due to the fuselage-pylon interference flow. When the fuselage alone is introduced, the aft rotor BPF shows an increase in the noise emissions whereas when the pylon and fuselage are added together resulted in marginal increase in noise emissions (see Figure 1.8). The interaction tones show large changes due to installation of fuselage alone. Acoustic diffraction from the various bodies in the surrounding areas of the noise sources might be one of the reasons for the observed changes [16].

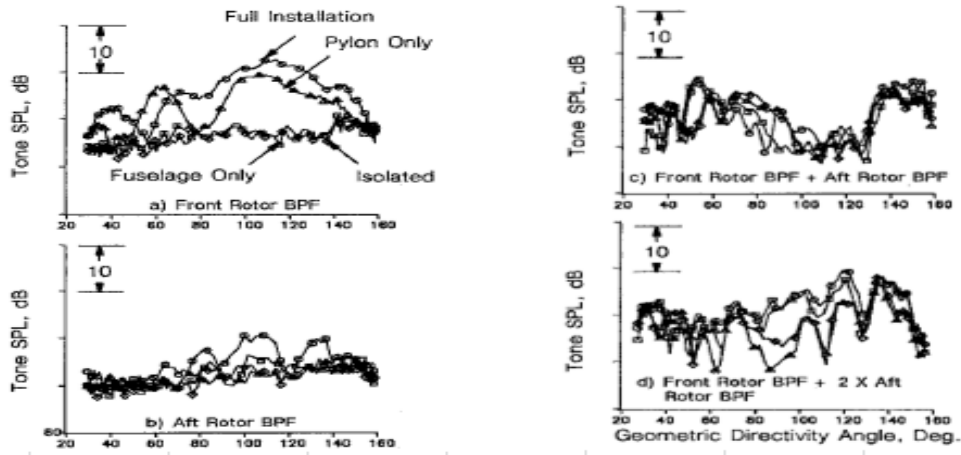


Figure 1.8: Installation effects on the noise emissions [16]

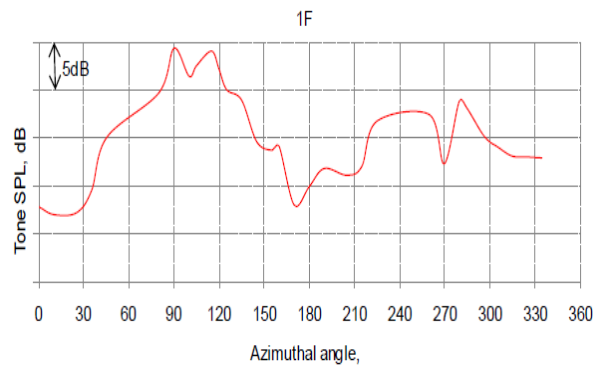


Figure 1.9: Pylon- Front rotor interaction tone at first BPF's azimuthal directivity [3]

### 1.6.2. EFFECT OF PYLON SPACING

The spacing of the pylon from the propeller has a significant impact on the noise characteristics as can be observed from Figure 1.10. Reduced noise emissions and a changed directivity pattern are evident when the pylon spacing was changed from 0.1c to 0.3c. The effect of pylon-propeller spacing on the overall tonal noise emissions is analysed with the help of spacing penalty. It is defined as the difference between the overall sound pressure level at 0.1c and 0.3c spacings. The variation of spacing penalty is relatively flat when compared to the pusher configuration noise penalty. The spacing penalty increased upstream of  $\theta < 50^\circ$  and remained constant downstream of  $\theta > 50^\circ$  (see Figure 1.10). The low flow gradient of the wake at a larger pylon spacing reduces the noise emissions [27].

$$\Delta OASPL = OASPL_{0.1c} - OASPL_{0.3c} \quad (1.8)$$

where

$\Delta OASPL$  = Spacing Penalty (dB)

$OASPL$  = Circumferentially Averaged Sound Pressure Level (dB)

## 1.7. RESEARCH AIM AND OBJECTIVES

The pusher propeller is considered as an option for future generation aircraft. It is subjected to non-uniform flow due to the upstream pylon wake and thereby affecting the pusher propeller performance and noise emissions. The sensitivity of propeller response to the upstream wake forms the main topic of the thesis which leads to the following research aim and objectives:

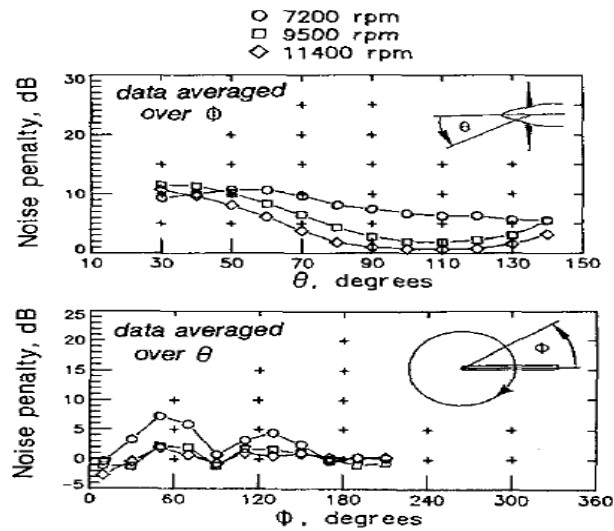


**Figure 1.10:** Variation of spacing penalty with polar and circumferential angles [27]

### Research Aim

The aim of the research is to analyse the performance of a pusher propeller both numerically and experimentally when it is subjected to an upstream wake of varying depth and width generated by placing a pylon based on NACA 0012 airfoil and different combinations of cylinder-splitter plate ahead of the flow. Due to the limitations on the availability of experimental apparatus, the wind tunnel experiments will be conducted on a single rotation tractor propeller with a pylon upstream of the propeller.

### Research Objectives

The research aim is planned to be achieved by meeting the following objectives:

- Experiments will be conducted on a propeller for different operating conditions such as advance ratio, propeller spacing, different upstream bodies.
  - Data sets on the wake measurements will be obtained for different upstream bodies such as wing based on a NACA airfoil, combination of cylinder and splitter plate using Particle Image Velocimetry.
  - Data on the performance and noise characteristics of the pusher propeller when subjected to an upstream wake will be extracted for different wake widths and velocity deficits.
- A numerical model will be developed to estimate the effects of an upstream wake on the performance and noise characteristics of a pusher propeller.

## 1.8. OUTLINE OF THE THESIS PROJECT

This section provides an overview of the contents of the report. The entire report is organised into 11 chapters. The layout of the report is shown in Figure 1.11.

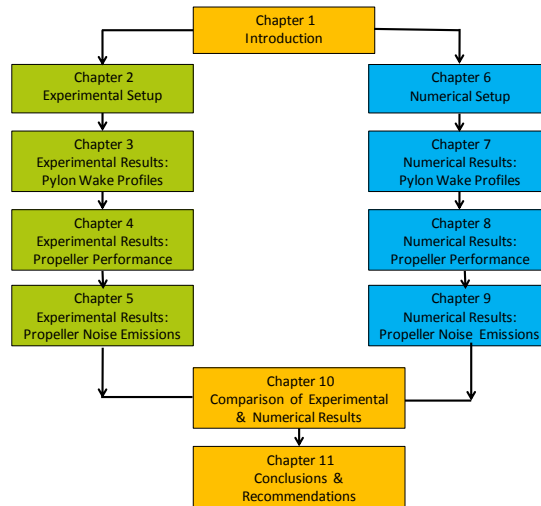


**Figure 1.11:** Layout of the thesis report

Chapter 1 introduces the research topic and the motivation behind the research. Subsequently, the research aim and objectives are elaborated in detail in the same chapter. In Chapter 2, the entire experimental setup is presented. Later, the pylon wake profiles obtained at various operating conditions are given in Chapter 3. After the pylon wake profiles, the propeller performance measurements are given in Chapter 4. The influence of advance ratio, upstream object-propeller spacing and upstream object are discussed in detail in this chapter. Then, Chapter 5 presents the propeller noise measurements which finishes the experimental part of the project. The influence of operating conditions such as advance ratio, pylon-propeller spacing and upstream object are discussed here.

After completing the experimental part of the project, the next four chapters deal with the numerical computations performed to estimate the effect of pylon wake on the performance and noise emissions. Before moving into the numerical results, Chapter 6 details the numerical models used to predict the pylon wake, propeller performance and noise emissions. Then, Chapter 7 treats the wake profiles obtained for different operating conditions. Thereafter, estimating the effect of pylon wake on pusher propeller performance and noise emissions using a numerical model is treated in Chapter 8 and Chapter 9, respectively.

The comparison of results obtained from the experiments and numerical methods is done in Chapter 10. All the results of wake profiles, propeller performance and noise emissions are compared in this chapter. The report ends with concluding remarks and possible extensions to the present project in Chapter 11.



# 2

## EXPERIMENTAL SETUP

The present chapter describes the equipment, setup and the techniques used to perform the experiments conducted to meet the aim of the project. First, an overview of the experimental campaign is treated in Section 2.1. Subsequently, the coordinate system used during the experimental campaign is defined in Section 2.2. Next, Section 2.3 describes the various testing equipment used such as propeller, wind tunnel, microphones, upstream objects and Particle Image Velocimetry (PIV) equipment. Then, the measurement procedures for the pylon wake profiles and propeller performance are detailed in Section 2.4 and Section 2.6 respectively. Finally, the propeller noise measurement process is discussed in Section 2.5.

### 2.1. EXPERIMENTAL CAMPAIGN OVERVIEW

The aim of current research project is to evaluate the performance and noise emissions of a pusher propeller in a wide variety of inflow wake conditions differing in wake width and wake velocity deficit. Keeping this mind, the test campaign focussed on the performance and noise emissions for the isolated, pylon-installed and cylinder-splitter plate installed conditions. The experiments are conducted in two stages with the first and second campaigns at the Low Speed Lab (LSL) and Open Jet Facility (OJF) of Delft university of Technology, respectively. An overview of both the campaigns is given in Figure 2.1.

The experimental tests for the first and second campaign are conducted on a completely in-house designed propeller and a scaled model of Fokker F-29 propeller, respectively. The first campaign focussed on the

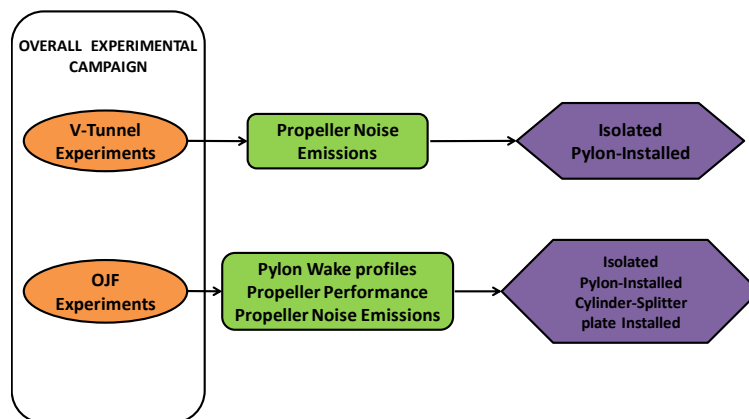


**Figure 2.1:** Overview of the experimental campaign at the OJF and LSL of TU Delft

propeller noise emissions for the isolated and pylon installed configurations only. The effect of various operating conditions such as microphone flyover angle, azimuthal angle, pylon-propeller spacing was studied in this campaign. Performance, noise and wake profile measurements are conducted for the isolated,

pylon-installed and cylinder-splitter plate installed configurations for the tests performed in the Open Jet Facility. Performance measurements are performed with the help of a six component rotating shaft balance (RSB). Noise and pylon wake profile measurements are performed with the help of microphones and Particle Image Velocimetry (PIV) respectively. More details of the experimental setup will be discussed in the later sections.

The pylon wake measurements are carried to evaluate the wake profile in front of the propeller just before its impingement on the propeller. A variety of objects are used to obtain wakes with differing characteristics. A NACA 0012 airfoil based pylon and a number of cylinder-splitter plate combinations are used to obtain wakes with a differing width and velocity deficit. Noise measurements are used to evaluate the impact of upstream object on the flyover directivity of the propeller. The influence of the advance ratio and object-propeller spacing on the noise measurements is also studied in this experimental campaign. The performance measurements are used to evaluate the impact of the upstream object wake on the performance parameters of the propeller. All the measurements are performed for a range of advance ratios, freestream velocities, object-propeller spacing and differing upstream object.

## 2.2. COORDINATE SYSTEM

This section describes the coordinate systems used during the experiments. Different coordinate systems are used to define the direction of flow from the wind tunnel and the flow at local blade sections. The wind tunnel based coordinate system is defined in Figure 2.2. It follows a standard Cartesian coordinate system with all the three axis perpendicular to each other. The origin of the coordinate system is at the center of the wind tunnel edge section. Therefore, the wind tunnel velocity is positive in sign.

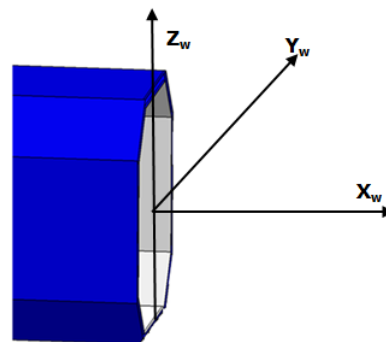


**Figure 2.2:** Isometric view of the wind tunnel coordinate system

Since, the numerical model for performance and noise emissions has to depict the flow at a local blade section, a new spherical coordinate system is defined at the propeller disk. The radial coordinate is defined by  $\eta$ , whereas the axial and circumferential coordinates are defined by  $\theta$  and  $\psi$ , respectively. The propeller spherical coordinate system is defined in Figure 2.3 and Figure 2.4. For the experiments conducted, the pylon is positioned upstream of the propeller at  $\psi = 0^\circ$ .

## 2.3. TESTING EQUIPMENT AND FACILITY

This section presents the various details of the testing equipment and facilities used for the experiments conducted in the current research project. First, the description of wind tunnels used during the experimental campaign is given in Subsection 2.3.1. Next, the specification and characteristics of the propellers used are described in Subsection 2.3.2. Thereafter, the details of the geometry of the objects used during the OJF experimental campaign is presented in Subsection 2.3.3. Finally, the specification of microphones used to record the noise measurements are mentioned in Subsection 2.3.4.

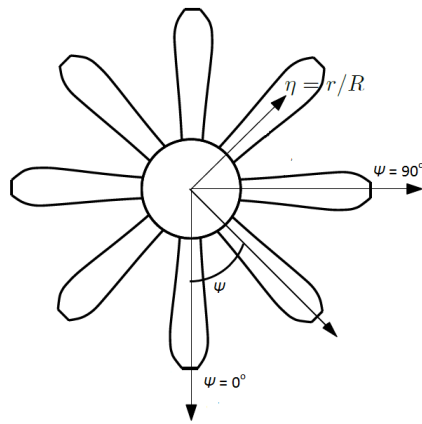


**Figure 2.3:** Propeller spherical coordinate system indicating  $\eta$  and  $\psi$

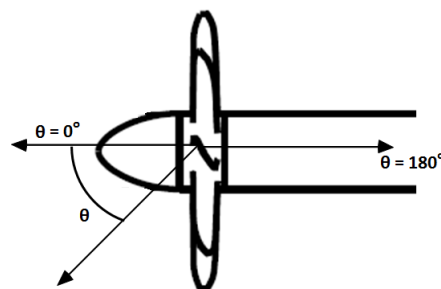


**Figure 2.4:** Propeller spherical coordinate system indicating  $\theta$

### 2.3.1. WIND TUNNEL FACILITY

The first campaign of experiments was conducted at the TU Delft's vertical low turbulence tunnel (abbreviated as V-tunnel). The V-tunnel is an open circuit wind tunnel with an outlet diameter of 0.6 m and maximum velocity of 45 m/s. The test section receives the inflow from below through a circular exit. The turbulence levels are of the order of 0.1% due to the high contraction ratio of the settling chamber. The tunnel is ideal for performing aeroacoustic measurements due to low reflections. Figure 2.5 shows a picture of Vertical Low turbulence tunnel.

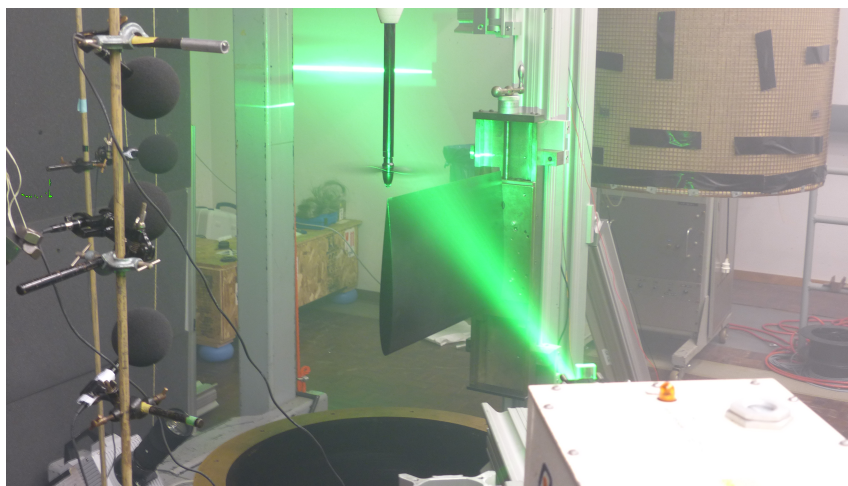


**Figure 2.5:** Picture of the Vertical Low turbulence tunnel

The second experimental campaign was conducted at TU Delft's Open Jet Facility (abbreviated as OJF).

A large fan powered by a electric engine drives the flow to an octagonal outlet of width and height of 2.85 m. The maximum velocity that can be achieved here in this closed circuit section is 30 m/s. A honey comb flow rectifier along with five screens (mesh like structures) here ensures the flow is straightened with low turbulence levels. The turbulence levels are of the order of 0.24% [17]. Figure 2.6 shows a schematic of the Open Jet Facility at TU Delft.

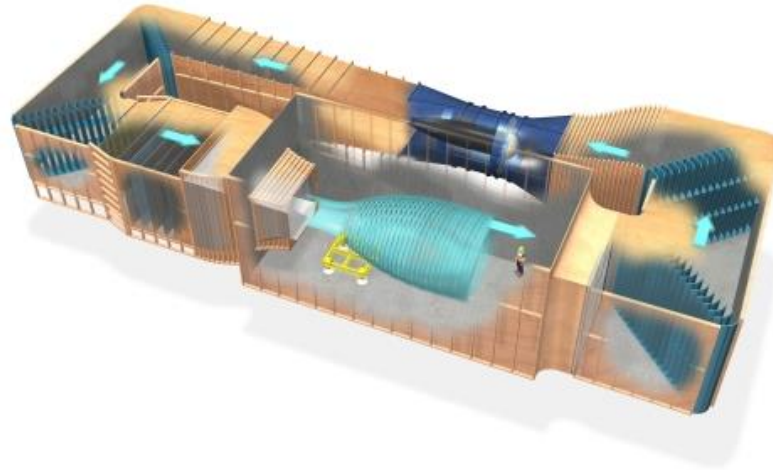


**Figure 2.6:** Schematic of the TU Delft's Open Jet Facility [17]

### 2.3.2. PROPELLER MODELS

The first experimental campaign is conducted at Low Speed Lab (LSL) of TU Delft with an in-house designed propeller referred from here on as DEL-PROP. The DEL-PROP consists of a 2-bladed rotor which runs on a DC-motor housed inside a 3D printed aerodynamic casing. Figure 2.7 shows the entire propulsor unit used for the experiments at the Low Speed Lab. The propeller loads namely thrust and torque are measured by a single point load cell and reaction torque sensor respectively. The rotor is supported by a shaft which is connected to an extension bar to move the center of gravity towards the torque sensor which reduces the measurement error by removing the torque component due to the force in Y-direction. The shaft is long enough to ensure the interaction effects between the upstream propeller and downstream casing is reduced. Since the propeller is designed for operation in horizontal condition and the experiments are conducted in the V-tunnel, the weight of the entire propulsor unit is added to the thrust generated by the propeller which introduced an error in the measurement of the propeller thrust. In spite of adding a counter weight, the thrust measurement was found to be erroneous and hence propeller force measurements are not discussed from here on for the tests conducted on DEL-PROP.

**Table 2.1:** Geometric details of DEL-PROP model

Parameter	Symbol	Value	Unit
Diameter	$D_{\text{prop}}$	0.23	m
No of Blades	B	2	-
Hub diameter	$D_{\text{hub}}$	0.02	m

The second experimental campaign conducted at the Open Jet Facility (OJF) used the scaled model of a Fokker F-29 propeller (here on, this propeller will be referred as F-29 propeller model). The F-29 propeller is a single rotating propeller with a diameter of 0.3046 m and 8 blades. The blade angle was fixed at 40 degrees at 70% of blade span. The propeller assembly consists of a six component rotating shaft balance, TDI 1999 pneumatic motor, slip ring lubrication system, oil pump, data acquisition system and a support structure. A rotating shaft balance (RSB) is used to measure the forces ( $F_x, F_y, F_z$ ) and moments ( $M_x, M_y, M_z$ ) on the

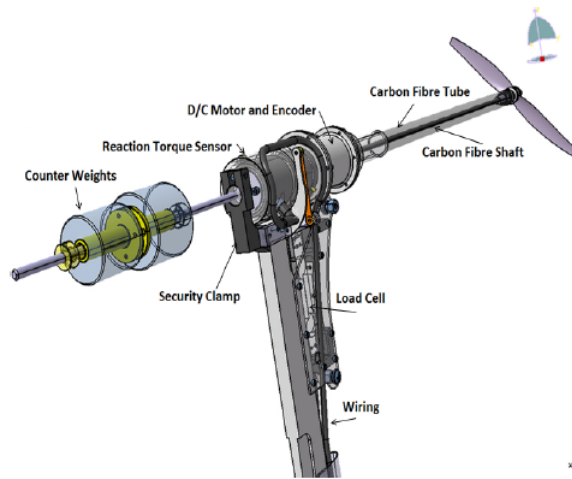


**Figure 2.7:** Propeller unit used for LSL experiments [18]

propeller. The propeller is driven by a Tech Development 1999 pneumatic motor, with the help of air supply system at the Open Jet Facility of Delft University of Technology. Similarly, oil pump is used to lubricate the bearings of the propeller. The support structure consists of a nacelle which houses the motor and a strut to which the nacelle is attached. A detailed description of the propeller setup and operating procedure is given in reference [19]. The geometric details of the propeller are described in Table 2.2.

**Table 2.2:** Geometric details of scaled Fokker F-29 model

Parameter	Symbol	Value	Unit
Diameter	$D_{prop}$	0.3046	m
No of Blades	B	8	-
Hub diameter	$D_{hub}$	0.084	m
Blade angle	$\beta_{70\%}$	40	deg

A technical drawing of the scaled F-29 propeller model and a photograph of the propeller setup in the wind tunnel are shown in Figures 2.8 and 2.9, respectively.

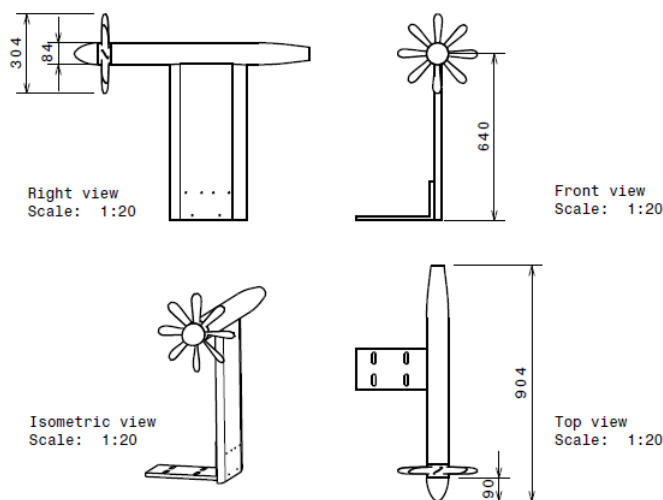


**Figure 2.8:** Technical drawing of the Fokker F-29 scaled model [10]

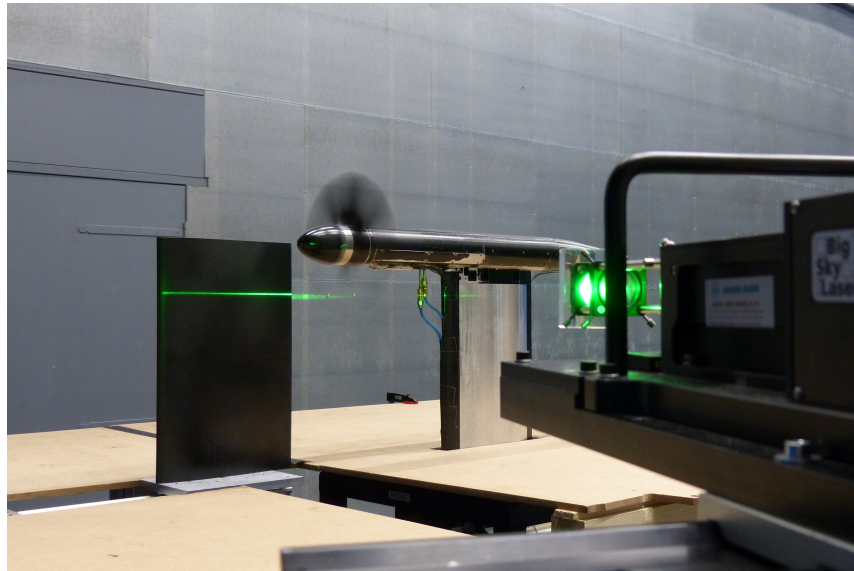


**Figure 2.9:** Propeller model in the pylon-installed configuration at TU Delft's Open Jet Facility

### 2.3.3. UPSTREAM OBJECTS

A number of upstream objects are used to obtain wakes with differing characteristics. A pylon and three cylinder-splitter plate combinations are used to obtain the wakes with distinct characteristics. The pylon design is based on NACA 0012 profile with a span of 450 mm and chord length of 300 mm. The chord length is same as the propeller diameter and the span is based on the geometry of the wind tunnel and support structure of the propeller. The pylon model is unswept and untapered. The geometry of the pylon is described in the Table 2.3. The pylon model was traversed manually during the V-tunnel campaign. Hence, the measurements for different pylon-propeller spacings are obtained by stopping the entire setup for every run. The measurements during the OJF campaign are recorded consecutively without stopping the propeller. The upstream object propeller spacing was controlled with the help of an electronic traverse system.

**Table 2.3:** Geometric details of the pylon model

Parameter	Symbol	Value	Unit
Airfoil type	-	NACA 0012	-
Chord	$c$	0.300	m
Span	$b$	0.450	m
Taper ratio	$\lambda$	0	-
Sweep	$\Lambda$	0	deg

Cylinder-splitter plate combination is used to generate wakes with distinct wake characteristics. The flow past a circular cylinder separates in the shear layers and rolls up as vortices, which lowers the pressure downstream of the cylinder significantly [20]. The pressure downstream of the cylinder along the center-line is found to be varying as the vortices are shed alternatively [20]. As suggested by Roshko [20], it is likely that the low pressure is associated with the center of the vortex. Since the shedding of vortices is lowering the pressure downstream of the cylinder, any object placed behind the cylinder would significantly alter the flow properties. One such object which was investigated before was the splitter plate. The splitter plate was found to increase the center-line pressure downstream of the cylinder and also to prevent periodic vortex shedding [21]. Apelt [21, 22] has studied the effects of splitter plates both short ( $L/D < 1$ ) and long ( $L/D > 1$ ) on the flow past a circular cylinder. Apelt suggested the wake width can be reduced considerably by increasing the length of the short splitter plate ( $L/D < 1$ ). The length of the vortex formation region can also be altered significantly by changing the length of the splitter plate and thereby moving the points of separation round the

cylinder [21]. For longer splitter plates ( $L/D$  between 5-7), Apelt observed that the vortex shedding is completely eliminated and the flow reattaches itself on the splitter plate generating a wake of finite depth and width [21].

Wakes of finite depth and width are obtained for a cylinder splitter plate combination for  $L/D$  greater than 5. The cylinder-splitter plate combination is designed based on  $L/D$  value of 6.5. Three circular cylinders of diameter 20mm, 30 mm and 50 mm are joined with splitter plates of length 135 mm, 195 mm and 325 mm respectively. These objects are referred as CYL20, CYL30 and CYL50 respectively. The thickness of the plates are around 1% of the length of the plates basing on the availability. The geometric details of the cylinder-splitter plate model are given in Table 2.4.

All the cylinder-splitter plate combinations have a span of 450 mm similar to the pylon wing model. The

**Table 2.4:** Geometric details of the cylinder-splitter plate model

Object	Diameter [m]	Width [m]	Length [m]
CYL20	0.02	0.450	0.130
CYL30	0.03	0.450	0.195
CYL50	0.05	0.450	0.325

technical drawing of the CYL50 cylinder-splitter plate combination is shown in Figure 2.10.

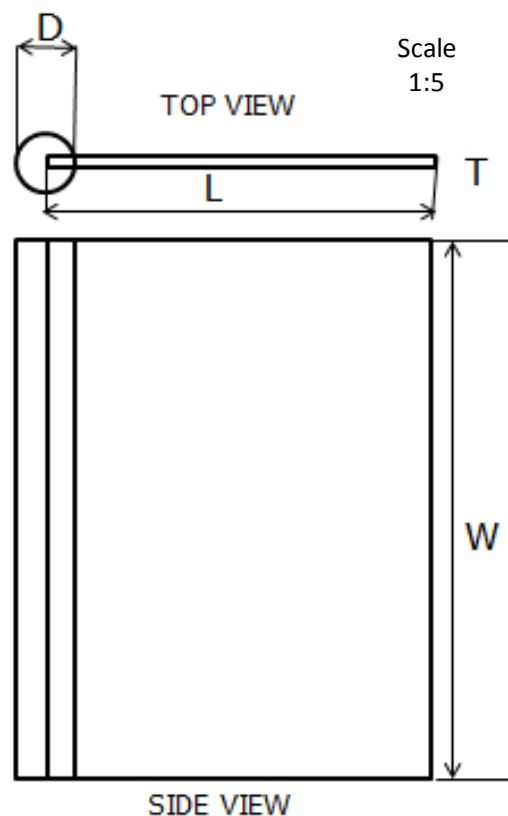


**Figure 2.10:** Scaled technical drawing of cylinder-splitter plate model CYL50

#### 2.3.4. MICROPHONES

Propeller noise measurements are done with the help of two types of microphones: LinearX M51 and LinearX M53. Both are high performance low voltage electret condenser microphones. The M51 features a low distortion, 150 dB SPL capability and wide frequency response whereas M53 features low noise, low distortion,

130dB SPL capability and wide frequency response. Both the microphone types have zero Directivity Index (DI) for frequencies below 5 kHz. A picture of M-51 microphone is depicted in Figure 2.11.

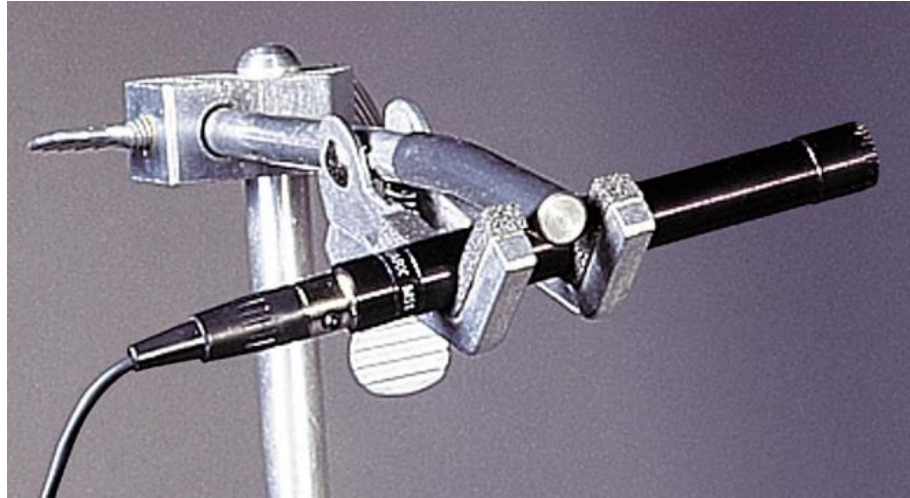


**Figure 2.11:** Photograph of Linear X M-51 microphone[23]

Four M51 microphones are used in the experimental campaign at Low Speed Lab (LSL) as per the position given in Table 2.5.

**Table 2.5:** Position of microphones for the experiment campaign at Low Speed Lab

Microphone (No)	Type	Azimuthal angle[deg]	Flyover angle [deg]	Distance from the center of propeller [m]
M1	M51	180	60	0.6
M2	M51	180	90	0.6
M3	M51	180	120	0.6
M4	M51	270	90	0.6

For the experiments at Open Jet Facility, eight microphones are used as per the position given in the Table 2.6.

**Table 2.6:** Position of Microphones for the experiment campaign at Open Jet Facility

Microphone No	Type	Azimuthal angle[deg]	Flyover angle [deg]	Distance from the center of propeller [m]
M1	M53	86	45	1.82
M2	M53	86	60	1.50
M3	M51	86	75	1.35
M4	M53	86	90	1.31
M5	M51	86	105	1.35
M6	M53	86	120	1.50
M7	M53	86	135	1.82
M8	M51	90	90	1.27

## 2.4. PROCESSING OF PYLON WAKE PROFILE MEASUREMENTS

In the current research project, Stereoscopic PIV is used to determine the inflow velocity profiles at varied operating conditions. The details of PIV setup used during the OJF campaign are given in Table 2.7.

Two LaVision Imager Pro LX 16M high resolution CCD camera(CCD sensor of 4,870 x 3,246 pixels, 12 bit resolution, 7.4  $\mu\text{m}$  pixel pitch) were positioned on the same side of propeller at different viewing angles to

obtain the velocity data in a 300 mm x 300 mm window just in front of the propeller. Due to the limitation of size of the wind-tunnel, the distance between each camera and the field of view was more than 1.6 m. In order to get high image resolution, lenses with 200 mm focal length and 105 mm are used, resulting in a resolution of 1.2 mm. The flow was seeded with the help of a SAFEX Twin Fog Double Power smoke generator which

**Table 2.7:** Details of the Stereoscopic PIV setup

Parameter	Value
Laser	Quantel Evergreen
Camera	LaVision Imager Pro LX 16M
Image Sensor size	4870 x 3246
Pixel size	7.4 $\mu$ m
Focal length	105 mm and 200 mm

releases micron-sized water-glycol particles. The smoke generator was placed in the wind-tunnel settling chamber. A double-pulsed Nd:YAG laser (Quantel Evergreen 200) emitting pulses with wavelength of 532nm, 200 mJ energy per pulse is used to illuminate the target. The laser sheet having a thickness of 1.0 mm is triggered with a pulse separation time of 25  $\mu$ s. The laser and cameras were connected to a host computer via a Digital Delay Generator, which is used to control the laser trigger and image acquisition system.

**Table 2.8:** Details of the Stereoscopic PIV data acquisition

Parameter	Value
Field of View	300 mm X 300 mm
Resolution	1.22 mm X 1.22 mm
No of PIV Images	300
radial location of PIV plane	0.75
laser pulse separation time	25 $\mu$ s

After acquisition of raw wake profiles data, the measurement data requires post processing to remove the effect of reflections and noise. The post processing of wake profile data is elaborated in the following steps.

- Stereo-self calibration
- Elimination of background noise and reflections
- Intensity normalisation
- Geometric masking
- Vector processing
- Vector post processing to obtain the required parameters

#### **Stereo-self calibration**

For the reconstruction of images, the camera orientation and magnification must be known. These characteristics of the setup are computed by using a calibration plate which consists of a grid. The images of the calibration plate from both the cameras are mapped and the geometric parameters like viewing angle, position are computed.

#### **Elimination of background noise and reflections**

The background noise and reflections are eliminated by calculating the local minimum intensity across all the images and removing it from the source image. Only the steady source of reflections is removed. In the present experimental campaign, the propeller blades rotate and hence the reflections vary over the measurement time. However, by the application of the time filter, the back ground noise component is removed considerably indicating the unsteady component of reflections is very small.

#### **Intensity normalisation**

Intensity normalisation is essential if the interrogation domain is illuminated with varying degree across the domain over the period of measurement time. A high pass filter, sliding minimum is applied to filter out the local mean background intensity and leaving out only the fluctuations in intensity.

### Geometric masking

The pylon and the spinner shield the measurement domain as they are positioned in front. Masking of the spinner and the pylon is performed as the regions covered by these objects do not provide any information and add to the computational time.

### Vector processing

The velocity vectors are processed by using stereo cross correlation techniques. The processing is accomplished in two stages with different window sizes. Square window of sizes 64 x 64 and 32 x 32 are used for the first and second pass respectively. Also, an overlap of 50% and 75% are used during the first and second pass respectively.

### Vector post processing

From the velocity vectors computed in the previous step, the average velocity and the root mean square deviation of the velocity components in x,y,z direction are computed.

## 2.5. PROCESSING OF PROPELLER PERFORMANCE MEASUREMENTS

The propeller performance measurements are recorded using a six component Rotating Shaft Balance (RSB) which uses strain gauges to record the forces and moments in all three directions. The development and testing of the RSB is done by National Aerospace Laboratory of the Netherlands (NLR). Also, a 1-P signal is generated for one rotation of the RSB and thereby indicating the angular position of the RSB at every measurement point. The strain gauges measures all the force/ moments at a sampling frequency of 50 kHz and for a total measurement time of 15 secs. The recorded voltages are further processed to obtain the propeller force/ torque measurements by following the below given process.

- Calibrating the loaded propeller measurements with the unloaded propeller measurements
- Conversion of voltages to propeller force/ moments using the calibration matrices
- Computing the time accurate force/moments averaged over one rotation
- Correcting the propeller thrust for the pressure drag measured at the spinner
- Computing the time averaged propeller performance parameters

### Calibrating the loaded propeller measurements with the unloaded propeller measurements

The RSB measurements are recorded many times (say  $n_{meas}$ ) in a loaded condition for a measurement time of 15 seconds. RSB measurements are also recorded before and after the propeller is loaded. These measurements recorded are different and showed an offset from zero in both cases. Hence, the actual RSB measurements in the loaded condition are obtained by subtracting the zero loading offset in the below given manner:

$$V_{actual,i} = V_{meas,i} - \left[ V_{meas,0} + \frac{(V_{meas,n} - V_{meas,0}) * t_i}{t_{total}} \right] \quad (2.1)$$

- $V_{actual,i}$  = measured voltage for the  $i^{th}$  recording at loaded propeller condition  
 $V_{meas,0}$  = measured voltage for the zeroth recording at unloaded propeller condition  
 $V_{meas,n}$  = measured voltage for the  $n^{th}$  recording at unloaded propeller condition  
 $t_{total}$  = total time taken during all the (n+1) measurements  
 $t_i$  = time at  $i^{th}$  recording

### Conversion of voltages to propeller force/ moments using the calibration matrices

The RSB measurements with the help of strain gauges are in volts. Hence, they are converted into propeller force/ moments using the calibration data. The calibration was performed at National Aerospace Laboratory of Netherlands (NLR) and the data is provided in Appendix A. The forces and moments are obtained by Equation 2.2. Further, the measurements are scaled by an excitation voltage of 10 V.

$$F_i = \frac{1}{V_{exc}} \left[ \sum_{j=1}^6 AR(j, i) V_{actual,j} \right] \quad (2.2)$$

where

$F_i$  =  $i^{\text{th}}$  computed force/moment  
 $V_{\text{actual},j}$  =  $j^{\text{th}}$  component of the measured RSB voltages  
 $V_{\text{exc}}$  = RSB excitation voltage  
 $AR$  = calibration matrix

### Computing the time accurate propeller performance averaged over one rotation

After calculating the time accurate force/moments, these measurements are averaged over one rotation with the help of 1-P signal. The force/moment signal between two pulses of the 1-P signal is interpolated to 360 measurement points indicating 1 measurement point for every degree of rotation. The force/moment signal over the 360 degrees is averaged over many rotations providing the time accurate signal averaged for one complete rotation. **Correcting the propeller thrust for the pressure drag measured at the spinner**

The drag on the spinner due to the pressure at the back side of the spinner results in an additional thrust measured and hence needs to be corrected. The pressure at the back side of spinner is measured with the help of pressure orifices located on the plate installed behind the spinner. The 18 orifices are located over two perpendicular diameters of the plate. The corrected thrust measurement is obtained by the following equation

$$F_{\text{corrected}} = -F_{\text{meas}} - \frac{(p_i - p_{\infty})A_{\text{bp}}}{18} \quad (2.3)$$

where

$F_{\text{corrected}}$  = thrust corrected for the pressure drag on the spinner  
 $F_{\text{meas}}$  = measured axial force by the RSB  
 $p_i$  = pressure at the  $i^{\text{th}}$  orifice  
 $p_{\infty}$  = freestream static pressure  
 $A_{\text{bp}}$  = Area of the back plate

### Computing the propeller performance parameters

Finally, the propeller performance parameters are computed after obtaining the propeller force and moments by Equations 1.3, 1.4 and 1.6 respectively.

## 2.6. PROCESSING OF PROPELLER NOISE MEASUREMENTS

The experimental data is processed to obtain the required parameters which are then used to interpret the final results. The processing of microphone data is elaborated in the following steps.

- Conversion of microphone signal to pressure signal
- Spectral analysis of the pressure signal
- Computing the sound pressure level
- Applying correction for shear layer refraction and frequency response correction

### Conversion of microphone signal to pressure

The microphones are calibrated using a piston phone at the beginning and the end of every day of experiments. It is also ensured that calibration is performed every time the power supply to the microphones is switched off. Since the microphone records the pressure fluctuations in terms of voltages, the conversion of the measurement data from voltage to the pressure is performed. The root mean square of the fluctuation of the voltage signal with  $N_{\text{samp}}$  sampling measurements is computed by Equation 2.4.

$$V'_{\text{rms}} = \sqrt{\frac{(V_1 - \bar{V})^2 + (V_2 - \bar{V})^2 + (V_3 - \bar{V})^2 + \dots + (V_n - \bar{V})^2 + \dots + (V_{N_{\text{samp}}} - \bar{V})^2}{N_{\text{samp}}}} \quad (2.4)$$

The measured fluctuation of the voltage signal during the calibration process is related to a harmonic sound of  $SPL_{\text{cal}} = 114$  dB at a frequency of 250 Hz. Hence, the pressure signal during the measurement is related to the measured voltage signal by Equation 2.5.

$$P_{\text{meas}}(t) = V_{\text{meas}}(t) \frac{p_0 \cdot 10^{\frac{SPL_{\text{cal}}}{20}}}{V'_{\text{cal,rms}}} \quad (2.5)$$

$n$	= sampling point index
$N_{\text{samp}}$	= No of samples
$V_n$	= measured voltage at sampling point 'n'.
$\bar{V}$	= average of voltage signal.
$V'_{\text{rms}}$	= root mean square of the voltage fluctuation ( $V_n - \bar{V}$ )
$V_{\text{meas}}(t)$	= voltage signal during the measurement as a function of time
$V'_{\text{cal,rms}}$	= root mean square of the voltage fluctuation during the calibration
$p_0$	= reference acoustic pressure of 20 $\mu\text{Pa}$
$SPL_{\text{cal}}$	= sound pressure level of the sound emitted during calibration
$P_{\text{meas}}$	= computed pressure signal.

The pressure signal after the calibration process is then used as an input for the spectral analysis to estimate the power at different frequencies.

### Spectral analysis of the pressure signal

Spectral analysis of the pressure signal is performed using the Welch's method for power spectral density (PSD) estimation. Welch's method computes the power of pressure signal at different frequencies by using the time history of the pressure signal computed in the previous step. The time signal of pressure is now divided into a number of segments and then the discrete Fourier transform is applied to the individual segments to compute the modified periodogram. The spectral estimate of the time history is computed by averaging the periodograms obtained from the Fourier transformed data. More on the spectral analysis can be found in [24].

### Computing the Sound Pressure Level

The time history of the power spectral density is converted to obtain sound pressure level using Equation 2.6

$$SPL(f_n) = 10 \log_{10} \frac{P(f_n) \Delta f}{p_o^2} \quad (2.6)$$

$P(f_n)$	= power spectral density
$SPL(f_n)$	= sound pressure level as a function of frequency

### Applying correction for shear layer refraction and frequency response correction

Both the correction methods are detailed in Appendix B. The microphone response depends on the frequency of the sound emitted. Hence a necessary correction is applied to the sound pressure level at different frequencies. Since the testing is performed in an open jet wind tunnel and the microphones are placed just outside the wind tunnel test section, the sound waves emitted by the noise sources refract in the shear layer. Therefore, a necessary shear layer correction is applied to the sound pressure levels.

# 3

## EXPERIMENTAL RESULTS: PYLON WAKE PROFILES

The current chapter focuses on the pylon wake velocity profiles obtained for the isolated, pylon-installed and cylinder-splitter plate installed configurations. These wake velocity profiles are later used for a qualitative analysis of the propeller performance and noise emissions. A brief overview of different characteristics of wake profile measurements is presented in Section 3.1. Thereafter, the propeller inflow in the isolated configuration is treated in Section 3.2. Subsequently, the pylon wake velocity profiles in the installed configuration are discussed in Section 3.3. Finally, the inflow into the propeller for the cylinder-splitter plate configuration is considered in Section 3.4. In all the configurations, the effects of upstream object-propeller spacing and the advance ratio on the propeller inflow profiles are also discussed.

### 3.1. MEASUREMENT OVERVIEW

The measurements performed to evaluate the wake profiles are conducted at various operating conditions. A summary of the operating conditions is listed in Table 3.1.

**Table 3.1:** Summary of the various operating conditions for the experiments conducted at OJF

Parameter	Symbol	Value	Unit
Freestream velocity	$U_\infty$	[18,26]	m/s
Advance ratio	$J$	[0.6 1.0 1.4 1.8]	-
Pylon-propeller spacing	$\Delta X$	$[0.4-1]D_{\text{prop}}$	-
Radial location of PIV plane	$\left(\frac{r}{R_{\text{prop}}}\right)_{\text{PIV}}$	0.75	-
Upstream condition	$OBJ$	[ISO, PYL, CYL20, CYL30, CYL50]	-
Angle of attack	$\alpha$	0	deg
Angle of sideslip	$\beta_{\text{SS}}$	0	deg
Measurement time	$t_m$	7.5	s
No of images	N	300	-
Field of view	FOV	300x 300	mm

Table 3.1 shows that the measurements are recorded for isolated, pylon-installed and cylinder-splitter plate installed configurations. Stereoscopic PIV is used to determine the propeller inflow velocity profiles at a radial station of 0.75 times the radius of the propeller using two cameras of focal lengths are 105 mm and 200 mm respectively. The measurements are averaged over a sufficiently large period of time to ensure the differences which would be observed for different phase angles are averaged to zero. The PIV plane of size 300 mm x 300 mm lies in the Z-plane as shown in Figure 3.1. A rectangular portion is blacked out from the velocity profiles for the isolated configuration as the reflections from the propeller spinner are high in this location resulting in inaccurate velocity profiles. Some of the propeller inflow velocity profiles in the 300 mm x 300 mm window is lost as the laser beam is triggered at an angle. The lost wake information is not shown in

the wake profiles listed in this chapter. Also when the pylon is close to the propeller, information is lost due to the reflections of the pylon. However, this will not impact the observations since the lost information in the 300 mm x 300 mm window is

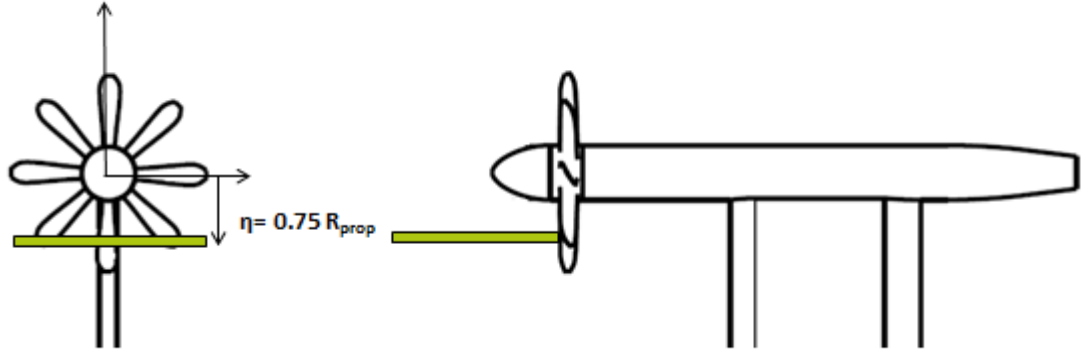


**Figure 3.1:** Location of PIV plane

For a comparison of wake profiles at different configurations, wake characteristics such as non-dimensional wake displacement thickness, non-dimensional wake momentum thickness, non-dimensional velocity deficit and non-dimensional wake width are introduced here. The wake nomenclature is shown in Figure 3.2 and the wake characteristics are given by the below equations

$$\epsilon = \frac{\int_{-\frac{b_w}{2}}^{+\frac{b_w}{2}} \left(1 - \frac{U(Y)}{U_{\text{edge}}}\right) dY}{D_{\text{prop}}} \quad (3.1)$$

$$\kappa = \frac{\int_{-\frac{b_w}{2}}^{+\frac{b_w}{2}} \frac{U(Y)}{U_{\text{edge}}} \left(1 - \frac{U(Y)}{U_{\text{edge}}}\right) dY}{D_{\text{prop}}} \quad (3.2)$$

$$v = \frac{U_{\text{edge}} - U_{\text{min,wake}}}{U_{\infty}} \quad (3.3)$$

- $\epsilon$  = Non-dimensional wake displacement thickness
- $\kappa$  = Non-dimensional wake momentum thickness
- $v$  = Non-dimensional velocity deficit
- $b_w$  = wake width
- $U_{\text{edge}}$  = Edge velocity of the wake
- $U_{\text{min,wake}}$  = Minimum velocity in the wake
- $U_{\infty}$  = Freestream velocity

## 3.2. ISOLATED CONFIGURATION

This section treats the propeller inflow velocity profiles for the isolated configuration. The results obtained are used to compare with the pylon-installed and cylinder-splitter plate installed configurations.

### 3.2.1. EFFECT OF ADVANCE RATIO

The propeller inflow velocity profiles are measured for a freestream velocity of 18 m/s and four different advance ratios: 0.6, 1.0, 1.4 and 1.8. The advance ratios 0.6, 1.0, 1.4 and 1.8 are also referred as high thrust condition (HTC), medium thrust condition (MTC), low thrust condition (LTC) and zero thrust condition (ZTC). The propeller inflow velocity profiles for the four propeller operating conditions are shown in Figure 3.6.

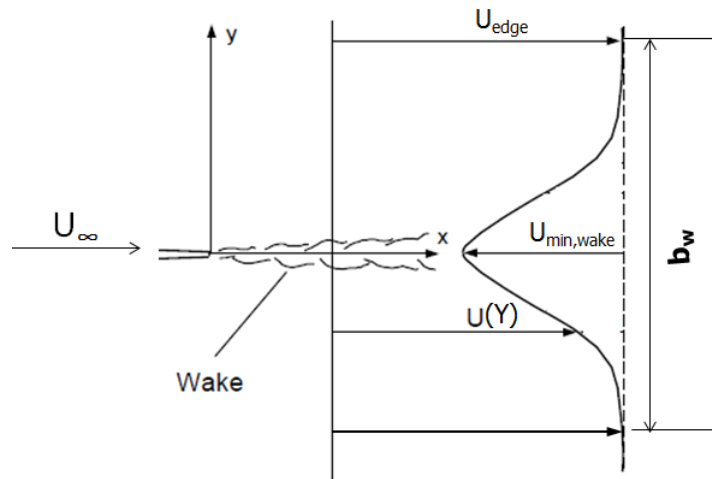


**Figure 3.2:** Wake structure nomenclature

The presence of propeller is seen as an increase in inflow velocity at all advance ratios. The velocity at the center is highest and decreases away from the center. This is expected as the average blade section loading is highest at the center and decreases away from the center. Figure 3.6c 3.6b and 3.6d indicate that the inflow velocity profile is not uniform. This is due to the phase angle variations between the images. At a high advance ratio, the phase angle variations do not average due to the insufficient number of images extracted. This non-uniformity can be reduced by increasing the number of images extracted or extracting phase-locked data when the propeller blade is at azimuthal angle of zero degrees.

The velocity profiles at non-zero thrust condition indicate an increase in velocity with decrease in advance ratio across the test section. This is due to the negative pressure gradient (suction) present as the propeller generates thrust at low advance ratios. Figure 3.4 also show the inflow velocity profiles as function of distance to propeller. The velocity profile just in front of the propeller is given by  $\frac{\Delta X}{D_{prop}} = 0.05$ . The observations made from Figure 3.6 can be observed here.

### 3.3. PYLON-INSTALLED CONFIGURATION

The pylon in front of the propeller generates a wake which is ingested into the propeller, and thereby affecting the propeller performance and noise emissions. Hence it is important to evaluate the propeller inflow velocity profiles in the pylon-installed configuration. The present section first treats the effect of advance ratio on the pylon wake (Subsection 3.3.1). Later, the effect of pylon-propeller spacing on the pylon wake is discussed in Subsection 3.3.2.

#### 3.3.1. EFFECT OF ADVANCE RATIO

##### STREAMWISE VELOCITY

The favourable pressure gradient in front of the propeller running at a low advance ratio might have an effect on the propeller inflow velocity profile. To determine the effect of the propeller suction (negative pressure gradient) on the propeller inflow velocity, a number of measurements are recorded at a freestream velocity of 18 m/s and different advance ratios. The wake profiles are recorded for a pylon-propeller spacing of 40% of the diameter of the propeller. The pylon wake ingested into the propeller at four different thrust conditions : High Thrust Condition (HTC), Medium Thrust Condition (MTC), Low Thrust Condition (LTC) and Zero Thrust Condition (ZTC) are shown in Figure 3.5.

In all the four operating points tested, the presence of pylon wake is clearly seen for  $-0.25 \leq \frac{Y}{D_{prop}} \leq 0.25$ . The local velocity at a specific location in the pylon wake increases with decrease in advance ratio. The wake accelerates into the propeller for the advance ratios 0.6, 1.0 and 1.4. For the advance ratio of 1.8, slight accel-

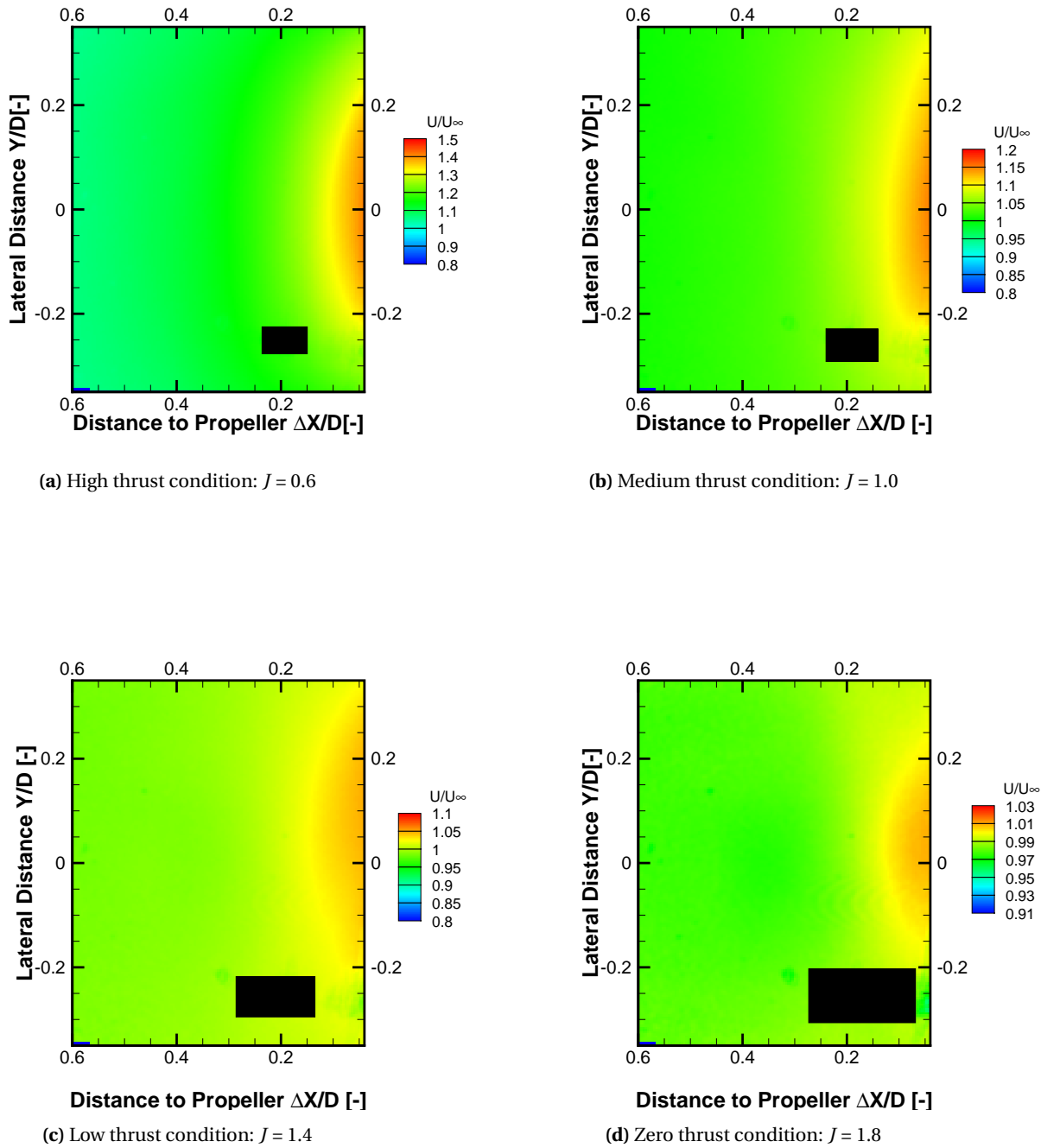


**Figure 3.3:** OJF campaign: Propeller inflow velocity contours  
Isolated Configuration:  $U_\infty = 18$  m/s,  $J = [0.6 \ 1 \ 1.4 \ 1.8]$

eration is visible indicating the local blade loading is generating thrust in the local blade section. The velocity contours are not symmetric with respect to  $y$ -axis indicating the presence of an angle of attack of the pylon or due to the phase angle variations between the images (as already mentioned in previous section). Preliminary inspection of the wake contours suggest a decrease in wake width with decrease in advance ratio. In order to compare the velocity profiles at different operating conditions, non-dimensional wake displacement

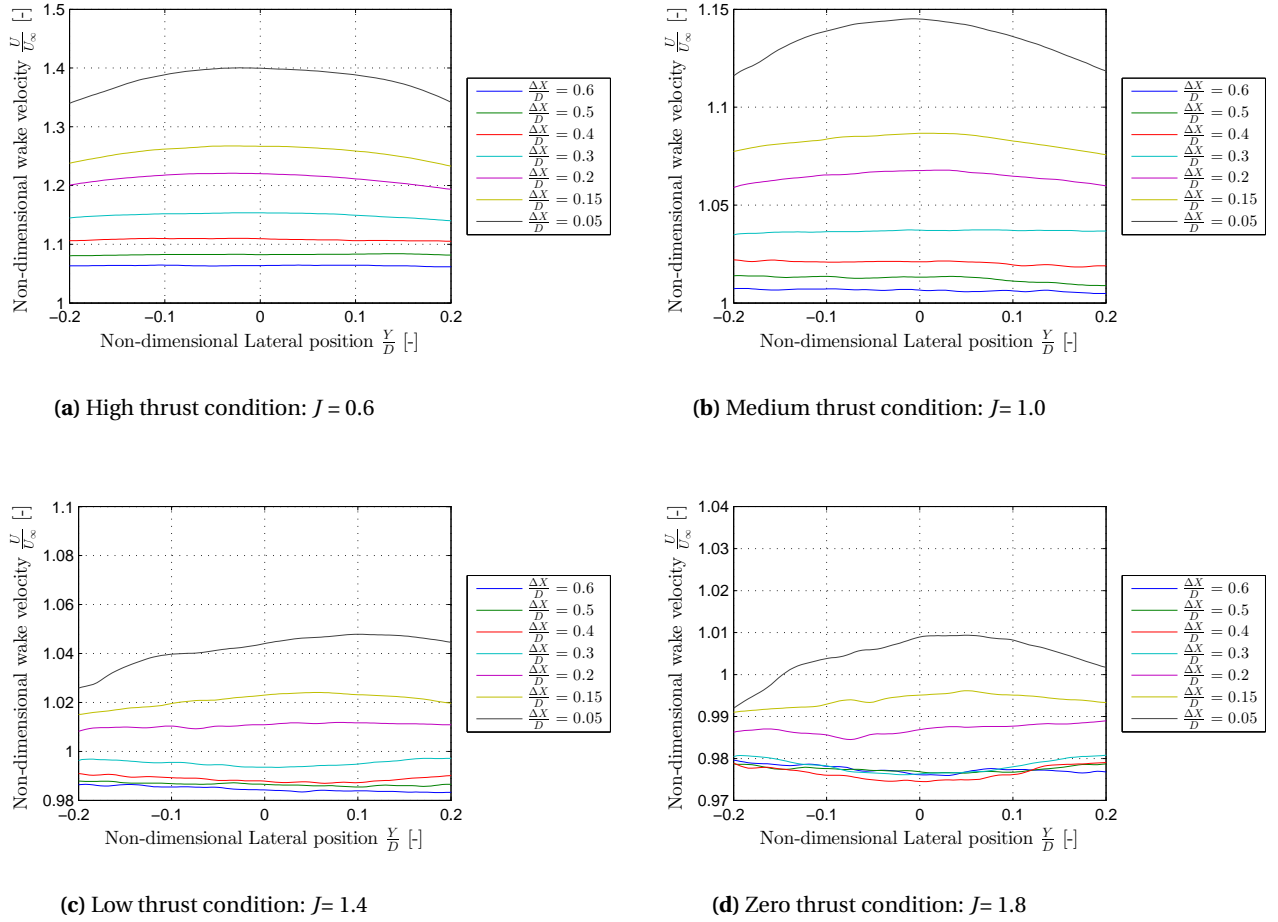


**Figure 3.4:** OJF campaign: Propeller inflow velocity profiles  
Isolated Configuration:  $U_\infty = 18$  m/s,  $J = [0.6 \ 1 \ 1.4 \ 1.8]$

thickness, non-dimensional velocity deficit, non-dimensional wake width and non-dimensional momentum thickness are computed and are presented in Figure 3.7.

The configurations presented are for the pylon-propeller spacing of 40%, 50% and 100% of the diameter of the propeller. It is noticed that the non-dimensional wake displacement thickness and non-dimensional wake velocity deficit decrease with a decrease in advance ratio at constant pylon-propeller spacing. This is due to the effect of propeller suction on the pylon wake. The increased mixing in the pylon wake when a negative pressure gradient (favourable) is present reduced the mass deficit and hence a decrease in non-dimensional wake displacement thickness is observed. The non-dimensional velocity deficit decreased as the increase in centerline velocity is greater than the increase in edge velocity. This is due to the higher rate of momentum exchange in the center of the wake than at the edge. The non-dimensional wake displacement thickness is maximum in the case of closest pylon-propeller spacing. This is due to the reduced mass deficit in the wake with distance from the pylon trailing edge. The non-dimensional velocity deficit also decreased with increase in spacing as the centerline velocity increases with distance from the pylon trailing edge. However, the results do not match at the operating condition of closest pylon spacing and lowest advance ratio. This is due to presence of the propeller affecting the pylon wake characteristics. The favourable pressure gradient in front of the propeller reduced the boundary layer thickness and thereby reducing the mass deficit in the wake. This resulted in a decrease in the non-dimensional wake displacement thickness. The thinner boundary layer resulted in a wake with higher centerline velocity which decreased the non-dimensional wake velocity deficit.

The non-dimensional wake width did not follow any trend with advance ratio erroneous as the resolution

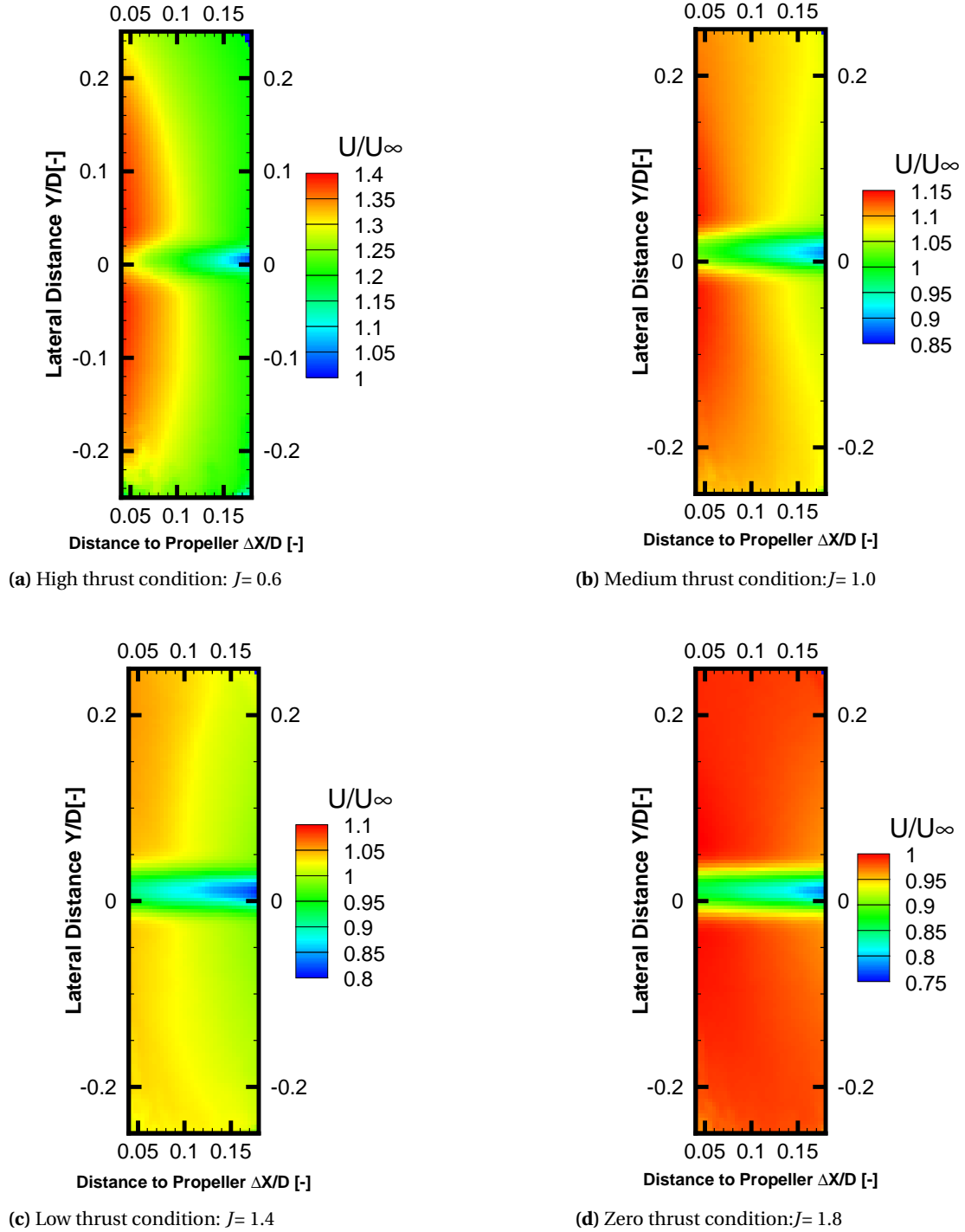


**Figure 3.5:** Propeller inflow velocity profiles in the Installed Configuration:  
 $U_{\infty} = 18 \text{ m/s}$ ,  $J = [0.6 \ 1 \ 1.4 \ 1.8]$   $\Delta X = 50\%D_{\text{prop}}$

of 1.22 is high for a thin wake. With increase in spacing, wake width increased which is due to the momentum exchange between the wake and the freestream. The non-dimensional wake momentum thickness increased with decrease in advance ratio. This is due to the increased momentum deficit in the wake due to the propeller suction. The momentum deficit close to the centerline increased leading to an increase in momentum thickness. However, the results do not match at the operating condition of closest pylon spacing and lowest advance ratio.  $J=0.6$  and  $\Delta X = 0.4D_{\text{prop}}$ . This is due to presence of the propeller affecting the momentum

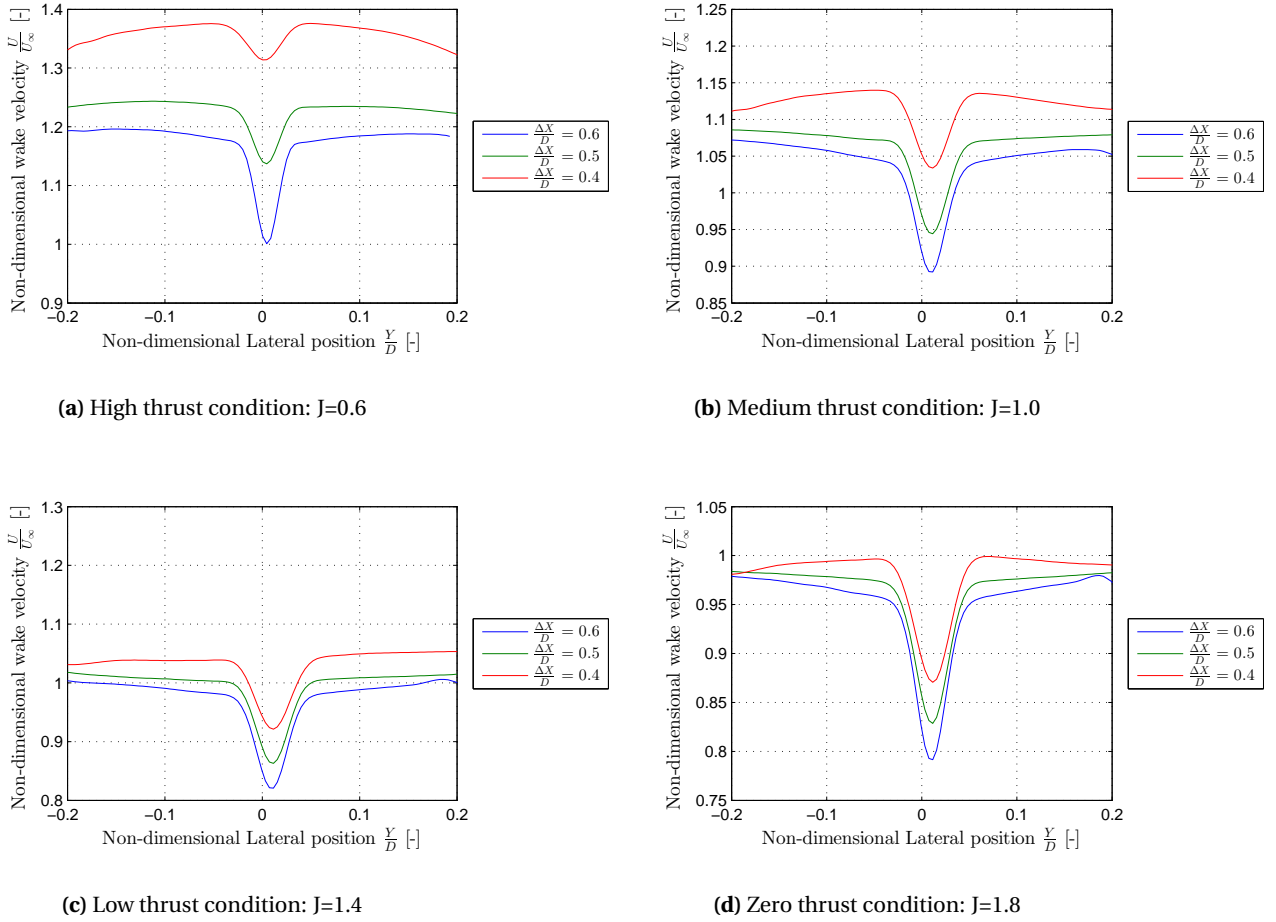


**Figure 3.6:** OJF campaign: Propeller inflow velocity profiles  
Isolated Configuration:  $U_\infty = 18$  m/s,  $J = [0.6 \ 1 \ 1.4 \ 1.8]$

deficit in the wake. The favourable pressure gradient in front of the propeller reduced the boundary layer thickness and thereby reducing the momentum deficit in the wake.

#### ROOT MEAN SQUARE DEVIATION OF STREAMWISE VELOCITY

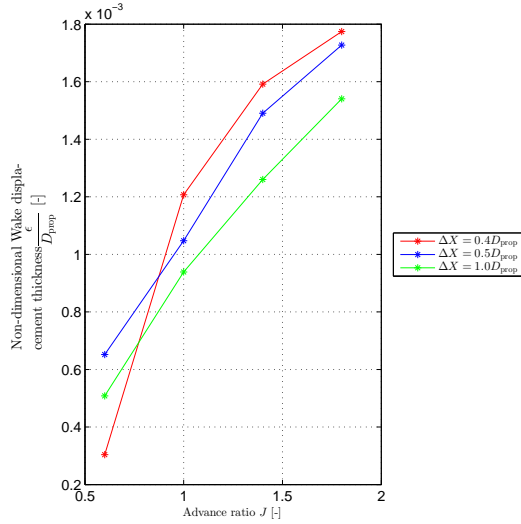
The effect of advance ratio on the root mean square deviation of the streamwise velocity component is discussed here. With decrease in advance ratio, the induced velocity in the axial direction increased resulting in a lower fluctuation. Hence the root mean square deviation of the streamwise velocity component decreased with decrease in advance ratio.

### 3.3.2. EFFECT OF PYLON-PROPELLER SPACING

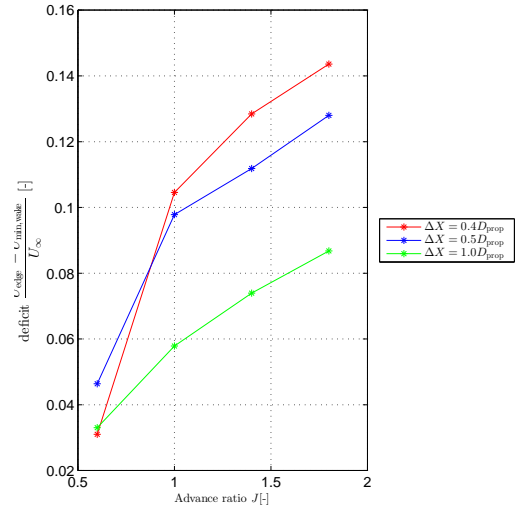
#### STREAMWISE VELOCITY

In this subsection, the effect of pylon-propeller spacing on the pylon wake is treated. The measurements are recorded for freestream velocities of 20 m/s and 26 m/s and at an advance ratio of 1. The pylon was traversed from 40% to 100% of the diameter of the propeller. The velocity contours for the closest and farthest pylon spacing are presented in Figures 3.9a and 3.9b respectively.

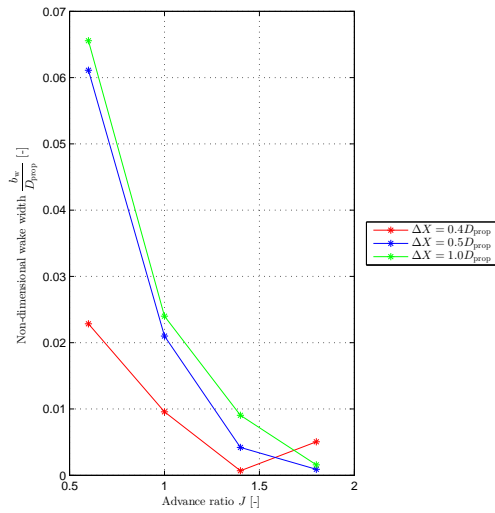
The velocity contours clearly show the presence of the pylon wake in both the installed configurations. The symmetry in the pylon wake is also observed in both the configurations. The acceleration of the wake in the presence of negative pressure gradient is also visible. The non-dimensional wake displacement thickness, wake velocity deficit, wake width and wake momentum thickness are computed and plotted in



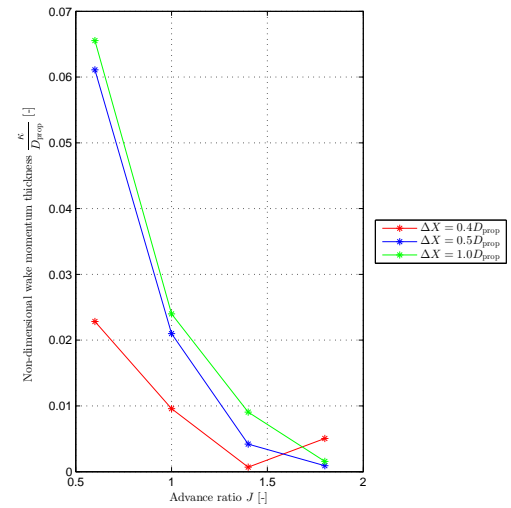
(a) Non-dimensional wake displacement thickness



(b) Non-dimensional velocity deficit



(c) Non-dimensional wake width



(d) Non-dimensional momentum thickness

**Figure 3.7:** Variation of wake parameters with advance ratio.  
Pylon-Installed Configuration:  $U_{\infty} = 18$  m/s,  $J = [0.6 \ 1 \ 1.4 \ 1.8]$

Figures 3.10a and 3.10d respectively.

As the advance ratio is constant in both the operating conditions, the influence of the pressure gradient is same in both the configurations. The non dimensional wake displacement decreases with increase in pylon-propeller spacing. This is due to the reduced mass deficit in the wake with distance from the pylon trailing edge similar to a wake in zero pressure gradient [33]. The non-dimensional velocity deficit also decreased with increase in spacing as the centerline velocity increases with distance from the pylon trailing edge. With increase in spacing, non-dimensional wake width increased which is due to the high momentum exchange between the wake and the freestream. The non-dimensional wake momentum thickness increased with increase in pylon-propeller spacing as the momentum deficit in the wake increases as

#### ROOT MEAN SQUARE DEVIATION OF STREAMWISE VELOCITY

The effect of pylon-propeller spacing on the root mean square deviation of the streamwise velocity component is discussed here. Theoretically, far downstream from the pylon trailing edge the wake velocity profile changes to uniform velocity with zero fluctuations. With increase in pylon-propeller spacing, the turbu-

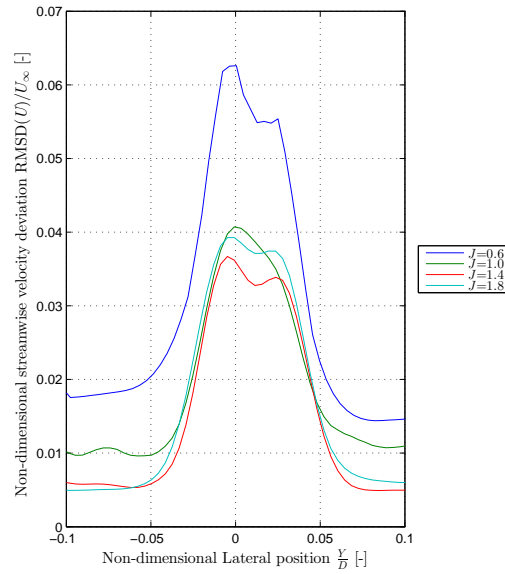
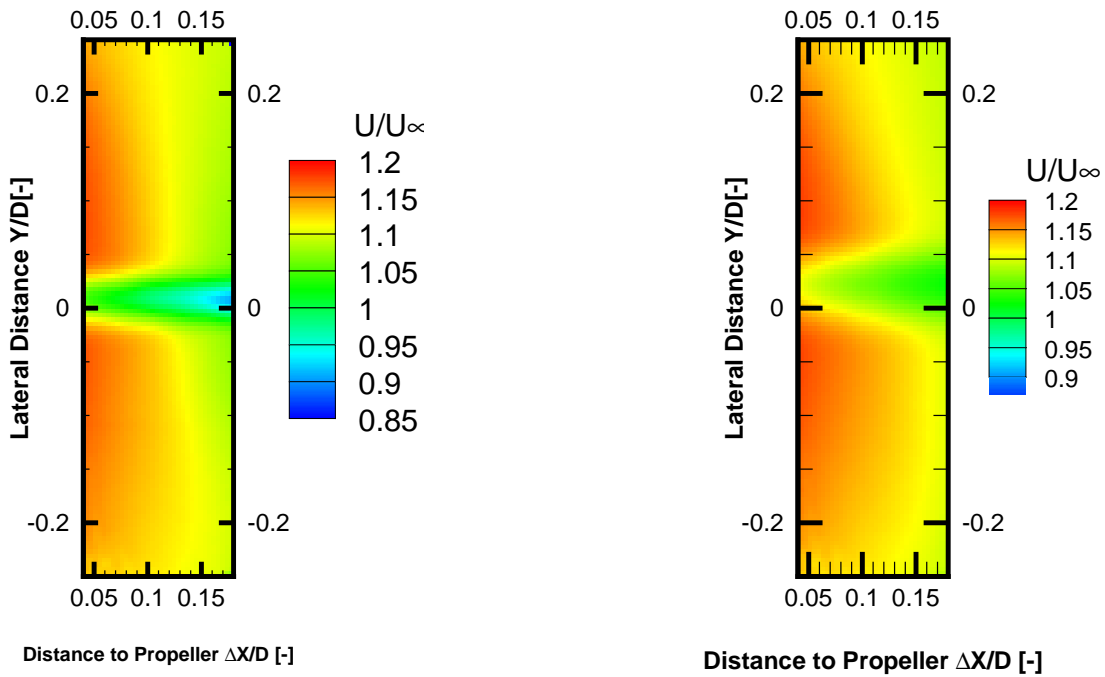


**Figure 3.8:** Non-dimensional root mean square deviation of the streamwise velocity component versus the advance ratio  
 Pylon-Installed Configuration:  $U_\infty = 18 \text{ m/s}$ ,  $J = [0.6 \ 1.0 \ 1.4 \ 1.8]$   $\Delta X = [50]\%D_{prop}$

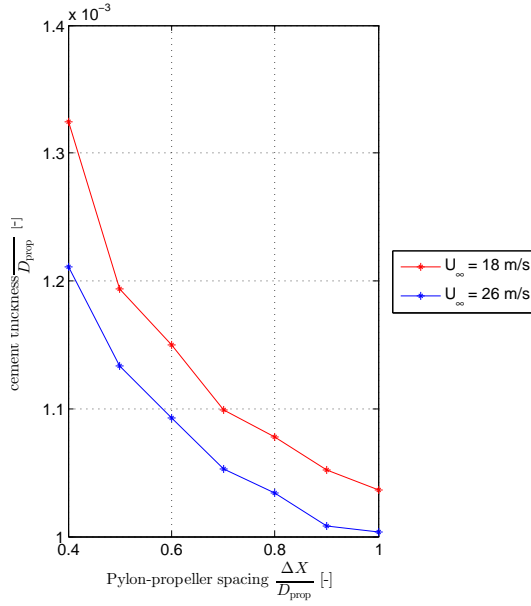


(a)  $\Delta X = 40\%D_{prop}$

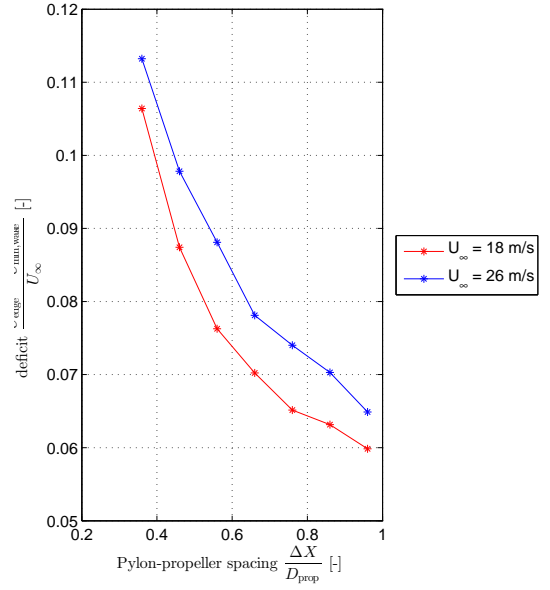
(b)  $\Delta X = 100\%D_{prop}$

**Figure 3.9:** Wake Velocity Contours.  
 Pylon-Installed Configuration:  $U_\infty = 18 \text{ m/s}$ ,  $J = 1.0$

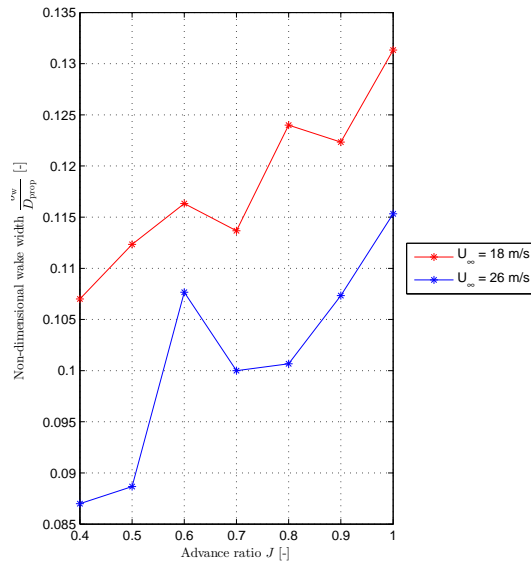
lent fluctuations dissipate due to reduced mixing in the wake. Hence the root mean square deviation of the streamwise velocity component decreased with increase in pylon-propeller spacing.



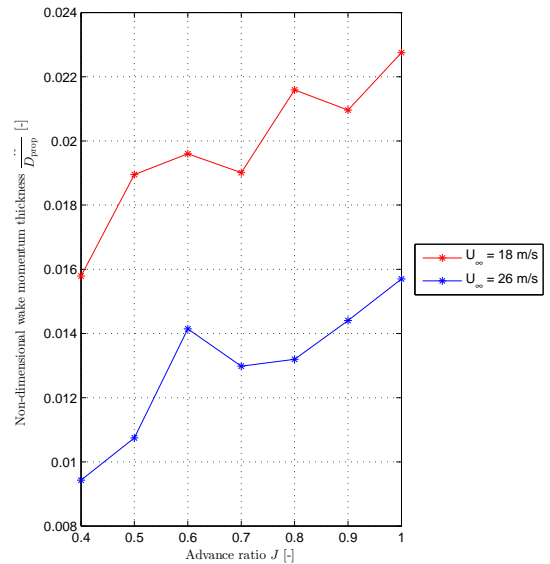
(a) Non-dimensional wake displacement thickness



(b) Non-dimensional velocity deficit



(c) Non-dimensional wake width



(d) Non-dimensional wake momentum thickness

**Figure 3.10:** Variation of wake parameters with pylon-propeller spacing.  
Pylon-Installed Configuration:  $U_{\infty} = 18$  m/s,  $J = 1.0$ ,  $\Delta X = [40 - 100]\%D_{prop}$

### 3.4. EFFECT OF UPSTREAM OBJECTS

In the previous sections, the wake velocity profiles for the isolated and pylon-installed configuration are dealt. Here in this subsection, the wake velocity profiles for the cylinder-installed configuration is treated. The various cylinder splitter configurations are labelled as CYL20, CYL30 and CYL50 for the diameters of the cylinder of 20 mm, 30 mm and 50 mm respectively. The geometry of the objects is already presented in Chapter 2. The velocity profiles for the isolated and pylon-installed configuration are also shown here as a reference and labelled in this section as ISO and PYLON Stereoscopic PIV measurements to record the wake velocity profiles

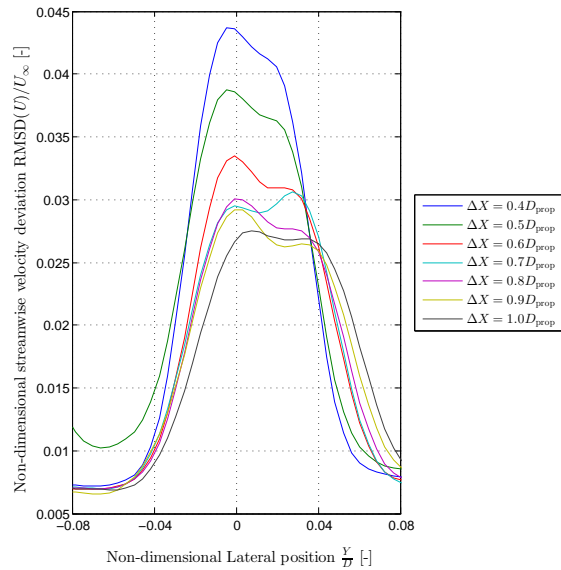
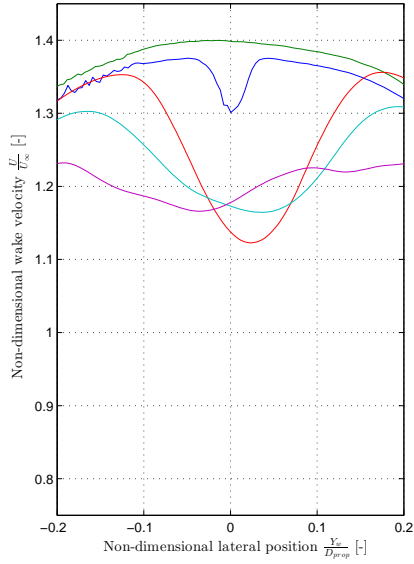


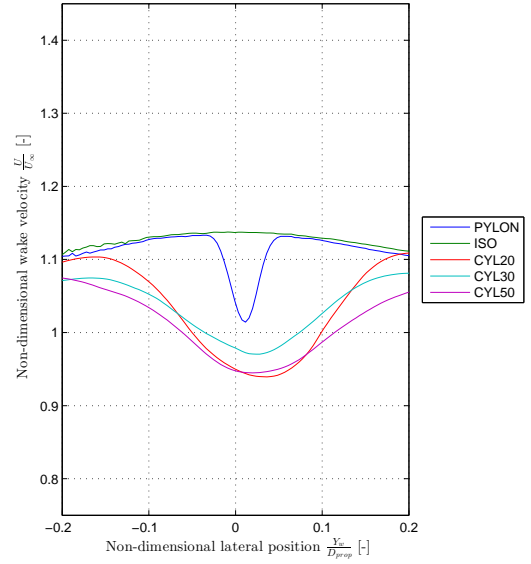
**Figure 3.11:** Non-dimensional root mean square deviation of the streamwise velocity component versus the pylon propeller spacing  
Pylon-Installed Configuration:  $U_\infty = 18 \text{ m/s}$ ,  $J = 1.0$   $\Delta X = [40 - 100]\%D_{\text{prop}}$

are conducted at a freestream velocity of 18 m/s, advance ratios of 0.6, 1, 1.4 and 1.8 and at a pylon-propeller spacing of 50% of the diameter of the propeller. The pylon is positioned at an angle of attack of zero degrees. The wake velocity profiles extracted at a location of 1 cm in front of the propeller are shown in Figure 3.12.

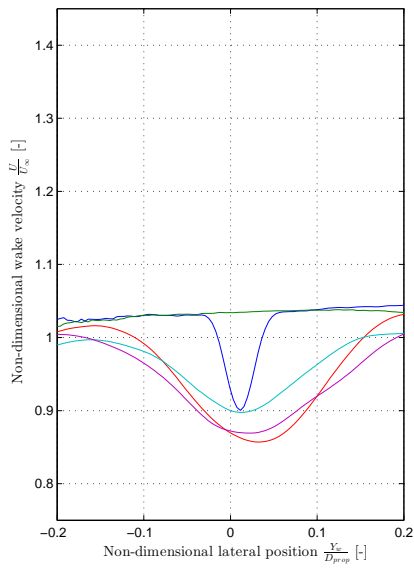
From Figure 3.12, the wakes obtained from the cylinder installed configuration are much wider compared to the pylon wakes. The pylon wake is nearly 4 times smaller than the cylinder-splitter plate wakes. The wake width increased with the diameter of the object. The wake velocity deficit of the pylon wake is comparable to the wake of the cylinder splitter wakes. The cylinder splitter plate wake at an advance ratio is not symmetric indicating a possible separation of flow in the wake.



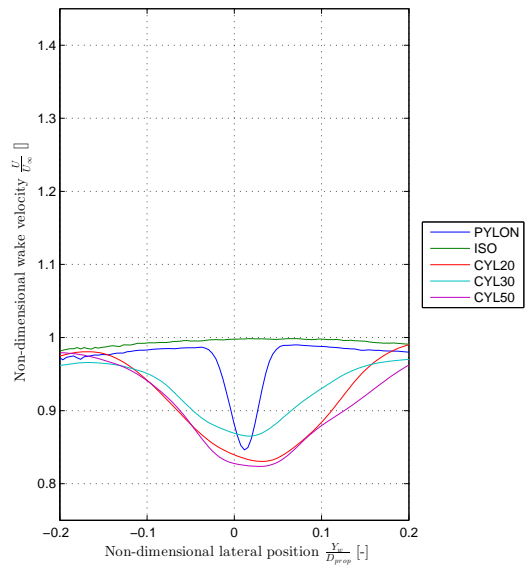
(a) High thrust condition



(b) Medium thrust condition



(c) Low thrust condition



(d) Zero thrust condition

**Figure 3.12:** Propeller inflow velocity profiles in the Installed Configuration:  
 $U_\infty = 18 \text{ m/s}$ ,  $J = [0.6 \ 1 \ 1.4 \ 1.8]$   $X_{pylon} = 50\%D_{prop}$

# 4

## EXPERIMENTAL RESULTS: PROPELLER PERFORMANCE

One of the objectives of the present thesis is to evaluate the effect of the advance ratio and the effect of upstream object-propeller spacing on the performance of the pusher propeller in the installed configuration. This chapter provides the propeller performance results in terms of thrust coefficient, torque coefficient and propeller efficiency for the experiments conducted in Open Jet Facility of TU Delft. An overview of the measurement conditions in the experimental campaign conducted at OJF is presented in Section 4.1. The reproducibility of the propeller performance results are discussed in Section 4.2. Propeller performance for the isolated configuration is given in Section 4.3. The propeller performance results for the pylon installed configuration are presented in Section 4.4. Subsequently, the effect of pylon-propeller spacing on the propeller performance is treated in Section 4.5. Finally, Section 4.6 elaborates the effect of cylinder-splitter plate installed configuration on the performance of propeller.

### 4.1. MEASUREMENT OVERVIEW

The experiments to evaluate the performance of the propeller are conducted at various operating conditions. A summary of the operating parameters is presented in Table 4.1.

**Table 4.1:** Summary of the various operating conditions for the experiments conducted at OJF

Parameter	Symbol	Value	Unit
Freestream velocity	$U_\infty$	[18,26]	m/s
Advance ratio	$J$	[0.5-1.6]	-
Pylon-propeller spacing	$\Delta X$	$[0.4-1]D_{\text{prop}}$	-
Upstream condition	$OBJ$	[ISO, PYL, CYL20, CYL30, CYL50]	-
Angle of attack	$\alpha$	0	deg
Angle of sideslip	$\beta_{SS}$	0	deg
Measurement time	$t_m$	15	s
Sampling frequency	$f_s$	50,000	Hz

### 4.2. REPRODUCIBILITY OF THE MEASUREMENT DATA

The propeller performance is evaluated at different configurations such as isolated, pylon-installed and cylinder-splitter plate installed. Before evaluating the performance of the propeller for these configurations, it is important to check the precision of the measurement method in terms of reproducibility. The reproducibility of the propeller performance is shown in Figure 4.1. The propeller performance measurements are recorded for two different runs (Run1: 14:00 hours, 17 March 2015 and Run2: 16:00 hours, 17 March 2015).

The entire testing equipment was stopped and switched off between the runs. The measurements are performed for the isolated configuration at a freestream velocity of 18 m/s and for advance ratios 0.6, 1.0 and 1.4.

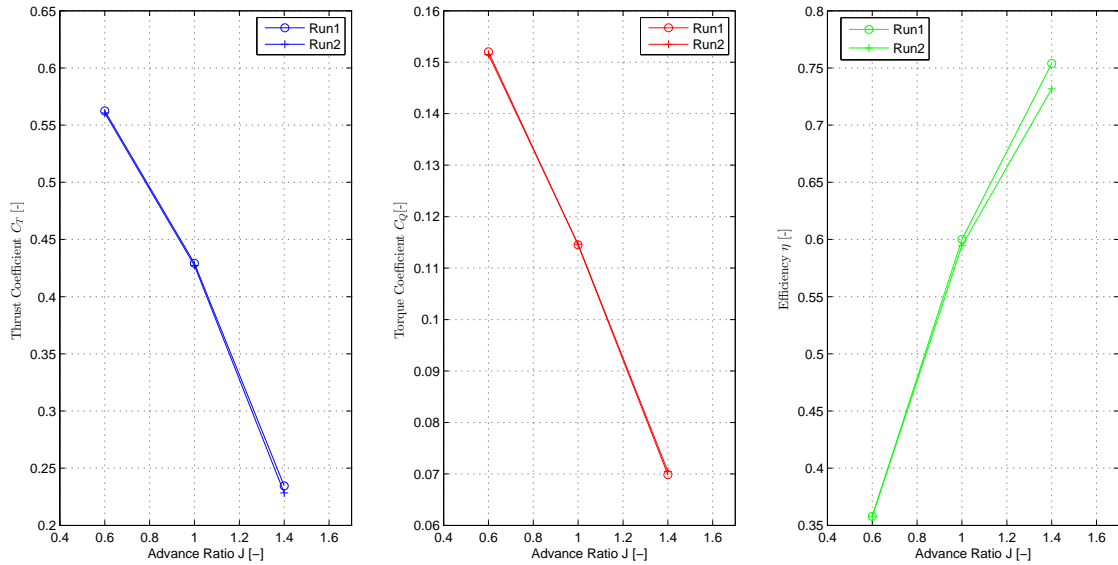
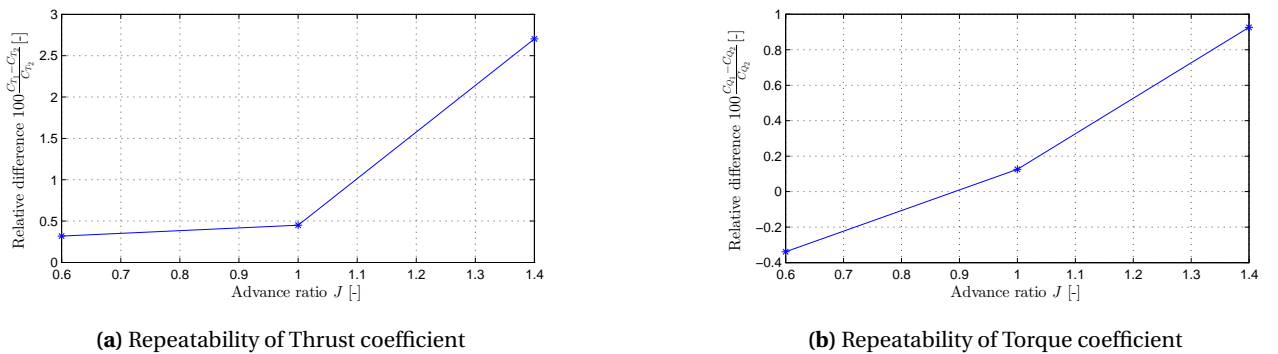


**Figure 4.1:** Repeatability of Propeller performance. Isolated configuration  $U_\infty = 18$  m/s,  $J = [0.6 \ 1.0 \ 1.4]$

The time averaged propeller performance measurements are consistent across different runs indicating that the RSB measurements are acceptable. Though the measurements are reproducible, the differences in measurements across different runs vary with advance ratio. To investigate further, the relative differences in measurements of thrust coefficient and torque coefficient for runs 1 and 2 are plotted in Figure 4.2a and 4.2b, respectively.



(a) Repeatability of Thrust coefficient

(b) Repeatability of Torque coefficient

**Figure 4.2:** Isolated Configuration:  $U_\infty = 18$  m/s,  $J = [0.6 \ 1.0 \ 1.4]$

The relative differences between the two measurement runs for the thrust coefficient and torque coefficient increase with increasing advance ratio. The relative differences between the measurement runs for thrust coefficient and torque coefficients are within  $\pm 1\%$  for advance ratios less than 1.4 indicating that the repeatability is good. However, the repeatability of thrust coefficient is not good for advance ratio of 1.4 as the relative difference between the two measurement runs is +2.5%. This is expected as the thrust signal has a lower signal-to-noise ratio at advance ratio of 1.4. The reproducibility of torque coefficient is good as the relative difference between the measurement runs is within  $\pm 1\%$  for all advance ratios tested.

### 4.3. ISOLATED CONFIGURATION

This section treats the propeller performance in the isolated configuration. The experimental results obtained are used to compare with other configurations such as pylon installed and cylinder-splitter plate installed configuration. First, the propeller performance averaged over one rotation for the isolated configuration is given in Subsection 4.3.1. Subsequently, the time averaged propeller performance in terms of thrust coefficient, torque coefficient and propeller efficiency for different advance ratios is presented in Subsection 4.3.2. The effect of freestream velocity on the propeller performance diagram is discussed in Subsection 4.3.3. Thereafter, the spectral analysis of the thrust and torque signals is treated in Subsection 4.3.4.

#### 4.3.1. ROTATION-AVERAGED PROPELLER PERFORMANCE

This section treats the propeller performance averaged over one rotation. The methodology of computing propeller performance over one full rotation is presented in Chapter 2. The operating point considered for analysis is freestream velocity of 18 m/s, advance ratio of 1.0. The thrust coefficient averaged over one full rotation is plotted in Figure 4.3. Figure 4.3 indicates that the propeller thrust coefficient varied over one full

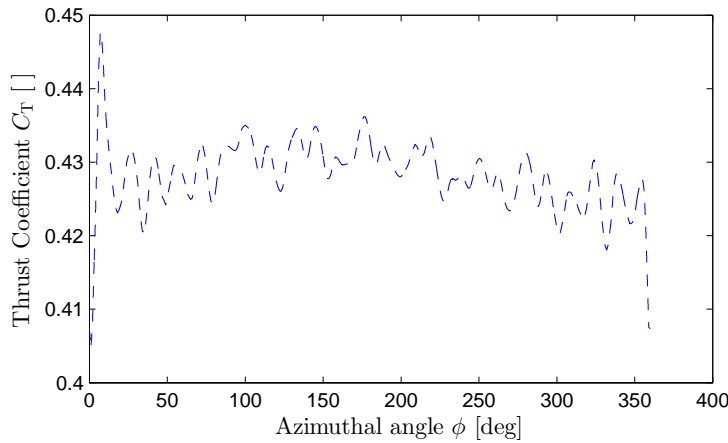


**Figure 4.3:** Thrust coefficient over one full rotation at  $J=0.6$   
Isolated Configuration:  $U_\infty = 18$  m/s,  $J = 1$

rotation. The variations during one full rotation is unexpected as a truly isolated propeller should generate constant thrust over one full rotation. Hence, the variations of thrust coefficient should be related to either the non-uniformity associated with the inflow (thereby generating variable thrust coefficient) or measurement variability. To find out the variability of the measured thrust coefficient, the standard deviation of the thrust coefficient averaged over one rotation is plotted in Figure 4.4. The plot indicates the level of uncertainty is high with standard deviation of around 0.1 which is around 20% of the mean thrust coefficient. Variations of this order are very high and are considered inaccurate. The variations are related to the low signal quality of the RSB.

#### 4.3.2. TIME-AVERAGED PROPELLER PERFORMANCE

The time averaged propeller performance diagram for the isolated configuration for a freestream velocity of 18 m/s is shown in Figure 4.5.

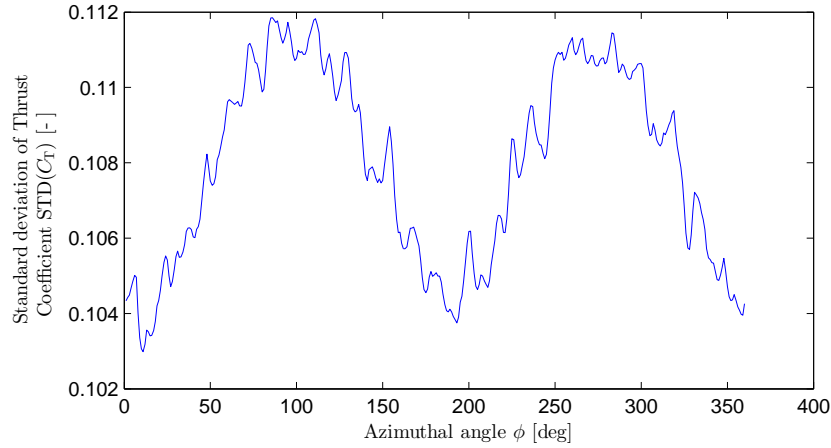


**Figure 4.4:** Standard deviation of thrust coefficient over one full rotation at  $J=1.0$   
Isolated Configuration:  $U_\infty = 18$  m/s,  $J = 1$

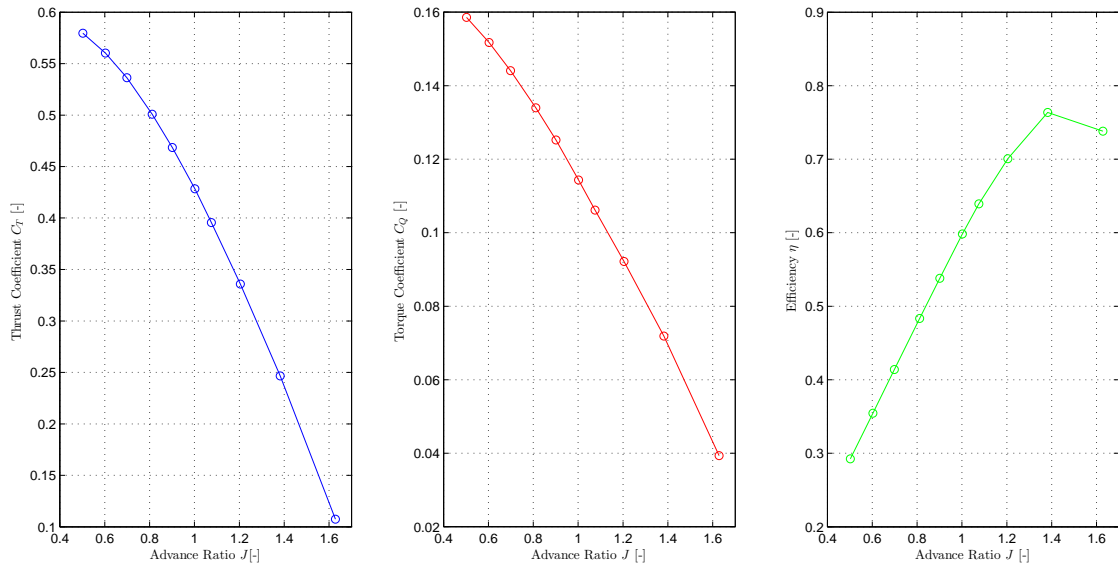


**Figure 4.5:** Propeller performance diagram for isolated configuration:  $U_\infty = 18$  m/s,  $0.5 \leq J \leq 1.6$ .

From Figure 4.5, it is seen that the thrust and torque coefficients increase with decreasing advance ratio. This is due to the increase in angle of attack on the propeller blade sections as the rpm of the propeller is increased for a constant freestream velocity. The maximum of thrust and torque coefficient is produced at the lowest of advance ratio tested. The trend of increase in thrust and torque coefficients is linear in the region  $1.0 \leq J \leq 1.6$  and non-linear in the region  $0.6 \leq J \leq 1.0$ . The non-linear increase is due to the onset of separation of the propeller blades at low advance ratios. At these low advance ratios, a portion of the blade is stalled resulting in a lift loss. The propeller efficiency increases with an increase in advance ratio for  $0.5 \leq J \leq 1.4$ . Further increase in advance ratio resulted in a drop in propeller efficiency.

### 4.3.3. EFFECT OF REYNOLDS NUMBER

At a constant advance ratio, the increase in freestream velocity increases the local blade section Reynolds number. This subsection investigates the effect of freestream velocity on propeller performance. Propeller performance measurements are performed for freestream velocities of 18 m/s and 26 m/s for advance ratios 0.6, 1.0 and 1.4. Figure 4.6 shows the effect of increase in freestream velocity on the propeller performance di-

agram at constant advance ratio. From Figure 4.6, both thrust and torque coefficients increase with increase in freestream velocity at a constant advance ratio. The increase in local Reynolds number on the propeller blades results in a thinner boundary layer, correspondingly increasing the effective camber of the local airfoil section of the propeller blade. The increase in camber results in an increase in the local superelevations and thus increases the local lift on the propeller blade section. The increase in local lift is seen as increase in thrust and torque coefficient at higher freestream velocity and constant advance ratio. The resulting thinner boundary layers also result in decrease in propeller blade drag. However, the contribution of lift to the torque coefficient is significantly more than the contribution of drag to the torque coefficient resulting in a net increase in torque coefficient at high freestream velocity. At high advance ratios, propeller efficiency is higher for higher freestream velocity as the relative increase in thrust coefficient is higher than the relative increase in torque coefficient. This is due to the reduced drag at higher Reynolds number.

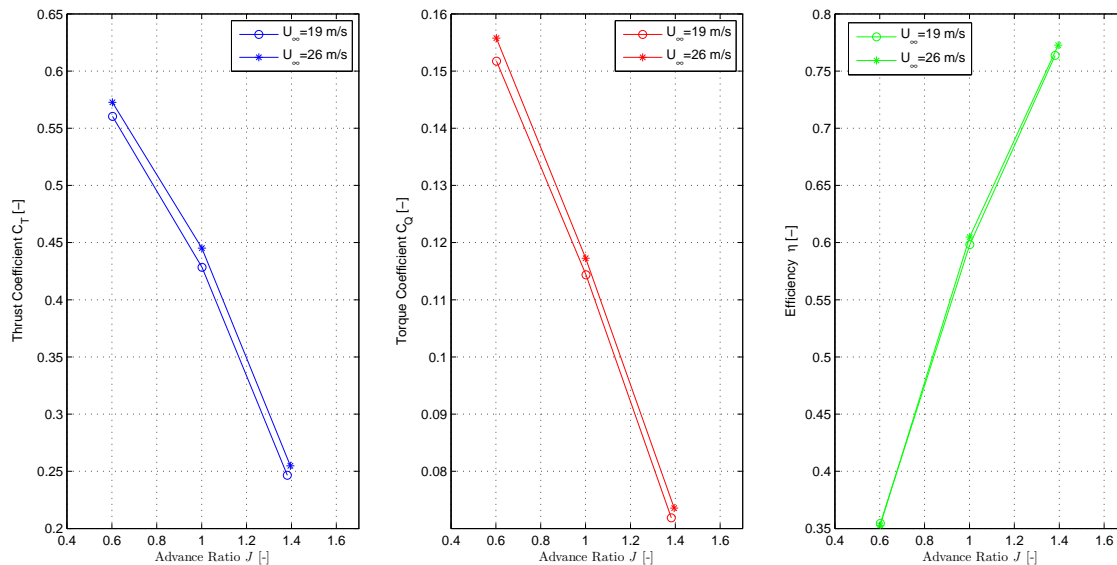


**Figure 4.6:** Effect of Reynolds number on the propeller performance diagram.  
Isolated configuration  $U_\infty = [18,26]$  m/s,  $0.6 \leq J \leq 1.4$ .

#### 4.3.4. SPECTRAL ANALYSIS OF THRUST AND TORQUE SIGNALS

Section 4.2 dealt with the reproducibility of the measurement data. It was observed that the relative differences of thrust and torque coefficients between two measurement runs increased with increase in advance ratio. At higher advance ratios, the RSB signal has a lower signal to noise ratio. To assess whether the noise signals are of particular frequency or broadband, spectral analysis was performed to both thrust and torque signals. This would also be useful in comparing with pylon installed and cylinder-installed configurations as the effect of pylon installation should be visible at blade passage frequency. Spectral analysis was performed for both thrust and torque signal for a freestream velocity of 18 m/s and for advance ratios of 0.5-1.6. The propeller performance data averaged over one rotation computed with the help of 1-P signal is used to perform the spectral analysis. The procedure followed for the spectral analysis is similar to the microphone analysis given in Section 2.6. The spectra for the thrust and torque signal at a freestream velocity of 18 m/s and advance ratio of 1.0 (medium thrust and torque setting) is given in Figures 4.7a and 4.7b respectively. The seven black dashed lines indicate the first seven multiples of blade passage frequency. The zero frequency component is marked by an asterisk.

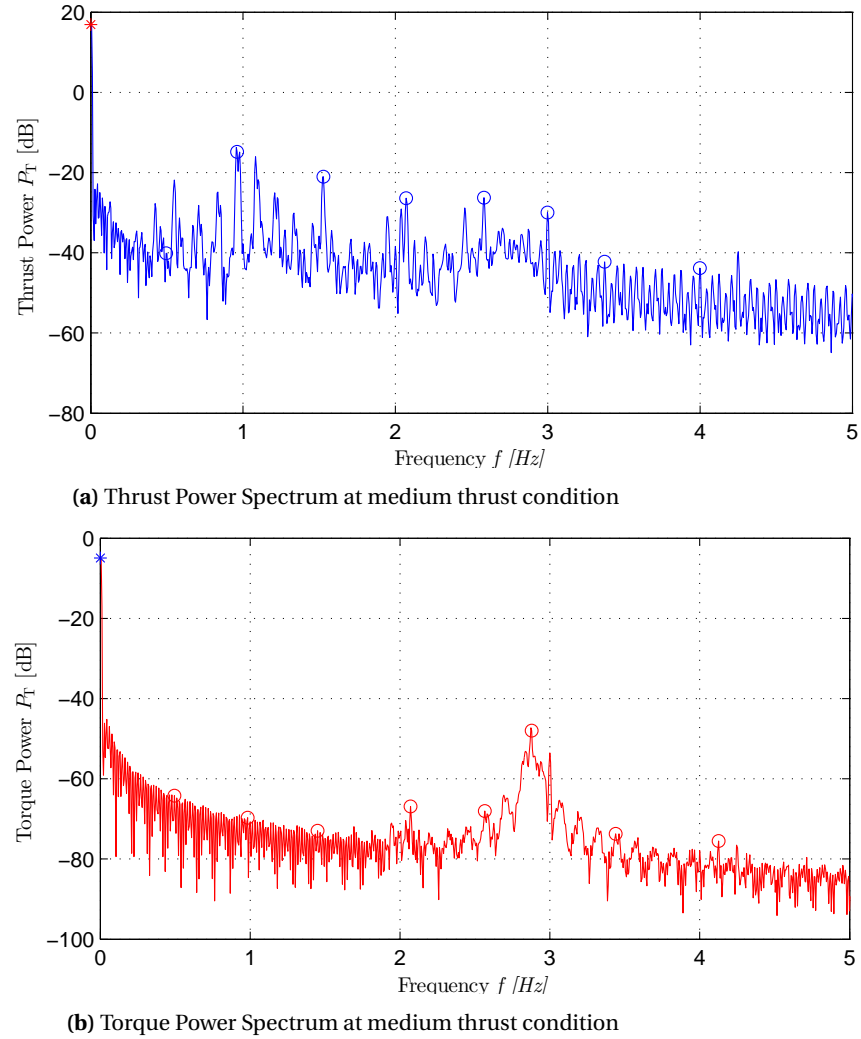


**Figure 4.7:** Isolated Configuration:  $U_\infty = 18$  m/s,  $J = 1$

The zero frequency component dominates the higher frequency content for both thrust and torque signals. The thrust power at zero frequency is higher by at least 30 dB when compared to the thrust power at higher frequencies. This is due to the relatively large mean value compared to the fluctuations observed. The non-zero frequency components are observed at multiples of one-fourth of blade passage frequency (0.25 BPF). The reason for the occurrence of multiples of one-fourth of BPF is probably due to the blade angle variations or due to the presence of small angle of attack and small angle of side slip due to the non-uniform outflow from the wind tunnel. However, this is not conclusive yet. In an ideal case, the thrust signal for the isolated configuration should contain only the mean component as the thrust signal is constant over the entire time period. The presence of higher BPF's might be due to non-uniform inflow into the propeller. To verify the present observations, the spectral analysis is performed for the entire advance ratio range and is shown in Figure 4.8.

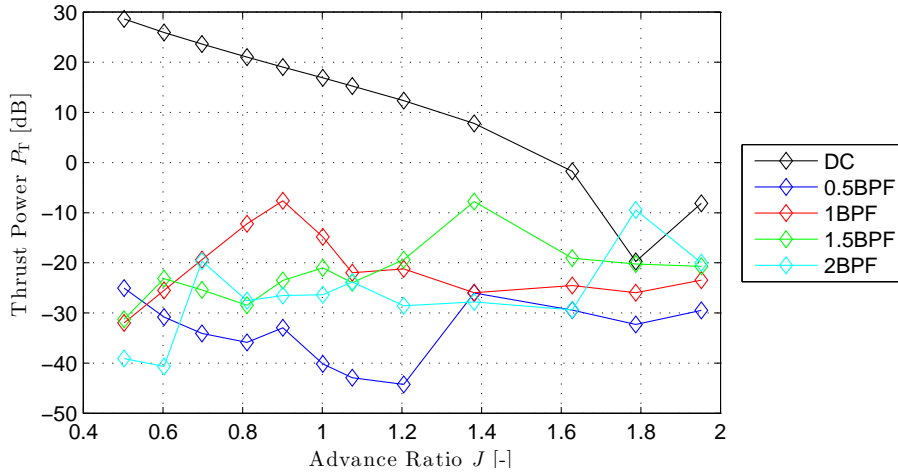


**Figure 4.8:** Variation of thrust signal power for the multiples of BPF with advance ratio. Isolated configuration  $U_\infty = 18$  m/s,  $J = [0.5-1.9]$

From the Figure 4.8, the thrust power at zero frequency is significantly higher than the thrust power at multiples of blade passage frequency at all advance ratios tested except at  $J = 1.8$ . The propeller generates zero thrust at  $J = 1.8$  leading to low thrust power at zero frequency. The presence of higher BPF's is also clearly seen from 4.7a. The first four half multiples of BPF i.e 0.5BPF, 1BPF, 1.5BPF, 2 BPF are shown in the figure. The thrust power for the 1BPF, 1.5BPF and 2 BPF peak at an advance ratio of 0.9, 1.4 and 1.8 respectively. The frequency at which these multiples of BPF peak is given in Table 4.2 and it is close to 500 Hz. Thus, the occurrence of peaks is possibly due to the harmonic vibration of the RSB at a frequency of 500 Hz. Hence the peaks seen in the spectrum are not related to the non-uniform inflow into the propeller or blade angle variations but due to the vibration of the RSB. This would lead to a conclusion that the thrust power of the spectrum does not relate to the propeller blade loading but to the harmonic vibration of the RSB. Hence, the resulting fluctuations does not correspond to the non-uniform inflow. The time averaged propeller performance results would not be altered due to the measurement error as the fluctuating component is averaged to zero over the sufficiently large measurement time. The torque spectral analysis plotted in Figure 4.7b shows that the zero frequency component dominates other higher frequency components, indicating that the torque signal is constant over the measurement time.

**Table 4.2:** Detailed analysis of the frequency contents of thrust signal at different advance ratios

BPF Index [-]	Advance ratio $J$ [-]	Observed frequency $f_{\text{peak,obs}}$ [Hz]	Computed frequency $f_{\text{peak,comp}}$ [Hz]
2	1.8	262	524
1.5	1.4	336	504
1	0.9	524	524
0.5	0.5	944	472

#### 4.4. PYLON INSTALLED CONFIGURATION

This section treats the propeller performance in pylon-installed configuration. The results obtained are used to compare with the other configurations such as isolated and cylinder- splitter plate installed configuration. First, the time accurate analysis averaged over one rotation is presented in Subsection 4.4.1. Thereafter, the time averaged propeller performance in terms of thrust coefficient, torque coefficient and propeller efficiency for different advance ratios is presented in Subsection 4.4.2. Finally, the spectral analysis of the thrust and torque signals is treated in Subsection 4.4.3.

#### 4.4.1. ROTATION-AVERAGED PROPELLER PERFORMANCE

This section treats the time accurate propeller performance averaged over a single rotation. The measurement recorded when the propeller is at a certain azimuthal angle is averaged over a number of rotations and the computed results are treated in this subsection. The thrust coefficient for a freestream velocity of 18 m/s, advance ratios of 0.6 and 1.0 and pylon-propeller spacing of 40% -100% of the diameter of the propeller is plotted in Figures 4.9 and 4.10 respectively.

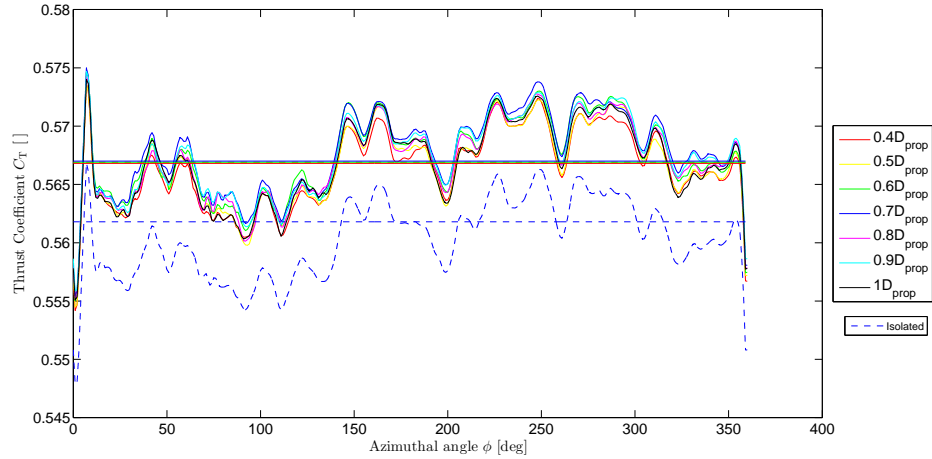


**Figure 4.9:** Thrust coefficient over one full rotation at  $J=0.6$   
Pylon Installed Configuration:  $U_\infty = 18$  m/s,

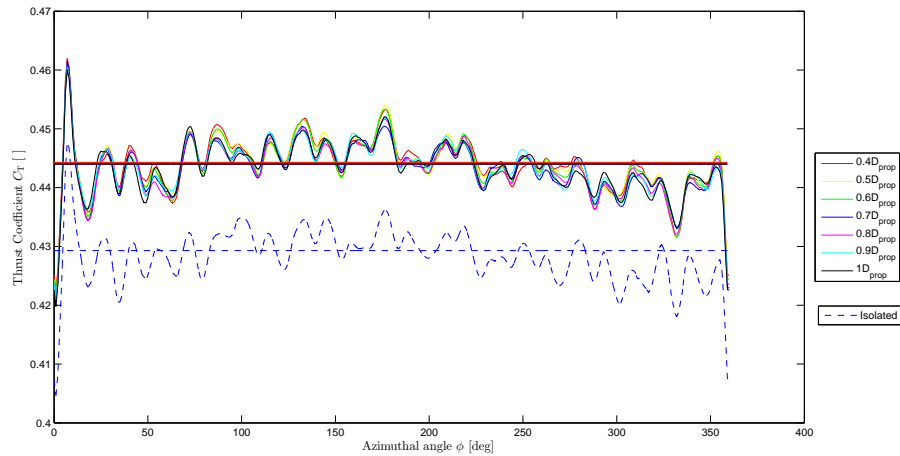


**Figure 4.10:** Thrust coefficient over one full rotation at  $J=1.0$   
Pylon Installed Configuration:  $U_\infty = 18$  m/s,

The isolated configuration is plotted using a dashed line whereas the pylon installed configuration is plotted using a normal line. Different propeller-pylon spacings are represented by different coloured lines. The influence of 1-P signal on the thrust signal is seen at the beginning and at the end of the rotation cycle. From Figures 4.9 and 4.10, it is clear that the effect of pylon on the thrust coefficient over the entire rotation is only seen as increase in the mean thrust coefficient which is not theoretically possible whereas the fluctuations observed are similar for isolated and pylon installed configurations. It is possible that the RSB is not capable of measuring the presence of wake at every degree due to the higher rotational velocity of the propeller and the thin pylon wake. The details of possible no of data points acquired during the wake passage by a single blade is summarised in Table 4.3. A wake angle of 12 degrees which is obtained for a blade section at a radial location of  $\eta = 70\%$  is used to calculate maximum number of sampling points acquired during the wake

passage. The rotation averaged analysis is also performed for a low advance ratio of 1.4 and the results are shown in Figure 4.11. In this case, there is an increase in mean observed and also the fluctuations through the passage of wake is clearly visible for different pylon-propeller spacings. However, the increase in mean cannot be attributed due to the presence of wake. Therefore, the measured increase in thrust coefficient is due to an error in measurement. The error in measurement is possibly due to the difference in advance ratio between the isolated and pylon-installed configuration leading to an increase in mean thrust coefficient. Spectral analysis performed also showed differences between the isolated and pylon-installed configuration at low advance ratios only which is discussed in subsequent subsections.

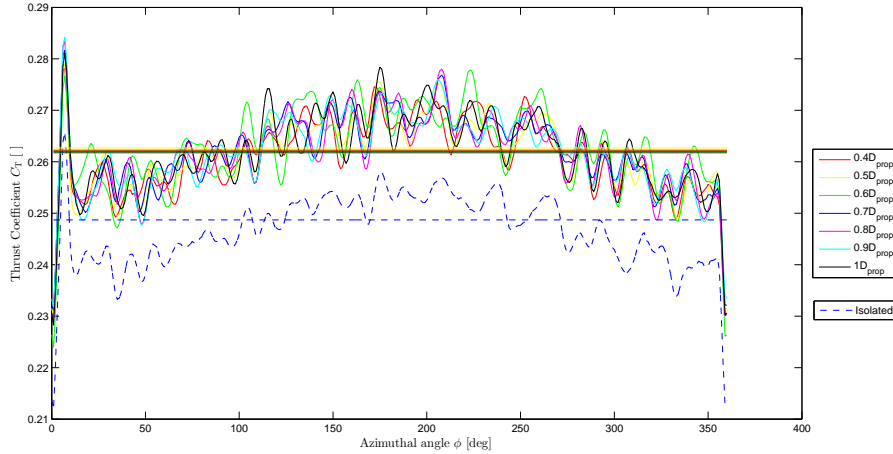


**Figure 4.11:** Thrust coefficient over one full rotation at  $J=1.4$   
Pylon Installed Configuration:  $U_\infty = 18$  m/s,

**Table 4.3:** Details of the number of sampling points acquired by the RSB during the wake passage at different advance ratios

Advance ratio	samples/rev	deg/sample	$N_{\text{samp,max}}$
0.6	292	1.2	10
1.0	451	0.8	15
1.4	682	0.5	24

#### 4.4.2. TIME-AVERAGED PROPELLER PERFORMANCE

The momentum deficit in the pylon wake affects the performance of the propeller behind in two different ways.

- Local increase in the angle of attack and thereby increasing the propeller blade loads.
- Reduction in dynamic pressure and thereby decreasing the propeller blade loads.

Past numerical evaluations [10] showed that the effect of reduction in dynamic pressure is less compared to the effect of increase in local angle of attack. Hence, it is expected that the propeller performance parameters: thrust coefficient and torque coefficient are expected to be higher for the installed configuration compared to the isolated configuration. Experimental measurements performed here also showed an increase in thrust and torque coefficient as depicted in Figure 4.12. The reason for the increase in performance parameters will be verified in subsequent sections. The experiments are performed at a freestream velocity of 18 m/s, advance ratios between 0.5 and 1.6 and for pylon-propeller spacing of 50% of the diameter of the propeller. Both isolated and installed cases are depicted in the same figure.

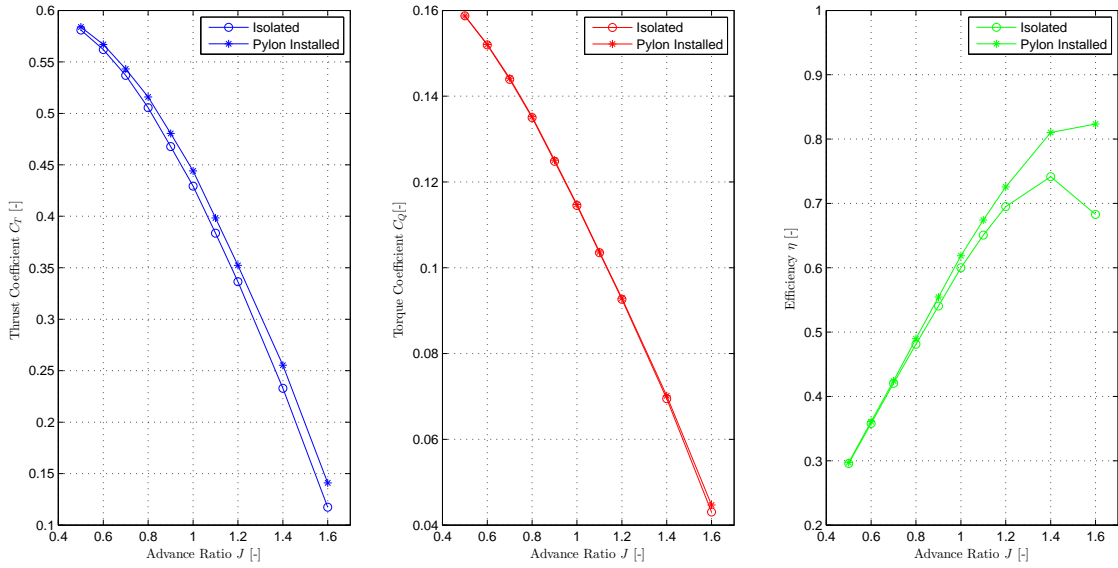


**Figure 4.12:** Propeller performance diagram: Effects of Installation.  
Pylon Installed configuration  $U_\infty = 18$  m/s,  $0.5 \leq J \leq 1.6$ ,  $\Delta X = .5D_{\text{prop}}$

Figure 4.12 shows an increase in thrust and torque coefficients due to the installation of pylon. Also, it is to be noted that the increase in thrust and torque coefficient is higher for high advance ratios. The increase in  $C_T$  and  $C_Q$  for low advance ratios is very small. To verify the dependency of installation effect on the advance ratio, the relative differences of thrust and torque coefficient are plotted for the entire advance ratio range in Figures 4.13a and 4.13b respectively.

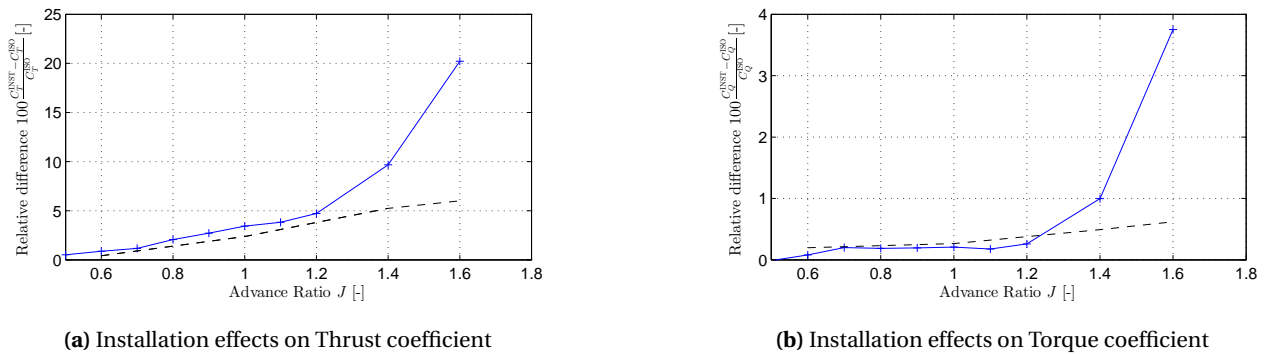


**Figure 4.13:** Variation of relative differences in performance coefficients with advance ratio.  
Pylon Installed configuration:  $U_\infty = 18$  m/s,  $0.5 \leq J \leq 1.6$ ,  $\Delta X = .5D_{\text{prop}}$

The results presented here are for a freestream velocity of 18 m/s and pylon-propeller spacing of 50% of the diameter of the propeller. Figures 4.13a and 4.13b indicate the effects of installation on the thrust and torque coefficient and its dependency on the advance ratio. For advance ratios less than 1.2, the effect of installation on the thrust coefficient is less than +5%. The effect of installation on the thrust coefficient at advance ratio of 1.4 and 1.6 is close to 10% and 20% respectively. Similarly the torque coefficient also increases with increase in advance ratio. For advance ratios less than 1.2, the effect of installation is less than 0.5%. At higher advance ratios of 1.4 and 1.6, the increase in torque coefficient is close to 1% and 4% respectively. This clearly indicates the presence of pylon is significant at high advance ratios. However, the reason for the observed increase in the time averaged propeller performance is not conclusive from the above analysis. At this stage, the increase in mean propeller performance might be attributed due to the presence of the pylon wake or measurement error. More detailed analysis of the thrust and torque signal such as Fourier analysis is required to evaluate the presence of the pylon wake and this is detailed in the next subsection.

### 4.4.3. SPECTRAL ANALYSIS OF THRUST AND TORQUE SIGNALS

The effect of installation of a pylon would result in an increase in blade loading only during the wake passage. This would increase the thrust power at multiples of the blade passage frequency. As a result, the thrust power for the pylon installed configuration at the multiples of BPF would be influenced by the presence of wake. Hence, a spectral analysis was performed for the thrust signal for the entire advance ratio range [0.5-1.6] and a freestream velocity of 18 m/s and is plotted in Figure 4.14.

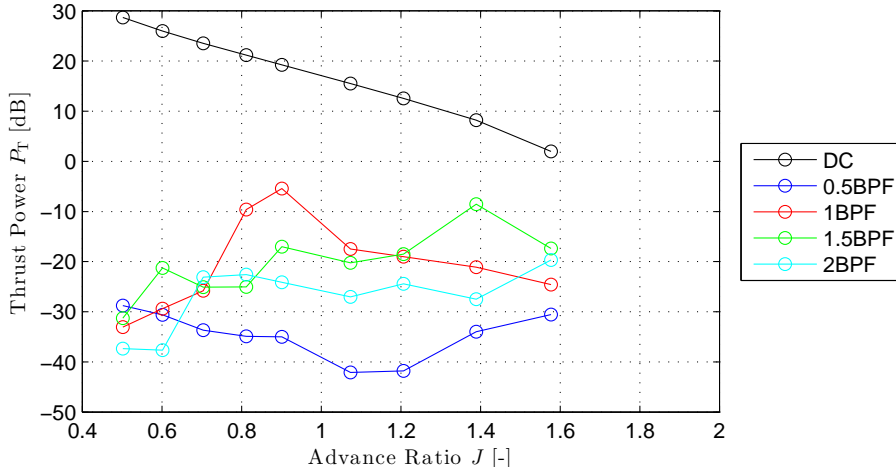


**Figure 4.14:** Variation of thrust signal power for the multiples of BPF with advance ratio. Pylon installed configuration  $U_\infty = 18$  m/s,  $0.5 \leq J \leq 1.6$ ,  $\Delta X = 0.5D_{prop}$

Figure 4.14 clearly shows the dominant presence of the steady component of the thrust. The presence of higher BPF's is also clearly seen. However, the thrust signal power for the pylon installed configuration is similar to the thrust signal power for the isolated configuration. Like in the isolated configuration, the harmonic vibration of the RSB results in maxima in the frequency content of the thrust signal. The influence of the wake is not clearly visible from Figure 4.14. The very slight differences observed between the isolated configuration and the pylon installed configuration might be due to the repeatability or due to the presence of wake. For this to be concluded, the rotation-averaged thrust coefficient averaged over the measurement time is plotted over the entire azimuthal angle range in the next subsection.

## 4.5. EFFECT OF PYLON-PROPELLER SPACING: TIME-AVERAGED PROPELLER PERFORMANCE

This section deals with the effect of pylon-propeller spacing on the performance of the propeller. The time averaged propeller performance for the pylon installed configuration for different pylon-propeller spacings is discussed in this section.

Experiments are conducted at a freestream velocity of 18 m/s and for advance ratios lying in the range of 0.5 and 1.6. The advance ratio is varied in steps only after varying the pylon-propeller spacing from  $40\%D_{prop}$  to  $100\%D_{prop}$ . The performance diagram for the pylon installed configuration in terms of the thrust coefficient, torque coefficient and propeller efficiency is plotted versus the advance ratio in Figure 4.20. From Figure 4.20, it is concluded that for all advance ratios the effect of pylon-propeller spacing on the thrust coefficient and torque coefficient is negligible. To gain further understanding, the relative differences of the thrust coefficient and torque coefficient between the pylon installed and isolated configuration (which is referred as installation impact here in this chapter) are calculated for various pylon-propeller spacings. Figures 4.16a and 4.16b presents the performed calculations for thrust coefficient and torque coefficient respectively. The installation impact for the thrust coefficient is varying around 3.3% whereas for the torque coefficient is varying around 0.3%. This indicates that the pylon-propeller spacing has negligible impact on the thrust and torque coefficients. The wake profiles for various pylon spacing indicated the velocity deficit showed a considerable decrease with increase in pylon spacing whereas the wake width was similar for various pylon spacings. The propeller performance data averaged over one rotation presented in Subsection 4.4.1 did not

show any change in propeller performance by varying the position of pylon.

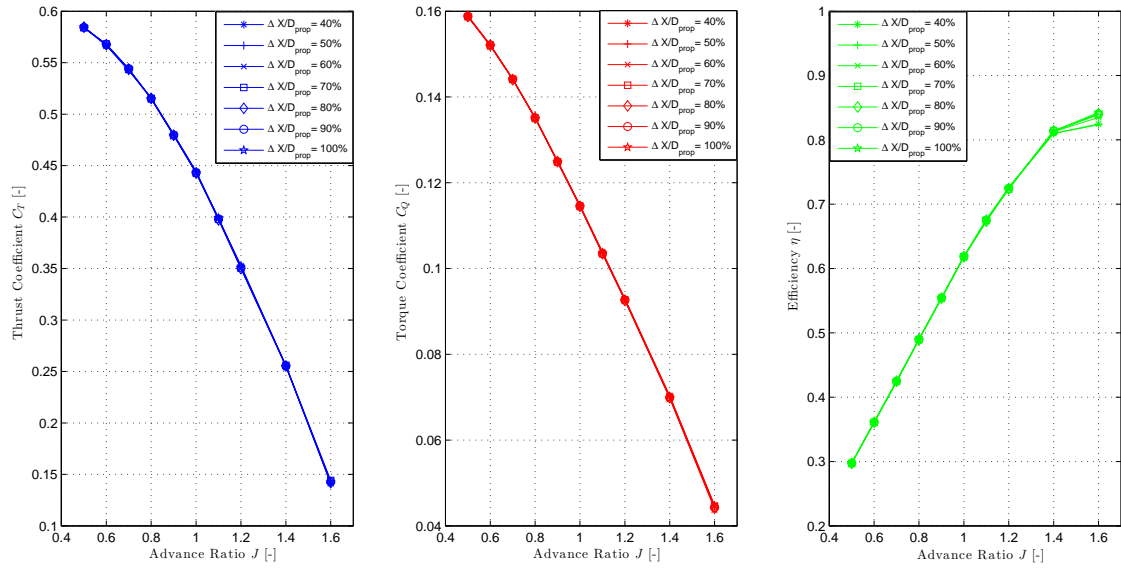


**Figure 4.15:** Propeller performance diagram: Effect of pylon-propeller spacing. Pylon Installed configuration  $U_\infty = 18$  m/s,  $0.5 \leq J \leq 1.6$ ,  $0.4D_{prop} \leq \Delta X \leq 1D_{prop}$



**(a)** Installation effect on Thrust Coefficient

**(b)** Installation effect on Torque Coefficient

**Figure 4.16:** Variation of relative differences in performance coefficients with pylon-propeller spacing. Pylon-Installed Configuration:  $U_\infty = 18$  m/s,  $J = [0.6 \text{ to } 1.4]$ ,  $0.4D_{prop} \leq \Delta X \leq 1D_{prop}$

From the pylon wake characteristics presented in Chapter 3, non-dimensional wake displacement thickness, non-dimensional wake velocity deficit and non-dimensional wake momentum thickness varied with change in pylon-propeller spacing. However, the change in wake characteristics did not effect the propeller performance. The increase in the thrust in the pylon-installed configuration is related to the momentum thickness of the upstream pylon wake. The change in momentum thickness in the pylon wake with change in pylon-propeller spacing is very small leading to constant thrust coefficient across different pylon-propeller spacings at a constant advance ratio.

from the trailing edge of the airfoil. The velocity deficit of the wake decreases and the wake width increases with the distance away from the trailing edge. However, the propeller behind the airfoil is likely to influence the wake in front of it. The effect of the propeller on the wake is already discussed in Section 3.3. The wake width and the velocity deficit are found to be decreasing with increase in pylon-propeller spacing. The decrease in wake width results in a decrease in thrust as the wake angle for a propeller blade section is reduced for thinner wakes. (The wake angle is defined as the angle during which a propeller blade section is under the influence of wake.) The decrease in velocity deficit tends to decrease the thrust as the local angle of attack is decreased resulting in low propeller blade section loads. However, experimental observation leads to no change of thrust with pylon propeller spacing.

## 4.6. CYLINDER-SPLITTER PLATE INSTALLED CONFIGURATION

As observed in previous section of the current chapter, the time averaged thrust and torque for the pylon installed configuration is constant for different pylon-propeller spacing. However, the change in wake characteristics with change in pylon-propeller spacing is small enough to effect the propeller performance. In order to find out whether different wake characteristics have an impact on the propeller performance, propeller performance measurements are performed for the cylinder-splitter plate installed configuration. This section first presents the time averaged propeller performance in the cylinder-splitter plate installed configuration (Subsection 4.6.1). Then, the effect of upstream object-propeller spacing on the propeller performance parameters is presented in Subsection 4.6.2.

### 4.6.1. TIME-AVERAGED PROPELLER PERFORMANCE

The time averaged propeller performance of the propeller for the three cylinder-splitter plate installed configurations along with the previously discussed isolated and pylon-installed configurations is presented here in this subsection. The diameters of the three cylinder-splitter plate objects are 20, 30 and 50 mm respectively. Additional details regarding geometry are presented in Section 2.3.3. The propeller performance is measured for advance ratios of 0.6, 1.0 and 1.4 for a freestream velocity of 18 m/s. The upstream object-propeller spacing used is 50% of the diameter of the propeller. The legends used for the cylinder-splitter plate installed configurations with diameter 20, 30 and 50 mm are CYL20, CYL30 and CYL50 (also referred in this section by their legends) respectively whereas the legends for the isolated and pylon-installed configuration are ISO and PYLON respectively.

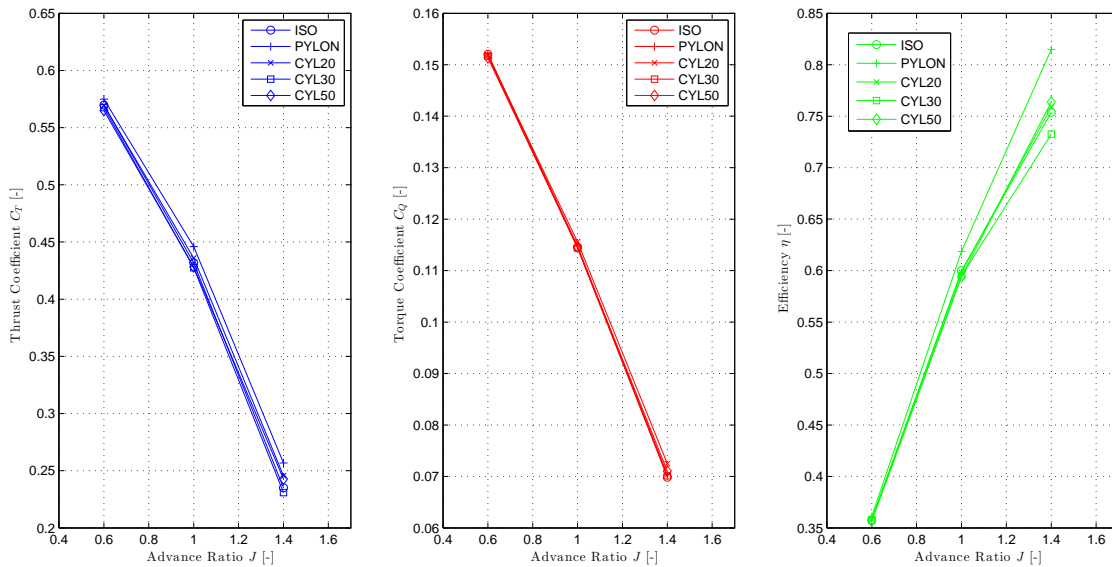


**Figure 4.17:** Propeller performance diagram: Effects of Installation.

Installed Configuration:  $U_\infty = 18$  m/s,  $J = [0.6 \ 1.0 \ 1.4]$ ,  $OBJ = [ISO, PYL, CYL20, CYL30, CYL50]$

The propeller performance diagram shown in Figure 4.17 indicates higher thrust coefficient and torque coefficient for the pylon-installed configuration. This is because the flow behind the pylon is smoother than the flow behind the cylinder splitter plate configuration. Flow behind the cylinder-splitter plate resulted in vortices which resulted in a decrease in angle of attack. The velocity profiles for cylinder-splitter configuration show that the flow is separated downstream and therefore resulted in wake which has less velocity deficit and hence less increase in the angle of attack. No clear conclusions can be drawn from the performance plot of other installed configurations. For a comparison between the objects, the relative differences between the installed and isolated configuration are calculated. Figure 4.18a and 4.18b presents the calculations along with the repeatability of RSB measurements.

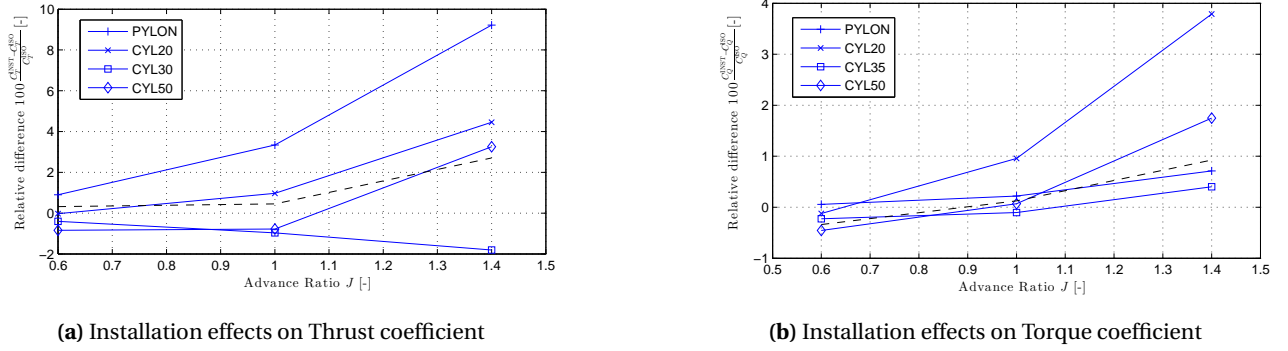


**Figure 4.18:** Variation of relative differences in performance coefficients with advance ratio.  
Installation effects:  $U_\infty = 18$  m/s,  $J = [0.6 \ 1.0 \ 1.4]$ ,  $OBJ = [ISO, PYL, CYL20, CYL30, CYL50]$

Though the wake characteristics are different for each configuration, the wake parameters did not impact the propeller performance. The differences observed are due to the error in measurement as in case of the pylon installed configuration. The time accurate measurements for the cylinder-splitter plate configuration did not show any significant impact during the wake passage as shown in Figure 4.19. Hence, the measurements did not confirm to any installation effect but related to the error in maintaining the same operating point.

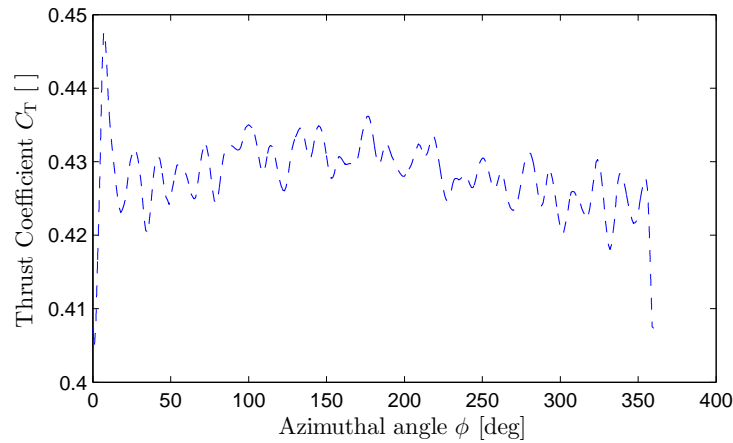


**Figure 4.19:** Thrust coefficient over one full rotation at  $J = 1.0$   
Isolated Configuration:  $U_\infty = 18$  m/s,  $J = 1.0$ ,  $\Delta X = 0.5D_{prop}$ ,  $OBJ = [CYL50]$

#### 4.6.2. EFFECT OF UPSTREAM OBJECT-PROPELLER SPACING

The propeller performance measurements for various object-propeller spacings were performed to find out whether the influence of spacing has an impact on the propeller performance. The time averaged propeller performance diagram for the different pylon spacings varying from 40% to 100 % of diameter of the propeller. The measurements are performed at an advance ratio of 1.0 and a freestream velocity of 18 m/s for all the installed configurations. The propeller performance diagram for various pylon spacings is shown in Figure 4.20.

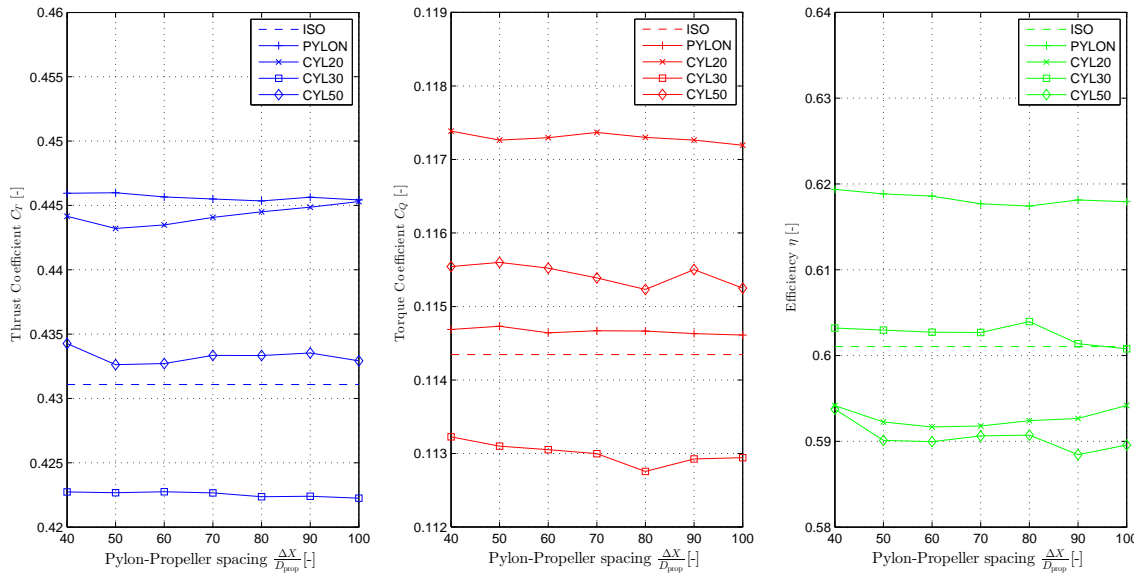
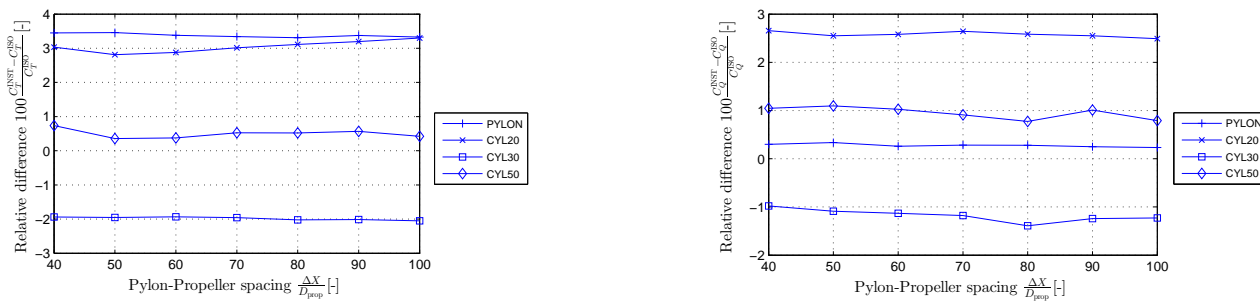


**Figure 4.20:** Propeller performance diagram: Effect of upstream object-propeller spacing. Installed Configuration:  $U_\infty = 18$  m/s,  $J = [1.0]$ ,  $OBJ = [ISO, PYL, CYL20, CYL30, CYL50]$

Figure 4.20 does not show any effect on the time averaged propeller performance for various object-propeller spacings. For comparison between objects, the thrust and torque coefficients show similar trends as discussed in Subsection 4.6.1. To gain additional insight, the relative differences between the installed and isolated configuration for the thrust and torque coefficients are plotted in Figures 4.21a and 4.21b respectively. The results depicted for both thrust and torque coefficient show that the effect of spacing is negligible. The differences measured are within the repeatability of the time averaged propeller performance. The wake profiles showed varied wake characteristics for different spacings which are small enough to change the time averaged propeller performance.



(a) Installation effects on Thrust coefficient

(b) Installation effects on Torque coefficient

**Figure 4.21:** Variation of relative differences in performance coefficients with upstream object-propeller spacing.

Installation effects:  $U_\infty = 18$  m/s,  $J = [1.0]$ ,  $OBJ = [ISO, PYL, CYL20, CYL30, CYL50]$



# 5

## EXPERIMENTAL RESULTS: PROPELLER NOISE EMISSIONS

The current chapter is aimed at evaluating the installation effect on the pusher propeller noise emissions for different flyover angles, advance ratios and upstream object-propeller spacings. The results discussed in this chapter include both the experimental campaigns conducted in the Open Jet Facility and the V-tunnel. An overview of the measurement conditions for the OJF and V-tunnel experimental campaigns is presented in Section 5.1. The reproducibility of the measurements is treated in Section 5.2. Subsequently, the propeller noise emissions for the isolated, pylon-installed and cylinder-splitter plate installed configurations are discussed in Section 5.3, Section 5.4 and Section 5.5, respectively.

### 5.1. MEASUREMENT OVERVIEW

The experiments at the V-tunnel campaign and the OJF campaign are conducted at different operating conditions. A summary of the measurement conditions is treated in this section. First, the operating conditions for the experimental campaign conducted at the V-tunnel are given followed by the experimental campaign conducted at the OJF.

#### Measurement Overview for the V-tunnel campaign

A summary of the operating conditions for the experiments conducted at the V-tunnel is given in Table 5.1.

**Table 5.1:** Summary of the operating conditions for the experiments conducted in the V-tunnel

Parameter	Symbol	Value	Unit
Freestream velocity	$U_\infty$	20	m/s
Advance ratio	$J$	[0.77-1.25]	-
Pylon-propeller spacing	$\Delta X$	$[0.3-0.7]D_{\text{prop}}$	-
Pylon azimuthal position	$\phi_{\text{pylon}}$	0	deg
Upstream condition	$OBJ$	[ISO, PYL]	-
Angle of attack	$\alpha$	0	deg
Angle of sideslip	$\beta_{SS}$	0	deg
Microphone flyover angle	$\theta_{\text{mic}}$	[60,90,120]	deg
Microphone sideline distance	$y_{\text{mic}}$	0.6	m
Microphone azimuthal angle	$\phi_{\text{mic}}$	[180,270]	deg
Measurement time	$t_m$	15	s
Sampling frequency	$f_s$	50000	Hz

Propeller noise measurements for the V-tunnel campaign are presented here in this chapter. The noise measurements are calibrated every day with the help of a piston phone. They are also calibrated when the power supply is switched off to the microphones. The post processing process for the microphone data

is presented in Chapter 2. The sound pressure levels obtained during the the V-tunnel campaign are not corrected for microphone's uneven frequency response and shear layer refractions.

### Measurement Overview for the OJF campaign

A summary of the measurement characteristics for the OJF experimental campaign is presented in Table 5.2. The noise measurements are calibrated on every day for all the microphones. The microphone measurements are processed as per the process mentioned in the chapter 2. All the tonal noise measurements presented for the OJF campaign are corrected for uneven microphone frequency response and shear layer refractions whereas the sound spectra shown are only corrected for uneven microphone frequency response.

**Table 5.2:** Summary of the operating conditions for the experiments conducted in the Open Jet Facility

Parameter	Symbol	Value	Unit
Freestream velocity	$U_\infty$	18	m/s
Advance ratio	$J$	[0.5-1.6]	-
Pylon-propeller spacing	$\Delta X$	$[0.4-1]D_{prop}$	-
Pylon azimuthal position	$\phi_{pylon}$	0	deg
Upstream condition	$OBJ$	[ISO, PYL, CYL20, CYL30, CYL50]	-
Angle of attack	$\alpha$	0	deg
Angle of sideslip	$\beta_{SS}$	0	deg
Microphone flyover angle	$\theta_{mic}$	[45,60,75,90,105,120,135]	deg
Microphone sideline distance	$y_{mic}$	1.27	m
Microphone azimuthal angle	$\phi_{mic}$	86	deg
Measurement time	$t_m$	15	s
Sampling frequency	$f_s$	25000	Hz

## 5.2. REPRODUCIBILITY OF THE MEASUREMENT DATA

The noise measurements are performed on different days for various operating conditions. To ensure the quality of the measurement setup and process, the reproducibility of the noise measurements for both the V-tunnel and OJF campaign are assessed in this section. First, the reproducibility of consecutive measurements is presented in Subsection 5.2.1. Subsequently, the reproducibility of non-consecutive measurements is dealt in Subsection 5.2.2.

### 5.2.1. CONSECUTIVE MEASUREMENTS

Consecutive measurements are performed at a constant wind tunnel setting and propeller operating condition for all the microphones. The entire setup is running continuously during the consecutive measurements. First, the reproducibility of the V-tunnel measurements is assessed followed by the reproducibility of the measurements recorded at the OJF campaign.

#### V-TUNNEL CAMPAIGN

The reproducibility of the microphone data is analysed by computing the variability and reproducibility of the noise measurements. Acoustic measurements are performed at a constant wind tunnel speed of 20 m/s, for a range of advance ratios varying from 0.77-1.25 and microphone flyover angle of 90 degrees. The measurements at the same operating point were not continuous, however the entire set-up is running continuously during these measurements. The reproducibility and variability of the measurement data at a freestream velocity of 20 m/s, an advance ratio of 1.0 and a microphone flyover angle of 90 degrees is shown in Figures 5.1 and 5.2 respectively. Only the first four BPF-tones are considered for the analysis. The variability of the propeller noise measurements is within  $\pm 0.4$  dB. Variability of this order is insignificant as we see later that the effect of installation on propeller noise emissions is much higher. The same observation is made from the measurements performed across the advance ratio range considered ( $0.8 \leq J \leq 1.1$ ).

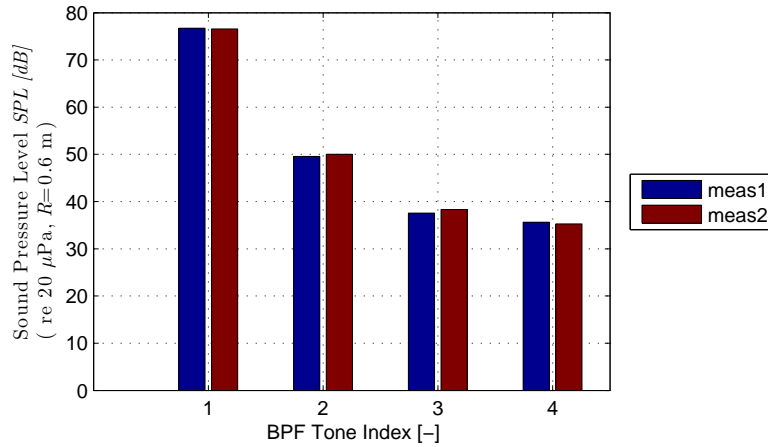


**Figure 5.1:** Reproducibility of propeller noise measurements  
V-tunnel campaign: Isolated configuration,  $U_\infty = 20$  m/s,  $J = 0.8$ ,  $\theta_{\text{mic}} = 90^\circ$ ,  $\phi_{\text{mic}} = 180^\circ$ .

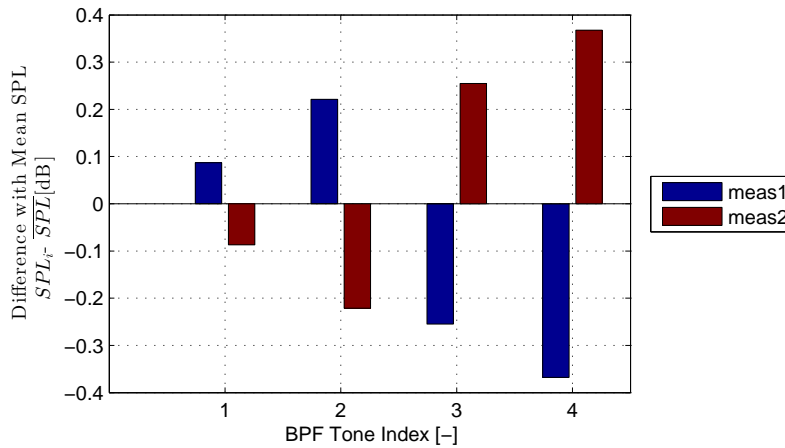


**Figure 5.2:** Variability of propeller noise measurements  
V-tunnel campaign: Isolated configuration,  $U_\infty = 20$  m/s,  $J = 0.8$ ,  $\theta_{\text{mic}} = 90^\circ$ ,  $\phi_{\text{mic}} = 180^\circ$ .

## OJF CAMPAIGN

The reproducibility of noise data for the experiments conducted at the Open Jet Facility is discussed here. The tonal noise emissions at a freestream velocity of 18 m/s, advance ratio of 0.6, microphone flyover angle of 45 degrees are presented in Figure 5.3. Six different runs are performed at this operating point consecutively without stopping any of the testing equipment. The variability of consecutive measurements for the first 5 blade passage frequencies is within  $\pm 0.8$  dB. The variability of consecutive measurements for all other microphones across the advance ratio range tested is within the same range. When comparing the noise emissions between isolated and installed configurations, the variations within  $\pm 0.8$  dB will be considered negligible. As the measurements are also performed on different days, the reproducibility of the non-consecutive measurements is also considered in the next subsection.

### 5.2.2. NON-CONSECUTIVE MEASUREMENTS

The experiments conducted on different days at different times tend to differ due to the varied experimental conditions over a period of time. Hence, the reproducibility of the non-consecutive measurements is also assessed.

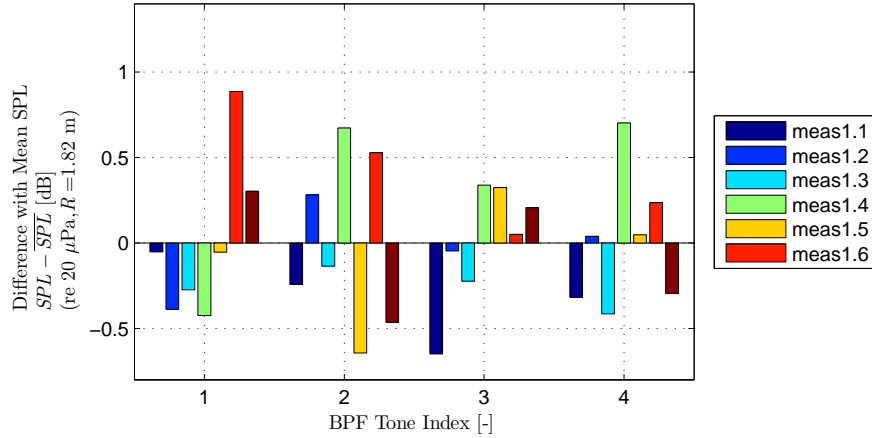


**Figure 5.3:** Variability of consecutive tonal noise emissions  
OJF campaign: Isolated configuration  $U_\infty = 18$  m/s,  $J = 1.0$ ,  $\theta_{mic} = 45^\circ$ ,  $\phi_{mic} = 86^\circ$ .

#### V-TUNNEL CAMPAIGN

The reproducibility of non-consecutive measurements is evaluated by running the propeller at the same operating point with intermediate stops of the propeller between each run. Two propeller noise measurements are performed at the same run resulting in four sets of data for each operating point. The resulting sound pressure levels at an advance ratio of 0.8, freestream velocity of 20 m/s, and microphone azimuthal angle of 180 degrees is presented in Figure 5.4, followed by the variability of non-consecutive measurements in Figure 5.5.

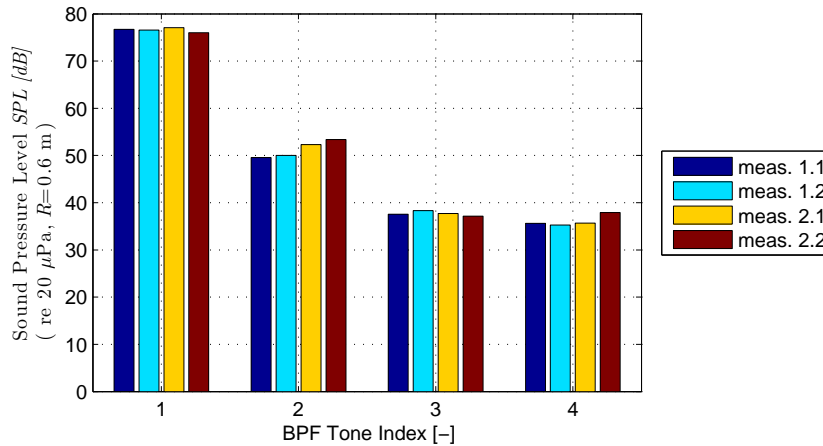


**Figure 5.4:** Reproducibility of propeller noise emissions measured in two different runs  
V-tunnel campaign: Isolated configuration,  $U_\infty = 20$  m/s,  $J = 0.8$ ,  $\theta_{mic} = 90^\circ$ ,  $\phi_{mic} = 180^\circ$ .

The variability for the non consecutive measurements is  $\pm 0.5$  dB for 1BPF and  $\pm 2.1$  dB for the higher harmonics, which is worse when compared to the variability of consecutive measurements. The largest differences between any two measurements for the same BPF is greater for even harmonics than for odd harmonics. A difference of 3.8 dB and 2.5 dB is observed for 2BPF and 4BPF and a small difference of 1 dB and 1.2 dB is observed for 1BPF and 3BPF. Higher variability of the non-consecutive measurements for the higher harmonics is probably due to the error in maintaining the same operating point in two different runs. As the non-consecutive runs were performed on two different days, the maintenance of the operating point at both the runs was difficult. The difference in propeller rpm in both the runs is 33 which is around 0.5%. The wind tunnel fan noise is also found to be variable in both the runs with a difference of 1 dB. The reproducibility of non-consecutive measurements reduce the effectiveness of comparisons between the isolated and installed configuration.

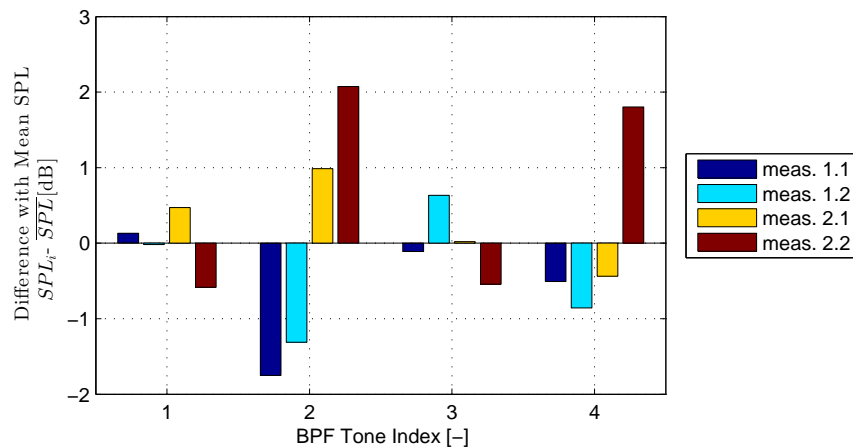


**Figure 5.5:** Variability of propeller noise emissions measured in two different runs V-tunnel campaign: Isolated configuration,  $U_\infty = 20$  m/s,  $J = 0.8$ ,  $\theta_{mic} = 90^\circ$ ,  $\phi_{mic} = 180^\circ$ .

#### OJF CAMPAIGN

The non-consecutive noise measurements for the experiments conducted at Open Jet Facility are recorded at a same propeller and wind tunnel setting for two different runs. The entire setup was stopped and restarted to measure the noise emissions for the isolated configuration. The tonal noise emissions are recorded at a freestream velocity of 18 m/s, advance ratio of 0.6, microphone flyover angle of 45 degrees. Two different runs on the same day with the first run (Run1 performed on 14:00 hours, 17 March 2015) having six measurements and the second run (Run2 performed on 16:00 hours, 17 March 2015) having two measurements performed consecutively. The mean of the consecutive measurements for two non consecutive runs for the first six blade passage frequency tones is calculated. The variability for two different runs is plotted in Figure 5.6.

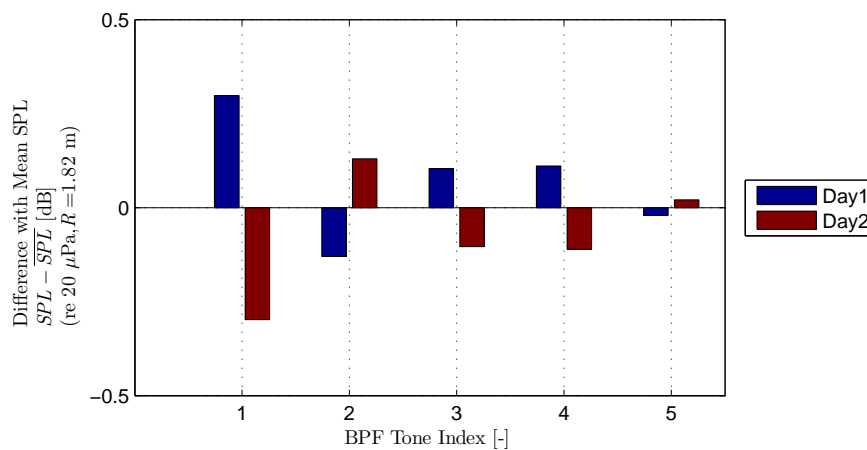


**Figure 5.6:** Variability of non-consecutive tonal noise emissions OJF campaign: Isolated configuration  $U_\infty = 18$  m/s,  $J = 1.0$ ,  $\theta_{mic} = 45^\circ$ ,  $\phi_{mic} = 86^\circ$ .

The variability for non-consecutive measurements is  $\pm 0.35$  dB which is better than the variability for the consecutive measurements  $\pm 0.8$  dB. The better reproducibility of the non-consecutive measurements is related to the averaging of the measurements recorded on different days.

### 5.3. ISOLATED CONFIGURATION

This section treats the propeller noise emissions for the isolated configuration. The measurements for this configuration are used as a reference to compare the noise emissions for pylon-installed and cylinder-installed configuration. First, the propeller noise spectra (Subsection 5.3.1) followed by the overall sound pressure levels in the isolated configuration (Subsection 5.3.2) are presented. Subsequently, the flyover directivity of the propeller in the isolated configuration is discussed in Subsection 5.3.3.

#### 5.3.1. PROPELLER NOISE SPECTRA

First, the propeller noise spectrum for the experiments conducted in the V-tunnel is presented, followed by the noise spectrum of the OJF campaign.

##### V-TUNNEL CAMPAIGN

The isolated propeller noise spectrum at an advance ratio of 0.8, freestream velocity of 20 m/s for the microphone at flyover angle of 90 degrees and azimuthal angle of 180 degrees is shown in Figure 5.7. The propeller tones which are integer multiples of BPF are shown with blue lines and the first wind tunnel tone is shown with a magenta line. The tonal sound pressure levels are identified with a circular marker at the integer multiple of propeller BPF. The first fundamental tone is clearly the loudest tone exceeding the other tones by at least 15 dB. Higher harmonics such as 3BPF, 4BPF, 5BPF, 6BPF and 7BPF are observed to be less prominent and the sound pressure level at their BPF is equivalent to the broadband noise levels. The sound pressure levels for the isolated configuration decrease with an increase in BPF tone index which is expected [36].

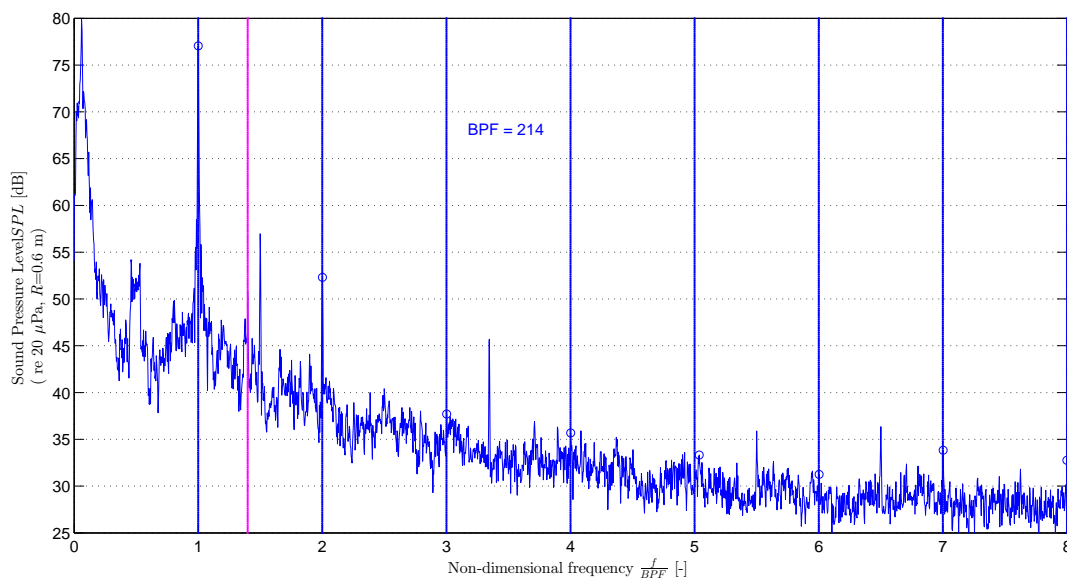


**Figure 5.7:** Propeller noise spectrum

V-tunnel campaign: Isolated configuration,  $U_\infty = 20$  m/s,  $J = 0.8$ ,  $\theta_{\text{mic}} = 90^\circ$ ,  $\phi_{\text{mic}} = 180^\circ$ .

The wind tunnel tone is observed at a frequency of 300 Hz (1.4BPF) with sound pressure level lower than the  $\frac{3}{2}$ BPF and 2BPF. A strong peak is observed around 700 Hz (3.34BPF) which is related to the noise emitted by the cooling system of the power supply used to drive the propeller model. The sound pressure level is of the order of 2BPF, which is relatively higher compared to other harmonics such as 3BPF, 4BPF and the background noise. However, the noise levels at frequencies of ( $\frac{3}{2}$ BPF and 2BPF) are also prominent in the considered isolated propeller condition. The integer multiple of power supply tone is also seen at a frequency of 1400 Hz (6.6BPF) with a relatively low sound pressure level. The unexpected peak at non-integer multiple of BPF i.e.  $\frac{3}{2}$ BPF can be understood by studying the low-frequency content of the spectrum with emphasis on sub-BPF scale.

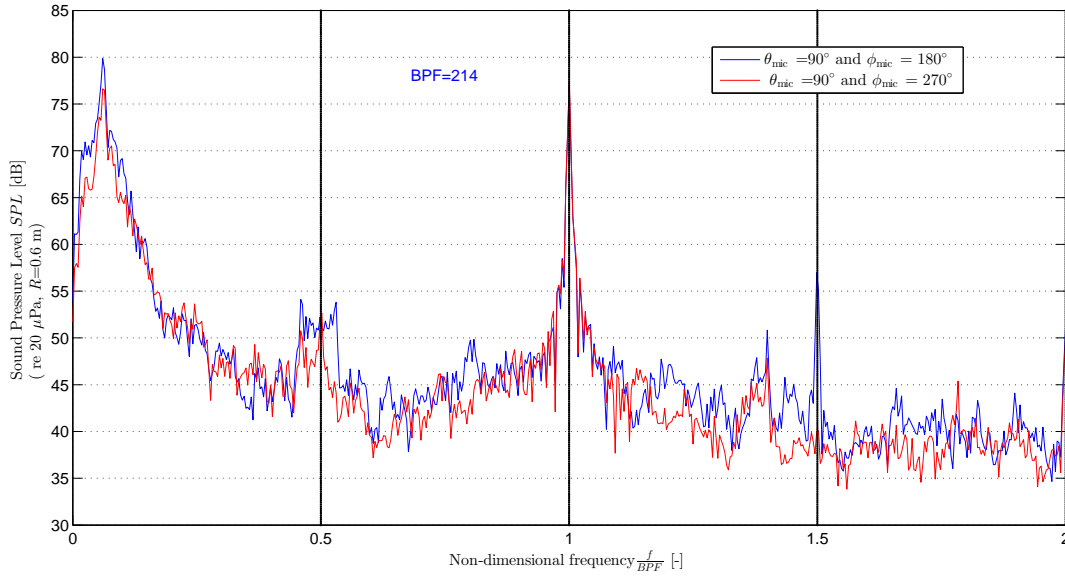


**Figure 5.8:** Low frequency analysis: Sub BPF scale analysis

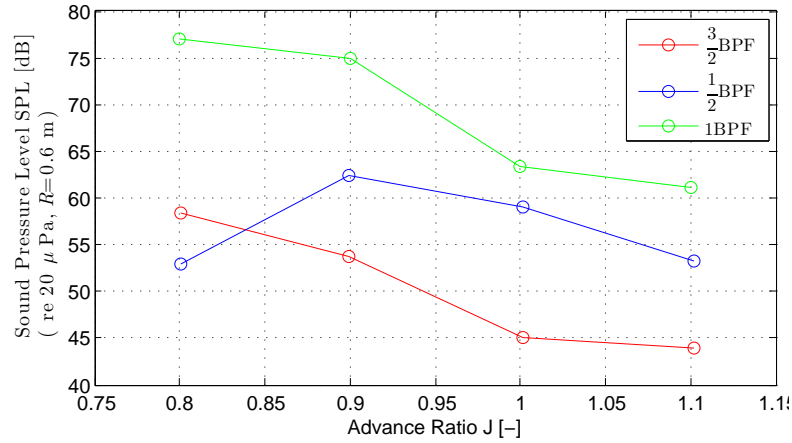
V-tunnel campaign: Isolated configuration,  $U_\infty = 20$  m/s,  $J = 0.8$ ,  $\theta_{mic} = 90^\circ$ ,  $\phi = [180 - 270]^\circ$ .

Figure 5.8 presents the low frequency spectra for the isolated configuration at a freestream velocity of 20 m/s, an advance ratio of 0.8, flyover angle of 90 degrees for microphones with azimuthal angle of 180 and 270 degrees. The black dashed line with a header  $\frac{1}{2}$ BPF represents the frequency of  $\frac{1}{2}$ BPF. Since the number of propeller blades is two, only  $\frac{1}{2}$ BPF is shown with a header. The sub-BPF peak observed is as expected (as  $\frac{3}{2}$ BPF is observed previously in the same spectrum) at  $\frac{1}{2}$ BPF which is due to the event of single blade passage. The sound pressure level of  $\frac{1}{2}$ BPF is of similar level compared to the  $\frac{3}{2}$ BPF and 2BPF. The existence of sub-BPF peaks shows the passage of each blade as a separate event, which could possibly be due to asymmetric shape of blade or asymmetric rotation of blade. To verify the presence of sub-BPF scale peaks, the low frequency spectrum content needs to be studied across the advance ratio range. Figure 5.9 has been plotted to show the variation of SPL of individual blade passage with advance ratio. As expected the SPL of all the tones increased with decreasing advance ratio. The plot clearly shows the dominant nature of 1BPF for advance ratios of 0.8-1.1. The contribution of sub-harmonics to the overall sound pressure level is low and hence they do not effect the overall noise levels. Some of the possible reasons for their presence are asymmetry in individual blade shapes, interactions between the shaft and support fairing or the shaft noise.

### OJF CAMPAIGN

The propeller noise spectrum for the isolated configuration is treated in this subsection. The propeller noise spectrum shown discussed below is recorded at an advance ratio of 1.0 and for microphone flyover angle of 90 degrees. The microphone is positioned at a distance of 1.31m and at an azimuthal angle of 86 degrees.

From Figure 5.10, it is observed that the noise spectrum has peaks at the multiples of blade passage frequency. Dominant peaks are observed at 1BPF, 3BPF, 4BPF and 6BPF. The 1BPF tone dominates the propeller noise spectrum with sound pressure level close to 75 dB which is higher by 10 dB than the next dominant tone which is expected. Various other peaks are also observed across the spectrum. The peak observed at low frequency of 113 Hz is due to the wind tunnel fan. The motor which runs the propeller also generates noise and is seen at a frequency of 2000Hz as a dominant peak. Since the frequency at which the motor generates its fundamental tone is high, the noise due to the motor does not effect the propeller noise measurements. Ideally, the propeller noise spectrum in the isolated configuration should show a decrease in SPL with increase in tonal index of the BPF [36]. From Figure 5.10, we observe that the SPLs of 3BPF and 4BPF are significantly higher than 2BPF. This is probably related to the non-uniform inflow into the propeller. However, the wake velocity profiles at a radial station  $\eta = 0.75$  for the isolated configuration did not show any non-uniformity. Another possible explanation is, considering that the measurements are in the far-field condition ( $R_{observer} = 1.32$  m and  $\lambda_{1BPF} = 0.71$  m), it is likely that sound waves produced from higher BPF (smaller wavelength)



**Figure 5.9:** SPL of sub BPF scale propeller tones across the advance ratio range  
V-tunnel campaign: Isolated configuration,  $U_\infty = 20$  m/s,  $J = 0.8$ ,  $\theta_{\text{mic}} = 90^\circ$ ,  $\phi_{\text{mic}} = 180^\circ$ .

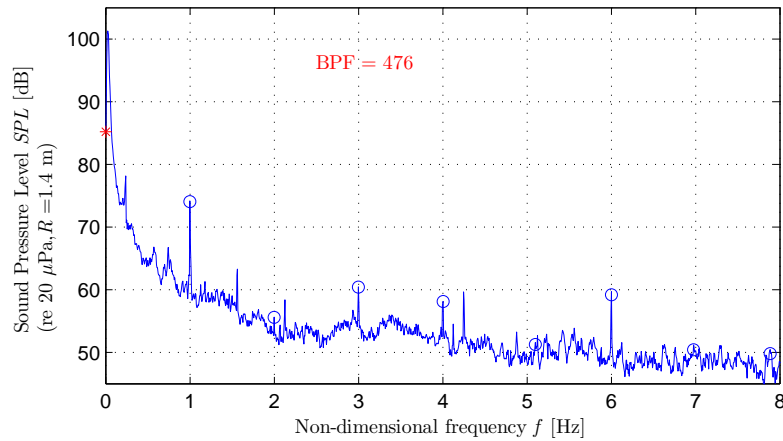


**Figure 5.10:** Propeller noise spectrum  
OJF campaign: Isolated configuration  $U_\infty = 18$  m/s,  $J = 1.0$ ,  $\theta_{\text{mic}} = 90^\circ$ ,  $\phi_{\text{mic}} = 86^\circ$ .

reflect from the flat surface supporting the propeller. It is to be noted that the background noise emissions are of the order of 50-60 dB for frequencies between 500-2000Hz. Both the tonal and background noise emissions increase with decrease in advance ratio. More on the effect of advance ratio is discussed in next subsection.

### 5.3.2. EFFECT OF ADVANCE RATIO

Since the noise emissions observed in the propeller noise spectra are observed to be tonal at a given operating condition, the propeller tonal noise emissions at different advance ratios are treated in this subsection.

#### V-TUNNEL CAMPAIGN

The noise spectrum for the isolated propeller shown in Figure 5.7 indicated the presence of tones at blade passage frequency. To understand the presence of tonal sources in detail, the variation of sound pressure level of all the harmonics across the advance ratio range is considered for analysis. Since the signal to noise ratio is very low for higher BPF starting from fifth, only the first four BPF are presented in Figure 5.11. From the figure, it is clear that the SPL of 1BPF and 2BPF increase with decreasing advance ratio, which is an expected

trend. As the propeller rpm is increased, propeller blade loads are increased. The associated increase in blade loading and the increase in helical Mach number contributes to the increase in tonal noise levels. The SPL of 1BPF is at least 15 dB louder than other higher BPF, which clearly suggests that 1BPF is the dominant tonal noise source in isolated propeller condition. 2BPF, 3BPF and 4BPF are insignificant in the operating advance ratio range when compared to 1BPF. At advance ratios of  $1 \leq J \leq 1.2$ , higher BPF such as 2BPF, 3BPF and 4BPF are around 43 dB with a variation of  $\pm 2$  dB. However, at very low advance ratios 2BPF starts to increase with advance ratio probably due to the increase of non-linear effects at high rpm. All the BPF shown in Figure 5.11 have a local maximum at advance ratio of 0.9. This is also observed in the case of  $\frac{1}{2}$ BPF and  $\frac{3}{2}$ BPF as shown in Figure 5.9. The existence of local maximum is probably due to the asymmetric rotation of propeller resulting in high sound pressure levels at advance ratio of 0.9. The broadband noise levels also showed an increase of 5 dB at this advance ratio. The propeller tones at higher multiples of blade passage frequency are significant at  $J = 0.9$ . The propeller noise spectrum at this advance ratio is attached in Appendix C. Below an advance ratio of 0.9, the SPL of all the BPF considered in the above analysis starts to decrease before increasing again and reaching to a peak at the lowest possible advance ratio tested i.e  $J = 0.77$ .

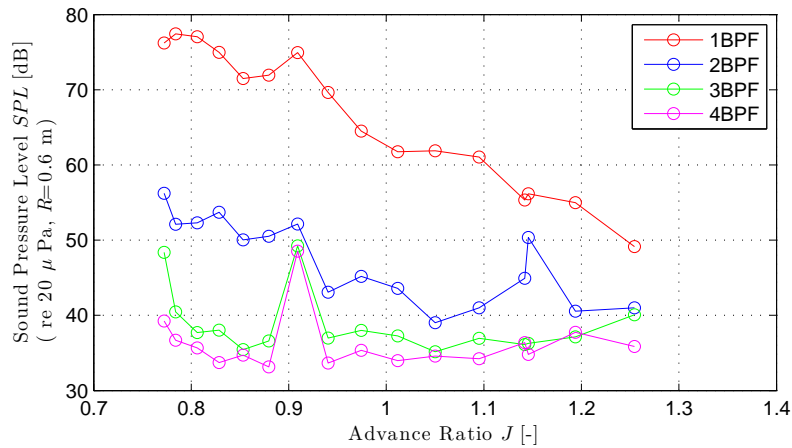


**Figure 5.11:** V-tunnel campaign: SPL of propeller tones across the advance ratio range  
Isolated configuration,  $U_\infty = 20$  m/s,  $J = 0.8$ ,  $\theta_{\text{mic}} = 90^\circ$ ,  $\phi_{\text{mic}} = 180^\circ$ .

### OJF CAMPAIGN

The propeller noise spectrum for the isolated configuration indicated that the noise emissions are tonal at multiples of blade passage frequency. Hence the tonal noise emissions are plotted for advance ratios between 0.5 and 1.6. The tonal noise levels recorded here are for a freestream velocity of 18 m/s and for flyover directivity angle of 90 degrees. 1BPF, 2BPF, 3BPF and the overall total noise levels are plotted in Figure 5.12. The tones below 1BPF are not discussed here. The overall total noise level is computed by considering the first 10 harmonics. The computations are also considered for the first four harmonics and is shown in Figure 5.13 and the observed differences between both the results are less. Hence, all the analysis presented from here on consider the first 10 harmonics.

From Figure 5.12, clearly the 1BPF tone dominates the overall noise emissions across the entire advance ratio range considered. The overall noise levels increase with decrease in advance ratio which is as expected. The higher multiples of BPF contribute to overall noise emissions substantially at low advance ratios than at high advance ratios. With decreasing advance ratio at a constant freestream velocity, the section blade loads increase as the local increase in angle of attack. This results in an increase in blade loading across the entire blade. This increase in blade loading and tip Mach number increases the thickness and loading noise leading to an increase in overall noise levels. However, the 1BPF tone does not increase with decrease in advance ratio across the entire range with a local minimum at an advance ratio of 0.7. This is also the same advance ratio range for which the 3BPF tone is dominant than the 2BPF tone. This increase is also observed for other microphone flyover angles but at different advance ratios. A possible explanation would be the presence of lobes in circumferential directivity due to a non-uniformity in the inflow of the propeller leading to an increase in sound pressure level. However, the inflow velocity profile for the isolated configuration for different

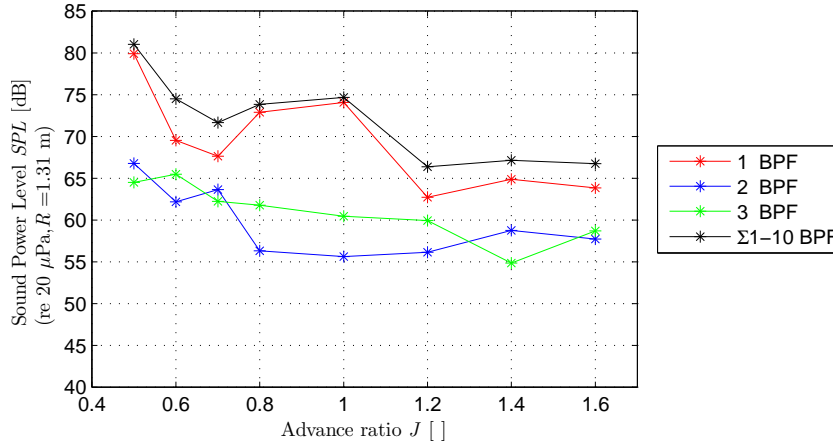


**Figure 5.12:** OJF campaign: Sound Pressure levels with varying advance ratio (10 harmonics). Isolated configuration  $U_\infty = 18$  m/s,  $J = 0.5$ -1.6,  $\theta_{\text{mic}} = 90^\circ$ ,  $\phi_{\text{mic}} = 86^\circ$ .

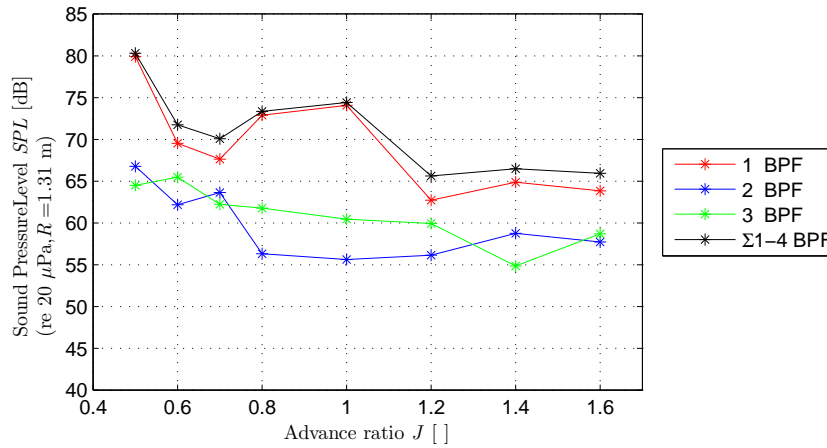


**Figure 5.13:** OJF campaign: Sound Pressure levels with varying advance ratio (4 harmonics). Isolated configuration  $U_\infty = 18$  m/s,  $J = 0.5$ -1.6,  $\theta_{\text{mic}} = 90^\circ$ ,  $\phi_{\text{mic}} = 86^\circ$ .

advance ratios shown in Figure 3.6 does not show any significant non-uniformity in the inflow. Another possible explanation (very unlikely considering the magnitude of increase) is, since the measurements are in the far-field condition ( $R_{\text{observer}} = 1.32$  m and  $\lambda_{1BPF, J=1.0} = 0.71$  m), it is possible that sound waves produced from higher BPF (smaller wavelength) at low advance ratio reflect from the flat surface supporting the propeller.

### 5.3.3. FLYOVER DIRECTIVITY

The directivity pattern of a dipole noise source depends on the square of the cosine of the flyover angle ( $\cos^2\theta$ ). Typically, propellers exhibit a dipole flyover directivity due to the fluctuating nature of forces exerted on the air by the rotational motion of the propeller blades. Analysis of the flyover directivity pattern from the experiments would serve as a basis for the theoretical dependence of propeller noise with flyover angle. This subsection deals with the analysis of flyover directivity of the isolated propeller.

#### OJF CAMPAIGN

This subsection discusses the flyover directivity pattern for the isolated propeller noise measurements recorded during the OJF campaign. The measurements are performed for an advance ratio of 1.0 and a freestream velocity of 18 m/s for seven microphones placed at flyover directivity angles of 45, 60, 75, 90, 105, 120 and 135 degrees. The overall tonal noise levels are computed by adding the tonal levels for the first

10 harmonics. The flyover directivity pattern for the isolated configuration is shown in Figure 5.14.

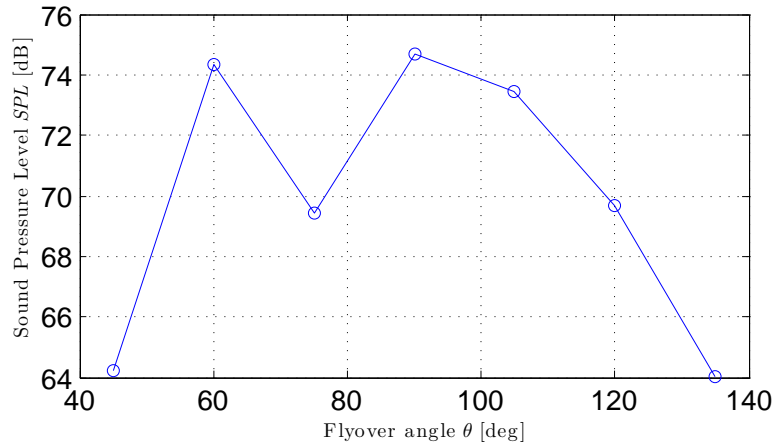


**Figure 5.14:** Flyover directivity

OJF campaign: Isolated configuration,  $U_\infty = 18$  m/s,  $J = 1.0$ ,  $\theta_{\text{mic}} = 90^\circ$ ,  $\phi_{\text{mic}} = 86^\circ$ , .

From 5.14, the downstream directivity pattern for the isolated configuration for the flyover angles of 105, 120 and 135 degrees is as expected. The overall noise levels decrease in the downstream direction with increase in flyover angle. This is due to the dipole nature of the isolated propeller noise source (radiation angle effecting the radiation efficiency). However the same is not reflected in the upstream direction for the microphone placed at flyover angle of 75 degrees. The dip in the flyover directivity is attributed to the sudden increase in sound pressure level observed at an advance ratio of 1.0 as seen in Subsection 5.3.2. This sudden increase in noise emissions happens at a slightly lower advance ratio of 0.9 for microphone flyover angle of 75 degrees. Hence, a dip is seen in the flyover directivity pattern. This difference in advance ratios at which a sudden increase in sound pressure level (a local peak in SPL vs  $J$ ) is observed might be related to the lobes in the circumferential directivity. The experiments performed does not provide a conclusive evidence.

## 5.4. PYLON-INSTALLED CONFIGURATION

This section presents the noise emissions for the pylon installed configuration. These measurements provide an understanding on the effects of an upstream pylon on the noise emissions of the propeller. The propeller noise spectrum for the installed configuration is discussed in Subsection 5.4.1. Subsequently, the effect of advance ratio on the propeller noise emissions and the flyover directivity is treated in Subsections 5.4.2 and 5.4.3 respectively. Next, the effect of installation on the flyover directivity for varying advance ratios is considered in Subsection 5.4.4. Then, the azimuthal directivity of the propeller is presented in Subsection 5.4.6. Finally, the effect of pylon-propeller spacing is discussed in Subsection 5.4.5.

### 5.4.1. PROPELLER NOISE SPECTRUM

#### V-TUNNEL CAMPAIGN

The propeller noise spectrum for the pylon installed configuration at a operating point with freestream velocity of 20 m/s , advance ratio of 0.8, pylon spacing of  $50\%D_{\text{prop}}$  for the microphone with azimuthal angle of  $180^\circ$  and flyover angle of  $90^\circ$  is presented in Figure 5.15. The isolated and pylon installed configuration are represented in blue and red respectively. The peaks at the BPF have been highlighted by circular markers for both the configurations. The BPF for the installed configuration is represented by red dashed lines. The wind tunnel noise at a frequency of around 300 Hz is represented by a magenta dashed line. Apart from the BPF and its harmonics, there are peaks observed in the spectrum which are related to the experimental setup. The peak at a frequency of 492 Hz for the installed configuration is associated with the cooling system of the laser equipment of particle image velocimetry setup. The cooling system for the voltage supply used to power the propeller generated tones at 700 and 1400 Hz. Since this power supply is used when the isolated

measurements are recorded, these tones exist only for the isolated propeller spectra. In addition, there is a difference in the propeller RPM of 136 between both the configurations which result in an offset between the BPF of pylon installed and isolated configuration.

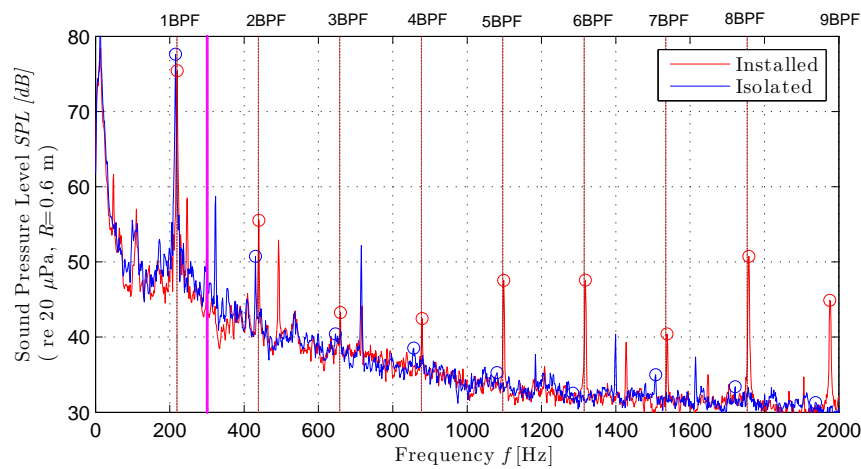


**Figure 5.15:** V-tunnel campaign: Propeller noise spectrum  
Pylon Installed configuration,  $U_\infty = 20$  m/s,  $J = 0.8$ ,  $\theta_{mic} = 90^\circ$ ,  $\phi = 180^\circ$ .

Figure 5.15 clearly shows the differences in the propeller noise spectrum between the isolated and pylon installed configuration. The spectrum for the pylon installed configuration has tonal peaks at all the first nine harmonics whereas the isolated configuration has peaks at 1BPF,  $\frac{3}{2}$ BPF and 2BPF. The SPL for 1BPF in the isolated configuration is higher than the SPL for 1BPF in the installed configuration. This is probably due to the introduction of unsteady loading noise source destructively interfering with the steady loading noise source. Pylon reflections might also have contributed to the decrease in noise levels. The SPL of  $\frac{3}{2}$ BPF is very low for the pylon installed configuration when compared to the isolated configuration. This essentially means the installation of pylon has reduced the asymmetric rotation of the propeller due to the vibration of shaft. The fractional BPF is not observed at higher advance ratio such as 1 and 1.1 ruling out the possibility of differing shapes of individual propeller blades as the reason for existence of high SPL fractional BPF. The introduction of pylon might have reduced the local advance ratio and thereby reducing the vibration of propeller. The difference in RPM between both the configurations and a locally lower advance ratio might also have reduced the vibration of the shaft. These reasons may have shifted the eigen-frequency of vibration. The broadband noise emissions are not effected by the installation of pylon ahead of the propeller.

#### OJF CAMPAIGN

In subsection 5.3.1, it is observed that the isolated noise spectra have tonal noise emissions at the blade passage frequency. With the installation of pylon, the velocity deficit in the wake increases the loading locally on the propeller blade and therefore increases the noise emissions. Since each blade cuts through the wake once a revolution, it is expected the propeller noise spectra show an increase in tonal noise levels at the multiples of blade passage frequency. Therefore, the propeller noise spectrum for the pylon-installed configuration for a freestream velocity of 18 m/s, advance ratio of 1.0, and for the microphone flyover angle of 90 degrees is plotted in Figure 5.16. The microphone is placed at an azimuthal angle of 86 degrees and at a distance of 1.31m. Figure 5.16 shows the propeller noise spectra for both installed and isolated configurations in red and blue colour, respectively. The spectrum for the pylon-installed configuration show an increase in tonal noise emissions when compared to the spectrum for the isolated configuration for the first four BPF. The SPL at 1BPF shows an increase of more than 2 dB whereas the higher tones 2BPF, 3BPF and 4BPF showed an increase of more than 5dB. The installation of pylon introduces an increase in the angle of attack during the wake passage resulting an increase in the local blade loading. The unsteady loading on the blade increases tonal noise levels of the first five BPF's. Also, the broadband noise levels measured for the pylon-installed configuration are similar to the broadband noise levels of the isolated configuration suggesting the broadband noise levels are related to the wind tunnel flow in both the configurations

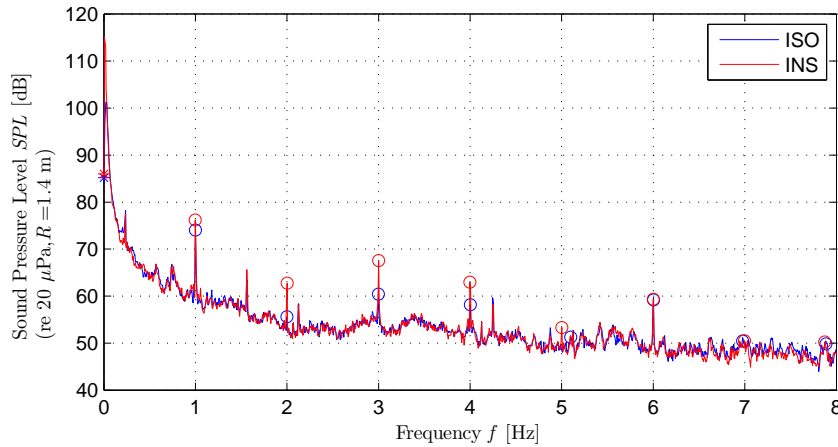


**Figure 5.16: Propeller noise spectrum**  
 OJF campaign: Isolated(blue) and Pylon-installed configuration (red)  
 $U_\infty = 18 \text{ m/s}, J = 1, \theta_{mic} = 90^\circ, \phi_{mic} = 86^\circ$

5.4.2. EFFECT OF ADVANCE RATIO

V-TUNNEL CAMPAIGN

The existence of tonal peaks is clearly seen in the propeller noise spectrum for the pylon installed configuration. To understand the effects of installation on the tonal noise sources, Figure 5.17 shows the variation of SPL of the first six harmonics with advance ratio varying from 0.8 to 1.1. The operating point for the measurements performed is at freestream velocity of 20 m/s, microphone azimuthal angle of 180 degrees and flyover angle of 90 degrees.

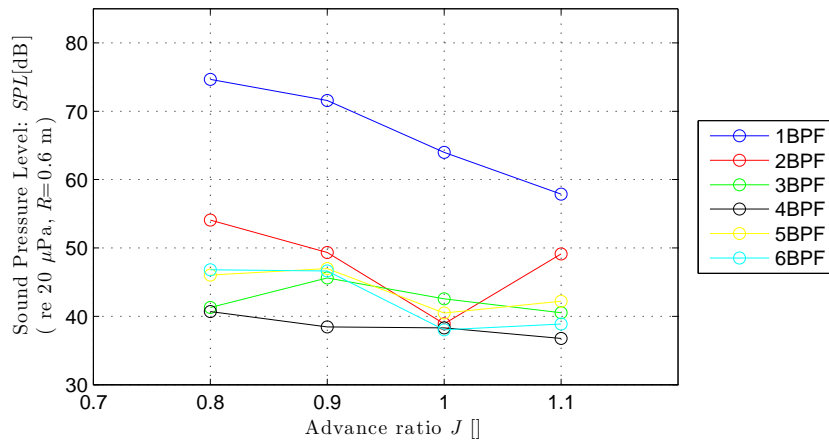


**Figure 5.17: Propeller noise spectrum**  
 V-tunnel campaign: Pylon Installed configuration  
 $U_\infty = 20 \text{ m/s}, J = 0.8, \theta_{mic} = 90^\circ, \phi_{mic} = 180^\circ$ .

The SPL of the 1BPF increased with decreasing advance ratio continuously throughout the advance ratio range. 1BPF is clearly higher than other BPF with a minimum difference of 8 dB. 2BPF, 3BPF, 4BPF and 5BPF also increased with decreasing advance ratio with some local minimum occurring at certain advance ratios. The presence of a local minimum is possibly due to the low signal to noise ratio at higher BPFs.

### OJF CAMPAIGN

The tonal noise levels for the pylon installed configuration for advance ratios ranging between 0.5 and 1.6 are presented here. The pylon-propeller spacing for the installed configuration is 50% of the diameter of the propeller. The first three multiples of the blade passage frequency and the overall noise levels computed using the first ten harmonics are shown in Figure 5.18. Overall the noise emissions for the pylon installed configuration are higher than the isolated case for the entire advance ratio range tested. The presence of pylon resulted in unsteady loading on the blade during the wake passage. This is observed as an increase in SPL at the multiples of blade passage frequency. The contribution of the higher BPFs to overall noise emissions is significantly higher in the installed configuration compared to the isolated configuration. Similar to the isolated configuration, the sound pressure levels of the 1BPF show a local minima at advance ratio of 0.7.

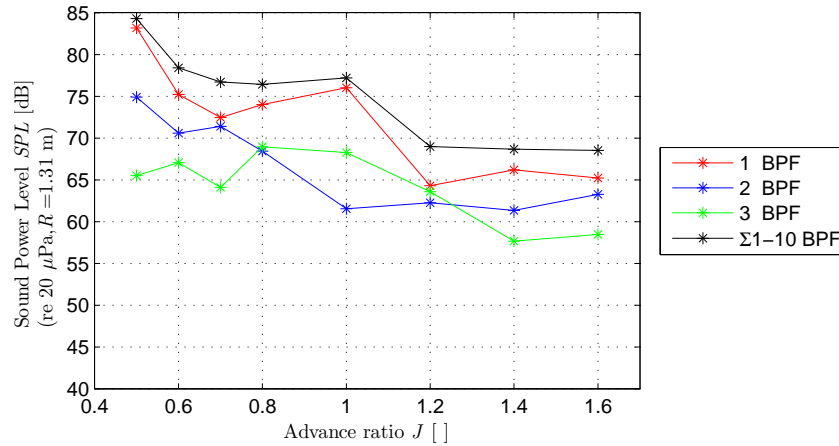


**Figure 5.18:** Tonal SPL levels with varying advance ratio  
Pylon installed configuration  $U_\infty = 18$  m/s,  $J = 0.5-1.6$ ,  $\Delta X = 0.5D_{prop}$

### 5.4.3. FLYOVER DIRECTIVITY

This section treats the flyover directivity of the pylon installed configuration for both the experimental campaigns.

#### V-TUNNEL CAMPAIGN

Isolated and Pylon installed propeller noise measurements were performed in the V-tunnel experimental campaign by placing microphones at flyover angles of 60, 90 and 120 degrees and at an azimuthal angle of 180 degrees at a distance of 0.6 m from the center of the propeller. The spacing between the propeller and pylon is varied from 30% to 70% in steps of 10% of the diameter of the propeller. The flyover directivity pattern for a freestream velocity of 20 m/s across the advance ratio range 0.8 is given in Figure 5.19.

From Figure 5.19, the sound pressure levels downstream of the propeller are lower than the sound pressure levels in the plane of the propeller which is expected due to the dipole nature of the dominant propeller noise sources. However, upstream of the propeller, a small increase in SPL is observed which is not expected. This is probably due to the reflections observed upstream due to the setup at the V-tunnel. It is likely that further upstream the sound pressure level would decrease and follow the expected trend. The effect of pylon-propeller spacing is discussed later in this chapter.

### OJF CAMPAIGN

In Subsection 5.3.3, the flyover directivity of the isolated configuration is presented. It is shown that the overall noise emissions decrease away from the propeller in both upstream and downstream directions (except for a local minima at flyover angle of 75 degrees). In this subsection, the flyover directivity of the pylon installed configuration is treated. The measurements recorded are for the freestream velocity of 18m/s, advance ratio of 1.0 and pylon-propeller spacing of 50% of the diameter of the propeller. The microphone flyover directivity

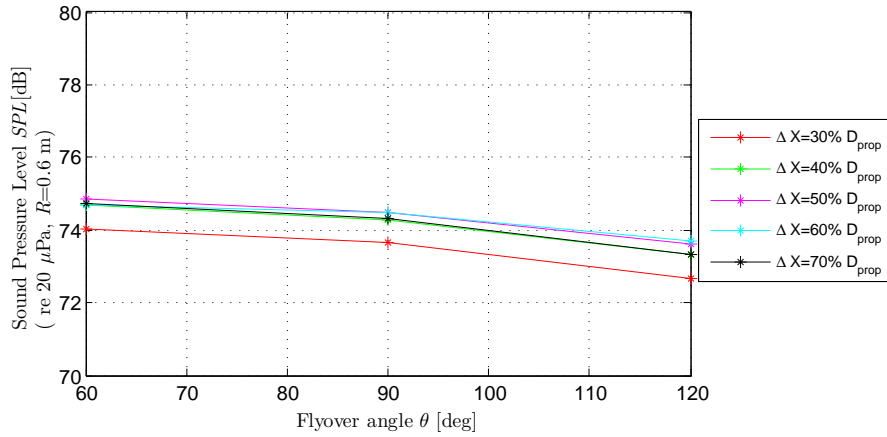


**Figure 5.19:** V-tunnel campaign: Flyover directivity  
 Pylon installed configuration  $U_\infty = 20$  m/s,  $J = 0.8\theta_{mic} = [60\ 90\ 120]^\circ$ ,  $\phi_{mic} = 180^\circ$ .

angles are 45, 60, 75, 90, 105, 120 and 135 degrees. The overall noise emissions are computed by considering the first ten harmonics and the result is shown in Figure 5.20.

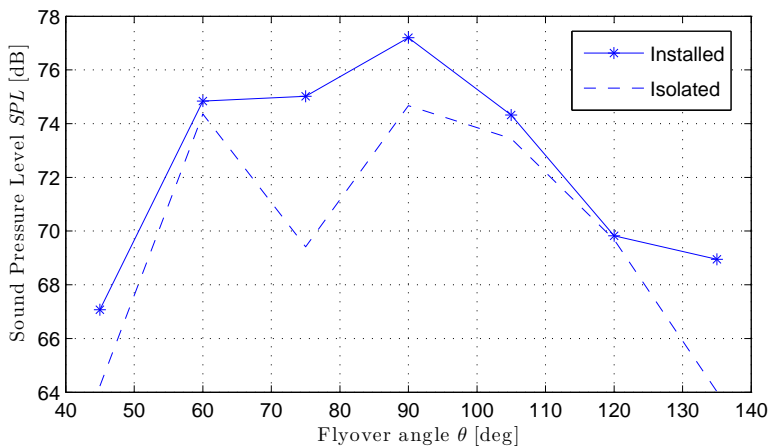


**Figure 5.20:** OJF campaign: Flyover directivity  
 Isolated and Pylon installed configuration  $U_\infty = 18$  m/s,  $J = 1.0$ ,  $\theta_{mic} = [45 - 135]^\circ$ ,  $\phi_{mic} = 86^\circ$ .

The noise emissions for the isolated configuration is shown in a dashed line. The noise emissions are higher for all the flyover angles tested except for 60 and 120 degrees. The presence of pylon provides an extra source of loading on the propeller blades. The pylon wake results in unsteady blade loading during the wake passage which is seen as an increase in SPL at multiples of the blade passage frequency. These unsteady loads act as noise source and hence an increase in noise emissions of 3 dB is observed at flyover angle of 90 degrees. This is also observed in Subsections 5.3.2 and 5.4.2 as an increase in 1BPF tonal emissions at an advance ratio of 1.0. However, the presence of unsteady noise source is not significant at directivity angles of 60 and 120 degrees possibly indicating the directivity pattern of unsteady noise source is different compared to the overall noise emissions. This is due to the higher SPL in the isolated configuration at these angles. The effect of the pylon on the flyover directivity is better understood by evaluating the difference in noise levels between the pylon installed and isolated configuration.

The difference in noise emissions is computed and plotted in Figure 5.21. The installation noise penalty shows an increase in noise emissions for all the directivity angles. However, the trend both upstream and downstream is unexpected. For flyover angles of 75, 90 and 105 degrees, the noise penalty is high which is

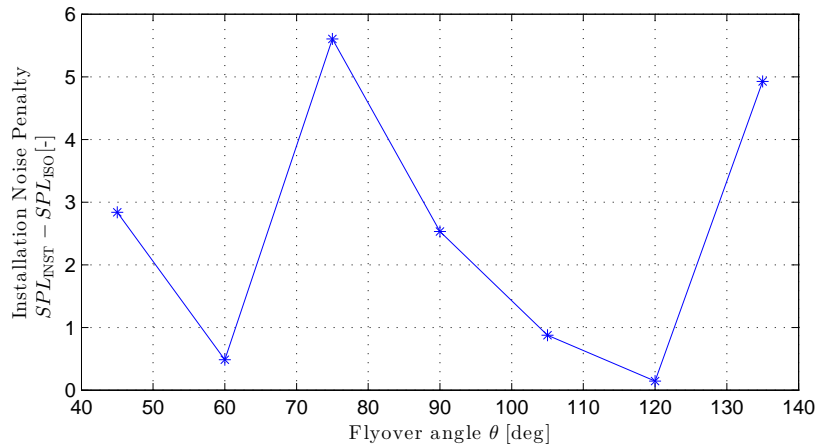


**Figure 5.21:** OJF campaign: Installation impact  
Pylon installed configuration  $U_\infty = 18$  m/s,  $J = 2.0$ ,  $\theta_{mic} = [45 - 135]^\circ$ ,  $\phi_{mic} = 86^\circ$ .

due to the local minima in the directivity pattern of isolated configuration at 75 degrees. The isolated configuration showed a dip at  $\theta$  of 75 degrees as the local peak (Refer 5.12) in SPL vs J is delayed to a lower advance ratio at this flyover angle. For the installed configuration, the local peak for all the flyover angles occurs at an advance ratio of 1.0 and hence the dip is not seen as shown in Figure 5.20. For the flyover angles of 45 and 135 degrees, the installation noise penalty is higher than the flyover angles of 60 and 120 respectively. This is expected as the pylon-propeller interaction noise increases in both upstream and downstream directions because of the increased radiation efficiency of the unsteady loading noise along the propeller axis than that of the steady noise sources [28].

#### 5.4.4. EFFECT OF ADVANCE RATIO ON THE FLYOVER DIRECTIVITY OF PYLON-INSTALLED CONFIGURATION

##### OJF CAMPAIGN

The previous subsection treated the flyover directivity at advance ratio of 1.0. However, the directivity pattern might change depending on the propeller blade loads. The present subsection treats the effect of advance ratio on the flyover directivity pattern. The measurements recorded are for a freestream velocity of 18 m/s, pylon spacing of 50% of diameter of the propeller and for the flyover angles of 45, 60, 75, 90, 105, 120 and 135 degrees. The flyover directivity pattern for advance ratios of 1.0 (blue line) and 1.2 (red line) are shown in Figure 5.22.

The flyover directivity pattern for advance ratio of 1.0 was already discussed in Subsection 5.4.3. The flyover directivity pattern for advance ratio of 1.2 indicates that the overall noise levels decreased for all the microphone angles. However, the maximum sound pressure level is observed at  $\theta = 105$  degrees. This is possibly due to the shift in directivity pattern due to the scattering of higher multiples of blade passage frequency by the propeller strut support. The effect of advance ratio on the flyover directivity is better understood by plotting the noise penalty for different advance ratios. The installation noise penalties for advance ratios of 1.0 and 1.2 are shown in Figure 5.23.

The installation impact for advance ratio of 1.2 is higher than for the advance ratio of 1.0 in the downstream direction. This is due to the difference in steady and unsteady loading on the propeller at different advance ratios. This is as expected as the ratio of unsteady to steady loading is higher at an advance ratio of 1.2 than at 1.0. However, upstream of the propeller, this is not observed. This is due to the presence of dip in the flyover directivity at 75 degrees for the isolated configuration which resulted in a higher installation noise penalty upstream of the propeller.

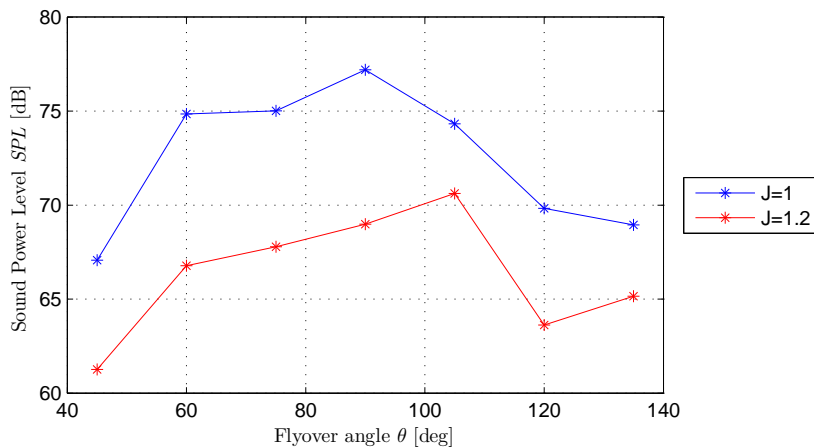


**Figure 5.22:** OJF campaign: Flyover directivity for different advance ratio  
Pylon installed configuration  $U_\infty = 18$  m/s,  $J = [1.0 \ 1.2]$ ,  $\theta_{mic} = [45 - 135]^\circ$ ,  $\phi_{mic} = 86^\circ$ .

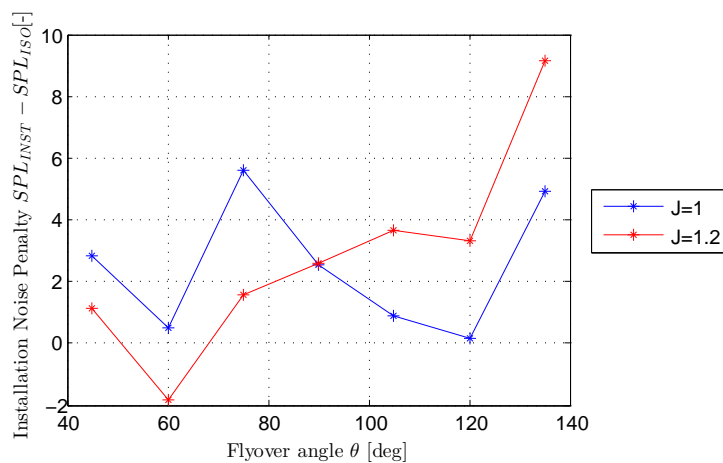


**Figure 5.23:** OJF campaign: Installation impact for different advance ratio  
Pylon installed configuration  $U_\infty = 18$  m/s,  $J = [1.0 \ 1.2]$ ,  $\theta_{mic} = [45 - 135]^\circ$ ,  $\phi_{mic} = 86^\circ$ .

#### 5.4.5. AZIMUTHAL DIRECTIVITY

This section presents the azimuthal directivity for the propeller noise emissions in the installed configuration. The propeller noise measurements are performed for different azimuthal angles only during the V-tunnel campaign.

##### V-TUNNEL

Isolated and pylon-installed propeller noise measurements were performed in the V-tunnel experimental campaign by placing microphones at azimuthal angles of 180 and 270 degrees and flyover angle of 90 degrees at a distance of 0.6 m from the center of the propeller. The spacing between the propeller and pylon is varied from 30% to 70% in steps of 10% of the diameter of the propeller. The azimuthal directivity pattern for a freestream velocity of 20 m/s at an advance ratio range 0.8 is given in Figure 5.24.

From Figure 5.24, the isolated propeller noise measurements are constant for both the azimuthal angles 180 and 270 degrees. However, the sound pressure levels for the pylon installed configurations is less than the isolated case by 1.2 dB and 1.6 dB in the plane perpendicular and parallel to the pylon, respectively. The decrease observed is probably due to destructive interference of the two steady loading and unsteady loading noise sources [27].

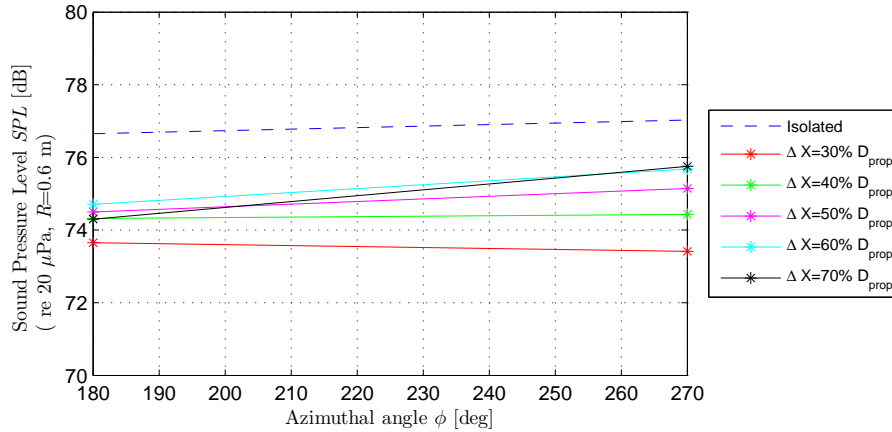


**Figure 5.24:** V-tunnel campaign: Azimuthal directivity  
Pylon installed configuration  $U_\infty = 20$  m/s,  $J = 0.8$ ,  $\theta_{mic} = [90]^\circ$ ,  $\phi_{mic} = [180 - 270]^\circ$ .

#### 5.4.6. EFFECT OF PYLON-PROPELLER SPACING

The current subsection treats the effect of pylon-propeller spacing on the overall sound pressure level for the pylon-installed configuration. The measurements recorded in both the V-tunnel campaign and the OJF campaign are considered for analysis.

##### V-TUNNEL CAMPAIGN

Propeller noise measurements are performed in the V-tunnel experimental campaign by placing microphones at flyover angles of 60, 90 and 120 degrees and azimuthal angle of 180 degrees at a distance of 0.6 m from the center of the propeller. The spacing between the propeller and pylon is varied from 30% to 70% in steps of 10% of the diameter of the propeller. The resultant tonal noise levels are plotted in Figure 5.25.

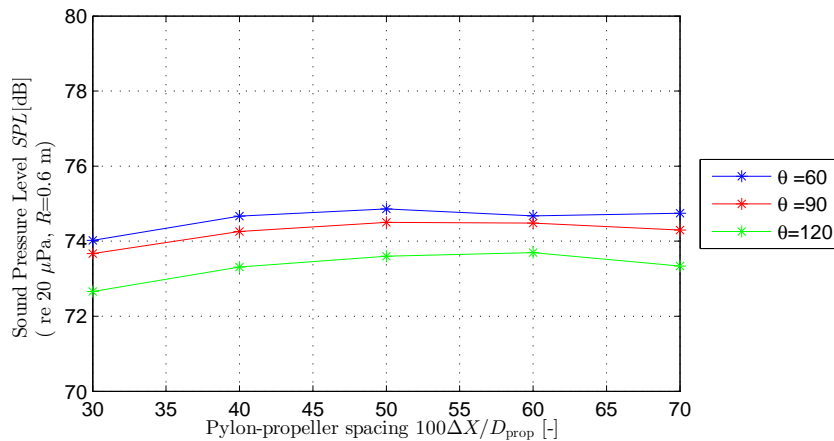


**Figure 5.25:** V-tunnel campaign: Effect of pylon spacing  
Pylon installed configuration  $U_\infty = 20$  m/s,  $J = 0.8$ ,  $\theta_{mic} = [60\ 90\ 120]^\circ$ ,  $\phi_{mic} = 180^\circ$ .

From Figure 5.25, the effect of increase in spacing from 30% to 50% of the diameter of the propeller has resulted in an increase in SPL. Further increase in spacing has no effect on the observed sound pressure levels. Theoretically, increase in spacing would likely result in a decrease in velocity deficit and thereby decrease in unsteady loading noise leading to a decrease in sound pressure level. However, previous experiments suggest

that the effects of installation are dominant in the plane perpendicular to the pylon and negligible in the plane of the propeller. Since, the noise levels in the pylon installed configuration decreased when compared to the isolated configuration, it is likely that the observed variation in SPL with pylon-propeller spacing is due to the destructive interference of steady and unsteady loading noise sources.

OJF CAMPAIGN

The measurements recorded are for a freestream velocity of 18 m/s and advance ratio of 1.0 and microphone flyover angles of 45, 60, 75, 90, 105, 120 and 135 degrees. The pylon position is varied from 40% to 100 % of diameter of the propeller from the pylon trailing edge. The flyover directivity for all the configurations including the isolated (dashed line) is shown in Figure 5.26.

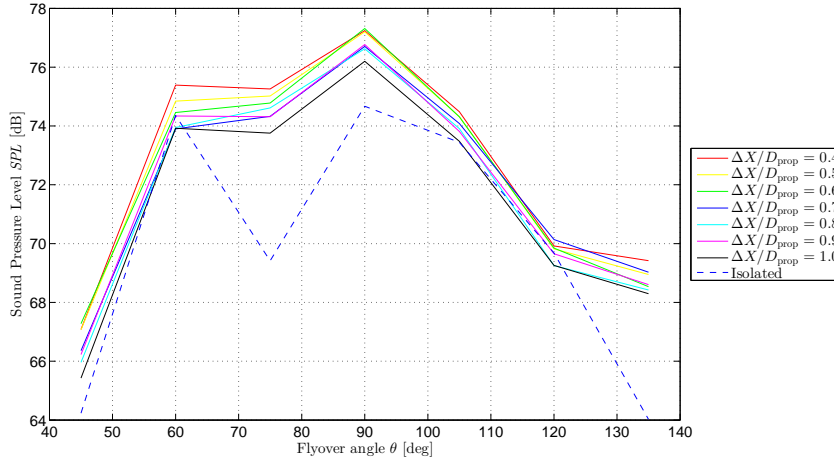


**Figure 5.26:** OJF campaign: Effect of pylon-propeller spacing  
 Pylon installed configuration  $U_\infty = 18 \text{ m/s}$ ,  $J = 1.0$ ,  $\theta_{mic} = [45 - 135]^\circ$ ,  $\phi_{mic} = 86^\circ$ .

The overall noise emissions for the closest pylon-propeller spacing are higher than for the farthest pylon-propeller spacing [26, 27]. The wake profiles indicated that the velocity deficit decreases with increase in pylon-propeller spacing (Refer Section 3.3.2). This might indicate that the unsteady loading is higher for the closest pylon-propeller spacing resulting in higher blade loads and thereby increasing the sound pressure level at all microphone flyover angles. Further, the root mean square deviation of the streamwise velocity also showed a decrease with increase in pylon-propeller spacing (Refer Section 3.3). The effect of pylon-propeller spacing on the installation noise penalty is plotted in Figure 5.27. The installation noise penalty increases in

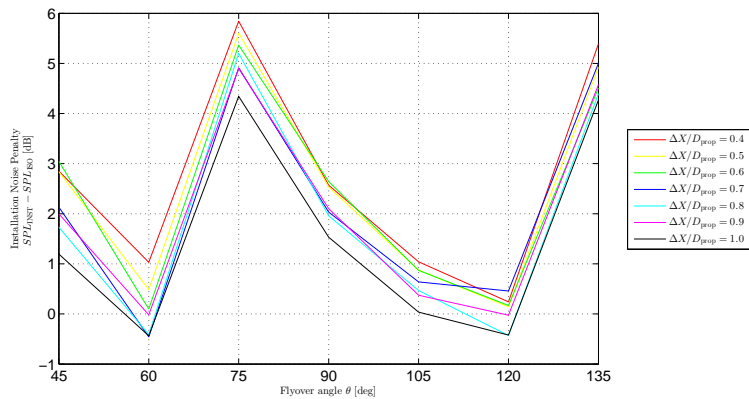


**Figure 5.27:** OJF campaign: Installation impact on the flyover directivity  
 Pylon installed configuration  $U_\infty = 18 \text{ m/s}$ ,  $J = 1.0$ ,  $\theta_{mic} = [45 - 135]^\circ$ ,  $\phi_{mic} = 86^\circ$ .

both upstream and downstream directions except for flyover angles of 75, 90 and 105 degrees. This is due to the presence of a local dip in the isolated flyover directivity. The effect of pylon-propeller spacing is clearly

seen in the Figures 5.27 and 5.28. As the spacing increases, the overall noise emissions at all directivity angles decreases due to decrease in unsteady blade loads [27].

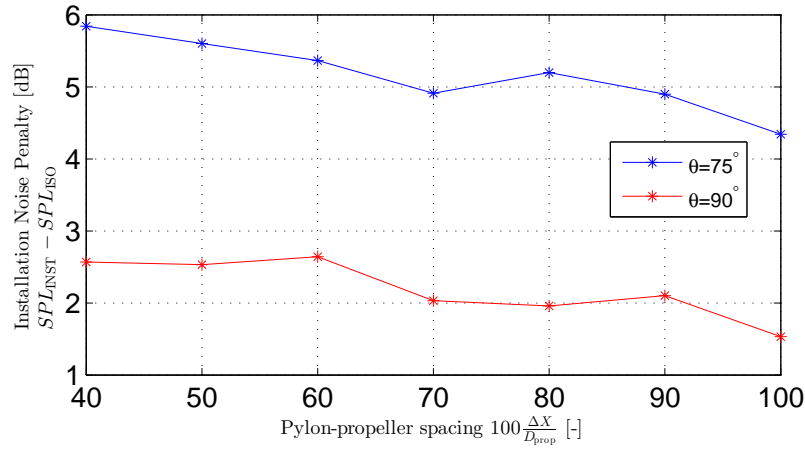


**Figure 5.28:** OJF campaign: Effect of pylon-propeller spacing  
Pylon installed configuration  $U_\infty = 18 \text{ m/s}$ ,  $J = 1.0$ ,  $\theta_{mic} = [75 - 90]^\circ$ ,  $\phi_{mic} = 86^\circ$ .

## 5.5. CYLINDER-SPLITTER PLATE INSTALLED CONFIGURATION

### OJF CAMPAIGN

One of the aims of the present thesis is to evaluate propeller noise emissions for varying wake characteristics. Wakes of different wake widths and velocity deficits are generated with cylinder-splitter plate configurations. The geometry of different upstream objects used is presented in Subsection 2.3.3 and referred here as CYL20, CYL30 and CYL50 respectively. The results presented here are for a freestream velocity of 18 m/s, advance ratio of 1 and for microphone flyover angles of 45, 60, 75, 90, 105, 120 and 135 degrees respectively. The flyover directivity for various configurations is shown in Figure 5.29. All the configurations indicate an increase

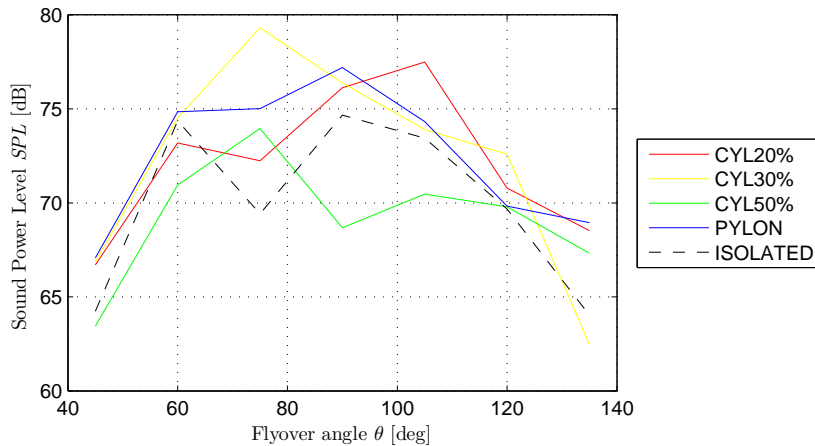


**Figure 5.29:** OJF campaign: Flyover directivity for various objects  
Installed configuration  $U_\infty = 18 \text{ m/s}$ ,  $J = 1.0$ ,  $\theta_{mic} = [45 - 135]^\circ$ ,  $\phi_{mic} = 86^\circ$ .

in noise emissions due to the presence of pylon except for the CYL50 configuration. The pylon installed and CYL30 configuration show an increase in noise emissions at flyover angle of 75 degrees whereas the CYL20

configuration indicate an increase in the downstream of the propeller at 105 degrees. The CYL50 configuration has noise emissions significantly lower than the isolated configuration at all directivity angles except for 75 degrees. Wake profiles indicate the velocity deficit for CYL50 configuration is similar to the CYL30 configuration. However, the noise levels are lower for the CYL50 show that there are other noise mechanisms in the cylinder-splitter plate configuration. Some of the possibilities are the level of scattering of the unsteady noise in CYL30 and CYL20 configuration is high due to the small size of objects when compared to the CYL50 configuration.



# 6

## NUMERICAL SETUP

The current chapter presents the numerical models used to predict the effect of an upstream wake on the propeller. First, the numerical model which is used to compute the velocity profile of the pylon wake is presented in Section 6.1, followed by the propeller performance estimation models for the isolated and pylon-installed configurations in Section 6.2. Finally, the propeller noise prediction methods for the isolated and pylon installed configuration are given in Section 6.3.

### 6.1. PYLON WAKE PROFILES

The propeller in the pylon installed configuration is disturbed by the incoming wake of the upstream pylon. The wake of the pylon results in a velocity deficit thereby affecting the performance and noise emissions of the propeller. The inflow into the propeller due to the presence of the pylon varies with the position. The velocity profile in the wake vary with the longitudinal and lateral separation between the pylon trailing edge and the position at which velocity profile is computed. Here, the velocity profiles are determined by using the Schlichting wake model. Schlichting wake model is based on Prandtl's mixing length hypothesis [29]. The 2D velocity profiles of an airfoil wake are determined with the help of 2D drag coefficient of the airfoil. The velocity deficit in the wake as function of  $X_{\text{wake}}$ ,  $Y_{\text{wake}}$  is given as

$$\Delta u(X_{\text{wake}}, Y_{\text{wake}}) = U_{\infty} \frac{\sqrt{10}}{18\beta} \sqrt{\frac{c_d c}{X_{\text{wake}}}} \left[ 1 - \frac{Y_{\text{wake}}^{\frac{3}{2}}}{b_{\text{wake}}} \right]^2 \quad (6.1)$$

$$b_{\text{wake}}(X_{\text{wake}}) = \beta \sqrt{10 c_d X_{\text{wake}}} \quad (6.2)$$

In the above formulation,  $U_{\infty}$  is the freestream velocity,  $X_{\text{wake}}$  and  $Y_{\text{wake}}$  are streamwise and cross streamwise distances from the trailing edge of the pylon and  $c_d$  represents the 2D drag coefficient of the pylon.  $\beta$  is obtained from correlation with experimental results and is taken here as 0.18 [29]. The wake velocity deficit and wake width are computed from Equations 6.1 and 6.2 respectively. The pylon drag coefficient is computed using XFOIL for a pylon angle of attack of zero degrees and Reynolds number based on the freestream velocity. Note that the transition point is free on both sides of the pylon and it is calculated by using XFOIL for the NACA 0012 airfoil.

### 6.2. PROPELLER PERFORMANCE

The methodology of predicting propeller performance in the isolated configuration and pylon-installed configuration is presented in the Subsections 6.2.1 and 6.2.2, respectively.

#### 6.2.1. ISOLATED CONFIGURATION

Propeller performance in the isolated configuration is predicted using XROTOR, an interactive program based on the propeller lifting line theory. Table 6.1 provides the inputs used to determine the propeller performance. The induced velocities are calculated by iterating equations based on blade geometry, blade section proper-

**Table 6.1:** XROTOR INPUTS

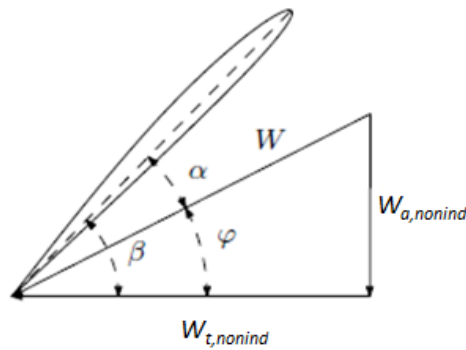
Parameter	Symbol	Value	Unit
Altitude	$h$	0	m
Freestream velocity	$U_\infty$	18	m/s
Advance ratio	J	[0.5-1.7]	-
Rotational direction	-	Counter clockwise	
Propeller diameter	$D_{prop}$	0.3043	m
Number of blades	$N_B$	8	-
blade rake	$\psi_{rake}$	0	deg
Pitch change axis position	$c_{PCA}$	0.4474	-
Nacelle perturbation axial velocity	$U_{ind,nacelle}$	0	m/s
duct/No duct	-	No duct	-
Number of blade sections	$N_r$	17	-
Wake mode	-	Self deforming mode	-

ties, operating conditions and the radial circulation distribution using a Newton method. Blade geometry details such as chord distribution  $c(r)$ , and twist distribution  $\beta(r)$  are provided as an input to solve the section velocity triangles. Blade section properties such as  $C_l$  and  $C_d$  as a function of angle of attack ( $\alpha$ ), Reynolds number (Re) and Mach number (M) for every section are required to determine the loading distribution on the propeller blade sections. Parameters such as freestream velocity  $U_\infty$ , Advance ratio (J), number of blades (B) describe the operating point of the propeller.

Newton iterative method is employed to solve the velocity triangle, section lift and drag relationships for each section to determine the circulation for each section. First the induced velocities are computed which determine the section angle of attack given by Equation 6.3 and as shown in Figure 6.1.

$$\alpha_i = \beta_i - \tan^{-1} \left( \frac{U_\infty + u_{a_i}}{\Omega r_i - u_{t_i}} \right) \quad (6.3)$$

- $\alpha_i$  = local angle of attack
- $u_{a_i}$  = local induced axial velocity
- $u_{t_i}$  = local induced tangential velocity
- $\Omega$  = rotational velocity of the propeller
- $R$  = radius of the propeller
- $r_i$  = radial distance of the local blade section

**Figure 6.1:** Velocity triangle at a local blade section

**Table 6.2:** Summary of the aerodynamics parameters for every local blade section given as input in XROTOR

Parameter	Symbol
Zero lift angle	$\alpha_0$
Slope of linear region of $c_l - \alpha$ curve	$c_{l\alpha}$
Slope of stalled region of $c_l - \alpha$ curve	$c_{l\alpha_{stall}}$
Maximum lift coefficient	$c_{l_{max}}$
Minimum lift coefficient	$c_{l_{min}}$
Lift coefficient increment to stall	$\Delta c_{l_{stall}}$
Minimum drag coefficient	$c_{d0}$
Derivative of drag coefficient with lift coefficient squared	$\frac{\partial c_d}{\partial c_l^2}$
Lift coefficient at minimum drag coefficient	$c_l^{c_d=c_{d0}}$
Reynolds number based on inflow velocity	$Re$
Reference Reynolds number at a local section	$Re_{ref}$
Reynolds number scaling exponent	$f$
Critical Mach number	$M_{crit}$

The local section angle of attack is used to compute the section  $c_l$  and  $c_d$  using the functions  $c_l(\alpha, Re, M)$  and  $c_d(\alpha, Re, M)$ . Table 6.2 provides the aerodynamic parameters which serve as input to XROTOR. The section parameters are obtained by obtaining the lift and drag polars for every section followed by an optimisation to fit the original and fitted polars. The original lift and drag curves for every section are determined by using an airfoil analysis program: RFOIL. The Reynolds number used for each section is computed by averaging the Reynolds number observed over the entire advance ratio range. Subsequent optimization determines the section parameters from the original lift and drag curves. Detailed description of the above process is given in Sinnige[10].

The blade section lift coefficient is computed using the parameters given in Table 6.2 as per the Equation 6.4.

$$c_l = c_{l_{lin}} - \left(1 - \frac{c_{l\alpha_{stall}}}{c_{l\alpha}}\right) \Delta c_{l_{stall}} \ln \left( \frac{1 + \exp\left(\frac{c_{l_{lin}} - c_{l_{max}}}{\Delta c_{l_{stall}}}\right)}{1 + \exp\left(\frac{c_{l_{lin}} - c_{l_{max}}}{\Delta c_{l_{stall}}}\right)} \right) \quad (6.4)$$

with the linear lift coefficient given by Equation 6.5.

$$c_{l_{lin}} = (\alpha - \alpha_0) \frac{c_{l\alpha}}{\sqrt{1 - M^2}} \quad (6.5)$$

The section drag coefficient is computed by the following relation

$$c_d = \left[ c_{d0} + \frac{\partial c_d}{\partial c_l^2} \left( c_l - c_l^{c_d=c_{d0}} \right)^2 \right] \left( \frac{Re}{Re_{ref}} \right)^f + \Delta c_{d_M} + \Delta c_{d_{non-linear}} \quad (6.6)$$

with

$$\Delta c_{d_{non-linear}} = 2 \left[ \left(1 - \frac{c_{l\alpha_{stall}}}{c_{l\alpha}}\right) \frac{\Delta c_{l_{stall}} \ln \left( \frac{1 + \exp\left(\frac{c_{l_{lin}} - c_{l_{max}}}{\Delta c_{l_{stall}}}\right)}{1 + \exp\left(\frac{c_{l_{lin}} - c_{l_{max}}}{\Delta c_{l_{stall}}}\right)} \right)}{c_{l\alpha} \sqrt{1 - M^2}} \right] \quad (6.7)$$

with

$$\Delta c_{d_M} = 10(M - M_{crit})^3 \quad (6.8)$$

for  $M \geq M_{crit}$ , otherwise  $\Delta c_{d_M} = 0$

- For high Re turbulent flow ( $Re > 2.10^6$ ), the Reynolds scaling exponent lies in the range of  $-0.2 < f < -0.1$
- For low Re turbulent flow ( $2.10^5 < Re < 8.10^5$ ), the Reynolds scaling exponent lies in the range of  $-1.5 < f < -0.5$

- For laminar flow ( $Re < 1.10^5$ ), Reynolds scaling exponent lies in the range of  $-0.5 < f < -0.3$

With the blade section lift and drag coefficients computed, the local circulation is computed with the relation

$$\Gamma_i = \frac{1}{2} W_i c_i c_{l_i} \quad (6.9)$$

$\Gamma_i$  = local circulation  
 $W_i$  = Local effective velocity  
 $c_i$  = local section chord  
 $c_{l_i}$  = local section lift coefficients

After the convergence of the iteration, final circulation, induced velocities, local angle of attack are computed. Using these the propeller performance variables ( $T_{iso}$ ,  $Q_{iso}$ ) are calculated as a summation of these parameters from the hub section to the tip section. The section thrust and torque are expressed as given in Equations 6.10 and 6.11, respectively.

$$T_i^{iso} = B \frac{1}{2} \rho W_i^2 (c_{l_i} \cos \varphi - c_{d_i} \sin \varphi) c_i \Delta \eta_i R \quad (6.10)$$

$$Q_i^{iso} = B \frac{1}{2} \rho W_i^2 (c_{l_i} \sin \varphi + c_{d_i} \cos \varphi) c_i \Delta \eta_i R^2 \quad (6.11)$$

$$T_{iso} = \sum_{\eta=\eta_{hub}}^{\eta=\eta_{tip}} T_i^{iso} \quad (6.12)$$

$$Q_{iso} = \sum_{\eta=\eta_{hub}}^{\eta=\eta_{tip}} Q_i^{iso} \quad (6.13)$$

The thrust, torque coefficients and the propeller efficiency for the isolated configuration are computed from the steady state thrust and torque by the below relations.

$$C_{T_{iso}} = \frac{T_{iso}}{\rho n^2 D^4} \quad (6.14)$$

$$C_{Q_{iso}} = \frac{Q_{iso}}{\rho n^2 D^5} \quad (6.15)$$

$$\eta_{iso} = \frac{J}{2\pi} \frac{C_{T_{iso}}}{C_{Q_{iso}}} \quad (6.16)$$

### 6.2.2. PYLON-INSTALLED CONFIGURATION

The numerical model to estimate the propeller performance in the pylon-installed configuration is presented in this subsection. The installed propeller performance uses the numerical model formulated by Takallu [11, 30]. Computation of the propeller performance in the installed configuration is carried out in 6 steps:

- Computation of the wake behind the pylon
- Variation of blade section angle of attack during wake passage
- Calculation of unsteady section lift coefficients
- Estimation of unsteady drag coefficient
- Computation of section propeller performance to include effects of change in angle of attack and loss of dynamic pressure during the wake passage
- Prediction of time averaged and time accurate propeller performance

It is also assumed that the individual propeller blade sections are considered as flat plates. The propeller influence on the pylon wake is ignored during the computations.

### 1. Computation of wake behind the pylon

The wake behind the pylon is modelled using the classic similarity solution formulated by Schlichting [29] which is already discussed in Section 6.1. In chapter 3, it is observed that the pylon wake characteristics are influenced by the propeller. The negative pressure gradient in front of the propeller changes the wake displacement thickness, wake momentum thickness and the wake velocity deficit. However, in the present numerical model, it is assumed that the influence of propeller on the pylon wake is negligible.

### 2. Variation of blade section angle of attack during the wake passage

The variation of blade section angle of attack is obtained by assuming a sinusoidal variation of angle of attack in the wake. Steady analysis for two different velocities,  $U_1 = U_\infty$  and  $U_2 = U_{\min, \text{wake}}$  provides the angle of attack  $\alpha_1$  and  $\alpha_2$  for all blade sections. With  $\alpha_1$  and  $\alpha_2$  obtained, the angle of attack during the wake passage is given by :

$$\alpha(t) = \begin{cases} \alpha_1 & : \psi \leq \frac{\pi}{2} - \hat{\psi} \\ \alpha_0 + \Delta\alpha \sin \omega_f t & : \frac{\pi}{2} - \hat{\psi} < \psi < \frac{\pi}{2} + \hat{\psi} \\ \alpha_1 & : \psi > \frac{\pi}{2} + \hat{\psi} \end{cases}$$

with the

$$\Delta\alpha = \frac{\alpha_2 - \alpha_1}{2} \quad (6.17)$$

$$\alpha_0 = \frac{\alpha_2 + \alpha_1}{2} \quad (6.18)$$

The reduced frequency for any given section is given by :

$$\omega_f = \frac{\pi\omega}{\hat{\psi}} \frac{a_{\text{map}}}{U_1} \quad (6.19)$$

with the angle of wake encounter:

$$\hat{\psi} = \sin^{-1}\left(\frac{\delta}{\eta R}\right) \quad (6.20)$$

- $\alpha_1$  = angle of attack when the steady analysis is performed at  $U_1$
- $\alpha_2$  = angle of attack when the steady analysis is performed at  $U_2$
- $\alpha_0$  = mean of the angle of attacks when the steady analysis is performed at  $U_1$  and  $U_2$
- $\omega_f$  = reduced frequency
- $\hat{\psi}$  = angle of wake encounter
- $\psi$  = azimuthal angle
- $\eta$  = non-dimensional radial spanwise station
- $a_{\text{map}}$  = radius of mapped circle for the airfoil section
- $\delta$  = semi wake width
- $t$  = time

### 3. Calculation of unsteady section lift coefficients

Since the angle of attack for a local blade section varies in a sinusoidal manner through the wake, the circulation of blade section should include the effects of the unsteady variation of angle of attack. The methodology used to obtain the unsteady lift of individual blade sections is presented below. First, the equations for the flow around a circle are given. Subsequently, individual blade sections are assumed as flat plates resulting in simpler expressions for variation of unsteady lift during wake passage.

Since the flow around a circle can be computed easily, airfoil sections are mapped to a circle using Theodorsen's method of complex conformal transformation. The wake is modelled by vortices inside and outside of a unit circle. The complex potential is given by

$$F(\zeta) = U_\infty \left( \zeta \exp^{-i\alpha} + \frac{a_{\text{map}}^2}{\zeta} \exp^{i\alpha} \right) + \frac{i\Gamma a U_\infty}{2\pi} \ln \left( \frac{\zeta}{\alpha} \exp^{-i\alpha} \right) + i \int_{x_{te}}^{\infty} a_{\text{map}} \gamma \left[ \ln \left( \frac{\zeta}{a_{\text{map}}} \right) + \ln \left( \frac{\zeta}{a_{\text{map}}} - \rho_w \right) - \ln \left( \frac{\zeta}{a_{\text{map}}} - \frac{1}{\rho_w} \right) \right] dx \quad (6.21)$$

with  $\zeta = a_{\text{map}} \exp^{i\theta}$

Here  $\theta$  is the angular measure in  $\zeta$  plane (a perfect circle). From 6.21, the complex velocity in the  $\zeta$  plane is given by Equation 6.22.

$$w(\zeta) = i \exp^{-i\theta} \left[ 2 \sin(\theta - \alpha) + \frac{\Gamma}{2\pi} \int_{x_{te}}^{\infty} Q y dx \right] \quad (6.22)$$

with

$$Q = \frac{2(1 - \rho_w \cos \theta)}{(1 + \rho_w^2 - 2\rho_w \cos \theta)} \quad (6.23)$$

The transformation of perfect circle to an airfoil is obtained in two stages. First, a transformation from perfect circle to near circle by a theodorsen transformation ( $\hat{\zeta} = \hat{\zeta}(\zeta)$ ) followed by transformation from near circle to airfoil section by a Joukowski transformation ( $z = z(\hat{\zeta})$ ) given by Equation 6.24.

$$z = \hat{\zeta} + \frac{b_J^2}{\hat{\zeta}} \quad (6.24)$$

$b_J$  = Joukowski transformation parameter

$\zeta$  = perfect circle

$\hat{\zeta}$  = near circle

$z$  = plane of airfoil section

Since the instantaneous angle of attack varies in a sinusoidal manner, the circulation is expressed in the below form:

$$\Gamma(t) = \Gamma_0 + \Delta\alpha\Gamma_1 \cos(\omega_f t) + \Delta\alpha\Gamma_2 \sin(\omega_f t) + \text{Higher order terms} \quad (6.25)$$

The expression allows for any phase lag or lead in the circulation and hence lift. Higher order terms are neglected as the velocity deficit in the wake is small compared to the freestream velocity and hence the change in angle of attack  $\Delta\alpha$  as well. Hence, terms involving  $(\Delta\alpha)^2$  and higher order terms are neglected. As the airfoil moves forward, the trailing vortices are left behind and hence The trailing vorticity is related to the bound circulation by Equations 6.27 and 6.28 [34].

$$\gamma(t) = \Delta\alpha\gamma_1 \cos(\omega_f t) + \Delta\alpha\gamma_2 \sin(\omega_f t) \quad (6.26)$$

$$\gamma_1 = -\omega_f \left[ \Gamma_1 \sin(\omega_f(x - x_{te})) + \Delta\alpha\Gamma_2 \cos(\omega_f(x - x_{te})) \right] \quad (6.27)$$

$$\gamma_2 = \omega_f \left[ \Gamma_1 \cos(\omega_f(x - x_{te})) - \Delta\alpha\Gamma_2 \sin(\omega_f(x - x_{te})) \right] \quad (6.28)$$

$$T = \left[ \frac{d\zeta}{d\hat{\zeta}} \cdot \frac{d\hat{\zeta}}{dz} \right] \quad (6.29)$$

Using the Equations 6.22, 6.21, 6.26,6.27, 6.28, 6.25, 6.24, 6.29 and the flat plate assumption, the steady and unsteady components of lift are calculated and given by Equations 6.30, 6.31 and 6.32 respectively.

$$c_l^{SS}(\eta) = c_{l_0} = 2\pi \sin(\alpha_0) \quad (6.30)$$

$$c_{l_1}(\eta, \phi) = -\frac{\omega_f C u_0 \cos(\alpha_0)}{\left(\frac{1}{2\pi} - \omega_f S u_0\right)^2 + (\omega_f C u_0)^2} \quad (6.31)$$

$$c_{l_2}(\eta, \phi) = -\frac{\left(\frac{1}{2\pi} - \omega_f S u_0\right) \cos(\alpha_0)}{\left(\frac{1}{2\pi} - \omega_f S u_0\right)^2 + (\omega_f C u_0)^2} \quad (6.32)$$

with

$$C u_0 = -4 \int_0^{-\infty} \frac{\cos(\omega_f(x-2))}{x-2 + \sqrt{x^2-4}} dx \quad (6.33)$$

with

$$Su_0 = -4 \int_0^{-\infty} \frac{\sin(\omega_f(x-2))}{x-2 + \sqrt{x^2-4}} dx \quad (6.34)$$

A discrepancy is observed between the steady state lift coefficients obtained using the method mentioned above and predicted using XROTOR. It was decided to use the steady state lift coefficient computed from XROTOR in the final expression for lift coefficient due to its accuracy.

$$c_l^{US}(\eta, \phi) = c_{l_0}^{SS, XROTOR}(\eta) + \Delta\alpha c_{l_1}(\eta, \phi) \cos(\omega_f t) + \Delta\alpha c_{l_2}(\eta, \phi) \sin(\omega_f t) \quad (6.35)$$

where  $c_{l_1}(\eta, \phi), c_{l_2}(\eta, \phi)$  are given by Equations 6.31 and 6.32 respectively.

The change in lift coefficient of during the wake passage is obtained by below equation

$$\Delta c_l(\eta, \phi) = c_l^{US}(\eta, \phi) - c_{l_0}^{SS, XROTOR}(\eta) \quad (6.36)$$

The above expression for change in lift coefficient includes the effect of change in angle of attack and reduced dynamic pressure. Hence,

$$\Delta c_l^{\Delta Q, \Delta\alpha}(\eta, \phi) = c_l^{US}(\eta, \phi) - c_{l_0}^{SS, XROTOR}(\eta) \quad (6.37)$$

#### 4. Estimation of unsteady drag coefficient

Wake ingestion on to the propeller results in a loss of dynamic pressure and increase in angle of attack locally resulting a variation of drag coefficient locally in the wake region. It is assumed that the isolated drag coefficient for a radial station is constant over one full rotation and hence neglecting Reynolds number effects. Also, the induced velocities for a radial section are constant over one full rotation. The velocity at any radial station for the isolated case is the square root of the sum of squares of the axial and tangential velocities.

$$U_{ISO}(\eta) = \sqrt{[(U_\infty + U_a(\eta))^2 + (\Omega\eta R - U_t(\eta))^2]} \quad (6.38)$$

- $U_\infty$  = freestream velocity
- $U_{ISO}(\eta)$  = Effective velocity as a function of radial location
- $U_a(\eta)$  = Axial induced velocity as a function of radial location
- $U_t(\eta)$  = tangential induced velocity as a function of radial location
- $\Omega$  = rotational velocity in revs/sec

With the installation of a pylon, the axial component of velocity has a deficit during the wake passage resulting in reduced dynamic pressure. Hence, the effective velocity for the installed configuration is given by Equation 6.39 as function of  $\eta$  and  $\phi$ .

$$U_{INS}(\eta, \phi) = \sqrt{[(U_\infty + U_a(\eta) + \Delta V_{wake}(\eta, \phi))^2 + (\Omega\eta R - U_t(\eta))^2]} \quad (6.39)$$

From Equations 6.38 and 6.39, the effect of reduction in dynamic pressure as a function of azimuthal angle for the drag and lift coefficient is given by Equations 6.40 and 6.43.

$$c_d^{US}(\eta, \phi) = c_d^{SS}(\eta) \left[ \frac{U_{INS}^2(\eta, \phi)}{U_{ISO}^2(\eta)} \right] \quad (6.40)$$

$$\Delta c_d^{\Delta Q} = c_d^{US}(\eta, \phi) - c_d^{SS}(\eta) \quad (6.41)$$

The change of drag coefficient with change in angle of attack is neglected.

$$\Delta c_d^{\Delta\alpha} = 0 \quad (6.42)$$

Similarly, the effect of reduced dynamic pressure on the lift coefficient is given by Equation 6.44. This equation is used to evaluate the effects of reduced dynamic pressure on the propeller performance whereas Equation 6.37 evaluates the effect of both reduced dynamic pressure and angle of attack.

$$c_l^{US}(\eta, \phi) = c_l^{SS}(\eta) \left[ \frac{U_{INS}^2(\eta, \phi)}{U_{ISO}^2(\eta)} \right] \quad (6.43)$$

$$\Delta c_l^{\Delta Q} = c_l^{\text{US}}(\eta, \phi) - c_l^{\text{SS}}(\eta) \quad (6.44)$$

### 5. Computation of propeller performance to include effects of change in angle of attack and loss of dynamic pressure during the wake passage

After computing the unsteady section lift coefficient and unsteady drag coefficient, the propeller performance is computed for the following cases:

- Including the effect of change in angle of attack and dynamic pressure during the wake passage (referred as  $\Delta\alpha$  and  $\Delta Q$  effects).
- Including the effect of change in angle of attack during the wake passage (referred as  $\Delta\alpha$  effects).
- Including the effect of change in dynamic pressure during the wake passage (referred as  $\Delta Q$  effects).

All the effects are calculated from Equations 6.45 and 6.46 where  $c_{l_i}^{\text{US}}(\eta)$  and  $c_{d_i}^{\text{US}}(\eta)$  for given radial station depend on the case under consideration

$$T_i^{\text{INS}} = \frac{1}{2} \rho (W_i)^2 (c_{l_i}^{\text{US}}(\phi) \cos \phi - c_{d_i}^{\text{US}}(\phi) \sin \phi) c_i \Delta \eta_i R \quad (6.45)$$

$$Q_i^{\text{INS}} = \frac{1}{2} \rho (W_i)^2 (c_{l_i}^{\text{US}}(\phi) \sin \phi + c_{d_i}^{\text{US}}(\phi) \cos \phi) c_i \Delta \eta_i R^2 \quad (6.46)$$

#### Case 1: $\Delta\alpha$ and $\Delta Q$ effects

The unsteady lift and drag variation for the case  $\Delta\alpha$  and  $\Delta Q$  effects (including the effect of increase in angle of attack and reduced dynamic pressure) are given by Equations 6.47 and 6.48 respectively.

$$c_{l_i}^{\text{US}}(\phi) = c_i^{\text{SS, XROTOR}} + \Delta c_{l_i}^{\Delta Q, \Delta\alpha}(\phi) \quad (6.47)$$

$$c_{d_i}^{\text{US}}(\phi) = c_{d_i}^{\text{SS}} + \Delta c_d^{\Delta\alpha}(\phi) + \Delta c_d^{\Delta Q}(\phi) \quad (6.48)$$

#### Case 2: $\Delta\alpha$ effects

The unsteady lift and drag variation for the case  $\Delta\alpha$  effects (including the effect of increase in angle of attack) are given by Equations 6.49 and 6.50 respectively.

$$c_{l_i}^{\text{US}}(\phi) = c_i^{\text{SS, XROTOR}} + \Delta c_{l_i}^{\Delta Q, \Delta\alpha}(\phi) - \Delta c_l^{\Delta Q} \quad (6.49)$$

$$c_{d_i}^{\text{US}}(\phi) = c_{d_i}^{\text{SS}} + \Delta c_d^{\Delta\alpha}(\phi) \quad (6.50)$$

#### Case 3: $\Delta Q$ effects

The unsteady lift and drag variation for the case  $\Delta Q$  effects (including the effect of reduced dynamic pressure) are given by Equations 6.51 and 6.52 respectively.

$$c_{l_i}^{\text{US}}(\phi) = c_i^{\text{SS, XROTOR}} + \Delta c_l^{\Delta Q} \quad (6.51)$$

$$c_{d_i}^{\text{US}}(\phi) = c_{d_i}^{\text{SS}} + \Delta c_d^{\Delta Q}(\phi) \quad (6.52)$$

### 6. Prediction of time accurate and time averaged propeller performance

The time accurate performance for a single blade is computed as a summation of thrust/torque generated as a function of azimuthal angle by individual blade sections. The summation is performed from hub to the tip station. The installed thrust and torque generated by single blade as a function of azimuthal angle is given by Equations 6.53 and 6.54 respectively.

$$T_{\text{INS, 1B}}(\phi) = \sum_{\eta=\eta_{\text{hub}}}^{\eta=\eta_{\text{tip}}} T_i^{\text{INS}}(\phi) \quad (6.53)$$

$$Q_{\text{INS, 1B}}(\phi) = \sum_{\eta=\eta_{\text{hub}}}^{\eta=\eta_{\text{tip}}} Q_i^{\text{INS}}(\phi) \quad (6.54)$$

The time accurate thrust/torque generated by propeller is computed as a summation of the thrust/torque generated by individual blades separated by an angle of 45 degrees.

$$T_{\text{INS}}(\phi) = \sum_{i=1}^{i=B} T^{\text{INS},1B}(\phi - (i-1)\frac{2\pi}{B}) \quad (6.55)$$

$$Q_{\text{INS}}(\phi) = \sum_{i=1}^{i=B} Q^{\text{INS},1B}(\phi - (i-1)\frac{2\pi}{B}) \quad (6.56)$$

The time accurate performance coefficients are computed by non-dimensionalising the thrust and torque generated by the propeller. Subsequently the efficiency is computed by using the thrust and torque coefficient.

$$C_{T_{\text{INS}}}(\phi) = \frac{T_{\text{INS}}(\phi)}{\rho n^2 D^4} \quad (6.57)$$

$$C_{Q_{\text{INS}}}(\phi) = \frac{Q_{\text{INS}}(\phi)}{\rho n^2 D^5} \quad (6.58)$$

$$\eta_{\text{INS}}(\phi) = \frac{J}{2\pi} \frac{C_{T_{\text{INS}}}(\phi)}{C_{Q_{\text{INS}}}(\phi)} \quad (6.59)$$

After the computation of time accurate propeller performance, the time averaged propeller performance is calculated by averaging the time accurate performance.

$$C_{T_{\text{INS}}} = \frac{\overline{(T_{\text{INS}}(\phi))}}{\rho n^2 D^4} \quad (6.60)$$

$$C_{Q_{\text{INS}}} = \frac{\overline{(Q_{\text{INS}}(\phi))}}{\rho n^2 D^5} \quad (6.61)$$

$$\eta_{\text{INS}} = \frac{J}{2\pi} \frac{C_{T_{\text{INS}}}}{C_{Q_{\text{INS}}}} \quad (6.62)$$

## 6.3. PROPELLER TONAL NOISE EMISSIONS

Propeller noise generating mechanisms can be classified into three categories: harmonic, broadband and narrow band noise. Harmonic noise as the name suggests is a periodic noise which can be identified by discrete frequencies as a multiple of blade passage frequency. Broadband noise is random in nature and contains different frequency components as a continuous spectrum. Narrow-band noise is close to periodic; the signal may appear periodic but does not repeat with time. In case of full-scale propellers in flight, harmonic noise sources dominates other noise sources [35]. Hence, a numerical model to estimate the propeller noise here contains only the harmonic noise sources. The numerical model dealt here comes in the category of frequency domain methods which eliminates the dependency of time in the equations considered. Here, Hanson's method of estimating propeller harmonic noise using the blade geometry, operating conditions and loading distributions is presented [2, 28, 37]. The current section presents the numerical model used to estimate the propeller noise emissions in both isolated and installed configurations. First, the numerical model used to estimate propeller harmonic noise for the isolated configuration is dealt in Subsection 6.3.1 and later the analytical model used to predict the propeller noise emissions in the pylon installed configuration is presented in Subsection 6.3.2.

### 6.3.1. ISOLATED CONFIGURATION

This subsection deals with the prediction of tonal noise levels for the propeller in the isolated configuration. Frequency domain methods formulated by Hanson [37] to estimate propeller harmonic noise are presented here. This method assumes that the loading and thickness noise sources act on the advance helix which translates and rotates simultaneously. The aerodynamic loading which is used as an input to determine the harmonic noise levels is obtained from performance computations. The sound radiation is calculated by transferring the loading and thickness sources to the advanced helix. After modelling the loading and thickness sources and Fourier transforming the resultant equations, the far field pressure is obtained is given by Equation 6.63.

$$p(t) = \sum_{m=-\infty}^{\infty} P_{mB} e^{-imB\Omega t} \quad (6.63)$$

where  $P_{mB}$  represents the Fourier transform of the pressure at the  $m^{\text{th}}$  harmonic which is due to the summation of effects of loading and thickness noise and  $B$  denotes the number of blades.

$$P_{mB} = P_{V_m} + P_{D_m} + P_{L_m} \quad (6.64)$$

The noise harmonics are given by :[37]

$$\begin{bmatrix} P_{V_m} \\ P_{D_m} \\ P_{L_m} \end{bmatrix} = \frac{\rho a_\infty^2 B D_{\text{prop}}}{16\pi R_{\text{obs}} (1 - M_\infty \cos \theta)} e^{imB \left( \frac{\Omega D_{\text{prop}} R_{\text{obs}}}{a_\infty} - \frac{\pi}{2} \right)} \int_{\eta_{\text{hub}}}^1 M_r^2 e^{i(\phi_o + \phi_s)} J_{mB} \left( \frac{mB\eta M_t \sin \theta}{1 - M_\infty \cos \theta} \right) \begin{bmatrix} 2k_x^2 t_b \psi_V(k_x) \\ ik_x c_{f_1} \psi_D(k_x) \\ ik_y c_{f_2} \psi_L(k_x) \end{bmatrix} d\eta$$

with wave numbers  $k_x$  and  $k_y$  given by:

$$k_x = \frac{2M_t}{M_r} \left[ \frac{mB}{1 - M_\infty \cos \theta} \right] \frac{c}{D_{\text{prop}}} \quad (6.65)$$

$$k_y = \frac{-2}{\eta M_r} \left[ \frac{mB(M_r^2 \cos \theta - M_\infty)}{1 - M_\infty \cos \theta} \right] \frac{c}{D_{\text{prop}}} \quad (6.66)$$

and the phase shift due to the sweep and blade offset are given by:

$$\phi_o = \frac{2}{\eta M_r} \left[ \frac{mB(M_r^2 \cos \theta - M_\infty)}{1 - M_\infty \cos \theta} \right] \frac{FA}{D_{\text{prop}}} \quad (6.67)$$

$$\phi_s = \frac{2M_t}{M_r} \left[ \frac{mB}{1 - M_\infty \cos \theta} \right] \frac{MCA}{D_{\text{prop}}} \quad (6.68)$$

- $\rho_\infty$  = air density
- $a_\infty$  = speed of sound
- $B$  = No of blades
- $D_{\text{prop}}$  = propeller diameter
- $R_{\text{obs}}$  = observer distance
- $M_\infty$  = freestream Mach number
- $\theta$  = flyover angle
- $m$  = harmonic number
- $\phi_o$  = phase shift due to the blade offset
- $\phi_s$  = phase shift due to the blade sweep
- $\eta$  = non-dimensional radial station
- $M_t$  = tip Mach number
- $M_r$  = local radial section Mach number
- $J_{mB}$  = Bessel function of the first kind of order  $mB$
- $k_x, k_y$  = non-dimensional wave numbers
- $t_b$  = local blade thickness to chord ratio
- $c_{f_1}$  = local blade section drag coefficient corrected for induced effects
- $c_{f_2}$  = local blade section lift coefficient corrected for induced effects
- $\psi_D$  = frequency domain distributions for drag
- $\psi_L$  = frequency domain distributions for lift
- $\psi_V$  = frequency domain distributions for thickness
- $FA$  = distance from blade section normal to the blade planform
- $MCA$  = distance between local mid chord point and the pitch change axis

The thickness and chord-wise loading distributions are given in terms of their Fourier transforms:

$$\begin{bmatrix} \psi_V \\ \psi_D \\ \psi_L \end{bmatrix} = \begin{bmatrix} H(x) \\ f_D(x) \\ f_L(x) \end{bmatrix} \int_{-\frac{1}{2}}^{\frac{1}{2}} e^{ik_x x} dx$$

The above equations are only applicable in the far-field. The  $\psi_D$  and  $\psi_L$  represent the non-compactness of chordwise loading. It is the measure of interference of signals of various noise sources along the chord.

However, it is assumed that the chordwise non-compactness is uniform across the chord which is a valid assumption for low wave number  $k_x$ . The effect of non-compactness is considered negligible [10]. Sweep introduces a lag between various signals emitted across the blade span and thereby reduces the effective noise. The effect of sweep and blade offset is considered negligible for the current project. The loading distributions obtained from XROTOR are calculated by considering the induced effects. Hence, the direction of the loading on the local blade section should consider the shift in advance angle due to the induced axial and tangential velocities.

The overall sound pressure levels calculated over all harmonics is given by:

$$SPL_{mB} = 10 \log_{10} \left( \frac{2P_{mB} \overline{P_{mB}}}{p_0^2} \right) \quad (6.69)$$

with  $p_0$  the acoustic reference pressure of 20 $\mu$ Pa

### 6.3.2. PYLON-INSTALLED CONFIGURATION

The effect of installation introduces a new noise source due to the unsteady loading on the blades. The methodology of estimation of noise emissions for the installed propeller is similar to the isolated propeller except for the introduction of non-uniform loading. The noise harmonics for the pylon installed configuration are derived by Hanson [28]. The original equations are defined for a counter-rotating propeller configuration. However, these equations can be used by simplifying the original equations by considering the front rotor as stationary with one blade (acting as pylon here). Hence the upstream field is considered non-rotating with fixed distortion.

$$\begin{bmatrix} P_{D_m} \\ P_{L_m} \end{bmatrix} = \frac{\rho a_\infty^2 B D_{\text{prop}}}{16\pi R_{\text{obs}} (1 - M_\infty \cos \theta)} e^{i \left( \frac{mB\Omega D_{\text{prop}} R_{\text{obs}}}{a_\infty} + (mB-k)(\phi - \frac{\pi}{2}) \right)} \int_{\eta_{\text{hub}}}^1 M_r^2 e^{i(\phi_o + \phi_s)} J_{mB-k} \left( \frac{mB\eta M_t \sin \theta}{1 - M_\infty \cos \theta} \right) \begin{bmatrix} i k_x c_{f_1} \psi_D(k_x) \\ i k_y c_{f_2} \psi_L(k_x) \end{bmatrix} d\eta$$

with wave numbers given by below equations:

$$k_x = \frac{2M_t}{M_r} \left[ \frac{mB}{1 - M_\infty \cos \theta} - k \right] \frac{c}{D_{\text{prop}}} \quad (6.70)$$

$$k_y = \frac{-2}{\eta M_r} \left[ \frac{mB(M_r^2 \cos \theta - M_\infty)}{1 - M_\infty \cos \theta} + k M_\infty \right] \frac{c}{D_{\text{prop}}} \quad (6.71)$$

and phase shift due to the sweep and blade offset are given by:

$$\phi_o = \frac{2}{\eta M_r} \left[ \frac{mB(M_r^2 \cos \theta - M_\infty)}{1 - M_\infty \cos \theta} + k M_\infty \right] \frac{FA}{D_{\text{prop}}} \quad (6.72)$$

$$\phi_s = \frac{2M_t}{M_r} \left[ \frac{mB}{1 - M_\infty \cos \theta} - k \right] \frac{MCA}{D_{\text{prop}}} \quad (6.73)$$

The loading harmonics from the performance computations are used as an input to evaluate the unsteady loading noise levels at blade passage frequency. The shift in loading direction due to the induced effects is to be considered in this analysis as well.



# 7

## NUMERICAL RESULTS: PYLON WAKE PROFILES

Numerical prediction of the performance and noise emissions for the pylon-installed configuration requires the computation of the pylon wake profiles. This chapter first presents an overview of the analytical model to determine the wake velocity profiles in Section 7.1. Then, the computed pylon-wake profiles which serves as an input for propeller performance and noise emissions is treated in Section 7.2.

### 7.1. OPERATING CONDITIONS

The wake profiles are computed using the Schlichting wake model presented in Chapter 6. The pylon drag coefficient is computed using XFOIL for a pylon angle of attack of zero degrees and Reynolds number based on the freestream velocity. Note that the transition point is free on both sides of the pylon and it is calculated by using XFOIL for NACA 0012 airfoil. The wake width and velocity deficit are calculated for a range of freestream velocities and pylon-propeller spacings as given in Table 7.1.

**Table 7.1:** Summary of the various operating conditions used to wake determine velocity profiles.

Parameter	Symbol	Value	Unit
Freestream velocity	$U_\infty$	[18,26,50]	m/s
Pylon-propeller spacing	$\Delta X$	$[10-100] * \frac{D_{prop}}{100}$	-
Pylon drag coefficient	$c_{d_{pylon}}$	[0.00702 0.02 0.03 0.04]	-
Angle of attack	$\alpha$	0	deg
Angle of sideslip	$\beta_{SS}$	0	deg
Empirical constant	$\beta$	0.18	-
pylon chord length	$c_{pylon}$	0.3	m
kinematic viscosity of air	$\nu$	$1.5 \times 10^{-6}$	$m^2/s$

### 7.2. PYLON WAKE PROFILES

First, the computed pylon wake profiles for a range of freestream velocities (7.2.1) and pylon-propeller spacings (7.2.2) are presented in this section. Later, the effect of pylon drag coefficient on the wake profile is treated in Subsection 7.2.3

#### 7.2.1. EFFECT OF FREESTREAM VELOCITY

Wake profiles obtained at a constant freestream velocity depend on the Reynolds number at which they are computed. As the freestream velocity increases, Reynolds number of the flow increases and the drag coefficient of the pylon decreases. Since velocity deficit and wake width are dependent on  $c_d$  of the pylon from

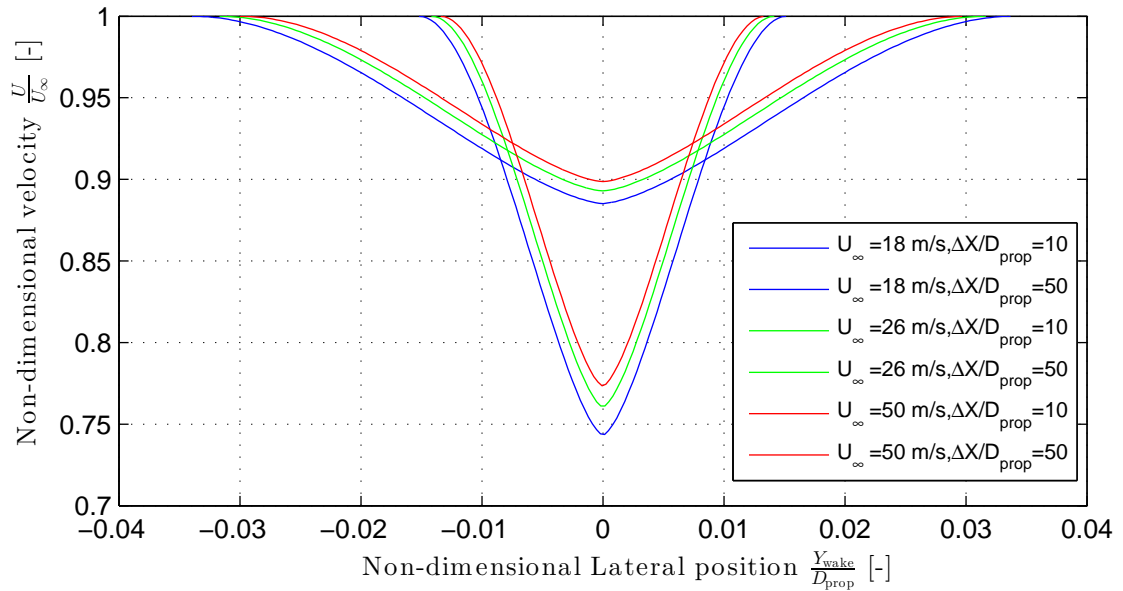
**Table 7.2:** Effect of freestream velocity at  $\Delta X = 0.1D_{prop}$ 

Freestream velocity $U_{\infty}$ [m/s]	Reynolds number $Re_c$ [-]	Drag coefficient $c_d$ [-]	Wake width $b_w$ [mm]	Non-dimensional velocity deficit $\frac{\Delta U}{U_{max}}$ [-]
18	$3.5 \times 10^5$	0.00702	9.1	0.25
26	$5.1 \times 10^5$	0.00611	8.5	0.23
50	$9.9 \times 10^5$	0.00547	8.0	0.22

**Table 7.3:** Effect of freestream velocity at  $\Delta X = 0.5D_{prop}$ 

Freestream velocity $U_{\infty}$ [m/s]	Reynolds number $Re_c$ [-]	Drag coefficient $c_d$ [-]	Wake width $b_w$ [mm]	Non-dimensional velocity deficit $\frac{\Delta U}{U_{max}}$ [-]
18	$3.5 \times 10^5$	0.00702	20.3	0.11
26	$5.1 \times 10^5$	0.00611	19.0	0.10
50	$9.9 \times 10^5$	0.00547	17.9	0.10

Equations 6.1 and 6.2, it is expected that the velocity deficit and the wake width decrease with increase in freestream velocity. The pylon wake velocity profiles are calculated for freestream velocities of 18, 26 and 50 m/s. The obtained drag coefficients for the associated Reynolds number along with wake characteristics are shown in Tables 7.2 and 7.3. The wake velocity profiles for  $\Delta X$  of are plotted in Figure 7.1.

**Figure 7.1:** Non-dimensional wake velocity profiles at different freestream velocities and pylon-propeller spacings.

$$U_{\infty} = [18 \ 26, 50] \text{ m/s}, \Delta X = [0.1 \ 0.5] D_{prop}$$

From Tables 7.2 and 7.3, it is observed that the increase in freestream velocity increases the Reynolds number and thereby decreases the drag coefficient. A decrease in drag coefficient results in a decrease in wake width and wake velocity deficit which is also observed in Figure 7.1.

### 7.2.2. EFFECT OF PYLON-PROPELLER SPACING

The distance between the pylon and the propeller is one of the parameters which affects the propeller performance and noise emissions. The current subsection treats the pylon wake profiles for a range of pylon-propeller spacings between 0.05-1 times the diameter of propeller at a freestream velocity of 18 m/s. The pylon wake profiles are plotted in Figure 7.2.

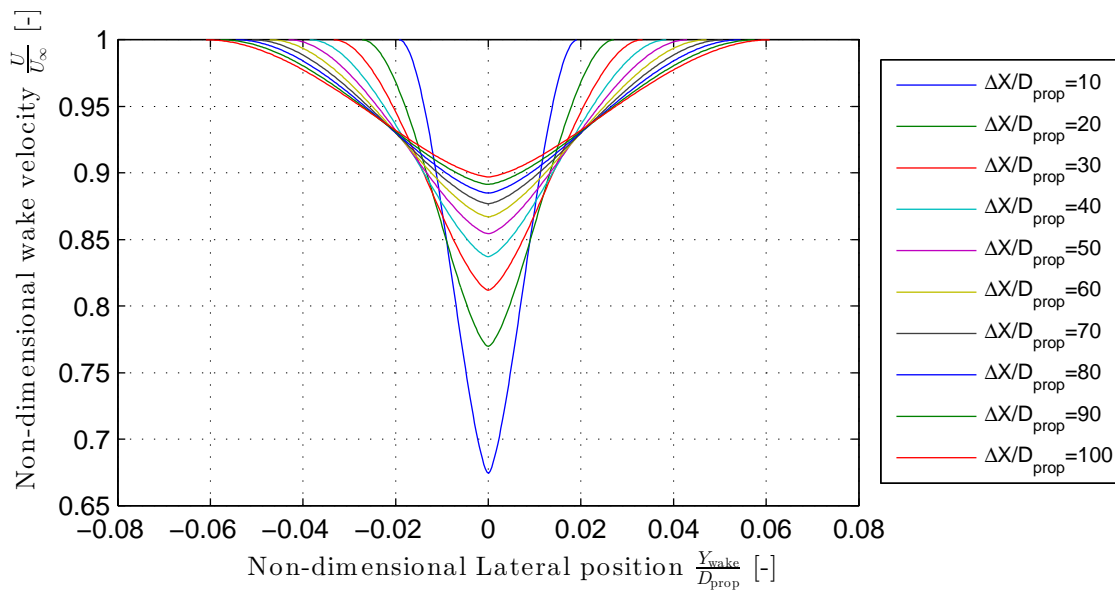


**Figure 7.2:** Non-dimensional wake velocity profiles for different pylon-propeller spacings.  
 $U_\infty = 18 \text{ m/s}$ ,  $\Delta X = [0.1-1]D_{prop}$

From Figure 7.2, it is observed that the non-dimensional wake width and velocity deficit increase and decrease respectively with increase in pylon-propeller spacing. The decay of velocity deficit and increase in wake width is plotted in Figure 7.3.

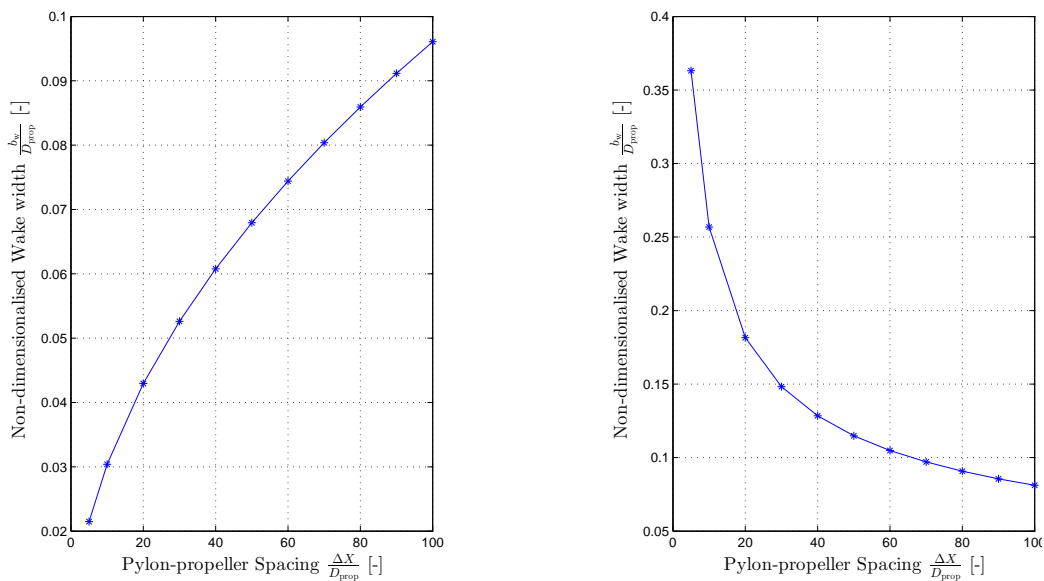


**Figure 7.3:** Variation of wake width and velocity deficit with pylon-propeller spacing.  
 $U_\infty = 18 \text{ m/s}$ ,  $\Delta X = [0.05-1]D_{prop}$

### 7.2.3. EFFECT OF PYLON DRAG COEFFICIENT

To understand the sensitivity of pusher propeller performance and noise emissions for different upstream wake characteristics, the pylon drag coefficient is varied to generate wakes with distinct wakes. The current subsection treats the pylon wake profiles for a range of pylon-propeller spacings between 10%, 50% and 100%

of the diameter of the propeller, at a freestream velocity of 18 m/s. The drag coefficient of the pylon are 0.00702, 0.02, 0.03 and 0.04. The wake profiles generated for different operating conditions are plotted in Figure 7.4.

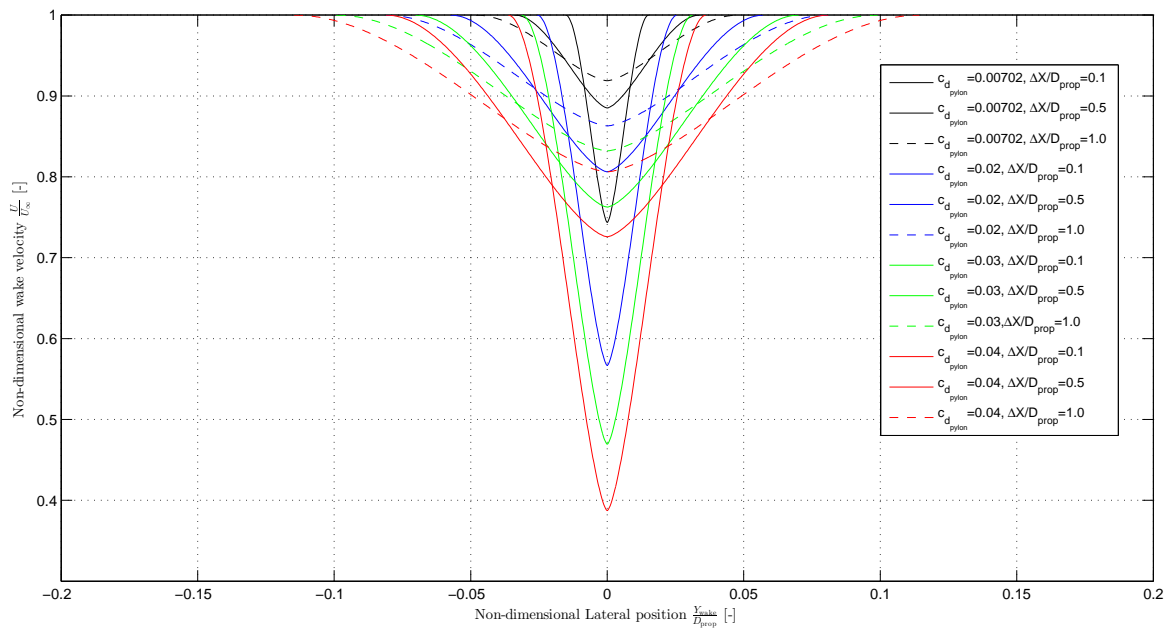


**Figure 7.4:** Effect of pylon drag coefficient on the wake velocity profiles.

$$U_{\infty} = 18 \text{ m/s}, \Delta X = [0.1 \ 0.5 \ 1] D_{\text{prop}}, c_{d_{\text{pylon}}} = [0.00702 \ 0.02 \ 0.03 \ 0.04]$$

Figure 7.4, shows that with increase in drag coefficient, the non-dimensional wake velocity deficit and wake width increases for the same pylon-propeller spacing. This is related to the increase in momentum deficit in the wake with increase in the drag coefficient of the pylon. Similar results are observed for different pylon-propeller spacings.

# 8

## NUMERICAL RESULTS: PROPELLER PERFORMANCE

To further understand the effects of an upstream wake on propeller performance, a numerical model to estimate the propeller performance in the installed configuration is presented in Chapter 6. The current chapter first presents the various operating conditions used to predict the propeller performance in Section 8.1. Subsequently, the propeller performance in isolated configuration and pylon-installed configuration are treated in Section 8.2 and 8.3 respectively. Finally, the effect of pylon spacing and wake sensitivity is dealt in Section 8.4 and Section 8.5 respectively.

### 8.1. OPERATING CONDITIONS

The propeller performance is computed using the analytical model given in Chapter 6. Different operating conditions are used to evaluate the propeller performance and a summary of it is presented in Table 8.1.

**Table 8.1:** Summary of operating conditions used to compute propeller performance

Parameter	Symbol	Value	Unit
Altitude	$h$	0	m
Freestream velocity	$U_\infty$	18	m/s
Advance ratio	$J$	[0.5-1.7]	-
Pylon-Propeller spacing	$\Delta X$	$[0.1-1]D_{\text{prop}}$	mm
Pylon drag coefficient	$c_d$	[0.00702 0.2 0.3 0.4]	-
Pylon azimuthal position	$\phi_{\text{pylon}}$	90	deg
angle of attack	$\alpha$	0	deg
angle of sideslip	$\beta_{SS}$	0	deg
blade rake	$\psi_{\text{rake}}$	0	deg
Pitch change axis position	$c_{\text{PCA}}$	0.4474	-
Nacelle perturbation axial velocity	$U_{\text{ind,nacelle}}$	0	m/s
Number of blade sections	$N_r$	17	-

### 8.2. ISOLATED CONFIGURATION

The propeller performance in the isolated configuration computed by running the matlab program (which uses XROTOR) is treated in this section. The propeller performance parameters thrust coefficient  $C_T$ , torque coefficient  $C_Q$ , and propeller efficiency  $\eta$  are plotted in Figure 8.1.

The propeller performance is evaluated at freestream velocity of 18 m/s, advance ratios lying in range between 0.5 and 1.7. Further, the blade section properties are evaluated from RFOIL and are provided as

input to XROTOR. The operating conditions selected here are also used during the experimental campaign at OJF and hence serve as a basis for comparison.

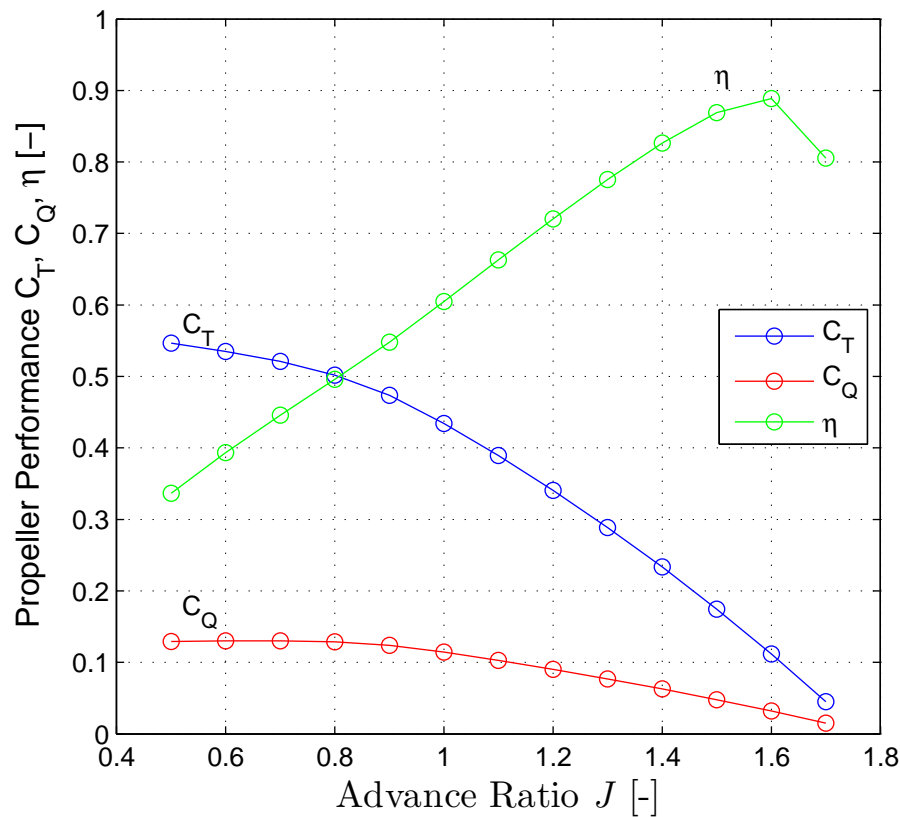


**Figure 8.1:** Propeller Performance diagram.  
Isolated configuration  $U_\infty = 18$  m/s,  $J = [0.5-1.7]$

From Figure 8.1, the thrust and torque coefficients vary linearly and non-linearly in the advance ratio range of 1-1.7 and 0.5-1, respectively. In the high advance ratio range, the lift response of the blade sections is linear and hence the thrust coefficient varies linearly. However at low advance ratios, the lift response of the blades is non-linear due to the onset of stall. The onset of stall is first triggered at the radial sections with  $\eta$  between 0.5 and 0.8 due to the high angle of attack experienced at these stations (Figure 8.3 shows small increments in  $c_l$  with change in advance ratio at these radial stations due to separated flow at  $J=0.5, 0.7$ ). At  $J = 1.7$ , the angle of attack across the radial span is close to zero. Decrease in advance ratio increases the local section angle of attack due to the increase in rotational velocity of the propeller and this can be seen in Figure 8.2. The maximum increase in the angle of attack is seen between  $\eta = 0.4$  and  $\eta = 0.7$ . The angle of attack at the inboard stations at high advance ratios is below zero indicating the inboard stations produce less lift (down force instead of lift is produced at  $J = 1.7$ ). The section lift distribution in Figure 8.3 shows the same.

The drag coefficient distribution is plotted in Figure 8.4. With decrease in advance ratio, drag coefficient first decreases before an increase is observed for all radial stations suggesting the range of angle of attack is within the drag bucket of the local airfoil section. Propeller efficiency shows a linear increase at all advance ratios except at advance ratio of 1.6 and 1.7. At these advance ratios, the lift generated at all radial stations is negligible and the high drag at inboard stations result in a low level thrust and consequently reducing the overall thrust coefficient and thereby reducing the propeller efficiency.

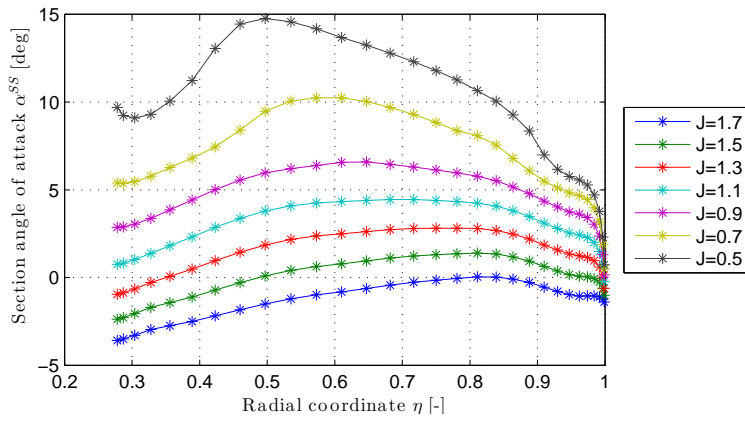


**Figure 8.2:** Radial angle of attack distribution .  
Isolated configuration:  $U_\infty = 18$  m/s,  $J = [0.5-1.7]$

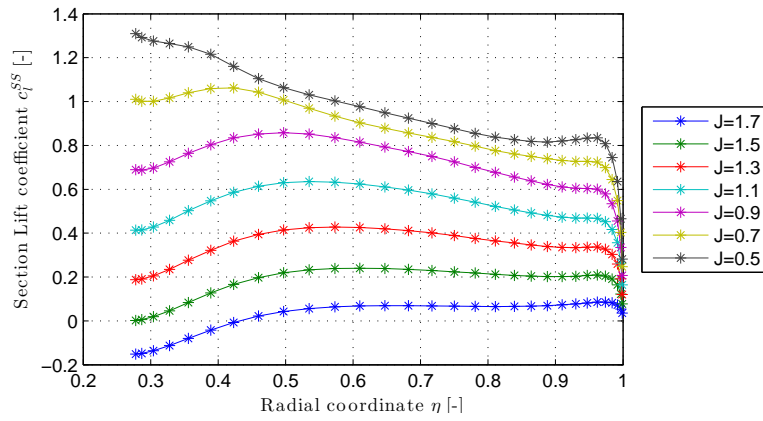


**Figure 8.3:** Radial Lift coefficient distribution.  
Isolated configuration:  $U_\infty = 18$  m/s,  $J = [0.5-1.7]$

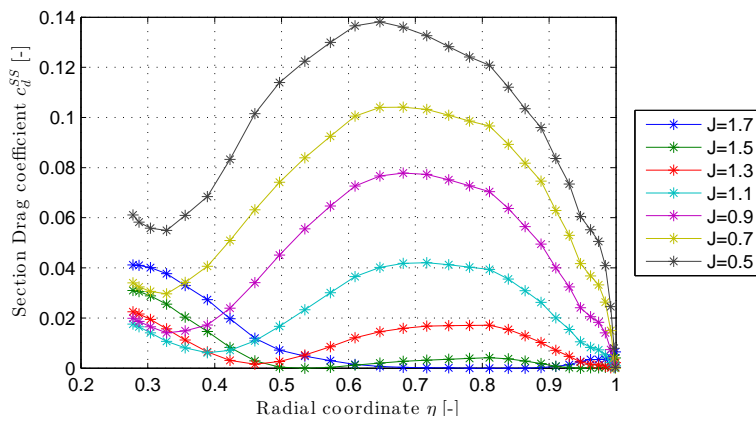


**Figure 8.4:** Radial Drag coefficient distribution.  
Isolated configuration:  $U_\infty = 18$  m/s,  $J = [0.5-1.7]$

### 8.3. PYLON-INSTALLED CONFIGURATION

To evaluate the effects of an upstream pylon wake on the pusher propeller performance, a numerical model is developed as mentioned in Chapter 6. The propeller performance results estimated for the pylon-installed configuration using the numerical model are presented in this section. First, the angle of attack distribution across the propeller blade is treated in Subsection 8.3.1. The angle of attack distribution in installed configuration which results in a loading distribution across the propeller blade is presented in Subsection 8.3.2. Later, the time accurate propeller performance is given in Subsection 8.3.3. Thereafter, the time averaged propeller performance for different advance ratios is dealt in Subsection 8.3.4. Finally, the effect of increase in angle of attack and reduced dynamic pressure in the wake on the time averaged propeller performance is detailed in Subsection 8.3.5. The propeller performance in this section is computed for a freestream velocity of 18 m/s, advance ratio of 0.5-1.7 and for a pylon-propeller spacing of 10%-100% of the diameter of the propeller.

#### 8.3.1. ANGLE OF ATTACK DISTRIBUTION

The wake velocity distribution obtained by assuming a Schlichting wake model is already shown in Chapter 7. The velocity deficit in the wake results in an increase in the angle of attack of the propeller blade during the wake passage. The propeller angle of attack during the wake passage is determined by assuming a sinusoidal distribution of angle of attack as defined in Chapter 6. The sinusoidal distribution is obtained by determining the mean of the angle of attack distribution at freestream and wake centreline velocity. The angle of attack distribution treated in this subsection is at an advance ratio of 1.0 and freestream velocity of 18 m/s. To assess the time accurate performance of the propeller, the increase in the angle of attack during the wake passage is determined and is plotted in Figure 8.5.

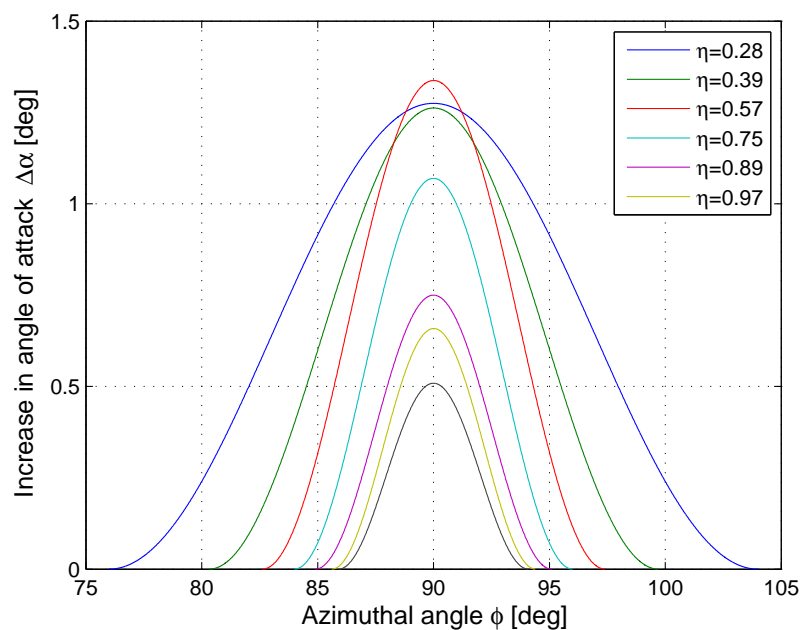


**Figure 8.5:** Increase in the angle of attack during wake passage .  
Pylon Installed configuration  $U_\infty = 18$  m/s,  $J = 1.0$ ,  $\Delta X = 50\% D_{prop}$

Figure 8.5 shows a sinusoidal variation of angle of attack during the wake passage. The sinusoidal distribution for only a few radial sections is plotted for clarity. From Figure 8.5, a maximum increase in the angle of attack of 1.3 degrees is observed at radial section of  $\eta = 0.57$ . The presence of the wake is longer for inboard sections than at the outboard sections. This is due to the increased wake angle<sup>1</sup> for inboard stations. The wake angle for a radial station  $\eta = 0.27$  is around  $28^\circ$  when compared to wake angle of  $8^\circ$  for the radial section of  $\eta = 0.97$ . The increased angle of attack would result in an increased loading on the blade which is treated in the next subsection.

<sup>1</sup> Wake angle or angle of wake encounter: angle during which the propeller blade encounters the wake

### 8.3.2. LOADING DISTRIBUTION

#### Lift distribution

The increase in the angle of attack of the propeller blades during the wake passage results in a local increase in lift coefficient. Prediction method to estimate the variation of lift coefficient during the wake passage is described in Section 6.2.2. Potential flow analysis in the complex plane determines the section lift coefficient as a function of azimuthal angle. The loading distribution shown in this subsection are plotted for a freestream velocity of 18 m/s, advance ratio of 1.0 and pylon-propeller spacing of 50% of the diameter of propeller.

For the pylon installed configuration, the section lift coefficient during the wake passage should increase during the wake passage and then back to steady state value, similar to the angle of attack. To verify the variation of lift coefficient during the wake passage, unsteady section lift coefficients as function of azimuthal angle are plotted for different radial stations as shown in Figure 8.6.

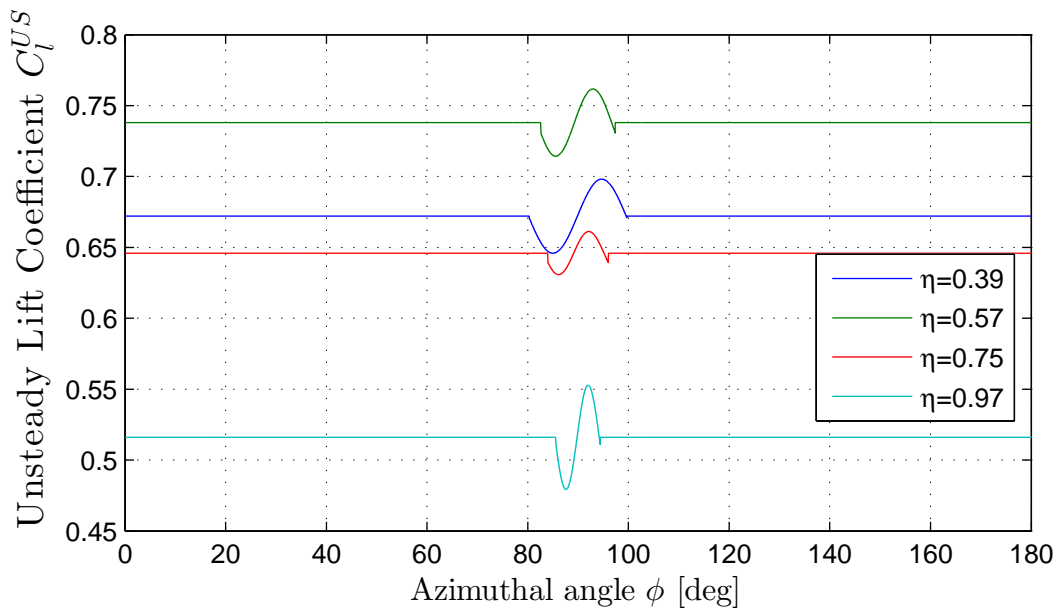


**Figure 8.6:** Variation of lift coefficient during the wake passage.  
Pylon Installed configuration  $U_\infty = 18$  m/s,  $J = 1.0$ ,  $\Delta X = 50\% D_{\text{prop}}$

From Figure 8.6, it is observed that the blade response during wake passage clearly shows a peak which is not at the center of wake, i.e. 90 degrees. This indicates the blade response due to the change of angle of attack is delayed. The delayed blade response is due to the time taken by the trailing vortices to induce a change in the angle of attack and thereby changing the lift coefficient. All the sections plotted in the figure showed a delayed response. The blade section response during the wake passage for all the sections shows the unsteady lift coefficient is lower than the steady lift coefficient for some azimuthal angles during the wake passage. This is due to the decrease in the effective angle of attack resulting from the downwash from the trailing vorticity. This is observed for all the propeller blade sections. To further investigate the blade response during the wake passage, the non dimensional lift coefficient is plotted against the non-dimensional angle of attack for the blade sections shown in Figure 8.7. The lift coefficient follows a hysteresis loop and the behaviour of each section depends on the reduced frequency of it. Also, the size of the loop and the orientation of the loop depends on the reduced frequency of the local section. The reduced frequency provides a measure of unsteadiness at a radial station and it depends on the local chord and the wake angle<sup>2</sup> of the blade section. Since the wake angle increases with decrease in radial coordinate and the chord distribution does not follow any trend with radial coordinate, the variation of reduced frequency or unsteadiness does not follow any trend with radial coordinate as well.

<sup>2</sup>Wake angle or angle of wake encounter: angle during which the propeller blade encounters the wake

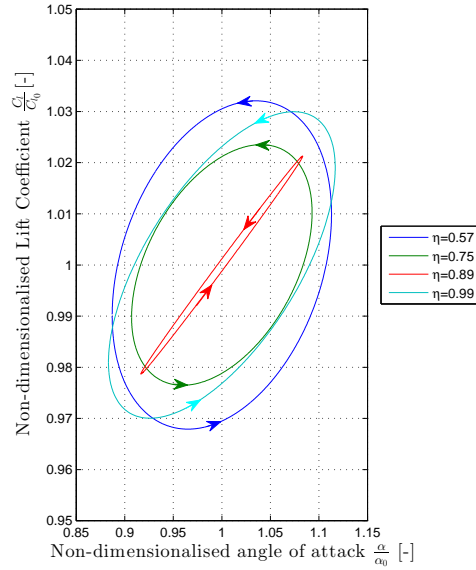


**Figure 8.7:** Normalised lift hysteresis for different propeller blade sections.  
Pylon Installed configuration  $U_\infty = 18$  m/s,  $J = 1.0$ ,  $\Delta X = 50\% D_{prop}$

### Drag distribution

Installation of pylon upstream effects the drag on the propeller blade during the wake passage. The effect of pylon on the drag coefficient is treated here. The change in drag coefficient due to the change in angle of attack is assumed to be negligible. The change in drag coefficient due to the reduced dynamic pressure in the wake is only considered. The operating condition of the propeller remains the same. The drag coefficient reduction during the wake passage is shown in Figure 8.8. The reduction in drag coefficient is dependent on the velocity deficit in the wake. The maximum reduction in drag coefficient is observed at the center of the wake as the velocity deficit is maximum here. The maximum reduction in drag coefficient is observed at the root section. With increase in distance from the center of the propeller, a decrease in reduction in drag coefficient is observed due to the higher effective velocity at the outermost radial stations. The velocity deficit only occupies a fraction of reduced dynamic pressure at the tip section when compared to the root sections where the velocity deficit in the wake reduces the dynamic pressure considerably.

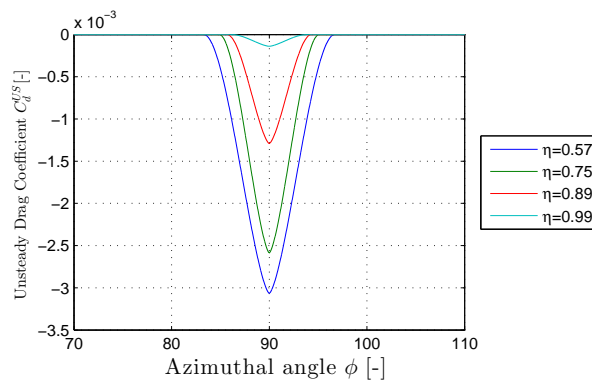


**Figure 8.8:** Variation of drag coefficient during the wake passage .  
Pylon Installed configuration  $U_\infty = 18$  m/s,  $J = 1.0$ ,  $\Delta X = 50\% D_{prop}$

### 8.3.3. TIME-ACCURATE PROPELLER PERFORMANCE

The installation of a pylon upstream results in a wake which would influence the propeller performance during the wake passage. The time accurate propeller performance as a function of azimuthal angle is treated in this subsection. Time accurate propeller performance for a freestream velocity of 18 m/s, advance ratio of 1.0 and a pylon-propeller spacing of 50% of the diameter of the propeller is presented here. Figures 8.9 and 8.10 plot the time accurate performance during one rotation. The wake signature on propeller thrust and torque coefficients is clearly seen in both the figures. The effect of installation is seen as change in propeller thrust coefficient from the steady state thrust coefficient. The eight peaks seen in the unsteady performance parameter corresponds to the number of blades.

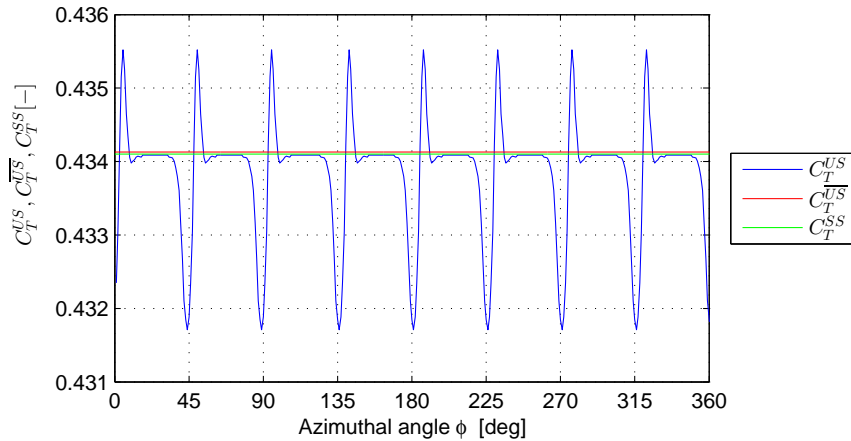


**Figure 8.9:** Unsteady thrust coefficient versus the azimuthal angle.  
Pylon-installed configuration:  $U_\infty = 18$  m/s,  $J = 1$ ,  $\Delta X = 50\% D_{prop}$

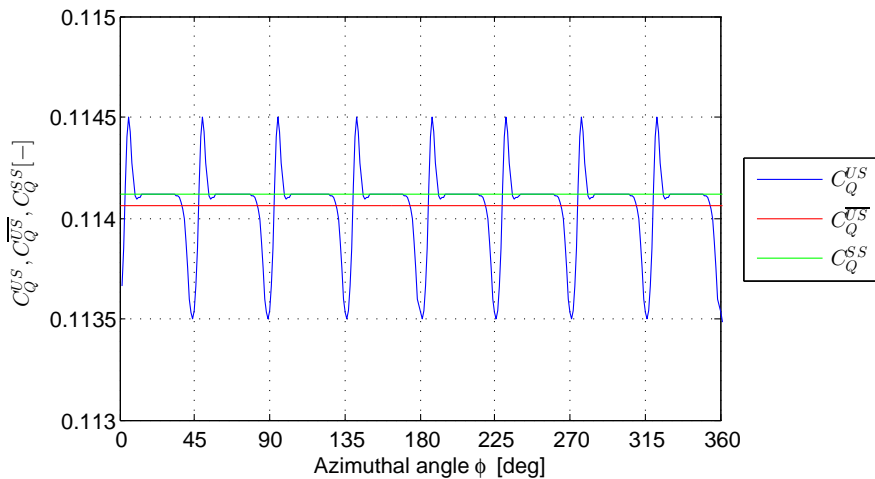


**Figure 8.10:** Unsteady torque coefficient versus the azimuthal angle.  
Pylon-installed configuration:  $U_\infty = 18$  m/s,  $J = 1$ ,  $\Delta X = 50\% D_{prop}$

The unsteady mean and steady mean (isolated) are also plotted in the same figure to show the time averaged impact of pylon on propeller performance. To understand the impact of installation, the propeller thrust and torque coefficients for both isolated and pylon-installed configurations is shown in Table 8.2. These results show that the effect of installation on the propeller performance is very small at the advance ratio of 1.0. A detailed analysis on the time averaged propeller performance across different advance ratios is dealt in next subsection.

**Table 8.2:** Installation impact on propeller performance.  
Pylon-installed configuration:  $U_\infty = 18$  m/s,  $J = 1$ ,  $\Delta X = 50\% D_{\text{prop}}$

Parameter [-]	Value [-]	Parameter [-]	Value [-]
$C_T^{\text{ISO}}$	0.4341	$C_Q^{\text{ISO}}$	0.1141
$\overline{C_T^{\text{INST}}}$	0.4343	$\overline{C_Q^{\text{ISO}}}$	0.1140
$100 \frac{\overline{C_T^{\text{INST}}} - \overline{C_T^{\text{ISO}}}}{\overline{C_T^{\text{ISO}}}}$	0.05	$100 \frac{\overline{C_Q^{\text{INST}}} - \overline{C_Q^{\text{ISO}}}}{\overline{C_Q^{\text{ISO}}}}$	-0.08

### 8.3.4. TIME-AVERAGED PROPELLER PERFORMANCE

The previous section showed the time accurate propeller performance in the pylon-installed configuration. In this subsection, the time averaged propeller performance computed by averaging the time accurate data is treated in this subsection. The propeller performance parameters are computed for a freestream velocity of 18 m/s, advance ratio range of 0.5-1.7 and for a pylon spacing of 50% of the diameter of the propeller. The computed data is shown in Figure 8.11. Also, the computed data for the isolated configuration is shown as it serves as a reference to compare both the configurations.

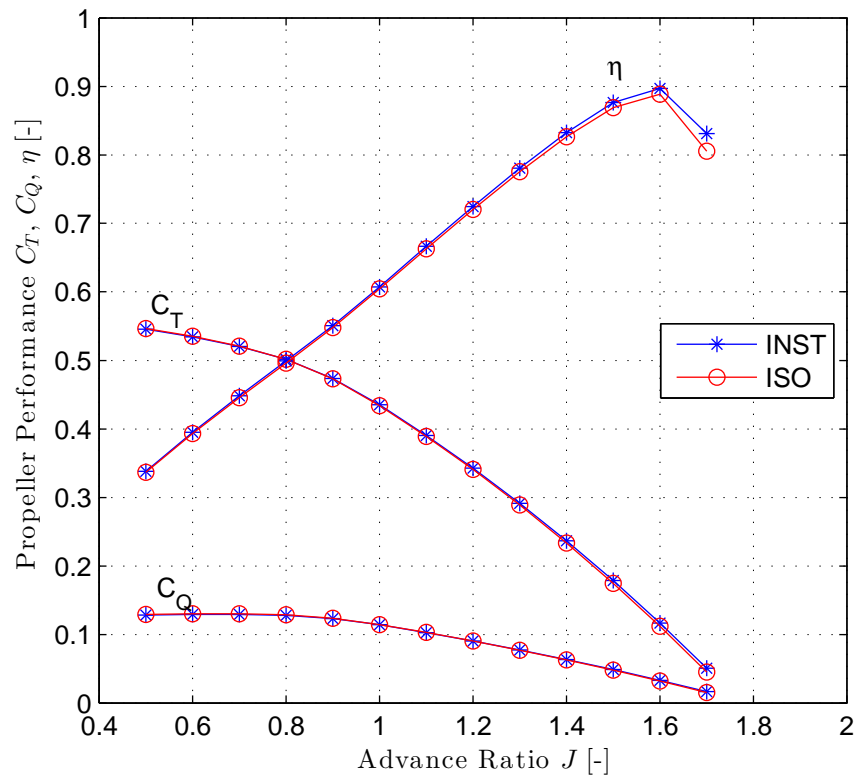


**Figure 8.11:** Propeller Performance diagram .  
Isolated and Pylon Installed configuration:  $U_\infty = 18$  m/s,  $J = [0.5-1.7]$ ,  $\Delta X = 50\% D_{\text{prop}}$

Figure 8.11 shows the effect of installation on the propeller performance is significant at only high advance ratios. At low advance ratios, the propeller performance showed negligible impact. The propeller performance shown accounts for the reduced dynamic pressure and increased angle of attack during the wake

passage. The reduced dynamic pressure case introduces a reduction in drag coefficient whereas the the lift coefficient includes both as it is obtained by potential method. To verify the effect of installation on the propeller performance, the relative difference between the performance parameters for the isolated and pylon installed configurations is calculated. The computed differences are plotted in Figure 8.12.

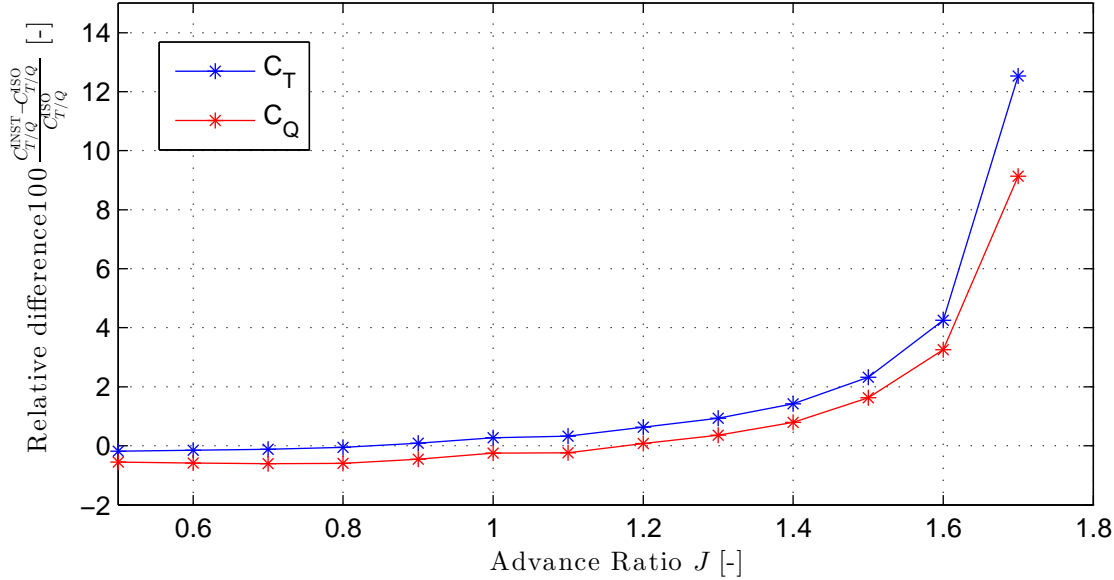


**Figure 8.12:** Effect of Installation on the thrust and torque coefficient.  
Pylon-installed configuration:  $U_\infty = 18$  m/s,  $J = [0.5-1.7]$ ,  $\Delta X = 50\% D_{\text{prop}}$

From Figure 8.12, the installation effect on both thrust and torque coefficients showed a decrease at low advance ratios. This is due to the effect of reduced dynamic pressure dominating the effect of increased angle of attack. At high advance ratios, ranging from 1.0-1.7, the effect of increased angle of attack dominated the effect of reduced dynamic pressure and thereby showing a net increase in thrust and torque coefficient. To show the effect of individual parameters (dynamic pressure and angle of attack), the propeller performance parameters are computed for different cases such as only reduced dynamic pressure effect with no change in angle of attack, only angle of attack effect without reducing the dynamic pressure and including both the effects. The computed results are shown in next subsection.

### 8.3.5. EFFECT OF ANGLE OF ATTACK AND DYNAMIC PRESSURE

The installation of a pylon upstream of the propeller introduces two effects in the pylon wake region: reduced dynamic pressure (referred as  $\Delta Q$  effect) and increased angle of attack (referred as  $\Delta\alpha$  effect). To evaluate these effects individually, the propeller performance parameters are computed such that the individual effects are only accounted. The methodology of computations is shown in Subsection 6.2.2. The final results for the thrust coefficient and torque coefficient are plotted in Figures 8.13 and 8.14 respectively.

Figure 8.13 and 8.14 show that the effect of only reduced dynamic pressure in decreasing the propeller thrust and torque coefficients is very small across the entire advance ratio range. This is due to the high effective velocities across the blade when compared to the velocity deficit. The effect of increased angle of attack in the wake varies with advance ratio. In the low advance ratio range of 0.5-1.0, the  $\Delta\alpha$  effect is very small. However, at high advance ratios the  $\Delta\alpha$  effect is very high. At  $J = 1.7$ , the  $\Delta\alpha$  effect is as high as 14%. The combined effect of reduced dynamic pressure and increased angle of attack is also shown in the same figure. The  $\Delta\alpha$  effect dominates the  $\Delta Q$  effect for high advance ratios 1.0-1.7. For very low advance ratios, the  $\Delta Q$  effect and  $\Delta\alpha$  effect are of similar levels, thereby showing a very small combined change in thrust coefficient and torque coefficient.

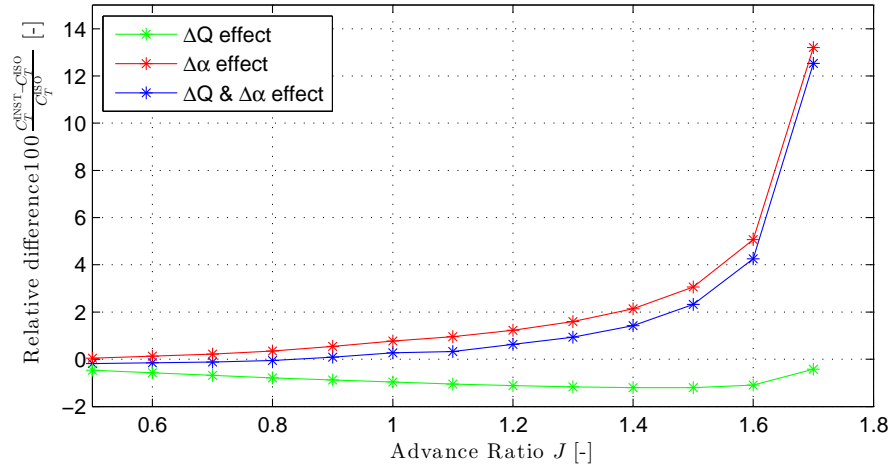


**Figure 8.13:** Effect of reduced dynamic pressure and increased angle of attack in the pylon wake region. Installation effect on thrust coefficient:  $U_\infty = 18$  m/s,  $J = [0.5-1.7]$ ,  $\Delta X = 50\% D_{\text{prop}}$

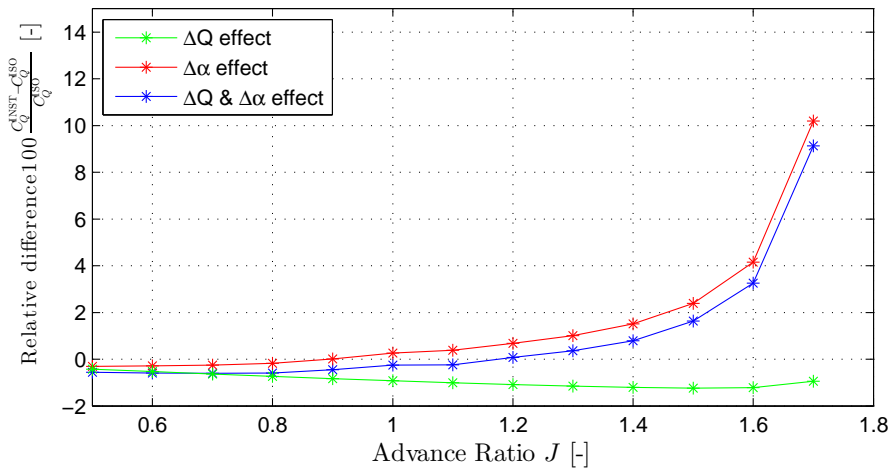


**Figure 8.14:** Effect of reduced dynamic pressure and increased angle of attack in the pylon wake region. Installation effect on torque coefficient:  $U_\infty = 18$  m/s,  $J = [0.5-1.7]$ ,  $\Delta X = 50\% D_{\text{prop}}$

#### 8.4. EFFECT OF PYLON-PROPELLER SPACING

In all the previous sections of this chapter, the propeller performance was computed for a constant pylon-propeller spacing. The current subsection evaluates the effect of pylon-propeller spacing on the performance of the pusher propeller. The numerical model computed performance for a freestream velocity of 18 m/s, advance ratio of 0.6-1.7 and for pylon propeller spacing of 10-100% of the diameter of the propeller. The effect of spacing is shown as the relative difference in thrust and torque coefficients between the isolated and pylon-installed configuration in Figure 8.15 and 8.16, respectively.

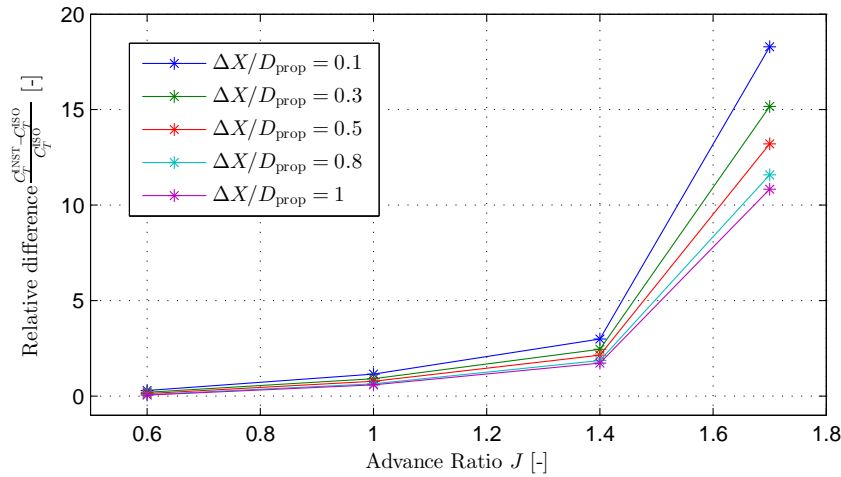


**Figure 8.15:** Effect of pylon-propeller spacing on the thrust coefficient.

Pylon-Installed configuration  $U_\infty = 18$  m/s,  $J = [0.6 \ 1.0 \ 1.4 \ 1.7]$ ,  $\Delta X = [10 \ 30 \ 50 \ 80 \ 100]\% D_{prop}$

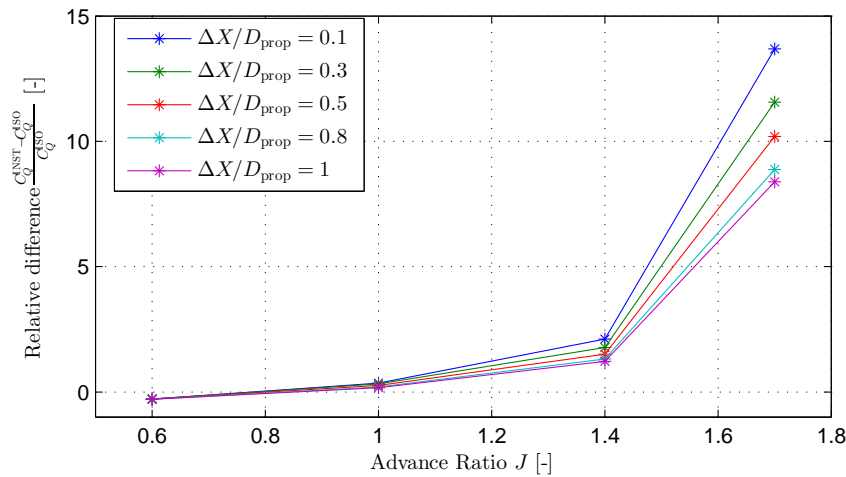


**Figure 8.16:** Effect of pylon-propeller spacing on the torque coefficient.

Pylon-Installed configuration  $U_\infty = 18$  m/s,  $J = [0.6 \ 1.0 \ 1.4 \ 1.7]$ ,  $\Delta X = [10 \ 30 \ 50 \ 80 \ 100]\% D_{prop}$

From Figures 8.15 and 8.16, it is clearly seen that the increase in pylon propeller spacing reduces the effect of installation. The decrease in the performance is dominant at high advance ratios. At an advance ratio of 1.7, increase in spacing from 10% to 100% of  $D_{prop}$  resulted in a decrease in the installation impact from 18% to 11%. A similar trend is observed for the torque coefficient. The increase in spacing resulted a net decrease in momentum deficit in the wake which resulted in a decrease in propeller thrust and torque coefficient.

## 8.5. WAKE SENSITIVITY ANALYSIS

In this section, the effect of wake velocity deficit and wake width on propeller performance is evaluated. Wakes with distinct velocity deficit and wake width are used as input to compute propeller performance. The computations are performed at a freestream velocity of 18 m/s, an advance ratio of 1.4 and pylon-propeller spacings of 10, 50 and 100% of the diameter of the propeller. The pylon drag coefficients used to compute the wake profiles are 0.00702, 0.02, 0.03 and 0.04. The wake profiles obtained for the above mentioned operating points are plotted in Chapter 7. The computed propeller thrust and torque coefficients for different wake widths and velocity deficits are plotted in Figures 8.17 and 8.18, respectively.

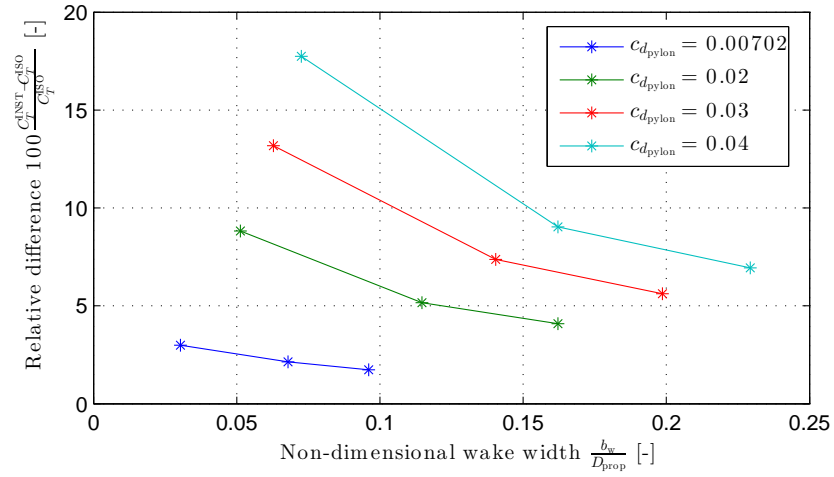


**Figure 8.17:** Effect of wake width on the thrust coefficient.

Pylon Installed configuration  $U_\infty = 18$  m/s,  $J = 1.4$ ,  $\Delta X = [10\ 50\ 100]\% D_{prop}$ ,  $c_{d_{pylon}} = [0.00702\ 0.02\ 0.03\ 0.04]$

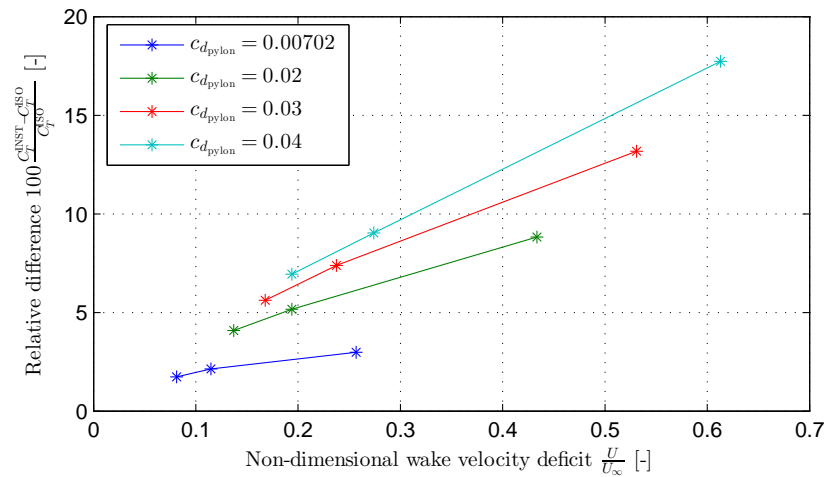


**Figure 8.18:** Effect of velocity deficit on the thrust coefficient.

Pylon Installed configuration  $U_\infty = 18$  m/s,  $J = 1.4$ ,  $\Delta X = [10\ 50\ 100]\% D_{prop}$ ,  $c_{d_{pylon}} = [0.00702\ 0.02\ 0.03\ 0.04]$

To understand the effect of velocity deficit on propeller thrust coefficient, two cases with same non-dimensional wake widths are shown in Table 8.4. Case A indicates that, at constant non-dimensional wake width, a change in non-dimensional velocity deficit from 0.11 to 0.61 increases the installation effect from 2% to 18%. Similarly, Case B also indicates that a change in non-dimensional velocity deficit from 0.13 to 0.27 increases the installation effect from 4% to 9%. These results show that an increase in velocity deficit at constant wake width would result in an increase in the installation effect. The differences observed in thrust coefficient at constant non-dimensional wake width is due to differences in momentum deficit in the wake. Higher momentum deficit in the wake would result in higher installation effect. To understand the effect of wake width on propeller thrust coefficient, two cases with same non-dimensional velocity deficits are shown in Table 8.4. Case C indicates that, at constant non-dimensional velocity, a change in non-dimensional wake width from 0.57 to 1.14 increases the installation effect from 5.1% to 6.9%. Similarly, Case D also indicates that a change in non-dimensional wake width from 0.15 to 0.81 increases the installation effect from 3% to 9%. These results show that an increase in wake width would also result in an increase in the installation effect. The differences observed in thrust coefficient at constant non-dimensional velocity deficit is due to differences in momentum deficit in the wake. Higher momentum deficit in the wake would result in higher installation effect.

From the above results, wakes with high velocity deficit and high wake width would lead to high installa-

**Table 8.3:** Effect of velocity deficit on propeller thrust coefficient.Pylon Installed configuration  $U_\infty = 18$  m/s,  $J = 1.4$ ,  $\Delta X = [10\ 50\ 100]\%$   $D_{prop}$ ,  $c_{d_{pylon}} = [0.00702\ 0.02\ 0.03\ 0.04]$ 

Case index [-]	Pylon drag coefficient $c_{d_{pylon}}$ [-]	Non-dimensional wake width $\frac{b_w}{D_{prop}}$ [-]	Non-dimensional velocity deficit $\frac{\Delta U}{U_\infty}$ [-]	Installation effect $100 \frac{C_T^{INST} - C_T^{ISO}}{C_T^{ISO}}$ [-]
A	0.04	0.07	0.61	18%
A	0.007	0.067	0.11	2%
B	0.04	0.16	0.27	9%
B	0.02	0.16	0.13	4%

**Table 8.4:** Effect of wake width on propeller thrust coefficient.Pylon Installed configuration  $U_\infty = 18$  m/s,  $J = 1.4$ ,  $\Delta X = [10\ 50\ 100]\%$   $D_{prop}$ ,  $c_{d_{pylon}} = [0.00702\ 0.02\ 0.03\ 0.04]$ 

Case index [-]	Pylon drag coefficient $c_{d_{pylon}}$ [-]	Non-dimensional wake width $\frac{b_w}{D_{prop}}$ [-]	Non-dimensional velocity deficit $\frac{\Delta U}{U_\infty}$ [-]	Installation effect $100 \frac{C_T^{INST} - C_T^{ISO}}{C_T^{ISO}}$ [-]
C	0.04	0.22	0.19	6.9%
C	0.02	0.11	0.19	5.1%
D	0.04	0.16	0.27	9%
D	0.007	0.03	0.26	3%

tion effect on propeller performance. It is due to the momentum deficit in the wake which leads to an increase in propeller performance.



# 9

## NUMERICAL RESULTS: PROPELLER NOISE EMISSIONS

This chapter presents the tonal noise levels for the isolated and pylon-installed configuration computed using the numerical model given in Chapter 6. First, an overview of the operating conditions used during the computations of the tonal noise levels both for the isolated and pylon-installed configurations is presented in Section 9.1. Subsequently, the tonal noise levels for different advance ratios and flyover angles for the isolated configuration are dealt in Section 9.2. Finally, the harmonic noise levels for the pylon-installed configuration are treated in Section 9.3.

### 9.1. OPERATING CONDITIONS

The noise computations are performed using Hansons' method for the isolated and pylon-installed configurations which are discussed in Chapter 6. The operating conditions used are freestream velocities 18, 30, 50 and 70 m/s. The range of advance ratios for which the noise computations are performed are lying between 0.5-1.7. The numerical model does not estimate the noise levels accurately at high tip Mach number. So for advance ratios for which the tip Mach number is greater than 0.7, the noise computation results are not listed here. The pylon was placed at spacing of 50% of the diameter of the propeller. Further, the pylon is placed at an azimuthal angle of  $90^\circ$  which is same in case of the performance computations performed in previous chapter. The other inputs required by the numerical model are the loading and thickness distributions. The thickness distribution is obtained by generating the coordinate files from the 3-D drawings of the blade. The loading distribution is assumed to be uniform in chord-wise direction. This assumption does not impact the noise levels at low tip speeds [10]. The phase shift effects due to the blade sweep and blade offset are assumed to be negligible and hence the parameters  $\phi_0$  and  $\phi_s$  are considered to be zero. Since the experiments are performed in wind tunnel conditions, the Doppler factor is set to unity. The spanwise loading distributions for the isolated and pylon-installed configuration are obtained from the performance computations performed in Chapter 8. The observer distance from the propeller is 1.31 m which is the distance used during the experiments at the Open Jet Facility. The model does not estimate any propagation effects. The computations are performed for a range of axial and azimuthal observer angles.

### 9.2. ISOLATED CONFIGURATION

The isolated propeller tonal noise levels vary with the operating condition of the propeller and with the observer position. The propeller noise sources due to thickness and loading contribute to the overall noise levels. In Subsection 9.2.1, the effect of advance ratio on the overall noise levels is presented. Later, the propeller noise sources as a function of directivity angle are discussed in Subsection 9.2.2.

**Table 9.1:** Summary of the operating conditions for the operating conditions used to compute propeller noise emissions

Parameter	Symbol	Value	Unit
Freestream velocity	$U_\infty$	[18, 30, 50, 70]	m/s
Advance ratio	$J$	[0.5-1.7]	-
Pylon-propeller spacing	$\Delta X$	$0.5D_{\text{prop}}$	-
Pylon azimuthal position	$\phi_{\text{pylon}}$	90	deg
Upstream condition	$OBJ$	[ISO, PYL]	-
Angle of attack	$\alpha$	0	deg
Angle of sideslip	$\beta_{SS}$	0	deg
Microphone flyover angle	$\theta_{\text{mic}}$	[0-360]	deg
Microphone sideline distance	$y_{\text{mic}}$	1.31	m
Microphone azimuthal angle	$\phi_{\text{mic}}$	90	deg

### 9.2.1. EFFECT OF ADVANCE RATIO

The loading on the isolated propeller varies with the operating conditions. As advance ratio decreases due to the increase in rotational velocity of the propeller, the loading on the isolated propeller increases. The associated increase in loading and the increase in helical Mach number at blade section contributes to the overall noise levels. In this section, the influence of advance ratio on the overall noise levels is discussed. The freestream velocities considered here are 18, 30 and 50 m/s. The range of advance ratios treated is 0.5-1.7. The overall noise levels in the propeller plane, i.e. for an axial directivity angle of 90 degrees, are presented in Figure 9.1. The overall noise levels are computed by considering the first 10 harmonics.

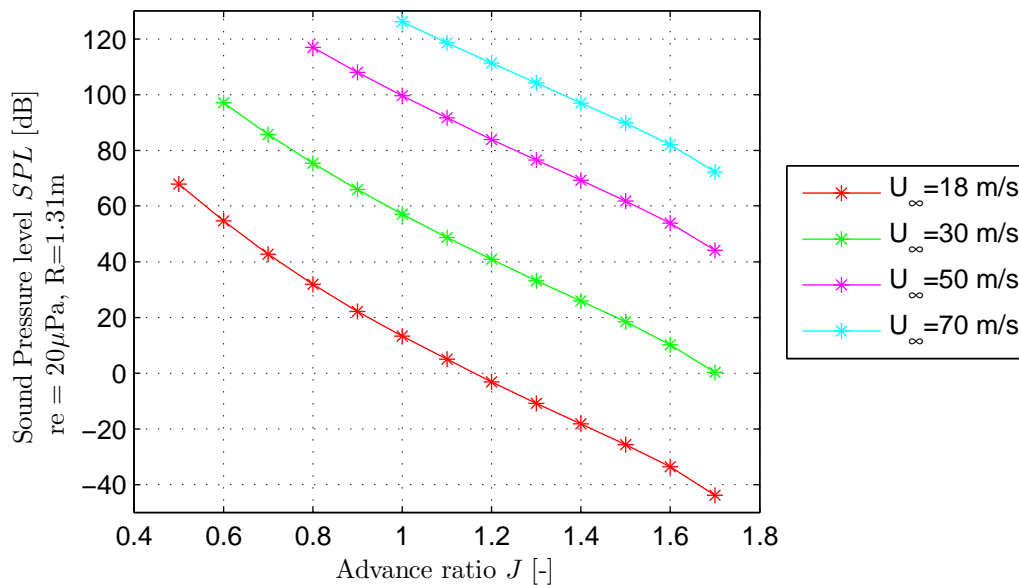


**Figure 9.1:** Variation of Sound Pressure Level with freestream velocity and advance ratio. Isolated Configuration:  $U_\infty = [18, 30, 50, 70]$  m/s,  $J = [0.5-1.7]$ ,  $\theta_{\text{mic}} = 90^\circ$ ,  $\phi_{\text{mic}} = 0^\circ$

Figure 9.1 shows the effect of freestream velocity on the overall noise levels. For low freestream velocities such as  $U_\infty \leq 30$  m/s, the sound pressure levels computed are less than zero for some advance ratios. This is probably due to the underprediction of the SPL at low freestream velocity as the radiation efficiency is underestimated. The results obtained are due to the limitation of the analytical model used here. By using the same analytical model, similar results were obtained [10]. Figure 9.1 also shows the increase in noise levels with decrease in advance ratio at a constant freestream velocity. The increase in noise emissions is

associated with the increase in tip Mach number and blade loading for the given operating condition. From Subsection 6.3.1, the noise levels of individual harmonics depend upon the input to the Bessel function of the first kind. The Bessel function input contains the parameter  $\eta$ , the non-dimensional radial location of the blade section. Hence, at any operating condition for a given blade number and noise harmonic, the tip section dominates the harmonic noise levels across the blade. Since the noise levels also depend on the local section Mach number, it is important to show the effect of tip Mach number on the overall noise levels. Figure 9.2 shows the variation of sound pressure level with the tip Mach number. The predictions are computed for freestream velocity of 18, 30, 50 and 70 m/s for advance ratios 0.5-1.7.

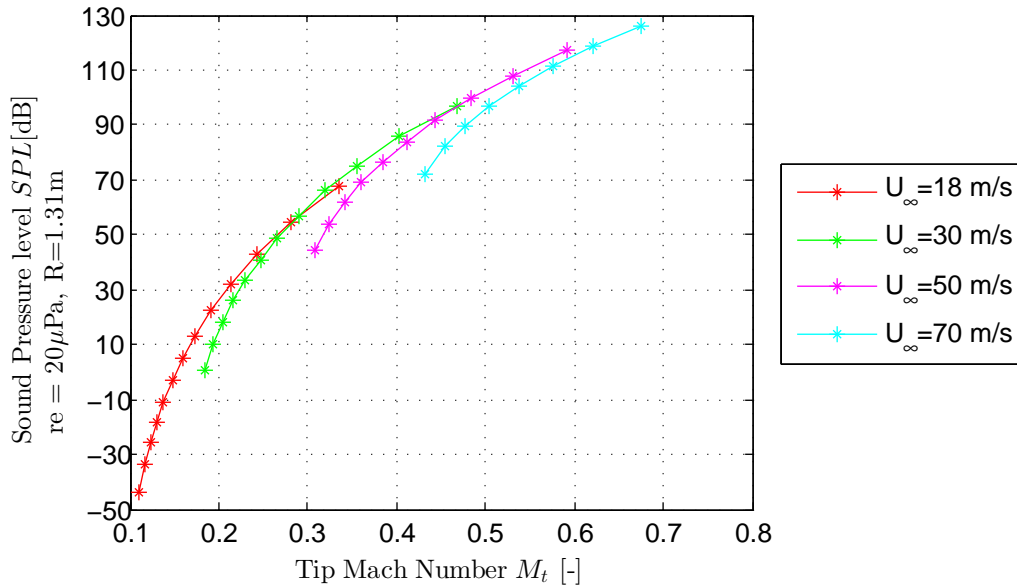


**Figure 9.2:** Variation of Sound Pressure Level with tip Mach number.  
Isolated Configuration:  $U_\infty = [18, 30, 50, 70]$  m/s,  $J = [0.5-1.7]$ ,  $\theta_{mic} = 90^\circ$ ,  $\phi_{mic} = 0^\circ$

The increase in SPL with increase in tip Mach number is shown in Figure 9.2. Clearly the plots show two different gradients of SPL with tip Mach number. The change in SPL with the change in tip Mach number for low tip Mach numbers  $M_t$  is much rapid than at high tip Mach numbers. This is probably due to the underprediction of SPL at low freestream velocities. At constant tip Mach number, the lower freestream velocity has higher SPL due to the lower advance ratios leading to higher blade loading. The difference between SPLs at a constant tip Mach number for any two freestream velocities increases with increase in tip Mach number. Since the lower freestream velocity corresponds to the lower advance ratio, the increase in tip Mach number results in onset of stall decreasing the difference.

Finally, the effect of advance ratio on tip Mach number is plotted in Figure 9.3. The increase in Mach number with decrease in advance ratio is due to the high rotational velocity associated with a low advance ratio. At a constant advance ratio, the increase in freestream velocity increases the tip Mach number.

### 9.2.2. AXIAL DIRECTIVITY

The present subsection discusses the axial directivity pattern associated with the isolated propeller configuration. The sound pressure levels are computed for a freestream velocity of 50 m/s and for an advance ratio of 1.0. The overall harmonic noise levels are computed by adding the first 10 harmonics. The various noise components presented in Figure 9.8 are thickness noise, loading noise due to F1<sup>1</sup> and loading noise due to F2<sup>2</sup>. Both F1 and F2 are considered relative to the advance direction without induced effects. The axial directivity plot indicates a decrease in overall sound pressure level both upstream and downstream directions,

<sup>1</sup>F1: Lift component

<sup>2</sup>F2: Drag component

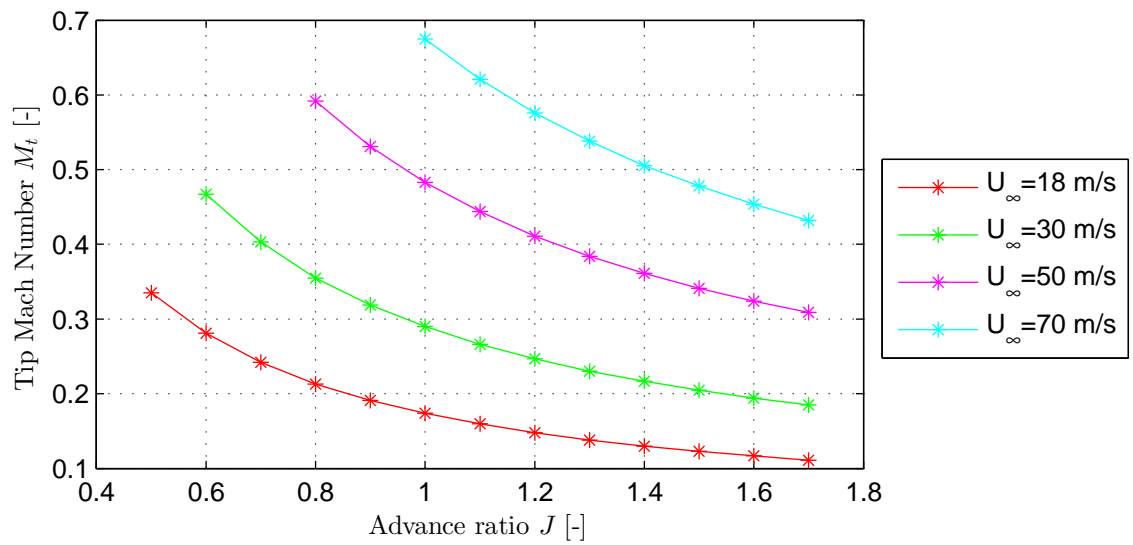


**Figure 9.3:** Variation of tip Mach number with advance ratio.  
Isolated Configuration:  $U_\infty = [18, 30, 50, 70]$  m/s,  $J = [0.5-1.7]$

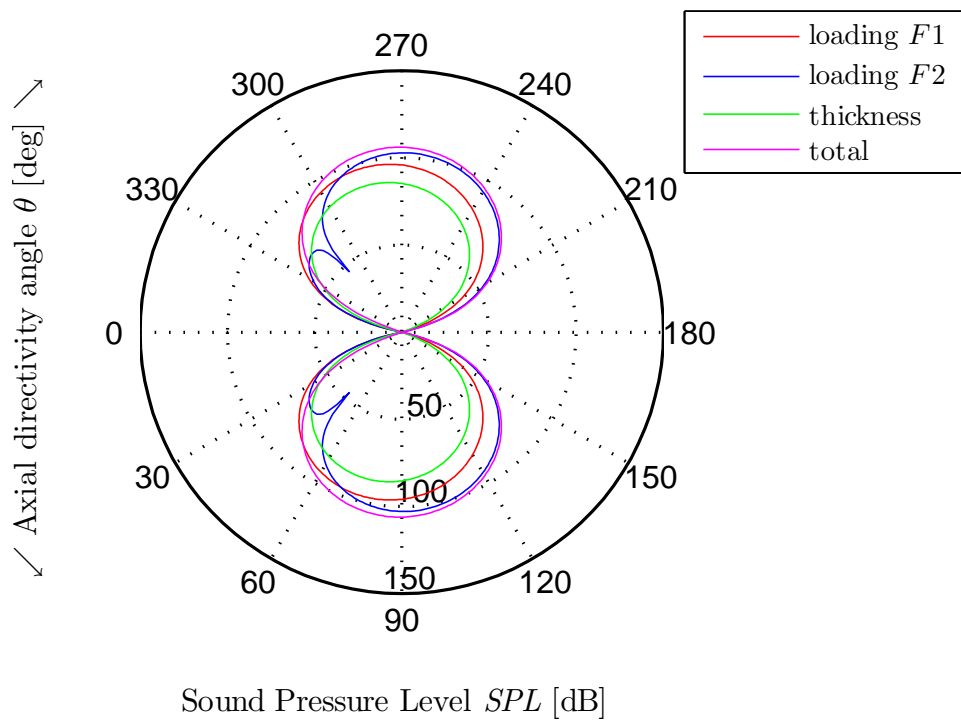


**Figure 9.4:** Isolated configuration: Axial directivity  
 $U_\infty = 50$  m/s,  $J = 1$ ,  $\theta_{\text{mic}} = [0^\circ-360^\circ]$ ,  $\phi_{\text{mic}} = 0^\circ$

as expected. The maximum overall sound pressure level is observed in the vicinity of the propeller. Both the loading noise due to  $F_1$  and thickness components contribute to the overall sound pressure levels. However, the loading noise due to  $F_2$  has multiple lobes with minima close to  $\theta = 50^\circ$  and  $\theta = 310^\circ$ . Equation 6.66 indicates that for the sound pressure level to show a minimum at an axial directivity angle,  $M_\infty - M_T^2 \cos \theta$  should be zero. Also, the sound pressure levels at these lobes are out of phase by 180 degree indicating that one lobe is contributing to the overall sound pressure level and the other lobe is reducing the overall sound pressure levels.

### 9.3. PYLON-INSTALLED CONFIGURATION

The installation of a pylon upstream results in a wake which introduces an extra loading on the propeller which increases the overall sound pressure levels for the propeller. The effect of the pylon on the overall noise levels is discussed in the present section. Subsection 9.3.1 presents the effect of advance ratio on the overall noise levels in the pylon-installed configuration. Later, the axial directivity of the propeller for the pylon-installed configuration is treated in Subsection 9.3.2. As already mentioned, the pylon is positioned at an azimuthal angle of 90 degrees.

#### 9.3.1. EFFECT OF ADVANCE RATIO

In this section, the propeller noise emissions are computed for a number of propeller operating points. The computations are performed for freestream velocities of 18, 30, 50 and 70 m/s, advance ratios lying between 0.5 and 1.7. The axial directivity angle considered here is 90 degrees, i.e. in the plane of propeller. Figure 9.5 shows the effect of freestream velocity and the advance ratio on the overall sound pressure levels. The overall sound pressure levels at a constant advance ratio increase with increasing freestream velocity similar to the case of isolated configuration. Also, the decrease in advance ratio resulted in an increase in the overall sound pressure levels. Figure 9.5 shows two regions with different slopes. To identify the effect on unsteady loading introduced by the wake, both isolated and installed sound pressure levels are plotted in Figure 9.6.

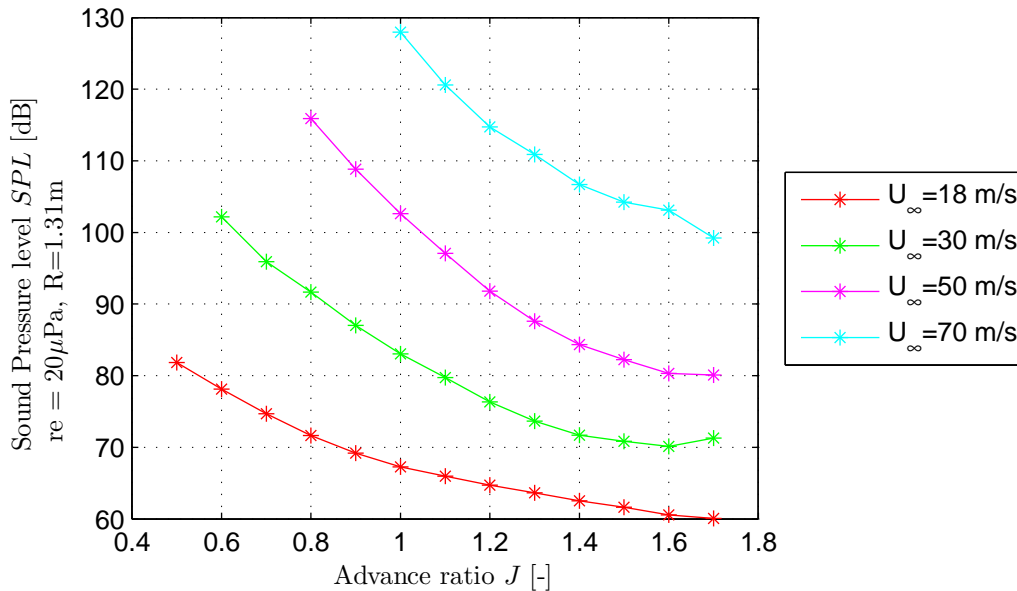


**Figure 9.5:** Variation of SPL with freestream velocity and advance ratio.

Installed Configuration:  $U_\infty = [18, 30, 50, 70]$  m/s,  $J = [0.5-1.7]$ ,  $\theta_{mic} = 90^\circ$ ,  $\phi_{mic} = 0^\circ$ ,  $\phi_{pylon} = 90^\circ$

From Figure 9.6, at low advance ratios, the steady state loads dominate the fluctuating unsteady loads and hence steady state loads act as a dominating noise generating mechanism. Further, at high advance ratios, the effect of the wake on the overall SPL is large when compared to the low advance ratios. The propeller

noise at high advance ratios is dominated by unsteady loading of the wake as the steady loads are relatively small at this advance ratio. Hence, the effect of wake is large at high advance ratios than at low advance ratios.

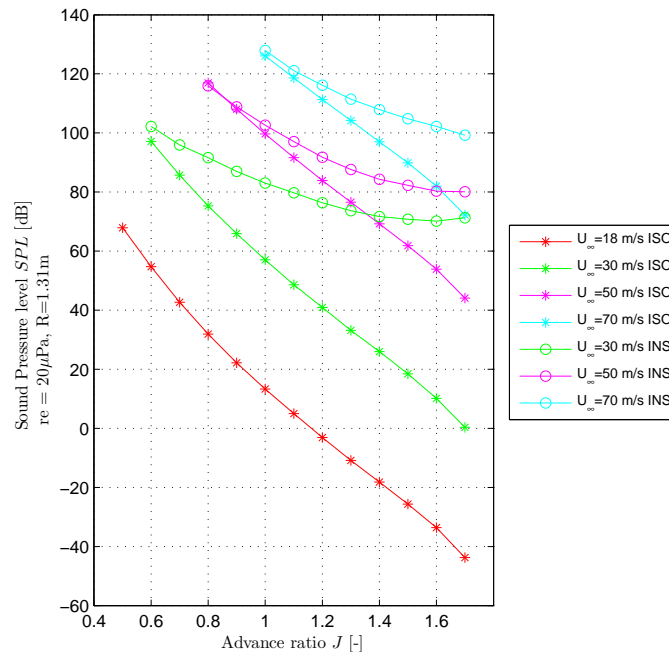


**Figure 9.6:** Variation of SPL with freestream velocity and advance ratio.

Isolated and Installed Configuration:  $U_{\infty} = [18, 30, 50, 70]$  m/s,  $J = [0.5-1.7]$ ,  $\theta_{mic} = 90^{\circ}$ ,  $\phi_{mic} = 0^{\circ}$ ,  $\phi_{pylon} = 90^{\circ}$

### 9.3.2. EFFECT OF INSTALLATION

To evaluate the effects of installation at different advance ratios and freestream velocities, the difference between the sound pressure levels from the installed configuration and isolated configuration is computed. The change in SPL computed is plotted in Figure 9.7.

From Figure 9.7, at a constant advance ratio, the effect of installation is highest for the lowest freestream velocity. The radiation efficiency for the isolated configuration increases more rapidly with the tip Mach number than for the pylon-installed configuration. This is also a limitation of the numerical model used as the noise levels predicted for low freestream velocity are underpredicted. At a constant freestream velocity, the increase in advance ratio increases the installation effect as the unsteady loading noise dominates at high advance ratio. Also, the effect of installation for freestream velocities 50 and 70 m/s is close to zero at low advance ratios indicating that the steady state loading noise dominates the unsteady loading noise.

### 9.3.3. AXIAL DIRECTIVITY

The present subsection discusses the axial directivity pattern associated with the pylon installed propeller configuration. The sound pressure levels are computed for a freestream velocity of 50 m/s, an advance ratio of 1.0 and a pylon-propeller spacing of 50% of the diameter of the propeller. The overall harmonic noise levels are computed by adding the first 10 harmonics. The isolated directivity pattern is also shown in the figure which serves as a base.

The installation of the pylon increases the noise levels across the flyover angles. The increase is related to the radiation efficiency of the isolated ( $J_{mB}$ ) and pylon-installed configuration ( $J_{mB-k}$ ). The radiation efficiency for the isolated configuration, which depends on the harmonic order, becomes zero for all the higher harmonics as the Bessel function governing it becomes zero for  $\theta$  equal to  $0^{\circ}$  (upstream) and  $180^{\circ}$  (downstream). Even, Bessel function with zero argument for zero harmonic order does not contribute to the SPL of the isolated configuration as the wave numbers are zero. For the installed configuration, Bessel function are

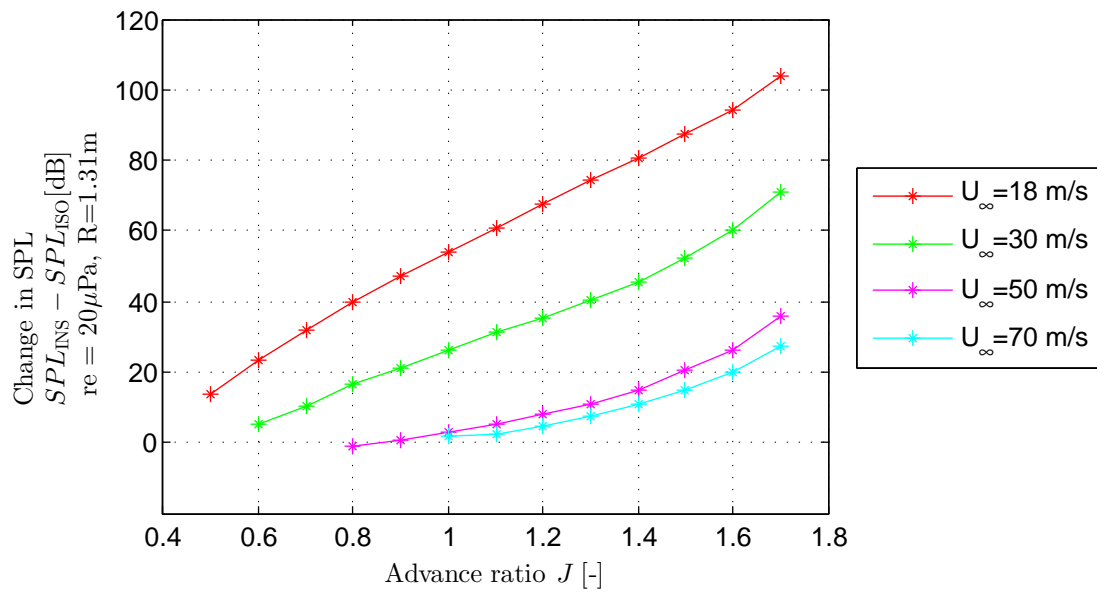


**Figure 9.7:** Effect of installation with freestream velocity and advance ratio. Installed Configuration:  $U_{\infty} = [18, 30, 50, 70]$  m/s,  $J = [0.5-1.7]$ ,  $\theta_{mic} = 90^{\circ}$ ,  $\phi_{mic} = 0^{\circ}$ ,  $\phi_{pylon} = 90^{\circ}$

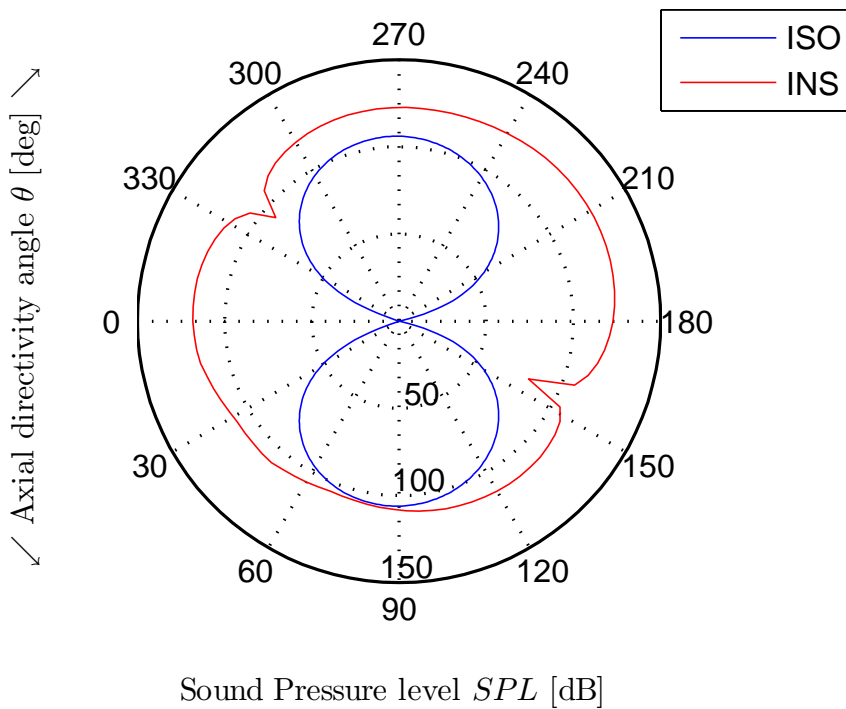


**Figure 9.8:** Pylon-Installed configuration: Axial directivity  $U_{\infty} = 50$  m/s,  $J = 1$ ,  $\theta_{mic} = [0^{\circ}-360^{\circ}]$ ,  $\phi_{mic} = 0^{\circ}$ ,  $\phi_{pylon} = 90^{\circ}$

defined for harmonic order  $mB-k$ . Even when this quantity is zero, wave numbers at this harmonic order are non-zero and hence contributes to the overall noise. Hence, the increase in noise levels due to the installation of pylon is maximum along the propeller axis.

# 10

## COMPARISON OF EXPERIMENTAL AND NUMERICAL RESULTS

The experimental and numerical parts of the thesis project were already presented in the previous chapters. A comparison between the numerical and experimental results is treated in this chapter. First, a comparison between the experimental and numerical results of the wake profiles is discussed in Section 10.1. Subsequently, the propeller performance results obtained with the numerical model and experiments for both isolated and pylon-installed configurations are treated in Section 10.2. Finally, the propeller noise emissions measured and computed for both isolated and pylon installed configurations are given in Section 10.3.

### 10.1. PYLON WAKE PROFILES

The present section compares the measured pylon wake profiles during the experimental campaign and the computed pylon wake profiles using the numerical model. The experimental pylon wake profiles are already discussed in Chapter 3. The wake profiles are measured using Stereoscopic PIV in the experimental campaign conducted at Open Jet facility. The details of the experimental setup are presented in Chapter 2. The measurements are recorded for a freestream velocity of 18 m/s, advance ratio of 0.6, 1.0, 1.4 and 1.8, pylon propeller spacing of 40%, 50% and 100% of the diameter of the propeller and pylon angle of attack of zero degrees. Since the time averaged propeller thrust is zero at advance ratio of 1.8, only the wake profiles at this advance ratio are treated here in this subsection. Figure 10.1 shows the wake profiles obtained for the above mentioned operating condition.

From Figure 10.1, it is observed that there are slight differences in wake profiles between the experimental and numerical results. The difference in velocity deficit between experimental and numerical results is of the order of 2%. The wake widths of the experimental and numerical wake profiles show differences of the order of 10%. Further, the wake profiles obtained during the experimental campaign are asymmetric with respect to the freestream direction. These differences are possibly due to multiple reasons:

- The pylon wake profile measured during the experimental campaign is not in the pylon only configuration but has the propeller running at zero time averaged thrust. From the velocity contour plots in Chapter 3, it can be understood that the propeller generates a local thrust which would influence the pylon wake profile.
- The potential field of the propeller also influences the pylon wake profile.
- Further, the drag coefficient, which is an input to the Schlichting wake model, was obtained by running XFOIL in free transition mode. Inaccuracies in the prediction of the transition might lead to inaccurate drag coefficient, thereby altering the pylon wake profiles.

### 10.2. PROPELLER PERFORMANCE

The propeller performance parameters are measured and computed to quantify the effects of the pylon wake on a pusher propeller. Subsection 10.2.1 first compares the propeller performance measured and computed

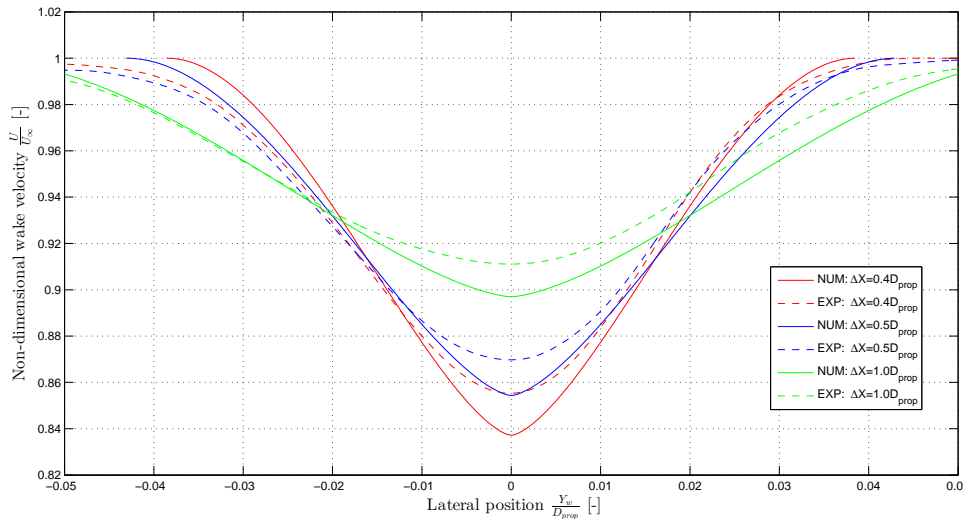


**Figure 10.1:** Comparison of measured and computed wake profiles .  
 $U_{\infty} = 18 \text{ m/s}$ ,  $J = 1.8$ ,  $\Delta X = [0.4 \ 0.5 \ 1.0] D_{\text{prop}}$

for the isolated configuration. Later, the pylon installed propeller performance measured and computed is presented in Subsection 10.2.2. Also, the effects of installation and the effect of pylon-propeller spacing are discussed in the same section.

### 10.2.1. ISOLATED CONFIGURATION

The propeller performance for the isolated configuration is treated in this section as these results serve as a basis for comparison with the pylon-installed configuration. The propeller performance was measured in the isolated configuration at a freestream velocity of 18 m/s, advance ratio range of 0.5-1.6. The details of the setup for the experimental campaign at Open Jet facility are given in Chapter 2. The propeller performance is computed using the numerical model given in Chapter 6 at a freestream velocity of 18 m/s and advance ratio range of 0.5-1.7. The measured and predicted propeller performance for the isolated configuration is shown in Figure 10.2. There is a good match between the predicted and measured propeller performance

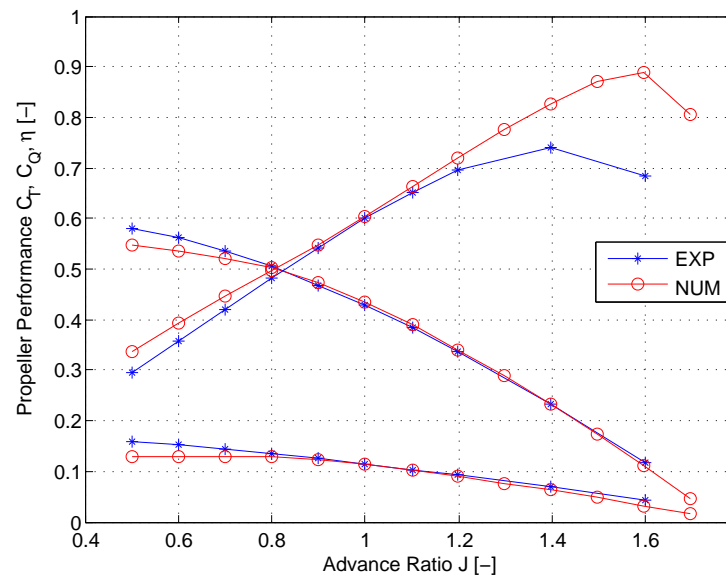


**Figure 10.2:** Comparison of measured and computed propeller performance.  
 Isolated Configuration  $U_{\infty} = 18 \text{ m/s}$ ,  $J = [0.5-1.7]$

parameters for advance ratios between 0.8-1.2. The difference in measured and predicted propeller performance is of the order of 2%. At low advance ratios, the difference in measured and computed thrust and torque coefficient is of the order of 6%. This is due to the inability of the numerical model to predict the blade response at high angles of attack. The prediction of onset of stall at low advance ratios is not accurate enough to estimate the propeller thrust and torque coefficients. Propeller efficiency for high advance ratios such as 1.2-1.6 is underpredicted due to the overprediction of torque coefficient. Since the thrust coefficient is predicted relatively accurately when compared to the torque coefficient, it is likely that the overprediction of the torque coefficient is due to the higher predicted drag coefficient. The drag coefficient is obtained by curve fitting process in XROTOR using the blade section properties obtained from the airfoil analysis program (XFOIL). The efficiency measured is lower than efficiency computed for all advance ratios. This is due to the differences between the measured and computed thrust and torque coefficients.

### 10.2.2. PYLON-INSTALLED CONFIGURATION

The propeller performance for the pylon installed configuration is treated in this section. The propeller performance was measured for the pylon-installed configuration at a freestream velocity of 18 m/s, advance ratio range of 0.5-1.6 and pylon-propeller spacing of 50% of the diameter of the propeller. The propeller performance is computed using the numerical model given in Chapter 6 at a freestream velocity of 18 m/s and advance ratio range of 0.5-1.7. The measured and predicted propeller performance for the pylon-installed configuration are shown in Figure 10.3.

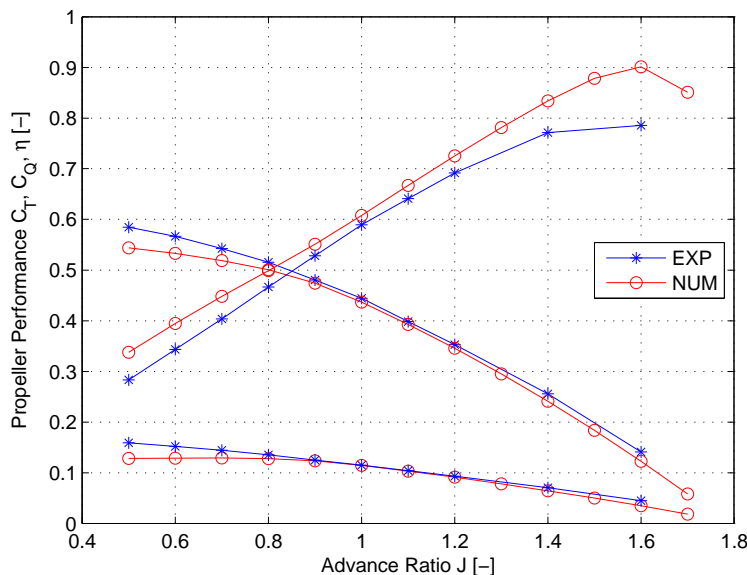


**Figure 10.3:** Comparison of measured and computed propeller performance. Pylon-Installed Configuration  $U_\infty = 18$  m/s,  $J = [0.5-1.7]$ ,  $\Delta X = 50\% D_{prop}$

From Figure 10.3, it is observed that the computed propeller efficiency is higher than the measured efficiency for all advance ratios. However, a close match is observed for advance ratios of 0.8-1.2. The differences in measured and computed efficiency are of the order of 4%. Both for high and low advance ratios, the differences between the computed and measured efficiency is large. At low advance ratios, the differences between the computed and measured efficiency are of the order of 15% and for higher advance ratios it is of the order of 12%. It is to be noted that the numerical model underpredicts the propeller thrust and torque coefficient at both low advance ratios (0.5-0.8) and high advance ratios (1.4-1.6) which accounts for the differences observed. Since, it is concluded in Chapter 5 that the measured propeller performance in the pylon-installed configuration is due to a measurement error, the effect of pylon-propeller spacing on the measured and computed propeller performance is not considered. It is to be noted that the effect of spacing on measured propeller performance is negligible whereas the computed installation effect decreases with increase in spacing. Within the limitation of the accuracy of the RSB, the measured propeller performance did not show any effect of pylon-propeller spacing.

### 10.3. PROPELLER NOISE EMISSIONS

In this section, the propeller noise emissions computed and measured for the isolated and installed configuration are compared in Subsections 10.3.1 and 10.3.2, respectively

#### 10.3.1. ISOLATED CONFIGURATION

Propeller tonal noise emissions are computed for a freestream velocity of 18 m/s and advance ratio of 0.5-1.7. The measured tonal noise levels are also obtained at the same operating parameters. The tonal SPLs are computed using the first ten harmonics. However, the contribution from higher harmonics is negligible. This is due to the low radiation efficiency of higher harmonics. Figure 10.4 plots the measured and computed tonal noise levels for the isolated configuration. The computed tonal noise levels are clearly underpredicted as the overall noise levels are less than zero which means not audible. Clearly, the model does not predict well at low freestream velocities. Hence, the computed noise levels do not form a comparison with the measured noise levels for the isolated configuration. Hence, directivity pattern for the isolated configuration is not considered here.

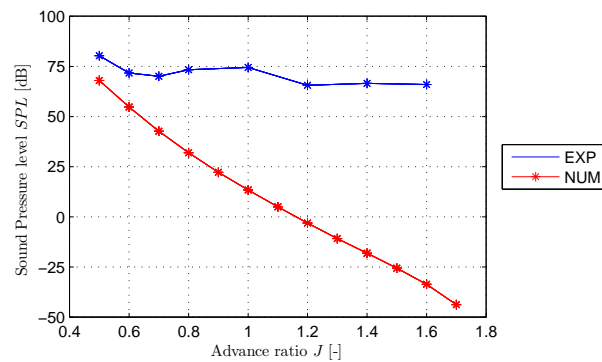


**Figure 10.4:** Comparison of measured and computed propeller tonal noise levels. Isolated Configuration  $U_{\infty} = 18$  m/s,  $J = [0.5-1.7]$

#### 10.3.2. PYLON-INSTALLED CONFIGURATION

The effect of installation on the overall tonal noise levels is presented in this subsection. The computed tonal noise emissions are at a freestream velocity of 18 m/s, advance ratio of 0.5-1.7 and pylon-propeller spacing of 50% of the diameter of the propeller. The tonal noise levels are measured at the same operating parameters. Figure 10.5 plots the measured and computed tonal noise levels for the pylon-installed configuration.

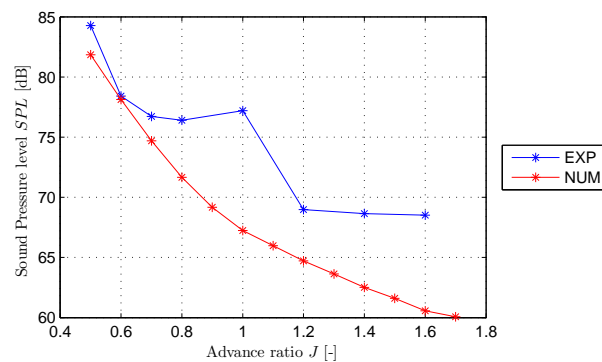


**Figure 10.5:** Comparison of measured and computed propeller tonal noise levels. Pylon-Installed Configuration  $U_{\infty} = 18$  m/s,  $J = [0.5-1.7]$ ,  $\Delta X = 50\% D_{prop}$

The computed SPL for the pylon-installed configuration is of comparable to the measured SPL. The trend

of increasing SPL with decreasing advance ratio is seen in both measured and computed results. The low radiation efficiency of harmonics at low freestream velocity as in case of computed isolated propeller noise levels is not seen in the pylon-installed configuration. The measured SPL does have local minima across the advance ratio range which is not the case with computed pylon-installed noise levels. Since the computed noise levels for the isolated configuration are underpredicted, the effect of installation is much higher for the computed tonal noise levels when compared to the measured tonal noise levels.



# 11

## CONCLUSIONS AND RECOMMENDATIONS

This chapter presents the conclusions and recommendations for possible future work obtained from the experimental and numerical investigation performed on the sensitivity of pusher propeller performance and noise emissions to the upstream wake characteristics. The conclusions from the investigations conducted are presented in Section 11.1, followed by recommendations in Section 11.2.

### 11.1. CONCLUSIONS

An experimental and numerical investigation on the effect of an upstream wake on pusher propeller performance and noise emissions is performed and the conclusions derived from the work are presented here in this section. Experimental part of this research is conducted in two campaigns : V-tunnel and OJF campaign. The V-tunnel campaign focussed on propeller noise emissions whereas the OJF campaign dealt with propeller performance, noise emissions and pylon wake profiles.

From experimental pylon wake profiles obtained through PIV measurements, it is observed that the negative pressure gradient in front of the propeller affects the upstream pylon wake characteristics. The pylon wake characteristics are affected by the propeller suction which is dependent on the advance ratio. The non-dimensional wake displacement thickness and velocity deficit decrease with a decrease in advance ratio. The acceleration of the propeller inflow due to the propeller suction reduces the mass deficit in the wake and thereby reduces the wake displacement thickness. As the advance ratio decreases, the increase in the streamwise velocity due to the stronger pressure gradient decreases the non-dimensional velocity deficit in the wake. The pylon-propeller spacing also affects the pylon wake characteristics. With increase in spacing from the trailing edge of the pylon, the wake displacement thickness decreases as the flow from outside the wake fills up the mass deficit in the wake at zero thrust condition. The same result is observed at non-zero thrust condition at different freestream velocities, all advance ratios and pylon-propeller spacings except at the very nearest pylon-propeller spacing of 40% of the diameter of the propeller and an advance ratio of 0.6 . The non-dimensional wake displacement thickness and velocity deficit at  $J = 0.6$  for the closest pylon spacing are more by 150% than for the farthest pylon spacing tested. This is probably due to the changing nature of the boundary layer on the pylon at the closest propeller spacing at an advance ratio of 0.6.

A numerical model based on the Schlichting wake model is developed to estimate the wake characteristics. The limitation of the model with respect to the current research project is the inability to estimate the effect of propeller on the wake. Despite the limitation, the wake profiles from the experiments (at zero thrust condition) and the numerical model match well, with differences in wake characteristics of the order of 2%. However, there is a slight asymmetry in the wake observed probably due to the phase angle variations across the images recorded during PIV resulting in an error in measurement. Phase locked measurements when the propeller blade is at an azimuthal angle of 90 degrees would remove the asymmetry in the wake profiles observed. The match between the experimental and numerical wake profiles is maintained for different pylon-propeller spacings.

An experimental investigation into the wake effects on propeller performance was carried out for isolated and different installed configurations. Comparison of the experimental data from the isolated and

pylon-installed configuration showed an increase in propeller performance particularly at high advance ratios. However, this increase was confirmed to be an error in measurement. The propeller performance data averaged over one rotation cycle for the pylon-installed configurations showed a mean offset when compared with the isolated configuration. Spectral analysis of the time accurate data also confirmed the variations observed during the measurement is due to the vibration of the RSB. Hence, the mean offset in propeller performance is confirmed to be a measurement error. Within the limitation of the accuracy of the current RSB, propeller performance measurements are carried out for different pylon-propeller spacings. The measured propeller performance showed no change as the pylon was moved from 40% to 100% of the diameter of the propeller, though the wake profiles observed are different. Propeller performance was also measured for different cylinder-splitter plate configurations. The effect of the pylon is significant on the propeller performance when compared to the cylinder-splitter plate configuration. This is attributed to the nature of the flow behind the cylinder-splitter plate resulting in high vorticity which lowers the angle of attack, thereby reducing the propeller performance when compared with pylon-installed configuration.

A numerical evaluation was performed to evaluate the effect of an upstream wake on the propeller performance and compare the results with the experimental measurements. A good match between the measured and computed performance parameters for the isolated configuration is observed for advance ratios 0.8-1.2 with differences of 2%. At low advance ratios, the numerical model underpredicted the performance due to the inaccurate computation of the blade section lift coefficient and drag coefficient at high angle attack. A maximum difference of 6% is observed at the lowest advance ratio tested. With the installation of pylon, the effect of wake on propeller performance computed is significant only at very high advance ratios of 1.5-1.7. For lower advance ratios, the installation effect is less than 2%. The effect of pylon-propeller spacing on the propeller performance is evaluated and the results showed a decrease in propeller performance with an increase in pylon-propeller spacing. Since the effect of wake on propeller performance is only significant at high advance ratios, the effect of pylon-propeller spacing evaluated at advance ratios lying in the range of 0.5-1.4 showed no significant impact. At a very high advance ratio, a change in pylon-propeller spacing from  $0.1D_{prop}$  to  $1.0D_{prop}$  resulted in an increase from 10% to 18% increase in thrust coefficient. The wake sensitivity analysis performed showed an increase in thrust coefficient of 18% for the thickest wake used during computations.

Experimental investigations are carried out at the Open jet facility to evaluate the effect of the pylon wake on propeller noise emissions. The experiments performed are reproducible with the variability of the measurement data is within  $\pm 0.8$  dB. The noise spectra for the isolated configuration indicated that the noise levels observed are at multiples of blade passage frequency. A decrease in advance ratio increased the SPL of all the multiples of the blade passage frequency. The isolated propeller also showed a significant peak at 3BPF and 6BPF indicating the flow in the isolated propeller configuration is not uniform. However, the pylon wake profiles for the isolated configuration at the 75% radial station did not show any non-uniformity. The reason for the presence of higher BPF's is still not conclusive with the current experimental data. Further investigations need to be performed. The flyover directivity pattern also showed a dip at flyover angle of 75 degrees. The dip in the flyover directivity pattern at  $\theta = 75$  degrees is related to the smaller advance ratio at which the presence of local maxima in the variation of  $SPL$  vs  $J$ . This might probably be due to the presence of circumferential lobes in the azimuthal directivity. The effect of the installation of pylon is found to be significant only at the multiples of blade passage frequency. The broad band noise levels measured for the pylon installed configuration are similar to the broadband noise levels in the isolated configuration. This is attributed to the wind tunnel broadband noise levels rather than the propeller noise levels. The increase in noise emissions for the pylon installed configuration is significant across the flyover directivity angles. The noise penalty due to the installation of the pylon increases with increase in advance ratio. This is due to a higher increase in unsteady loading at high advance ratio when compared with a low advance ratio case. The noise levels are also measured for different pylon-propeller spacings. The effect of installation of the pylon is seen at all pylon-propeller spacings. The increase in noise levels is observed to be highest at the closest pylon-propeller spacing. Further increase in pylon-propeller spacing decreased the noise levels at all advance ratios. This is due to the decrease in the root mean square deviation of the streamwise velocity observed with increase in pylon-propeller spacing.

Propeller noise measurements recorded in V-tunnel campaign served as a preliminary study to evaluate the effect of upstream wake on the propeller. The isolated and installed noise spectra showed the presence

of tones at the blade passage frequency. The contribution of 1BPF is significant to the overall noise levels when compared to the higher harmonics. The tonal noise levels due to the installation of the pylon showed a decrease for all pylon-propeller spacings. With increase in pylon-propeller spacing, the noise levels decreased initially for 30-40% before being constant for higher pylon-propeller spacings of 50-70%. The decrease is attributed to the destructive interference of steady and unsteady loading noise sources. The azimuthal directivity pattern showed a higher tonal noise level in the plane perpendicular to the pylon when compared to the noise levels in the plane of pylon. This is attributed to the lobes observed in the circumferential directivity pattern. The flyover directivity showed a decrease downstream of the propeller (similar to the OJF campaign results) whereas upstream noise levels showed a slight increase to the noise levels in the propeller plane which also might be related to the circumferential directivity.

Numerical evaluations are performed using an analytical model based on frequency domain method developed by Hanson. The isolated propeller noise levels are significantly underpredicted as the radiation efficiency of the harmonics is small for the eight bladed propeller at low freestream velocities. Low radiation efficiency leads to the decrease in noise levels at the tones. Considering this limitation, propeller tonal noise levels evaluated at high freestream velocities showed an increase with a decrease in advance ratio. The tonal noise levels are due to the contribution of only the first harmonic. Contribution of higher harmonics to the overall noise is very low due to the low radiation efficiency of higher harmonics. For the pylon-installed configuration, the performance computations are used as an input to calculate the tonal noise levels. The effect of installation increased the noise levels at all flyover directivity angles with highest increase observed along the propeller axis. This is attributed to the higher radiation efficiency of the unsteady loading noise than the steady loading noise along the propeller axis.

The current research work investigating sensitivity of pusher propeller to the upstream wake characteristics concludes that though the effect of the propeller on the upstream wake is present, the effect of the upstream wake on the propeller performance is not significant for the installed configuration with different pylon-propeller spacings and upstream wake conditions. However, the effect of the different wake characteristics is significant on the propeller noise emissions resulting in varied directivity patterns. Hence, an assessment of the wake sensitivity to the propeller performance serves as a starting point for the design of pusher propellers. To further understand the time accurate propeller performance and noise generating mechanisms, a number of possible research options are suggested as recommendations in the next section.

## 11.2. RECOMMENDATIONS

In the previous section, conclusions are derived from the experimental and numerical investigation performed. The current section deals with possible extensions to the research project which would improve the understanding of pylon-pusher propeller interactions. To further understand the effect of the pylon wake on the propeller, time accurate performance of all the three forces and moments needs to be evaluated. A RSB with a better signal quality can help in measuring the time accurate propeller performance. These force and moment components are an important consideration in the integration of the engine to the airframe as well as for the aircraft handling qualities. In the current experimental campaign, the pylon-propeller spacing used are 40-100% of the diameter of the propeller due to the limitation on the size of hub. Similar experiments should be performed for very close pylon-propeller spacing such as 5% to analyse the wake sensitivity on the propeller performance. The experiments conducted during this research work used the angle of attack of pylon as zero degrees. Further analysis for different angle of attacks of the pylon needs to be carried out to understand its influence on pusher propeller performance.

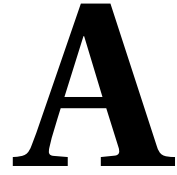
Phase-locked PIV measurements of the flow field on the blade needs to be evaluated to obtain the pressure distribution on the propeller blades. This would aid in the structural design of propeller blades and in understanding the propeller noise generation mechanism. Microphone arrays utilising the beamforming technique along with PIV phase locked measurements will help in noise source localization. The noise cancellation observed in the presence of pylon can be understood by identifying different noise sources and its generating mechanisms. It is suggested that the propeller noise measurements are required to be performed for different azimuthal and flyover angles. This would provide a better understanding of the directivity pattern. Along with the experiments, CFD analysis to predict the 3-D flow phenomena on the propeller blades

will help in analysing the propeller performance.

## BIBLIOGRAPHY

- [1] R.A.V. Robison, Turbulence Ingestion Noise of Open rotors, PhD Thesis, Jesus College, University of Cambridge, Cambridge, 2011.
- [2] B. Magliozzi, D.B. Hanson, and R.K. Amiet, Aeroacoustics of Flight Vehicles, chapter Propeller and Propfan Noise, pages 1-61, NASA Reference Publication 1258, Vol. 1 WRDC Technical Report 90-3052, NASA, 1992.
- [3] J. Ricouard, E.Julliard, M.Omais and V.Regnier, Installation effects on contra-rotating open rotor noise, AIAA 2010-3795, 16th AIAA/CEAS Aeroacoustics Conference, 2010.
- [4] R.D.Hager and D.Vrabel, Advanced Turboprop Project, NASA SP 495, NASA, 1988.
- [5] M.D. Bowles and V.P. Dawson, The Advanced Turboprop Project: Radical Innovation in a Conservative Environment. Engineering Science to Big Science: The NACA and NASA Collier Trophy Research Project Winners. Washington, D.C.: National Aeronautics and Space Administration, 1998.
- [6] M.Taylor, Open Rotor Engine Design and Validation, Rolls Royce[Online] Available at: <http://aerosociety.com/Assets/Docs/Greener/> [Accessed 26 November 2014].
- [7] ED Envia, Aeroacoustics of High-Speed Aircraft Propellers and Open Rotors, 14th CEAS-ASC Workshop and 5th Scientific Workshop of X3-Noise, Institute of Aviation, Warsaw, Poland, October 7-8, 2010.
- [8] S.A.E. Mann and C.A Stuart, Advanced Propulsion through the 1900's: An airframers view, AIAA-85-1192, 21st AIAA/SAE/ASME/ASEE Joint Propulsion Conference, Monterey, California, USA, July 8-10, 1985.
- [9] J.Godston and C.Reynolds, Future of Prop-fans: Tractor or Pusher, AIAA-85-1192, 21st AIAA/SAE/ASME/ASEE Joint Propulsion Conference, Monterey, California, USA, July 8-10, 1985.
- [10] T.Sinnige, The effects of pylon blowing on pusher propeller performance and noise emissions, Master of Science thesis, Delft University of Technology, Delft, 2013.
- [11] M.A.Takallu, Effect of an upstream wake on a pusher propeller, PRC Kentron, Inc., Hampton, Virginia, USA, 1986.
- [12] S.Farokhi, Pressure-Time history of pylon wake on a pusher propeller in flight, Journal of Propulsion, Vol.6, No.6, Nov.-Dec. 1990.
- [13] W.C.Horne and P.T.Soderman, Flow field survey of an empennage wake interacting with a pusher propeller, NASA Technical Memorandum 101003, Ames Research Center, Moffett field, California, USA, October 1988.
- [14] G.L.Gentry, E.R.Booth and M.A.Takallu, Effect of pylon wake with and without pylon blowing on propeller thrust, NASA Technical Memorandum 4162, NASA Scientific and Technical Information Division, February 1990.
- [15] J.E.Marte and D.W.Kurtz, A Review of Aerodynamic Noise From Propellers, Rotors and Lift Fans, NASA Technical Report 32-1462, Jet Propulsion Laboratory, California Institute of technology, Pasadena, California, USA, January 1, 1970.
- [16] B.Shivashankara, D.Johnson and R.Cuthbertson, Installation Effects on Counter rotation propeller noise, AIAA -90-4023, AIAA 13th Aeroacoustics Conference, Tallahassee, FL, October 22-24, 1990.
- [17] Delft University of Technology. Open Jet Facility, 2008. [Online] Available at: <http://www.lr.tudelft.nl/en/organisation/departments-and-chairs/aerodynamics-and-wind-energy/wind-energy/facilities/open-jet-facility/> [Accessed 15 November 2012].

- [18] Hartuc T, Boundary Layer Ingestion: Theoretical and Experimental Research, Delft University of Technology, 2015.
- [19] T.Sinnige. Propeller Test Rig Setup and Operating Manual, Delft, the Netherlands: Delft University of Technology, 2013.
- [20] A.Roshko, On the drag and shedding frequency of two dimensional bluff bodies, NACA TN 3149, California Institute of technology, Washington, July 1954.
- [21] C.J.Apelt and G.S.West, The effects of wake splitter plates on the flow past circular cylinder in the range  $10^4 < R < 5 \times 10^4$  Part 1, Journal of Fluid Mechanics, vol. 61, part 1, pp. 187-198, 1973.
- [22] C.J.Apelt, G.S.West, The effects of wake splitter plates on the flow past circular cylinder in the range  $10^4 < R < 5 \times 10^4$  Part 2, Journal of Fluid Mechanics, vol. 71, part 1, pp. 145-160, 1975.
- [23] LinearX Systems Inc. M51 Measurement Microphone Product Brochure, 2000. [Online] Available at: <http://www.linearx.com/files/pdf/M51MicBrochure.pdf> [Accessed 18 September 2015].
- [24] P.D. Welch. The Use of Fast Fourier Transform for the Estimation of Power Spectra: A Method Based on Time Averaging Over Short, Modified Periodograms. IEEE Transactions on Audio and Electroacoustics, AU-15(2): pp. 70-73, 1967.
- [25] T.J. Mueller (ed.) Aeroacoustic Measurements. Berlin, Germany: Springer-Verlag Berlin Heidelberg New York, 2002.
- [26] P.J.W Block, NASA Langley Research Center, Hampton, VA; R.J. Klatte, Hamilton Standard Div. UTC, Windsor Locks, CT; and P.M. Druez, Douglas Aircraft Co., Long Beach, CA, Counter-Rotating Propeller Noise Directivity and Trends, AIAA-86-1927, AIAA 10th Aeroacoustic conference, Seattle, Washington, July 9-11, 1986.
- [27] P.J.W Block, NASA Langley Research Center, Hampton, VA, Pusher propeller noise directivity and trends, AIAA-86-1929, AIAA 10th Aeroacoustic conference, Seattle, Washington, July 9-11, 1986.
- [28] D.B. Hanson. Noise of Counter-rotation Propellers. Journal of Aircraft, 22(7): pp.609-617, 1985.
- [29] A.B.Parry, Theoretical prediction of Counter rotating propeller noise, PhD thesis, University of Leeds, February 1988.
- [30] M.A.Takallu, Effect of an upstream wake on a pusher propeller, PRC Kentron, Inc., Hampton, Virginia, USA, 1986.
- [31] A.K.Prasad, Particle Image Velocimetry, review article, Current Science, Volume 79, No 1, 10 July 2000.
- [32] A.K.Prasad, Stereoscopic Particle Image Velocimetry, Review paper, Experiments in Fluids 29 (2000), 103-116, Springer-Verlag, 2000.
- [33] Xiaofeng Liu, A Study of wake development and structure in constant pressure gradients, Phd thesis, University of Notre Dame, 2001
- [34] M.A.Takallu and J.C.Williams, Lift Hysteresis of an oscillating slender ellipse, AIAA. Vol 18, No 10, pp 1213-1220, 1980.
- [35] Dobrzynski, Werner M, Heller, Hanno H, Powers, John O, and Densmore, James E, DFVLR/FAA Propeller Noise Tests in the German-Dutch Wind Tunnel DNW,86-3, FAA-AEE, DFVLR-IB-129-86/3, 1986.
- [36] F-R. Grosche and H. Stiewitt, Aeroacoustic windtunnel measurements on propeller noise, in Aerodynamics and Acoustics of Propellers, 366 (DFVLR Institute for Experimental Fluid Mechanics, Bunsenstrasse 10, D-3400 Gottingen, F.R.G., 1984).
- [37] D.B. Hanson. Helicoidal Surface Theory for Harmonic Noise of Propellers in the Far Field. AIAA Journal, 18(10): pp. 1213-1220, 1980.
- [38] T.J. Mueller (ed.). Aeroacoustic Measurements. Berlin, Germany: Springer-Verlag Berlin, Heidelberg New York, 2002.



## RSB CALIBRATION MATRIX

As previously mentioned in Chapter 2, the RSB data which is in voltages is converted to forces and moments using the calibration matrix AR. The AR is composed of transpose of matrices AR1, AR2, AR3, AR4, AR5 and AR6. The calibration data of the RSB was provided by National Aerospace Laboratories of Netherlands (NLR).

$$AR = \begin{bmatrix} AR1' \\ AR2' \\ AR3' \\ AR4' \\ AR5' \\ AR6' \end{bmatrix}$$

$$AR1 = \begin{bmatrix} +0.9925573275868420000 \\ -0.0018176001003483700 \\ +0.0126993595748687000 \\ -0.0002259499445613100 \\ +0.0007507568360677470 \\ -0.0002245094152718480 \end{bmatrix}$$

$$AR2 = \begin{bmatrix} -0.0012761519197576200 \\ +0.0194234025282508000 \\ +0.0131537043399597000 \\ +0.0752474846522140000 \\ +0.0000505714021016737 \\ -0.0006890463073458560 \end{bmatrix}$$

$$AR3 = \begin{bmatrix} -0.0007438850134917890 \\ -0.0042899808783843600 \\ +2.4511869826357700000 \\ -0.0000152990920305381 \\ +0.0417408573501090000 \\ +0.0000685081188337167 \end{bmatrix}$$

$$AR4 = \begin{bmatrix} -0.0030423010166290500 \\ -0.0000197667968873751 \\ +2.7001634616817300000 \\ -0.0000180226097857718 \\ +0.1001791508076810000 \\ -0.0000858753244198466 \end{bmatrix}$$

$$AR5 = \begin{bmatrix} +0.0026349144684776600 \\ +2.4646540183332000000 \\ +0.0070086809396260200 \\ +0.0002249154265347060 \\ +0.0000681784893195201 \\ -0.0422227288558063000 \end{bmatrix}$$

$$AR6 = \begin{bmatrix} -0.0011236032331435400 \\ +2.6875487367838100000 \\ +0.0048023836622482200 \\ +0.0003512587203141810 \\ +0.0001369346504810690 \\ -0.1000914303037250000 \end{bmatrix}$$



# B

## MICROPHONE CORRECTIONS

In Chapter 2, the post processing of microphone measurements is presented. It was mentioned that the microphone data is corrected for frequency response and shear layer refraction effects. The methodology followed to correct the microphone measurement for frequency response and shear layer refraction is elaborated in Section B.1 and B.2 respectively.

### B.1. MICROPHONE FREQUENCY RESPONSE CORRECTION

The microphone measurements are affected by the diffraction and reflections created by the physical presence of microphone in the sound field. The response of the microphone varies with the frequency and a correction needs to be applied. Figure B.1 presents the microphone frequency response correction for all the microphone used during the experiments conducted at the OJF campaign.

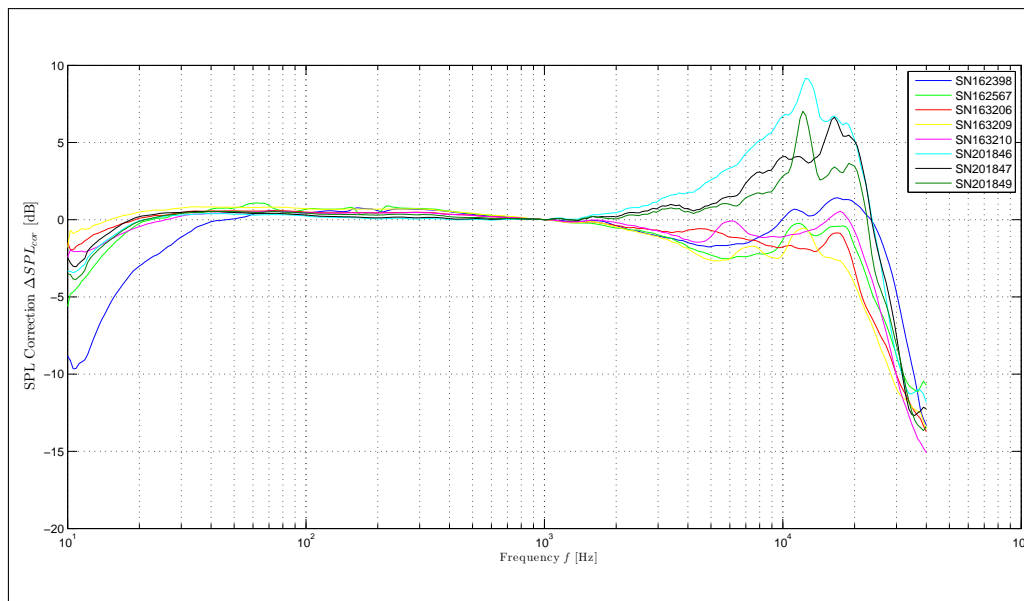


**Figure B.1:** Variation of Microphone response correction with frequency

The sound pressure level correction is applied by subtracting the computed SPL from the microphone measurements with the correction factor as given in Equation

$$SPL_{\text{fre,corr}}(f) = SPL_{\text{mic}}(f) + \Delta SPL_{\text{cor}}(f) \quad (\text{B.1})$$

The SPL correction factor is interpolated using a spline interpolation matlab function *interp1* to extract the correction factor at the actual frequency of interest. The microphone frequency response corrections are

applied for all the microphones used in OJF campaign. However, the corrections are not applied for the V-tunnel campaign.

## B.2. SHEAR LAYER REFRACTION CORRECTION

Bending of sound occurs when there is a velocity gradient causing different propagation speeds across the velocity gradient. Therefore, the sound will be deflected away from lower pressure region towards the higher pressure region. A wind tunnel shear layer having a velocity gradient at the edge of the test section also refracts the sound generated by a noise source. Both the pressure and direction of the sound wave change during the propagation of the sound wave through the shear layer. Hence, a correction needs to be applied to the microphone measurements to account for shear layer refraction effects. A correction method described by Mueller is employed to account for shear layer refraction effects [38]. The method assumes the shear layer as an infinitely thin cylindrical vortex sheet and the noise source is assumed to be on the open-jet center-line.

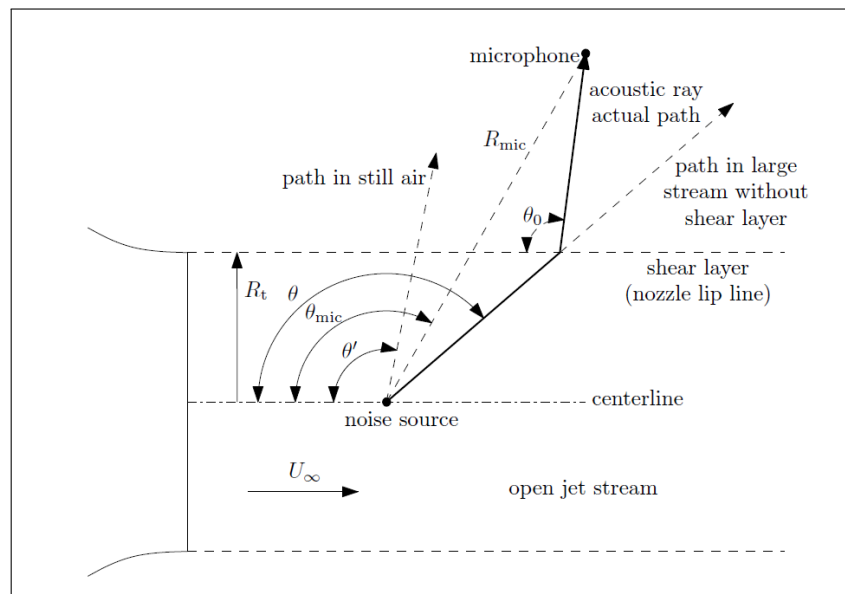


Figure B.2: Model representing the shear layer refraction process [38]

Figure B.2 shows the effect of shear layer refraction on the sound propagated from the noise source where

- solid line 'acoustic ray path' represents refracted acoustic ray
- dashed line 'path in large stream' is the propagation path of the same ray in large stream without shear layer
- dashed line 'path in still air' corresponds to the acoustic ray path at zero velocity

From the geometry of Figure B.2,

$$R_{mic} \cos(\theta_{mic}) = R_{sl} \cot(\theta) + (R_{mic} \sin(\theta_{mic}) - R_t) \cot(\theta_0) \quad (B.2)$$

where

$R_{mic}$  = source to microphone distance

$R_t$  = source to shear layer distance cross stream

$\theta_{mic}$  = angle to source-microphone vector

$\theta$  = propagation angle in flow

$\theta_0$  = angle to shear layer microphone vector

From wave convection,

$$\tan(\theta) = \frac{\sin(\theta')}{\cos(\theta') - M_\infty} \quad (B.3)$$



$\rho_0$  = air density outside the jet

$\rho_t$  = air density inside the jet

The Doppler factor is given by

$$D_t = \left[ 1 - M_\infty \cos(\theta') \right] \quad (\text{B.10})$$

The properties outside and inside the jet are considered the same and hence the ratios  $\frac{c_0}{c_t}$  and  $\frac{\rho_0}{\rho_t}$  are equal to 1.

# C

## ADDITIONAL RESULTS

### C.1. PROPELLER NOISE EMISSIONS

#### V-tunnel campaign

The propeller noise spectrum for the isolated configuration is treated in this subsection. Subsection 5.3.1 mentioned that the presence of fractional BPF,  $\frac{1}{2}$ BPF and  $\frac{3}{2}$ BPF, which is unexpected. Subsection 5.3.2 mentioned the presence of local maxima in the plot of SPL vs advance ratio.(refer Figure 5.11). To understand the presence of local maxima, propeller noise spectrum for this operating point is plotted in Figure C.1.

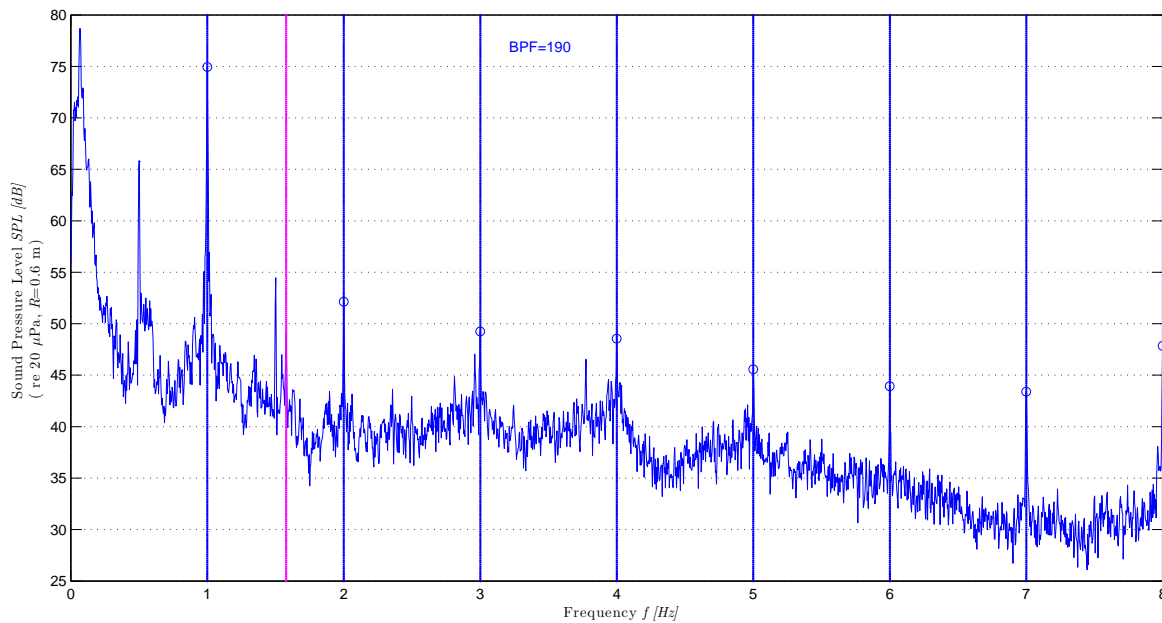


**Figure C.1:** Propeller noise spectrum

V-tunnel campaign: Isolated configuration,  $U_\infty = 20$  m/s,  $J = 0.9$ ,  $\theta_{\text{mic}} = 90^\circ$ ,  $\phi_{\text{mic}} = 180^\circ$ .

Figure C.1 clearly indicates the presence of tonal noise significantly at multiples of blade passage frequency. Sub-BPF scale harmonics,  $\frac{1}{2}$ BPF and  $\frac{3}{2}$ BPF, are also visible across the spectrum. Some of the possible reasons for the unexpected local minima at this advance ratio is the vibration of the propeller at advance ratio of 0.9.